CZECH TECHNICAL UNIVERSITY IN PRAGUE

Faculty of Civil Engineering
Department of Mechanics

Creep and Shrinkage of Concrete Subjected to Variable Environmental Conditions

DOCTORAL THESIS

Ing. Petr Havlásek

Ph.D. programme: Civil Engineering
Branch of study: Structural and Transportation Engineering

Supervisor: Prof. Ing. Milan Jirásek, DrSc

Prague, 2014

ČESKÉ VYSOKÉ UČENÍ TECHNICKÉ V PRAZE
Fakulta stavební
Thákurova 7, 166 29 Praha 6

PROHLÁŠENÍ

Jméno doktoranda: Petr Havlásek

Název disertační práce: Creep and Shrinkage of Concrete Subjected to Variable Environmental Conditions

Prohlašuji, že jsem uvedenou doktorskou disertační práci vypracoval/a samostatně pod vedením školitele prof. Ing. Milana Jiráska, DrSc.
Použitou literaturu a další materiály uvádím v seznamu použité literatury.

Disertační práce vznikla v souvislosti s řešením projektu:

v Praze dne 9. 5. 2014

podpis

Abstrakt

Tato práce je zaměřena na numerické modelování dotvarování a smršťování betonu vystaveného proměnlivým podmínkám okolního prostředí. Při nízké relativní vlhkosti dotvaruje beton méně než při plném nasycení, ale v průběhu vysychání dotvaruje více. Zvýšená nebo proměnlivá teplota rovněž vede ke zrychlení dotvarování.

Model založený na teorii solidifikace a mikropředpětí (MPS) je jedním z fyzikálně motivovaných materiálových modelů pro popis dotvarování a smršťování betonu, které zohledňují vliv teploty a relativní vlhkosti. V porovnání s modely z norem, které pracují s průměrnými hodnotami na úrovni průřezu, je tento model určen pro úroveň materiálového bodu. Tímto přístupem je možné věrněji vystihnout rozložení napětí v konstrukci. Vlastnosti modelu MPS jsou hlavním předmětem této práce. V práci je identifikována řada základních nedostatků modelu MPS a jsou představeny možnosti vedoucí k jejich odstranění. Při porovnání s experimenty vykazuje model MPS opačný vliv velikosti vzorku na dotvarování spojené s vysycháním, příliš vysokou poddajnost při opakovaných teplotních a vlhkostních cyklech a příliš vysokou citlivost na konkrétní volbu relativní vlhkosti zapečetěných vzorků.

Nejprve byla řídící rovnice modelu MPS ekvivalentně přeformulována a zjednodušena. Následně byl model zdokonalen a jeho chování bylo ověřeno na klasických experimentálních datech z literatury. Model byl naimplementován do konečně-prvkového programu OOFEM, který má otevřený zdrojový kód a je vyvíjen na Katedře mechaniky Fakulty stavební ČVUT v Praze.

Po kalibraci na experimentálních datech byl model použit pro analýzu skutečné konstrukce - vysychající betonové podlahy. Výsledky analýzy naznačují, že především vztah mezi smrštěním a relativní vlhkostí vyžaduje další vylepšení. Tento vztah bohužel zatím nelze s dostupnými experimentálními daty jednoznačně popsat. V práci je rovněž zpochybněn inženýrský přístup pro aktualizaci smrštění vycházející z výsledků krátkodobých měření.

Klíčová slova: beton, dotvarování, smršťování, vysychání, mikropředpětí, konečné prvky, numerické modelování

Abstract

This thesis deals with the numerical modeling of concrete creep and shrinkage at variable environmental conditions. At lower relative humidity concrete creeps more slowly than at full saturation but during drying it creeps faster. Creep is also accelerated at elevated temperature or by temperature variations.

One of the physically based models for concrete creep and shrinkage that takes into account variable temperature and humidity is based on the theory of microprestress and solidification (MPS). Unlike the MPS model to the models from the design codes which use the average cross-sectional approach, the MPS model operates at the material point level, which makes it possible to capture the stress distribution more realistically. Assessment of the MPS model is the main topic of this work. Several severe deficiencies of this model have been identified and appropriate remedies have been proposed. Comparing to the experiments, the original formulation of the MSP model exhibited the opposite size-effect on drying creep, spurious sensitivity to the particular choice of relative humidity and excessive compliance during the repeated cycles of temperature and relative humidity.

First, the model was reformulated, making the governing equations simpler yet equivalent. Afterwards, the model was improved and validated on typical examples from the literature. The MPS model was implemented into the open-source finite element package OOFEM developed mainly at the Department of Mechanics, Faculty of Civil Engineering, CTU in Prague.

The model was calibrated on the experimental specimens, and afterwards applied in the analysis of a real-world structure - a concrete floor subjected to drying. The results indicate that even the improved model needs further improvements regarding the relationship between shrinkage and relative humidity; however, this relationship cannot be uniquely identified from the currently available experimental data. The engineering approach of shrinkage updating based on short-time measurements has also been questioned.

Keywords: concrete, creep, shrinkage, drying, microprestress, finite elements, numerical modeling

Acknowledgments

I would like to express my sincere thanks and warmest gratitude to all those who encouraged and supported me throughout my Ph.D. study. Without their support this thesis would have never been written.

My special thanks belong to

- my supervisor, Prof. Milan Jirásek, for his patient guidance and support
- Prof. Zdeněk P. Bažant who was my mentor during my visit at Northwestern University
- members of the Department of Mechanics: Bořek Patzák, Vít Šmilauer, Jaroslav Kruis, Daniel Rypl, Jan Zeman, Zdeněk Bittnar, Jan Sýkora, Jan Vorel, Matěj Lepš
- people who helped me in the experimental work: Pavel Padevět, Petr Bittnar and Zdeněk Vyskočil
- Prof. Carlos Videla and Carlos Aguilar for providing me with the experimental data utilized in Chapter 8
- my colleagues: Martin Horák, Jan Stránský, David Krybus, Petr Hlaváček, Filip Kolařík, Adéla Pospíšilová and Eva Myšáková
- my colleagues from Northwestern University: Mija Hubler, Roman Wendner and Marco Salviato
- my colleagues from Červenka Consulting where I mentally relaxed working on real-world problems
- my family and friends

During the four years of the Ph.D. study, the financial support was provided by

- the Czech Science Foundation under projects No. P105/10/2400 and 103/09/H078,
- the Grant Agency of the Czech Technical University in Prague, grants No. SGS10/020/-OHK1/1T/11, SGS11/021/OHK1/1T/11, SGS12/027/OHK1/1T/11, SGS13/034/OHK1/-1T/11, SGS14/029/OHK1/1T/11,
- the European Union, OP RDI project no. CZ.1.05/2.1.00/03.0091 - University Centre for Energy Efficient Buildings.

The financial support is gratefully acknowledged.

Contents

Notation

Lowercase Latin symbols

Symbol	Unit	Description
a	kg/m^3	aggregate content in the concrete mixture
c	kg/m^3	cement content in the concrete mixture
c	kg/m·s	permeability
c	J/kg·K	specific heat
f_{ck}	MPa	characteristic compressive strength
f_{cm}	MPa	mean compressive strength
$f_{cm,28}$	MPa	mean compressive strength at the age of 28 days
f_t	MPa	tensile strength of concrete
h	$-$	relative humidity (of pores)
h_{env}	$-$	relative humidity of the ambient environment
k_{sh}	$-$	shrinkage constant - MPS theory
m_w	kg	water mass
m_s	kg	mass of the dried solid
p	Pa	pressure
p_{sat}	Pa	saturation vapor pressure
p, $\tilde{p}$	-	exponents - MPS theory
q	W/m^2	heat flux
q_1–q_4	MPa^{-1}	basic creep parameters - B3 model
t	day	time
t_e	day	equivalent time
t_r	day	reduced time
t_S	day	reduced microprestress time
t'	day	age at loading
t_0	day	age at the end of curing, age at the beginning of drying
$\hat{t}$	day	duration of loading $= t - t'$
u	$-$	moisture ratio
w	kg/m^3	moisture content
w	kg/m^3	water content in the concrete mixture
w/c	$-$	water-to-cement ratio by mass
w_e	kg/m^3	content of evaporable water
w_{frozen}	kg/m^3	content of frozen water
w_f	kg/m^3	moisture content at free saturation

Uppercase Latin symbols

Symbol	Unit	Description
C	1/Pa	specific creep
$C(\varphi)$	m^2/s	diffusivity of concrete
D	m	effective thickness
E	GPa	modulus of elasticity or spring stiffness
E_0	GPa	asymptotic modulus of elasticity
$E_c(t)$	GPa	secant modulus of elasticity at time t
E_{ci}	GPa	tangent modulus of elasticity
$E_{c,28}$	GPa	modulus of elasticity at the age of 28 days
E_{dyn}	GPa	dynamic modulus of elasticity
G_f	N/m	fracture energy
H	$-$	Heaviside function
H	J/m^3	total enthalpy
$J(t,t')$	MPa^{-1}	compliance function
J	$kg/m^2{\cdot}s$	water mass flux density
J_b	MPa^{-1}	compliance function for basic creep
J_f	MPa^{-1}	compliance function for purely viscous part of creep
J_v	MPa^{-1}	compliance function for viscoelastic part of creep
J_v	$kg/m^2{\cdot}s$	vapor diffusion flux density
J_w	$kg/m^2{\cdot}s$	liquid water flux density
Q	W/m^3	heat source or sink
Q_e/R	K	activation energy for the hydration process
Q_r/R	K	activation energy for the processes in the microstructure
Q_S/R	K	activation energy for the microprestress relaxation
$R(t,t')$	MPa	relaxation function
S	MPa	microprestress
S_w	$kg/m^3{\cdot}$ s	moisture source or sink
T	°C, K	temperature, absolute temperature
T_0	K	reference (room) temperature
V_w	m^3	water volume
V_{pores}	m^3	volume of pores
V_{tot}	m^3	total volume

Greek symbols

Symbol	Unit	Description
α_e	$-$	constant - MPS theory, hydration
α_r	$-$	constant - MPS theory, rate of bond breakages
α_s	$-$	constant - MPS theory, microprestress relaxation
α_T	K^{-1}	coefficient of thermal expansion
δ	m^2/s	thermal diffusivity
ε	$-$	strain
ε_c	$-$	creep strain
ε_{cr}	$-$	cracking strain
ε_e	$-$	elastic strain
ε_f	$-$	flow (purely viscous) strain
ε_v	$-$	visco-elastic strain
ε_{sh}	$-$	shrinkage strain
ε_T	$-$	temperature strain
$\varepsilon_{sh,a}$	$-$	autogenous shrinkage strain
$\varepsilon_{sh,d}$	$-$	drying shrinkage strain
$\varepsilon_{sh,u}$	$-$	ultimate shrinkage strain
η	$Pa \cdot s$	viscosity
η_f	$Pa \cdot s$	viscosity of the aging dashpot in the MPS model
λ	W/m·K	thermal conductivity
μ_S	$Pa^{-1} \cdot s^{-1}$	constant controling fluidity - MPS theory
ν	$-$	Poisson's ratio
ω	$-$	damage
ρ	kg/m^3	density
ρ_{dry}	kg/m^3	dry material density
σ	MPa	normal stress
τ	s	retardation time
τ_{sh}	s	shrinkage half-time
τ_w	s	drying half-time
φ	$-$	creep coefficient
φ_∞	$-$	ultimate creep coefficient
Φ	MPa^{-1}	non-aging creep function of the C-S-H gel
Δw_∞	kg/m^3	ultimate moisture loss at given relative humidity
∇		gradient operator
$\nabla\cdot$		divergence operator

1 Introduction, Motivation & Goals

Even though the importance of rheological properties of concrete in structural design has been known for many decades (see examples in Fig. 1.1 and 1.2), the current civil engineering practice of designing ordinary reinforced-concrete structures is focused mainly on the first ultimate state (ULS) – the ultimate load-bearing capacity – and often very simplistic methods are used for the second ultimate state – the serviceability limit state (SLS).

Figure 1.1: Veurdre bridge over Allier (1911–1912) designed by E. Freyssinet [1], flattened three-span arch concrete bridge with central span 72.5 m; increasing deflections caused by shrinkage and creep (12 - 13 cm in three years); problem solved by additional thrust jacks in the center of the arches.

Figure 1.2: Bridge at Villeneuve-sur-Lot (1914–1920) designed by E. Freyssinet [1], plain concrete arch bridge with 96m span; decentering jacks at the crown introduced already in the design phase.

The latter limit state covers criteria which are necessary for the functional and intended purpose of the structure, as well as for the occupants' comfort. Very often, only the most common criterion – the ultimate deflection (deflection/span ratio) – is considered, keeping the other

conditions, such as the criteria on crack width or structural vibrations, unresolved. Meeting the requirements of the first limit state does not essentially mean that the second limit state is fulfilled. Certainly, considering only the ULS can save certain amount of money during the construction process; the same amount or even more will be necessary after several years for inevitable maintenance and repairs.

In the structural design, very often, only the linear computation is performed and only the "active loads" are considered. In linear analysis indirect loading caused by temperature and shrinkage cannot be applied realistically. According to the design codes, concrete is assumed to have zero tensile strength, but in the numerical computations the tensile stresses (caused by the shrinkage or thermal contraction due to cooling) are transmitted. (E.g. assuming that the homogeneous restrained member with Young's modulus 30 GPa shrinks 300×10^{-6}, tensile stress of 9 MPa develops, which naturally cannot be transmitted; this would lead to crack formation and development, which in turn makes the linear analysis inappropriate for the purpose.)

Shrinkage is sometimes considered in the design of the floor slabs (Figs. 1.5, 1.6), underground monolithic walls (Fig. 1.3) or "white tanks" – underground waterproof concrete basement system without additional hydro-insulation layer (Fig. 1.4). The presented pictures indicate that even nowadays the taken measures do not have the desired effect. The technological (concrete class, cement type, additives, admixtures) or structural measures (e.g. "shrinkage stripes") are often preferred to additional reinforcement. Very often, the problem is not the quality of the material but the poor knowledge of the material behavior. For example in the design of the white tanks, in contrast to the ordinary structural members, the higher class of concrete does not necessarily mean better performance.

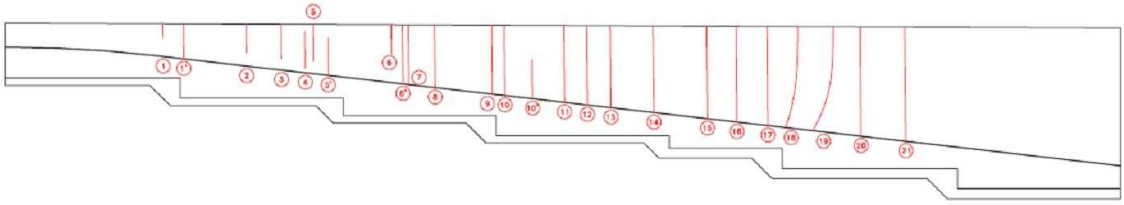

Figure 1.3: Shrinkage cracking in a cantilever retaining wall (reinforced concrete of thickness 400/250 mm).

Comparing to shrinkage, the other time-dependent phenomenon characteristic of concrete – creep – does not necessarily cause problems if properly considered. One beneficial effect of creep is the relaxation of stresses induced by the above-mentioned shrinkage strains or by the support movement of statically indeterminate structures. On the other hand, creep leads to bigger deflections, in slender compressed structures creep can even cause collapse due to the delayed buckling. Creep reduces forces in the prestressing cables and is also responsible for the stress redistribution from concrete to reinforcing steel, which can eventually start yielding (e.g. columns in high-rise buildings). Creep is often responsible for the excessive bridge deflections [21].

Both concrete creep and shrinkage depend on the development of moisture distribution in concrete, which in turn depends on the environmental humidity, temperature, on the size and shape of the concrete member as well as on the highly non-linear dependence of concrete diffusivity on relative humidity. Moreover, temperature and its changes influence creep.

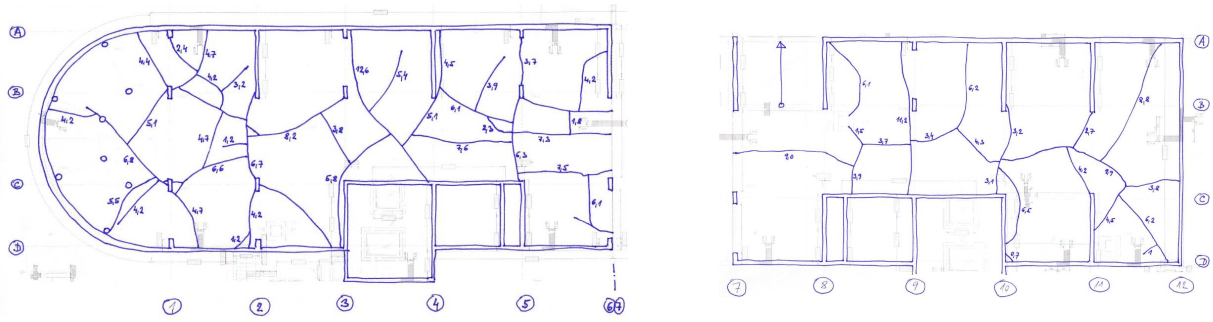

Figure 1.4: Shrinkage cracking (average crack width 1 mm) in a slab foundation designed as a white tank (thickness 400 mm, concrete grade C30/37, bottom reinforcement ⌀12/200 mm and top ⌀10/200 mm).

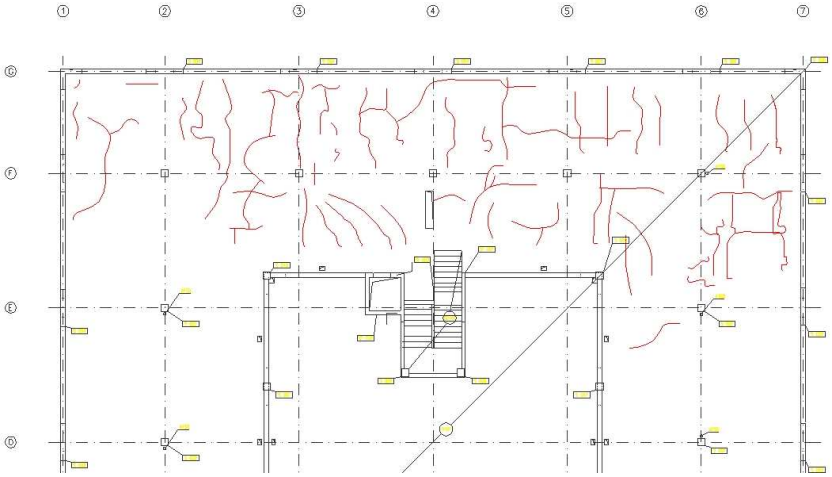

Figure 1.5: Cracks in the bottom surface of the floor slab (thickness 220 mm, average crack width 0.2 mm); cracking caused by concreting in hot weather and by keeping the structure unsheltered for 3 years.

Sometimes the effects of elevated temperature are considered, but only in relation to the ULS; the effect of elevated temperature or temperature cycles on the concrete creep or the development of concrete maturity is usually neglected. However, some nuclear reactor vessels or prestressed bridges suffer from excessive deflections or prestress losses caused by thermally accelerated creep.

Significance of the thermally induced creep is declared by the number of extensive research studies and projects from the 1960s and 70s e.g. [66], [71], [70], [51] when the nuclear industry experienced a boom in the USA.

The main goals of the thesis are to

- make a review of the existing models for concrete creep and shrinkage with regard to ambient conditions;
- present, apply and calibrate models for moisture and temperature transport including the choice of boundary conditions;

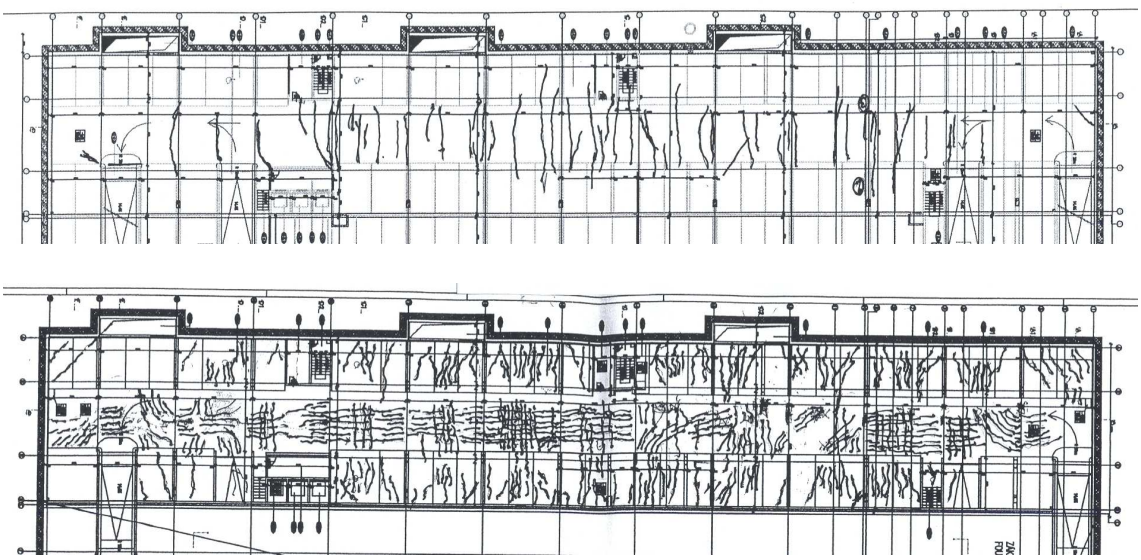

Figure 1.6: Cracking (partially due to shrinkage) in the top and the bottom surface of the floor slab in underground garages accompanied by excessive deflections (incorrect design of reinforcement).

- critically assess the performance of the material model based on the theory of solidification and microprestress and to propose its improvement if necessary;
- revise the existing methodology for shrinkage updating based on short-term measurements;
- develop and implement a universal and realistic material model for concrete creep and shrinkage with possibility of tensile cracking, applicable to real structures

2 Introduction to Creep and Shrinkage

It is generally accepted that the total deformation of concrete can be decomposed into the instantaneous and delayed components, or into the stress-induced (instantaneous deformation and creep) and stress independent components (shrinkage or swelling, thermal strains).

2.1 Elastic modulus

The instantaneous deformation is characterized by the Young modulus and Poisson's ratio. The initial Young's modulus E_{ci} is defined as the tangent modulus of elasticity at the origin of the stress-strain diagram. Its approximate value corresponds to the slope of the experimentally measured unloading branch in the stress-strain diagram obtained from the static loading test [48]. This loading test is performed on cylinders subjected to uniaxial compression, loaded to specified fraction of the mean ultimate compressive strength f_{cm}(33 % (British Standards) – 40 % (*fib* [48], American Society for Testing and Materials (ASTM)).

Sometimes it is more convenient to use the secant modulus E_c, which includes also the plastic and creep strains. This modulus can be estimated from the same experiment as E_{ci}. It corresponds to the slope of the line connecting the origin and the point of 40 % f_{cm} (or different value according to the code specifications) of the loading branch of the stress-strain diagram. The Eurocode 2 [91], uses this approach and does not use initial modulus E_{ci} at all.

The interpretation of the "instantaneous deformation" might be misleading; based on observations, it is almost impossible to accurately split the deformation into the instantaneous and the delayed part. To make a practical distinction between the instantaneous and delayed deformation, the deformation occurring during loading is (from the engineering point of view) considered as elastic, while the subsequent deformation as delayed.

The stiffness of the concrete grows as the duration of loading decreases, for load durations approx. 10^{-7} day, the corresponding modulus is denoted as the "dynamic modulus", E_{dyn}, and for the loading durations $(t - t')$ approaching zero, the modulus is called "asymptotic", E_0.

The modulus of elasticity is closely related to the compressive strength of concrete. Time evolution of the compressive strength and the hydration degree is similar. The hydration degree is influenced by several factors, such as cement type, water-to-cement ratio, curing and environmental conditions, additives, admixtures and time. At elevated temperatures the hydration reaction is accelerated and the compressive strength (and elastic modulus as well) grows faster; on the other hand, the final value of the compressive strength (and elastic modulus) is lower. The reduced value of the compressive strength is probably caused by lower hydration degree. Due to the accelerated hydration reaction, the hydration products do not diffuse uniformly in the cement paste and remain non-uniformly distributed only in the vicinity of the cement particles. This phenomenon is taken into consideration in the *fib* Model Code [49], see Section A.14

According to reference [72], the final value of elastic modulus is strongly temperature-dependent. At temperatures below zero, its value is higher than at room temperature, on the other hand, with increasing temperature it almost linearly decreases (starting from approx. 100 °C). However, in the range 21–96 °C there is no significant change in elastic modulus.

For prediction of the elastic modulus, the design codes introduce expression, according to which the modulus is related to a certain power (ACI 1/2, *fib* 1/3) of the mean compressive strength multiplied by a correction factor related to the aggregate type or density. Since the aggregates usually have higher modulus of elasticity than the hydrated cement paste (except

light-weight aggregates), a higher aggregate content in concrete mixture results in a higher modulus of elasticity.

2.2 Poisson's ratio

In the linear stress range, the Poisson ratio ν usually lies in the interval from 0.14 to 0.26 (according to [48]), and from 0.15 to 0.22 (according to [72]). Very often it is taken as 0.18 or 0.2. It is assumed that its value does not evolve in time (of course except fresh concrete before hardening). Therefore, for the same loading, the ratio between the lateral and longitudinal strains is the same for both elastic and creep deformation.

2.3 Creep

Creep refers to the stress-induced delayed deformation.

Concrete creep has many beneficial as well as negative aspects. Creep reduces stresses due to the differential (or restrained) shrinkage or temperature, which leads to less pronounced cracking; in statically indeterminate structures creep reduces stresses caused by support settlement. On the other hand, creep leads to bigger deflections, and in slender compressed structures can even cause collapse due to the delayed buckling. Creep reduces forces in prestress cables and is also responsible for redistribution of stresses to reinforcing steel, which might start yielding.

Creep can be considered as linear (principle of superposition holds) if the (compressive) stress does not exceed 40–60% of the mean compressive strength of concrete and 80–85% of mortar. Nonlinear creep at excessive stresses is mainly caused by microcracking close to the aggregates.

The creep deformation is usually additively split into the "basic" creep (sometimes called "true") and the "drying" creep component. Basic creep refers to the deformation of a sealed concrete member (i.e. no moisture transfer to or from the surrounding environment) and at room temperature. Additional creep caused by drying (moisture changes in general) or elevated temperature is referred to as "drying creep". Similarly to shrinkage, drying creep is assumed to be bounded.

To determine the basic creep experimentally, usually one (referring to geometry not quantity) specimen is sufficient. In case of pronounced autogenous shrinkage characteristic of modern concretes, two specimens are necessary: one specimen loaded and the second stress-free; basic creep is then the difference of the measured strains. Similar procedure can be used to determine the drying creep: shrinkage is measured on the first load-free drying specimen, basic creep is measured on loaded and sealed specimen, and finally basic and drying creep and the shrinkage deformation on the last one. The dimensions of the drying specimens must be equal, sealed specimens can differ.

Concrete creep is influenced by all its constituents as well as by the loading time, its duration and environmental conditions. Very generally, the used constituents, the type and duration of curing and the age of loading affect mainly the amplitude of creep, while the environmental conditions affect not only the amplitude, but also the time development of creep. Concrete behaves as an aging viscoelastic material. Earlier age at loading and longer duration of loading increase creep (see Fig. 2.1).

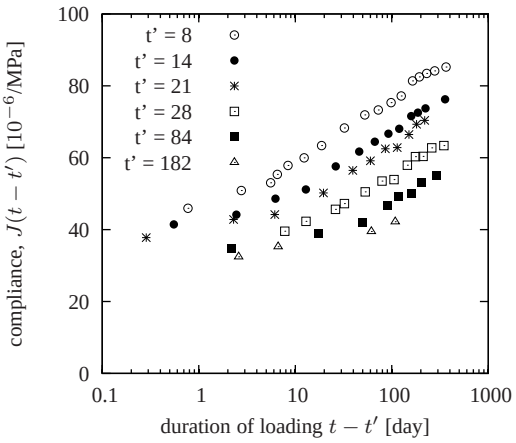

Figure 2.1: Influence of the loading age on the compliance function as reported in [45]; all specimens were sealed.

Aggregates usually do not creep and are stiffer than the hydrated cement paste. Therefore, a higher content of stiffer aggregates of bigger notional size acts as a powerful restraint and the concrete creeps less. Creep is related to the content of cement paste, but the relation is not linear [72]; however, reference [47] recommends proportionality as a first approximation. Other relevant factors are: type of cement and its fineness, water-to-cement ratio, compressive strength, stress-strength ratio, admixtures and additives, and of course environmental conditions and size of the structural member.

2.3.1 Influence of the ambient relative humidity and temperature

Concrete creep is influenced by both ambient relative humidity and ambient temperature. If a concrete member is placed in the environment with a lower relative humidity, it will start drying. The drying rate depends on the size (see Fig. 2.3) and shape of the concrete member and on the concrete diffusivity. Until the relative humidity of the pores is equilibrated with the environmental humidity (and perhaps even later), concrete creeps more than if it were sealed, see Fig. 2.2. On the other hand, the rate of creep of predried concrete is lower than the creep rate of sealed concrete. It seems that creep is influenced also by the rate of drying.

Temperature influences concrete creep in a similar way. The higher the temperature, the higher the creep rate, see Fig. 2.4 and 2.5. Sudden changes in temperature or its other (cyclic) variations lead to a further increase in creep rate, see Fig. 2.6. As was mentioned previously, a higher temperature accelerates the hydration reaction and thus leads to a faster growth of stiffness but the final value of the stiffness/strength is smaller compared to normal conditions.

2.3.2 Creep in compression, tension and bending

Since the concrete is used mainly in compressed structural members, most of the creep tests studied creep on the laboratory specimens subject to compression. Creep in tension and bending has always been assumed to be the same as in compression. Creep experiments in compression are also easier to carry out and the compliance function can be easily expressed as a difference between the total deformation measured on a loaded specimen and the deformation measured on an unloaded companion specimen divided by the loading stress. Creep in tension and bending

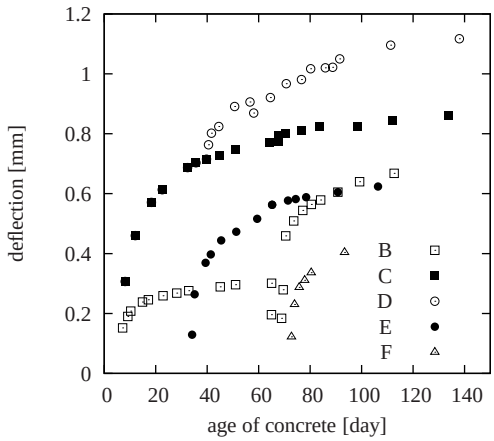

Figure 2.2: Pickett [79] measured prismatic concrete beams subjected to bending; B = sealed specimen, unloading, reloading + drying; C, E, F = cured until loading, then drying; D = drying and wetting cycles.

is harder to separate from the total deformation since certain (yet unknown) portion of the total deformation is represented by the cracking strain. Tensile creep of young concrete is even harder to measure and the scatter of the experimental results is quite substantial. This is due to the fact that the creep strain in tension is of the opposite sign and similar magnitude as the autogenous shrinkage which develops mainly during the first several days of hydration.

Many publications from the last several years examined creep in tension and bending in relation to the creep in compression [85] [86] [41] [75] [82] [81] [90] [83]. The summary presented in [61] indicates that no unanimous conclusion can be drawn.

To start with, reference [90] studied basic creep of concrete in compression, tension and bending. The 28-day compressive strength was 39.9 MPa and the tensile strength at the same age was 2.4 MPa. The concrete mixture contained 340 kg/m^3 of cement, 184 kg/m^3 of water (w/c = 0.54), and 1811 kg/m^3 of aggregates; no other additives or admixtures were used. The autogenous shrinkage was almost negligible. At the age of 64 days the specimens were loaded to 50 or 70 % of the concrete strength. Tensile creep specimens showed almost no nonlinearity and the specific creep in tension after 30 days was about 1/3 or 1/4 of the specific creep in compression measured at 50 % and 70 % of strength, respectively. However, in bending (4-point bending, L = 60 cm, H = 20 cm) the axial strains were symmetrical about the center of gravity which indicates the same creep both in tension and compression. This difference was explained by the size-effect on basic creep in tension. Such a size-effect was presented in [75] but only on beams loaded at 80% of the instantaneous carrying capacity, a way beyond the linear creep range. More results with the same concrete as in [90] are presented in [85] which shows that the creep of the drying specimens is in tension and compression very similar. In this study the specimens loaded in tension had different diameter (13 cm) than for compression test (16 cm). This should not play any role in case of basic creep but it influences the rate and the magnitude of the drying creep. The same concrete was used in [86]. This paper presents a link between the creep in general and the cumulative amount of microcracking, this relationship being almost linear. The microcracking was detected using the acoustic emission sensors. However, the stress/strength ratio used in the experiments of this study was in the range 0.54–0.8 which exceeds the limit of the linear creep 0.4. The higher was the stress the better was the agreement of the linear relationship. The same reference presents a theory based on microcracking

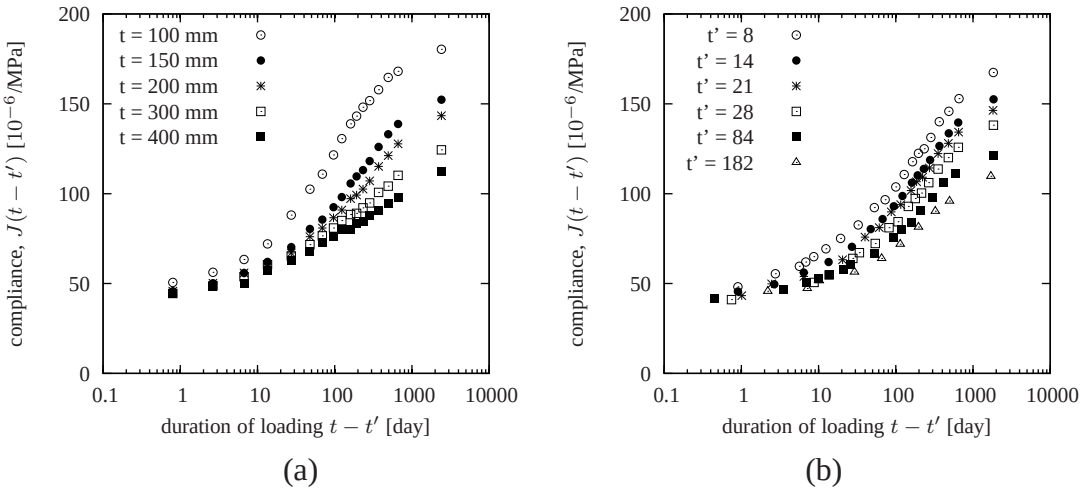

Figure 2.3: Compliance functions of the slabs drying at 60% relative humidity [45] (a) variable thickness, D, constant age at loading $t' = 14$ days (b) thickness 150 mm, variable age at loading; onset of drying at $t_0 = 8$ days.

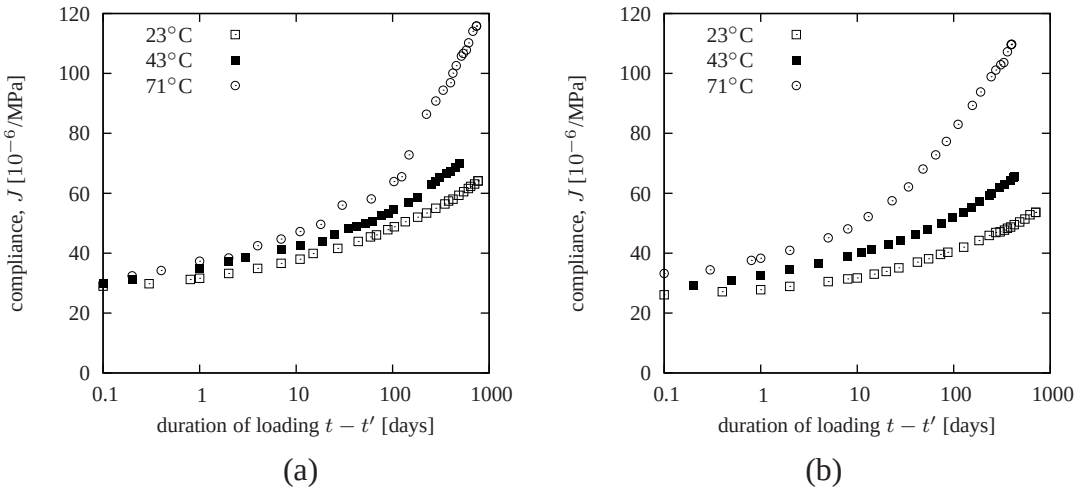

Figure 2.4: Compliance function at elevated temperature reported by Kommendant et al. [66], (a) t' = 28 days, (b) t' = 90 days.

which tries to clarify the differences between the magnitude of the basic creep in tension and compression.

References [82] and [81] focused on basic creep of HPC (c = 400 kg/m^3- CEM I 52.5R, w = 178 kg/m^3 (w/c = 0.45), a = 1803 kg/m^3, superplasticizer 2.2 kg/m^3) with compressive strength 69.7 MPa and tensile strength 3 MPa. The specimens were loaded at 50% of the compressive or tensile strength at the age of 28 days. The specific creep in tension was increasing up to approx. 10 days with the maximum value 4×10^{-6} MPa^{-1} (1/3 of the specific compressive creep at that time) and then decreasing at constant rate; zero specific creep was crossed at 70 days after loading. During the first 5 days of loading the specific creep in bending was almost the same as in tension and afterwards its rate was the same as in compression. The autogenous shrinkage recorded since the age of 28 days was increasing approximately linearly with the maximum value 15×10^{-6} after the additional 80 days. However, the experimental measurements for

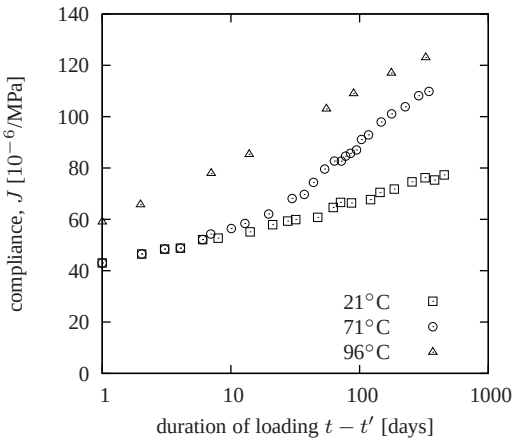

Figure 2.5: Compliance function at elevated temperature reported by Nasser and Neville [71], $t' = 14$ days, all specimens cured already at the desired temperature.

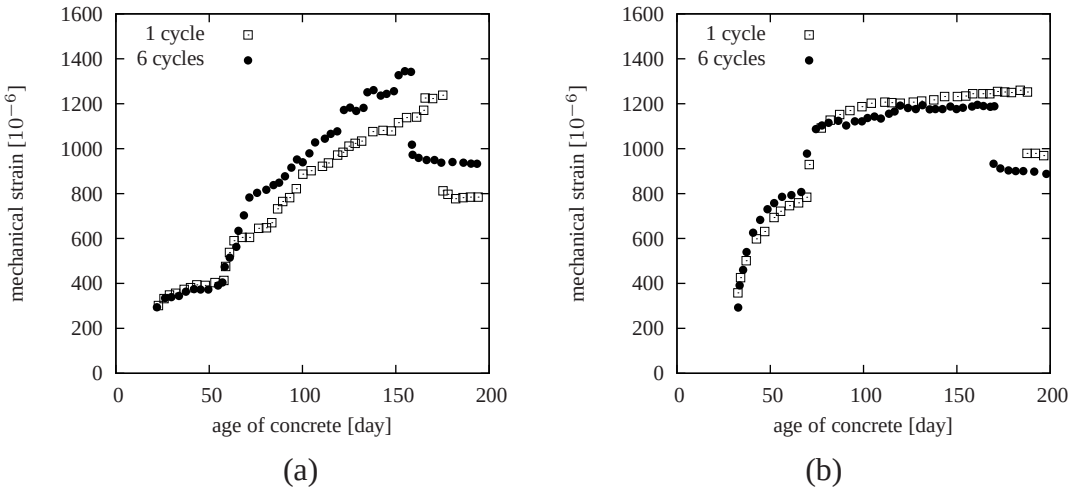

Figure 2.6: Mechanical strain for one and six thermal cycles and (a) sealed specimens (b) drying specimens; experimental data from [51].

tension and bending exhibited rather high scatter.

Creep of concrete at early age in compression and tension is documented in [41], here the kinetics as well as the creep rate was found to be very similar.

In [83] the specific basic creep in compression and tension was recognized to be in the ratio approximately 2:1. The concrete mixture was the same as "B11" in [57], concrete cylinders 13×50 cm were loaded at the age of 90 days, but the creep experiment took only 6 days (3 days loading and 3 days creep recovery).

Even though the ratio between the specific creep in compression and tension might be quite high, the ratio between the compliance functions (when 1/E is added to the specific creep) is much lower. E.g. for [90] the ratio of the specific creep (compression:tension) was approximately 3:1, but the compliance functions are in ratio 1.3:1. In most concrete structures the overall structural behavior is governed by the behavior in compression, therefore the compliance function in tension can be taken the same as in compression.

2.3.3 Different ways for creep description

There are three ways to express stress-induced delayed deformation. The first one, in engineering practice most common, uses the so-called "creep coefficient", $\varphi(t,t')$ [-] (usually 0–6), which relates the creep deformation ε_c to the instantaneous deformation ε_e. For constant stress

$$\varepsilon_c(t) = \varphi(t,t')\varepsilon_e \tag{2.1}$$

The total deformation caused by constant stress $\hat{\sigma}$ acting since time t' is then

$$\varepsilon(t) = \varepsilon_e + \varphi(t,t')\varepsilon_e = \hat{\sigma}\frac{1+\varphi(t,t')}{E_0(t')} \tag{2.2}$$

(In several design codes, the instantaneous modulus is replaced by the secant modulus E_c or even by its value at the age of 28 days, $E_{c,28}$.)

The second approach (widely used in the U.S.) expresses the delayed deformation in terms of "specific creep" $C(t,t')$ [1/Pa], which has a meaning of the delayed deformation caused by a unit stress.

$$\varepsilon(t) = \varepsilon_e + \varepsilon_c(t) = \hat{\sigma}\left(\frac{1}{E_0(t')} + C(t,t')\right) \tag{2.3}$$

The last approach is based on the "compliance function", $J(t,t')$ [1/MPa]. This function corresponds to the total strain caused by a constant unit stress acting since time t'.

$$\varepsilon(t) = \varepsilon_e + \varepsilon_c(t) = \hat{\sigma}J(t,t') \tag{2.4}$$

The conventional elastic modulus at age t' does not even have to be part of a compliance function, but it can be evaluated as

$$E_c(t') = 1/J(t'+\Delta t, t') \tag{2.5}$$

where Δt is usually taken as 0.01 day or 15 minutes.

2.4 Shrinkage and swelling

Shrinkage and swelling refer to a gradual change in volume, which is not caused by external stress. Shrinkage or swelling can be categorized according to its origin into the plastic shrinkage (physical origin), autogenous shrinkage (physical origin caused by chemical reaction), carbonation shrinkage (chemical origin) and drying shrinkage and swelling (physical origin). These types of shrinkage have different magnitude and develop differently in time. Free (unrestrained) shrinkage means that it can fully develop and the concrete member is stress-free. On the other hand during restrained shrinkage macroscopic stresses develop. Concrete member can be restrained externally (e.g. fixed supports) or internally (e.g. drying shrinkage in concrete beam – restraint is its planar cross-section resulting in a non-uniform stress distribution).

Shrinkage and swelling is believed to be bounded. This idea is accepted also in all design codes and recommendations (known to the author) except for GL2000 model [54], see Section A.12.

2.4.1 Plastic shrinkage

Plastic shrinkage refers to the concrete contraction when it is in a plastic state. It origins from the surface water loss caused by concreting in inappropriate environmental conditions or due to the moisture migration to neighboring dry material (old concrete or soil). This type of shrinkage can result into considerable surface cracking; the cracking pattern is (comparing to the plastic settlement cracking) usually randomly oriented. This type of shrinkage and resulting cracking can be prevented if the amount of evaporated moisture does not exceed the amount provided by "bleeding" (the limit value is considered 1 kg/m^2); therefore concreting should take place at high relative humidity, low wind speed and temperature. Also, the higher the content of cement and fine aggregates and the lower the water-to-cement ratio, the more prone is the concrete to plastic shrinkage.

2.4.2 Autogenous shrinkage

During the cement hydration reaction the unhydrated cement reacts with the mixing water creating hydration products (mainly calcium silicate hydrates and calcium hydroxide) and heat. The hydration products have slightly smaller volume than the reactants – this decrease in volume is referred to as a chemical shrinkage. The chemical shrinkage is partially restrained by the solid phase composed of the hydration products. This results in emptying of capillary pores and in the drop of relative humidity (so called internal drying or self-desiccation) and in the simultaneous increase of capillary tensile forces. These forces cause the bulk contraction referred to as an autogenous shrinkage. The autogenous shrinkage, comparing to the other types of shrinkage, occurs even in completely sealed concrete (i.e. no moisture transfer to or from it) and is not differential (the same magnitude on the surface and in the core of the specimen). Of course, in massive structures, the autogenous shrinkage can develop differently across the cross-section owing to the hydration heat which is produced. The generated temperature additionally accelerates the hydration reaction and thus accelerates the autogenous shrinkage.

The typical values of the autogenous shrinkage of an ordinary concrete ($w/c > 0.4$) are almost negligible (approximately 40×10^{-6}) compared to the magnitude of the drying shrinkage. The decrease in relative humidity of pores of the sealed specimens is called a self-desiccation. In ordinary concretes the final value is usually taken as 92 % to 98 %. However, in the high-performance concretes with very low water-to-cement ratio the autogenous shrinkage cannot be neglected, it can even exceed the drying shrinkage. In these concretes, the relative humidity of the pores can decrease only due to self-desiccation to 70 %.

In older design codes, the autogenous shrinkage was not treated or was lumped with the drying shrinkage. However, for modern concretes it is necessary to consider it separately. The reason is its higher magnitude and the time evolution different from the evolution of the drying shrinkage. (In the Model Code, the autogenous shrinkage has been considered since 1999 [47].)

2.4.3 Carbonation shrinkage

The carbonation shrinkage [72] is accompanied by two chemical reactions. In the first one, the carbon dioxide reacts with water and forms carbonic acid, $CO_2 + H_2O \rightarrow H_2CO_3$. In the stressed areas, the carbonic acid dissolves the crystals of calcium hydroxide and creates calcium carbonate $H_2CO_3 + Ca(OH)_2 \rightarrow CaCO_3 + 2H_2O$, which is deposited in the stress-free spaces. This process results in higher compressibility and usually is treated as shrinkage. This

reaction is humidity-dependent, the highest reaction rate is at 50% relative humidity, while at full or zero saturation this reaction almost stops. Carbonation reaction can lead to misinterpretation of the drying shrinkage, when only the weight decrease is measured. The reason is that this reaction results in mass increase (carbon dioxide is absorbed) of the concrete member, while during drying shrinkage the weight is lost. When these two phenomena are combined together, at a certain time, there is a very small mass change, incorrectly indicating that the hygral equilibrium has been reached. Carbonation shrinkage is not considered in any design codes or recommendations.

2.4.4 Drying shrinkage

Comparing the average ultimate drying shrinkage of concrete in 40% ambient relative humidity, 780×10^{-6} (negative strain) [3], to the average values of other kinds of shrinkage, it is clear that this kind is of a major importance. In fact, the phenomenon of drying shrinkage was known to the structural engineers long before creep.

Different relative humidity in the concrete structure and in the surrounding environment causes moisture exchange (from higher relative humidity to a lower relative humidity). As the concrete starts drying, first, the free water from cavities and big pores is lost. This leads to a remarkable weight loss, but only to minor deformations. As the drying process continues, the adsorbed water from capillary pores is being removed, which results in an increase in capillary tension and causes shrinkage of the hydrated cement paste.

Drying starts at the exposed surface of the concrete member; the gradient of the relative humidity is on the boundary initially very high. The core of the member starts drying after some delay which depends on its size and shape and the material diffusivity. The differential drying leads to a differential shrinkage, which creates a non-uniform stress distribution and eventually can cause surface cracking if the tensile strength is exceeded.

The drying shrinkage strains are not fully recoverable after re-wetting, which is probably due to the newly formed bonds in the concrete microstructure.

The magnitude of shrinkage depends on many factors: ambient relative humidity, water and cement content and their ratio, aggregate stiffness, size distribution and content, additives and specimen size.

The magnitude of the drying shrinkage is closely related to the water loss, which is bigger for lower relative humidity of the environment and for higher water-to-cement ratio. Drying shrinkage grows with the cement content, because it is mainly the hydrated cement products that shrink. Most of the additives (silica fume and slag) and admixtures (superplasticizers) also increase shrinkage. Higher content of stiffer aggregates of bigger notional size act as a restraint and decrease shrinkage (assuming that non-shrinking aggregates are used). The cement type (fineness and chemical composition – except cement deficient in gypsum which exhibits greatly increased shrinkage [72]) does not influence drying shrinkage of concrete, even though it can influence drying shrinkage of the pure cement paste.

In the large specimens the drying process is slower and so internal self-equilibrated stresses which are caused by the differential shrinkage become more relaxed due to creep (and surface cracking). Therefore the observed final magnitude of shrinkage is smaller.

The shrinkage rate depends mainly on the size and shape (effective thickness (see Fig. 2.7) and volume-to-surface ratio) of the specimen and on the microstructure. The shrinkage kinetics is closely related to the kinetics of the moisture diffusion. The so-called shrinkage half-time is

approximately proportional to the square of the effective thickness.

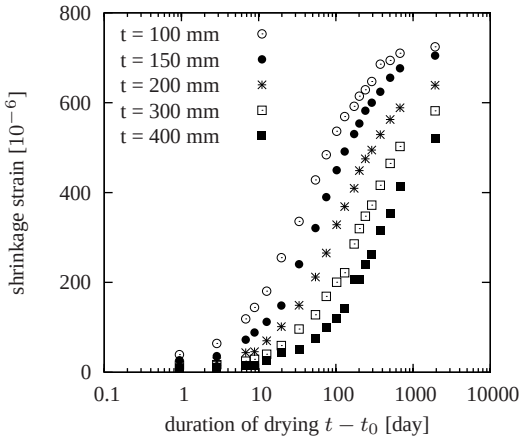

Figure 2.7: Evolution of shrinkage strains measured on slabs of various thicknesses [45].

Shrinkage is also influenced by the type of curing. For example during autoclaving (high-pressure steam curing) the resulting microstructure of the hydration products is more coarse and largely microcrystalline with about 0.05 specific surface comparing to the ordinarily-cured concrete. This results in significantly reduced shrinkage which is about 1/6 to 1/3 of the shrinkage of the normally cured concrete [72].

2.4.5 Swelling

Swelling refers to (positive) increase of strain observed in concrete and other cementitious materials (and clays) when placed under water or in environment with 100% relative humidity. The increase of strain is accompanied by weight gain. Typically, the swelling strain is around 100×10^{-6}.

When the concrete is submerged, water starts gradually filling large pores, capillary pores, where it reduces capillary tension and tension in the skeleton (with negligible volume increase) and finally gets absorbed by the hydration products causing chemical expansion. It is also adsorbed as the inter-layer water in the cement gel microstructure.

The codes of practice or other recommendations treat swelling in several ways. Either it is assumed that in 100% relative humidity the shrinkage/swelling deformation is zero (e.g. EC2 [91], ACIs [2], [3]), or in a certain interval of relative humidity of the environment (e.g. from 98% to 100%) its magnitude is described by a linear function with zero value at the lower bound (e.g. models of Gardner, Bažant) or a constant function (e.g. Model Code 2010 [48].

There are two reasons why the swelling strains can be omitted: 1) the swelling strains are relatively small 2) the restrained swelling strains induce compression and not tension comparing to shrinkage.

Swelling can be observed not only at elevated relative humidity, but also at elevated temperature. Thermal expansion of the solid phase (aggregates and hydrated cement paste) is lower than the thermal expansion of the adsorbed water. This results in decrease in capillary tension and in the origin of swelling pressure.

3 Numerical Analysis of Creep

In linear viscoelasticity, the time evolution of strain is computed using the integral formula

$$\varepsilon(t) = \int_0^t J\left(t, t'\right) \mathrm{d}\sigma\left(t'\right) \tag{3.1}$$

where σ is the stress and J is the compliance function, which describes the strain at time t due to unit stress applied at time t'. For non-aging materials, J would depend only on the difference $t - t'$, i.e., on the duration of loading, but for aging materials such as concrete, a more general dependence must be considered.

For the prescribed strain history, the time development of stress is expressed by

$$\sigma(t) = \int_0^t R\left(t, t'\right) \mathrm{d}\varepsilon\left(t'\right) \tag{3.2}$$

where R is the relaxation function, which describes the stress at time t caused by a unit strain applied at time t'. The analytical evaluation of the integral, such as in equation (3.1), is possible only for the simple loading histories and compliance functions. For more complex problems it is necessary to use the approximate numerical evaluation.

The two basic types of such solutions [22] are usually referred to as the "integral approach" and the "rate-type approach". The first one (older and more straightforward) replaces the integral in (3.1) with a sum and the strain at time t_k is evaluated as

$$\varepsilon(t_k) = \int_0^{t_k} J\left(t_k, t'\right) \mathrm{d}\sigma\left(t'\right) \approx \sum_{i=1}^{k-1} J_{k,i} \Delta\sigma_i \tag{3.3}$$

with

$$\Delta\sigma_i = \sigma(t_{i+1}) - \sigma(t_i) \tag{3.4}$$

and

$$J_{k,i} = \frac{J(t_k, t_{i+1}) + J(t_k, t_i)}{2} \tag{3.5}$$

The final strain is obtained as a sum of the strain increments; the strain increment from time t_k to t_{k+1} is

$$\Delta\varepsilon_k = \varepsilon_{k+1} - \varepsilon_k = J_{k+1,k}\Delta\sigma_k + \sum_{i=1}^{k-1} \left(J_{k+1,i} - J_{k,i}\right) \Delta\sigma_i \tag{3.6}$$

where the first part on the right-hand side corresponds to the increment of the instantaneous deformation and the sum represents the increment of the delayed deformation. The last equation shows the main drawback of this method – it is very demanding on the computer memory (the whole stress history must be stored) and the computational time.

The second (rate-type) approach is less straightforward, but the memory and CPU demands are constant during the whole analysis, independently of the number of time steps. Only the information of the previous time step needs to be stored and updated. In every time step, the same two-step procedure is repeated.

1) The compliance function is approximated by the Dirichlet series corresponding to Kelvin chain (see e.g. Fig. 3.1); retardation times of such a chain should be evenly distributed in the log-scale. Parameters of the Kelvin chain can be determined using the least-squares method or from the retardation spectrum [9], [38] of the corresponding compliance function. An overview of

this method and the summary of the recommended formulae is for the most common compliance functions in the engineering practice presented in [62].

2) The efficient (exponential) algorithm developed for the Kelvin chain evaluates the instantaneous stiffness, creep strain and strain increment [22] (algorithm for Maxwell chain is presented [37]).

In the case that the compliance function is non-aging (i.e. depending only on the loading duration) or solidifying (see Section 4.1), the parameters of the Kelvin chain can be evaluated only once and stored in the computer memory.

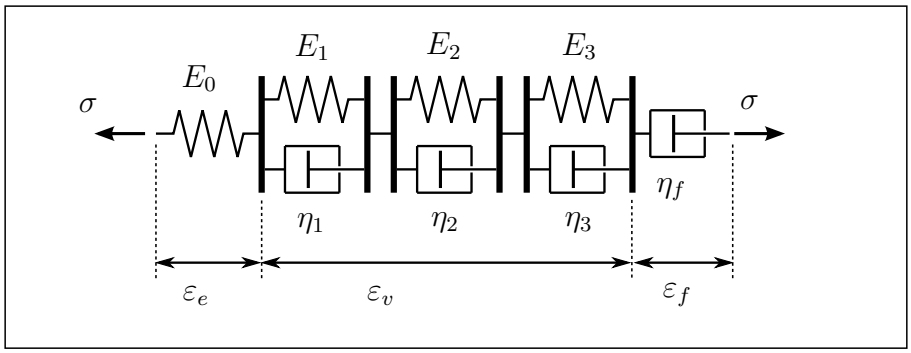

Figure 3.1: Kelvin chain composed of three serially connected Kelvin units, one spring (can be treated as a Kelvin unit with zero viscosity and zero retardation time) and one dashpot (can be considered as a Kelvin unit with zero spring stiffness and infinite retardation time); the total deformation is split into elastic ε_e and viscoelastic ε_v parts, which are recoverable after unloading, and purely viscous part ε_f, which does not recover upon unloading.

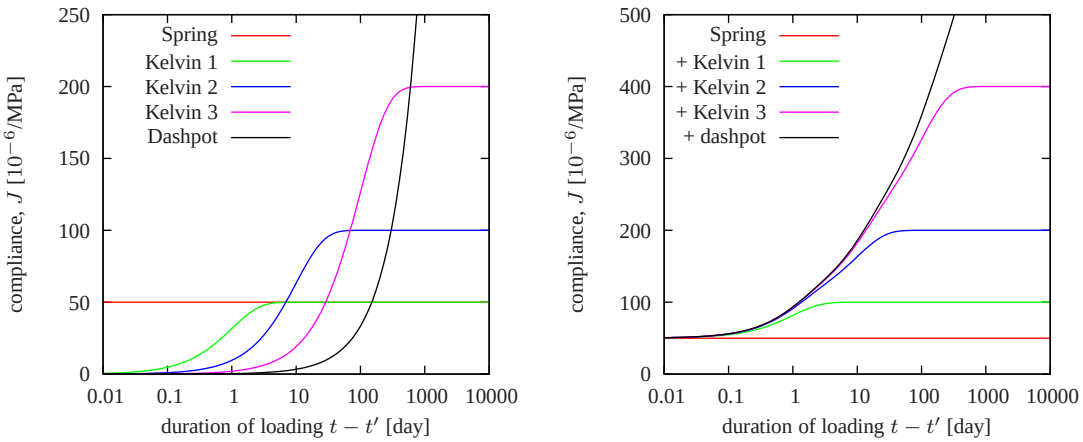

Figure 3.2: Compliance of (a) the individual components and (b) of the whole chain from Fig. 3.1 obtained with the following parameters: $E_0 = E_1 = 20$ GPa, $E_2 = 10$ GPa, $E_3 = 5$ GPa, $\eta_1 = 20$ GPa·day, $\eta_2 = 100$ GPa·day, $\eta_3 = 500$ GPa·day, and $\eta_f = 3000$ GPa·day; retardation times of the Kelvin units are $\tau_1 = 10$ days, $\tau_2 = 100$ days and $\tau_3 = 1000$ days (the resulting compliance functions are evenly spaced on the log-time scale).

4 Material Models for Modeling Creep and Shrinkage (Material Point Approach)

The averaged cross-sectional approach is a very simple and computationally very efficient method for the analysis of creep and shrinkage in concrete structures and therefore is widely used in the engineering practice. The idea consists in replacing the real behavior of the structural member by the idealized behavior, which is on average the same and is common for the whole cross-section. The error caused by this simplification is very small for the basic creep. This method can be also used when the total deformation due to shrinkage or creep is of importance. On the other hand, more complex phenomena, such as a non-uniform stress distribution across the cross-section caused by the shrinkage or the drying creep cannot be captured correctly due to the nature of this method (the whole cross-section shrinks uniformly) and a more general method is needed.

In the averaged cross-sectional approach the size and shape of the structural member is reflected using either the volume-to-surface ratio or the equivalent thickness. In order to realistically describe the time evolution of the shrinkage and drying of the specimens with the same volume-to-surface ratio and different geometry, the model B3 introduces so-called shape factor.

In comparison to the cross-sectional approach presented in Appendix A, the material point approach enables to realistically simulate more complex phenomena, such as a non-uniform stress distribution across the cross-section due to shrinkage, drying creep, transient thermal creep (TTC), and if the material strength is exceeded, due to cracking.

This chapter presents two theories - the Solidification theory [35], [36] and its extension to the Microprestress-solidification theory (MPS) [19], [20], [15]. The first theory provides a model which is embedded in the well-known B3 model and provides a physically-based description of the basic creep and concrete aging. The latter theory extends the first one with the effects of variable hygral and thermal conditions; it should be capable of reflecting phenomena such as the Pickett effect, TTC, or creep at elevated temperatures.

The Section on Microprestress-solidification theory also presents the model in a novel but fully equivalent approach which simplifies the original governing equation of the Microprestress-solidification theory and eliminates the parameters which turn out to be redundant.

Verification and assessment of the model based on the classical data from the literature is presented in Chapter 6.

4.1 Solidification theory

The solidification theory represents a very powerful tool for the description of time-dependent behavior of a sealed concrete. This theory justifies the formula describing basic creep in the B3 model [10], [13].

As was already mentioned in Chapter 3, for non-aging materials, the compliance function J depends only on the difference $t - t'$, i.e., on the duration of loading, while in real materials, such as concrete, a more general dependence must be considered. This makes the determination of the compliance function and the integral (3.3) quite difficult.

Solidification theory relates the concrete aging to the process of cement hydration, which leads to volume growth and densification of the solidified interconnected hydration products (mainly calcium-silicate-hydrate gels, C-S-H). It is assumed that the creep of C-S-H is described

by non-aging viscoelasticity, and aging is caused by the growth in volume of the solidified material.

According to the B3 model, the function characterizing the non-aging viscoelastic response of the solidifying material is taken in the form

$$\Phi\left(t-t'\right)=q_2\ln\left[1+\left(\left(t-t'\right)/\lambda_0\right)^n\right] \tag{4.1}$$

and the reciprocal value of the increasing function describing the growth of the volume fraction of the interconnected hydration products is given by

$$v^{-1}\left(t\right)=\alpha+\left(\lambda_0/t\right)^m \tag{4.2}$$

Here, α, λ_0, n, m and q_2 are empirical constants.

The compliance function of the solidifying material is then introduced in the rate form written as

$$\dot{J}_v\left(t,t'\right)=\frac{1}{v\left(t\right)}\dot{\Phi}\left(t-t'\right) \tag{4.3}$$

Substituting (4.1) and (4.2) into (4.3) and integrating, the compliance function for viscoelastic behavior of material is expressed as

$$J_v\left(t,t'\right)=\frac{\Phi\left(0\right)}{v\left(t'\right)}+\int_{t'}^{t}\frac{\dot{\Phi}\left(s-t'\right)}{v\left(s\right)}\mathrm{d}s=q_3\ln\left[1+\left(\frac{t-t'}{\lambda_0}\right)^n\right]+q_2Q\left(t,t'\right) \tag{4.4}$$

where $q_3=\alpha q_2$. Function Q is not available in a closed form but can be computed numerically or approximated with an analytical expression. However, if function Φ is approximated by Dirichlet series and the integral form of the stress-strain law is converted into a rate form, the function Q does not need to be evaluated at all. In model B3, the variable λ_0 is set to 1 day and the exponents are $n=0.1$ and $m=0.5$.

Since concrete properties change even after the end of the hydration reactions (the effective modulus still increases), a compliance function $J_f\left(t,t'\right)$ describing this phenomenon must be added. This term corresponds to an aging viscous dashpot in the rheological scheme in Fig. 4.1. Another term

$$J_e\left(t-t'\right)=q_1H\left(t-t'\right) \tag{4.5}$$

corresponding to a non-aging elastic spring is added in order to capture the instantaneous deformation. In (4.5), q_1 is the instantaneous elastic compliance and H is the Heaviside function. Experiments show that the graph of the compliance function plotted in the semi-logarithmic scale approaches a straight line as the load duration tends to infinity. The long-term creep is captured by the flow term, which is modeled by an aging viscous dashpot with viscosity

$$\eta_f\left(t\right)=t/q_4 \tag{4.6}$$

where q_4 is a material constant. After integration one gets the compliance function

$$J_f\left(t,t'\right)=\int_{t'}^{t}\frac{\mathrm{d}s}{\eta_f\left(s\right)}=q_4\ln\left(\frac{t}{t'}\right) \tag{4.7}$$

In summary, the general form of the compliance function for basic creep (i.e. creep of a sealed specimen; no water is accepted or released) used by model B3 reads

$$J_b\left(t,t'\right)=J_e\left(t-t'\right)+J_v\left(t,t'\right)+J_f\left(t,t'\right) \tag{4.8}$$

As already mentioned, parameters q_1, q_2, q_3 and q_4 are related to the basic creep and can be predicted from the composition of the concrete mixture and its average 28-day compressive strength using empirical formulae [13].

The descendant of the B3 called simply "B4" is currently being developed by Bažant and coworkers at Northwestern university. This model uses the same structure of the compliance function (4.8) but the prediction formulae are different, they take into account more factors and the model is calibrated on an extended experimental database ($3\times$ larger compared to the original). Most likely, this model will approved as a new RILEM recommendation.

The part of the compliance function that contains q_2 and q_3 is related to the viscoelastic effects in the solidifying part of the model. In numerical simulations, this part of compliance is approximated by the Dirichlet series corresponding to a solidifying Kelvin chain. The stiffnesses and viscosities of the individual Kelvin units can be conveniently determined from the continuous retardation spectrum of the non-aging compliance function that describes the solidifying constituent and stored in the computer memory (since these parameters correspond to non-aging compliance function, they are constant).

Using the solidification theory, a method offering a simple solution for a complex problem is obtained. An aging compliance function which cannot be integrated is replaced by a product of a non-aging creep function and a function that characterizes aging. Aging is taken into account by simple multiplication by a time-dependent function, which can be easily evaluated.

4.2 Microprestress-solidification theory: reformulated version

Microprestress-solidification theory (MPS) [14], [15] and [22] is an extension of the above model to variable humidity and temperature. Elevated temperature leads to faster cement hydration and thus to faster reduction of compliance due to aging, but it also accelerates the viscous processes that are at the origin of creep and the process of microprestress relaxation. The microprestress is understood as the stress in the microstructure generated due to large localized volume changes during the hydration process; it is considered as the stress which acts in narrow transverse bonds across nanopores in reaction to capillary and disjoining pressure. It builds up at very early stages of microstructure formation and then is gradually reduced by relaxation processes, which is related to material aging. The microprestress is considered to be much bigger than any stress acting on the macroscopic level, and therefore it is not influenced by the macroscopic stress. Additional microprestress is generated by changes in internal relative humidity and temperature.

The theory is based on the assumption that if the relative humidity and temperature remains constant (temperature is equal to room temperature), the governing equations simplify to the equations describing basic creep in the form presented in the previous section. It is necessary to mention that even if both theories (solidification theory and MPS theory) are based on a description of the microstructure of concrete, they are not contradictory but rather complementary, because they describe different processes.

Under variable humidity and temperature, the MPS theory replaces the explicit dependence of the viscosity η_f on time by its dependence on the so-called microprestress, S, which is governed by a separate non-linear differential equation. As discussed in [19], high microprestress facilitates sliding in the microstructure and thus accelerates creep. Therefore, the viscosity of the dashpot that represents the long-term viscous flow is assumed to be inversely proportional to the microprestress. This viscosity acts as a proportionality factor between the flow rate and

the stress. The model is thus described by the equations

$$\sigma = \eta_f \frac{\mathrm{d}\varepsilon_f}{\psi_r(T,h)\mathrm{d}t} \tag{4.9}$$

$$\frac{1}{\eta_f} = c\, p\, S^{p-1} \tag{4.10}$$

where ψ_r is a temperature and humidity-dependent factor to be defined in (4.33), c [Pa^{-p} s^{-1}] and p [-] are constant parameters and $p > 1$. In the original paper, parameter p was always set to 2.

The equation governing the microprestress evolution can be written as

$$\frac{\mathrm{d}S}{C_S\,\mathrm{d}t_S} + \frac{S}{\eta_f(S)} = \frac{\mathrm{d}s}{C_S\,\mathrm{d}t_S} \tag{4.11}$$

where its left-hand side describes the microprestress relaxation under constant temperature and humidity conditions while the right-hand side causes microprestress generation under variable temperature and humidity. In this equation $\mathrm{d}s$ denotes the infinitesimal increase in the instantaneous microprestress induced by changes of capillary tension, surface tension and crystal growth pressure, C_S is the spring stiffness shown in Fig. 4.1 where it is placed perpendicularly to the loading direction and transmits the normal stress on the slip plane. This equation is written with respect to the time t_S which is referred to as the *reduced microprestress time*. It can be linked to the real physical time t via

$$\frac{\mathrm{d}t_S}{\mathrm{d}t} = \psi_S(T,h) \tag{4.12}$$

and the equation (4.11) becomes

$$\frac{\dot{S}}{C_S} + \frac{\psi_S S}{\eta_f(S)} = \frac{\dot{s}}{C_S} \tag{4.13}$$

The concept of microprestress is useful for the theoretical justification of evolving viscosity and of the general format of governing equations. On the other hand, the microprestress cannot be directly measured, and a separate calibration of the microprestress relaxation equation (4.13) and of equation (4.10) describing the dependence of viscosity on microprestress is difficult, if not impossible.

Recently it has been shown [63] that the microprestress can be completely eliminated, and the equation (4.13) can be reformulated in terms of viscosity, which has a direct physical interpretation. The resulting model is still fully equivalent to the original one, but its structure becomes simplified, and the role of the model parameters becomes more transparent. Another benefit is the reduction of model parameters which turn out to be in the new version redundant.

From equation (4.10) the microprestress and its time derivative can be expressed as

$$S = (c\, p\, \eta_f)^{\frac{1}{1-p}} \tag{4.14}$$

$$\dot{S} = \frac{c\, p}{1-p}(c\, p\, \eta_f)^{\frac{p}{1-p}}\dot{\eta}_f \tag{4.15}$$

Substitution of (4.14) and (4.15) into (4.13) yields to

$$\dot{\eta}_f + (p-1)(c\,p)^{\frac{1}{p-1}}\,\dot{s}\,\eta_f^{\frac{p}{p-1}} = (p-1)C_S\psi_S \tag{4.16}$$

Under sealed conditions, the evolution of viscosity η_f must be equivalent with the expression of the flow term of the B3 model (4.6). At constant relative humidity, the second term on the left-hand side in (4.16) vanishes and after inserting the time derivative of (4.6) it provides a link between the model parameter C_S of the MPS theory and the parameter q_4 of the B3 model.

$$C_S = \frac{1}{(p-1)q_4} \tag{4.17}$$

The rate of the microprestress generation $\dot{s}$ is assumed to have a similar form as the rate of the disjoining pressure or the surface tension.

$$\dot{s} = \frac{c_1}{T_0}\left|\frac{d(T\ln h)}{\mathrm{d}t}\right| = \frac{c_1}{T_0}\left|\dot{T}\ln h + T\frac{\dot{h}}{h}\right| \tag{4.18}$$

where T_0 [K] is the room temperature and c_1 [Pa] is a constant parameter. Owing to the presence of the absolute value operator on the right-hand side of (4.18), additional microprestress is generated by both drying and wetting, and by both heating and cooling, as suggested in [15].

Substituting (4.17) and (4.18) into (4.16), the governing equation changes to

$$\dot{\eta}_f + (p-1)(cp)^{\frac{1}{p-1}}\frac{c_1}{T_0}\left|\dot{T}\ln h + T\frac{\dot{h}}{h}\right|\eta_f^{\frac{p}{p-1}} = \frac{\psi_S}{q_4} \tag{4.19}$$

To make it even simpler, a new parameter with the physical meaning of fluidity [Pa^{-1}s^{-1}] can be introduced

$$\boxed{\mu_S = c\,p\,[c_1\,(p-1)]^{p-1}} \tag{4.20}$$

and the resulting equation becomes

$$\boxed{\dot{\eta}_f + \frac{1}{\mu_S T_0}\left|\dot{T}\ln h + T\frac{\dot{h}}{h}\right|(\mu_S\eta_f)^{\frac{p}{p-1}} = \frac{\psi_S}{q_4}} \tag{4.21}$$

The last two equations show that the former parameters c and c_1 are not independent and can be replaced by a single parameter μ_S. For the standard choice $p = 2$ the entire solution depends only the product $c \times c_1$, not on the values c and c_1 independently because

$$\mu_S = 2\,c\,c_1 \tag{4.22}$$

The initial condition supplementing the differential equation (4.21) reads $\eta_f(t_0) = q_4/t_0$, where t_0 is a suitably selected time that precedes the onset of drying and temperature variations.

To capture the influence of relative humidity and temperature, the MPS theory introduces three transformed times, which become equivalent to the actual physical time t in standard conditions, i.e. at reference (room) temperature T_0 and under constant relative humidity $h = 1.0$ (different from the $h = 0.98$ which gives no shrinkage in the B3 model). These times are: the equivalent time t_e representing equivalent hydration period, the reduced time t_r capturing rate

of bond breakages in the microstructure, and finally the reduced microprestress time t_s, and are introduced in the rate form

$$\frac{\mathrm{d}t_e}{\mathrm{d}t} = \beta_{e,T}(T)\beta_{e,h}(h) \tag{4.23}$$

$$\frac{\mathrm{d}t_r}{\mathrm{d}t} = \beta_{r,T}(T)\beta_{r,h}(h) \tag{4.24}$$

$$\frac{\mathrm{d}t_s}{\mathrm{d}t} = \beta_{s,T}(T)\beta_{s,h}(h) \tag{4.25}$$

where

$$\beta_{e,T}(T) = \exp\left(\frac{Q_e}{R}\left(\frac{1}{T_0} - \frac{1}{T}\right)\right) \tag{4.26}$$

$$\beta_{r,T}(T) = \exp\left(\frac{Q_r}{R}\left(\frac{1}{T_0} - \frac{1}{T}\right)\right) \tag{4.27}$$

$$\beta_{s,T}(T) = \exp\left(\frac{Q_s}{R}\left(\frac{1}{T_0} - \frac{1}{T}\right)\right) \tag{4.28}$$

$$\beta_{e,h}(h) = \frac{1}{1 + \alpha_e\left(1-h\right)^4} \tag{4.29}$$

$$\beta_{r,h}(h) = \alpha_r + \left(1-\alpha_r\right)h^2 \tag{4.30}$$

$$\beta_{s,h}(h) = \alpha_s + \left(1-\alpha_s\right)h^2 \tag{4.31}$$

The transformed times are influenced not only by the history of relative humidity and temperature, but depend also on the "choice" of activation energy of particular process Q_x/R (temperature influence) and constant α (influence of humidity). The recommended values of these parameters are $Q_e/R = 2700$ K, $Q_r/R = 5000$ K, $Q_s/R = 3000$ K, $\alpha_e = 10$, $\alpha_r = 0.1$, $\alpha_s = 0.1$.

Acceleration or deceleration caused by the temperature and relative humidity can be for convenience expressed by functions

$$\psi_e(t) = \beta_{e,T}(T(t))\beta_{e,h}(h(t)) \tag{4.32}$$

$$\psi_r(t) = \beta_{r,T}(T(t))\beta_{r,h}(h(t)) \tag{4.33}$$

$$\psi_s(t) = \beta_{s,T}(T(t))\beta_{s,h}(h(t)) \tag{4.34}$$

The newly introduced transformed times must be appropriately incorporated into the Solidification theory. The rate of viscoelastic strain becomes

$$\dot{\varepsilon}_v(t) = \frac{\dot{e}(t)}{v\left(t_e\left(t\right)\right)} \tag{4.35}$$

with

$$e(t) = \int_0^t \Phi\left[t_r(t) - t_r(\tau)\right]\dot{\sigma}\,\mathrm{d}\tau \tag{4.36}$$

Both shrinkage and thermally induced strains are defined by a simple and linear rate form

$$\dot{\varepsilon}_{sh} = k_{sh}\dot{h} \tag{4.37}$$

$$\dot{\varepsilon}_T = \alpha_T\dot{T} \tag{4.38}$$

To summarize, the complete constitutive model for creep and shrinkage of concrete can be represented by the rheological scheme shown in Fig. 4.1. It consists of (i) a non-aging elastic spring, representing instantaneous elastic deformation, (ii) a solidifying Kelvin chain, representing short-term creep, (iii) an aging dashpot with viscosity dependent on the microprestress, S, representing long-term creep, (iv) a shrinkage unit, representing volume changes due to drying, (v) a unit representing thermal expansion, and (vi) a unit representing cracking. All these units are connected in series, and thus the total strain is the sum of the individual contributions, while the stress transmitted by all units is the same.

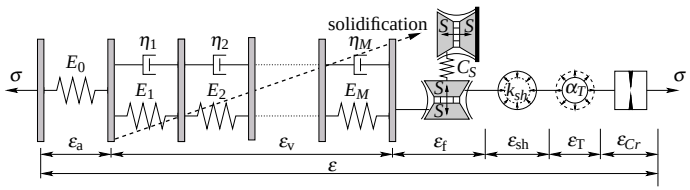

Figure 4.1: Rheological scheme of the complete hygro-thermo-mechanical model

5 (Coupled) Heat and Moisture Transport in Concrete

Modeling of moisture transport in cementitious materials has many applications, ranging from predictions of shrinkage (e.g. equation (4.37) in the MPS model) and creep (e.g. equation (4.21) in the MPS model) of concrete to durability of materials and structures or health issues. A coupled transport of heat and moisture is a necessity for a realistic assessment of the problematic details in civil engineering.

As has been shown earlier, temperature influences among others the creep rate and the concrete maturity. Non-uniform temperature field in the cross-section leads to the non-uniform distribution of the normal stresses, which can initiate cracking. The high temperature gradients can be observed in the massive concrete structures where, caused by the hydration heat, the temperature in the core can exceed 60 °C. High gradients of temperature can be also produced by the sudden changes in the environmental conditions (heavy rain after a hot sunny day).

In the last five decades, many models for simultaneous non-linear heat and moisture transport in concrete and other porous materials have been developed, see e.g. [56], [67]. The latter model (much simpler than the former) is briefly described in Section 5.4.

A simple comparison of the typical values of the heat and moisture diffusivity of concrete reveals that these two processes occur at different rates. Admitting a certain error, these processes can be solved as decoupled. If there temperature gradient is small, the heat transport does not have to be solved at all.

One of the most frequently used models for moisture transport was proposed by Bažant and Najjar [39] forty years ago. This model is presented in Section 5.2. This model provides quite accurate predictions of the time development of the relative humidity in concrete structures while its formulation still remains simple enough for the engineering practice. For these reasons the model has been recommended in a prestandard document *fib* Model Code, see section 5.1.12.2.1 - Diffusion of water in [48].

The governing equations for the heat transfer and the typically applied boundary conditions are presented in Section 5.3.

5.1 Moisture in concrete

The amount of moisture in the porous materials can be expressed in several ways. The first one uses the so-called “moisture ratio” u [-] or [%] defined as a mass fraction of evaporable water to the dried solid.

$$u = \frac{m_w}{m_s} \tag{5.1}$$

The second option to express moisture quantity is by means of moisture content, w [kg/m^3], which is defined as the mass of evaporable water per unit volume of the porous material.

$$w = \frac{m_w}{V_{tot}} \tag{5.2}$$

Moisture content can be easily computed from the moisture ratio and the dry material density as

$$w = u\rho_{dry} \tag{5.3}$$

The degree of saturation S [-] is defined as a volume of water per unit volume of pores

$$S = \frac{V_w}{V_{pores}} = \frac{V_w}{V_w + V_{air}} \tag{5.4}$$

The relative humidity is defined as a ratio between the partial pressure of water vapor and its saturation pressure

$$h = \frac{p}{p_{sat}(T)} \tag{5.5}$$

Compared to the previous definitions, the relative humidity refers more to the state of water at equilibrium than to the water quantity.

In concrete, water can be found either as chemically bound in the solid phase, physically bound (adsorbed) to the solid surface, in form of a water vapor in the pore system, or as a liquid pore water. The two most important examples of sorption are the surface adsorption and the condensation in capillaries and gel pores; the first one is characteristic for the lower range of relative humidities while the latter is typical for higher RH.

Surface adsorption was first described by Langmuir, but only for one layer of water molecules (monomolecular sorption, 2 parameters). The model was later extended to multilayer adsorption by Brunauer, Emmett and Teller covering the range of relative humidity up to 40% (BET equation, 2 parameters). The next milestone was Dent's equation which is used for the extrapolation from the lower range of relative humidity (only adsorption) to the higher relative humidity (adsorption + capillary condensation); this equation has three parameters.

Two types of adsorbed water can be distinguished: free and hindered. The hindered adsorption develops in nanopores with diameter less than 10 water molecules ($\approx$ 2.7 nm). This restraint is the origin of the disjoining pressure which is believed to be equilibrated by the tensile stresses in transverse bonds across the nanopores. The stress is called "microprestress" and its generation and relaxation was presented in Section 4.2.

Capillary condensation can be described by the combination of Young-Laplace and Kelvin equations. It is important to note that capillary condensation takes place on top of the layer of adsorbed water. The radii of pores must be significantly bigger than the size of the water molecule (0.35 nm) but must not exceed 100 nm (in such pores the capillary condensation occurs at relative humidity 99%). The size distribution of pores as well as their shapes influence the shape and the hysteresis of the sorption and desorption isotherm.

5.1.1 Sorption isotherm

A sorption isotherm represents a group of equilibrium states of relative humidity and the corresponding moisture ratio (or moisture content) related to the amount of evaporable water, not the total water (i.e. not chemically bound water). When it is measured at decreasing relative humidity, it is referred to as the "desorption" isotherm, in the opposite case it is called "absorption" (or sometimes only "sorption") isotherm. The absorption and desorption isotherms usually do not coincide, they exhibit "hysteresis". Scanning curves represent a transition from one type of isotherm to the other when the process becomes reversed.

The sorption isotherm can be divided into three parts, the hygroscopic region (0% RH – approx. 95-98% RH, where the equilibrium is reached in contact with moist air), capillary region up to free water saturation (water uptake by suction, specimen in contact or submerged in water), and from that above, when external pressure or vacuum must be applied to increase moisture uptake – this region is referred to as the supersaturated region.

Also the hygroscopic region of the sorption isotherm can be subdivided into three parts (starting from zero relative humidity): the first concave part, where the water molecules are adsorbed in one monolayer, the second (almost linear) part where the water molecules are ad-

sorbed in several layers and finally the last (convex) interval with dominating capillary condensation.

Sorption isotherms are influenced by many factors. Figure 5.1a shows the influence of temperature and Fig. 5.1b presents the effect of composition and hydration degree denoted as α. Unfortunately, in the latter case, the amount of cement is not known, so it cannot be compared to Figs. 5.8 and 5.4b.

As shown in Fig. 5.2, aging seems to affect more desorption isotherm than absorption isotherm.

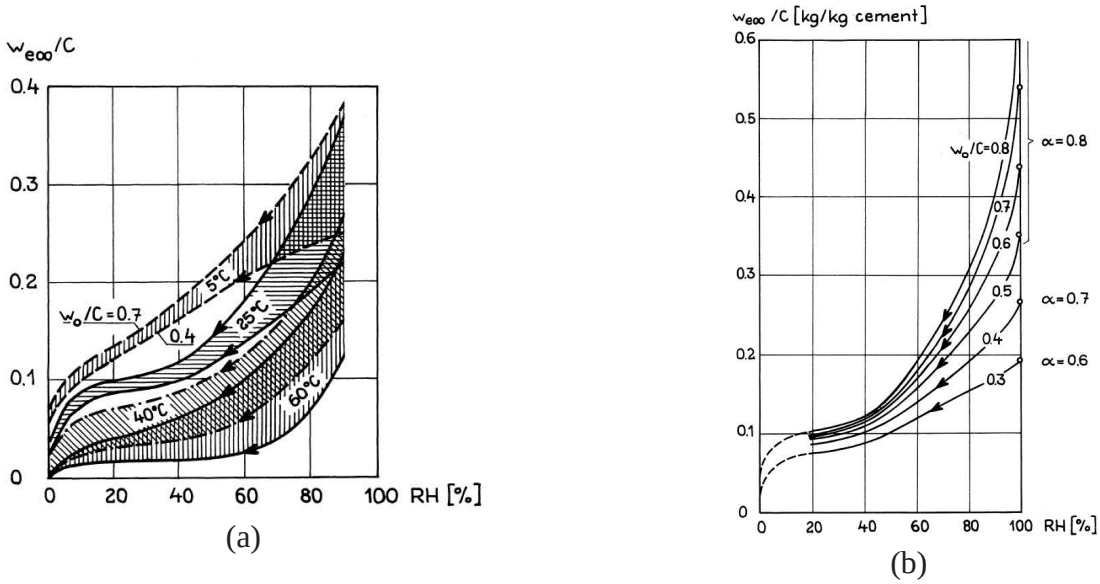

Figure 5.1: Sorption isotherms (expressed as mass ratio of evaporable water to cement) for (a) concrete at different temperatures (b) concrete with different water-to-cement ratio; figures adapted from [73] and partially from [80].

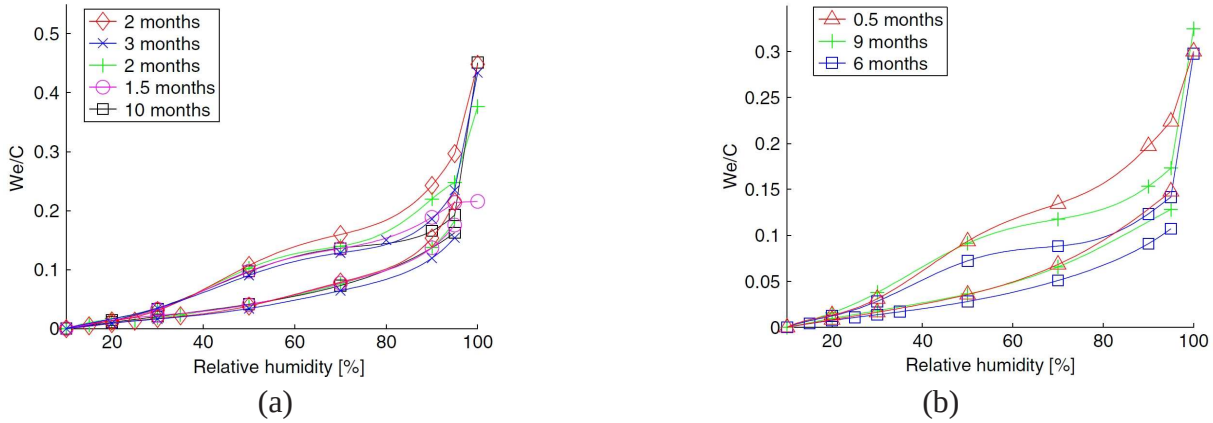

Figure 5.2: Sorption isotherms (expressed as mass ratio of evaporable water to cement) for concrete of different ages and (a) w/c = 0.65, (b) w/c = 0.55; isotherms determined by gravimetric vapor sorption balance using a mix of dry and saturated nitrogen; figures adapted from [7].

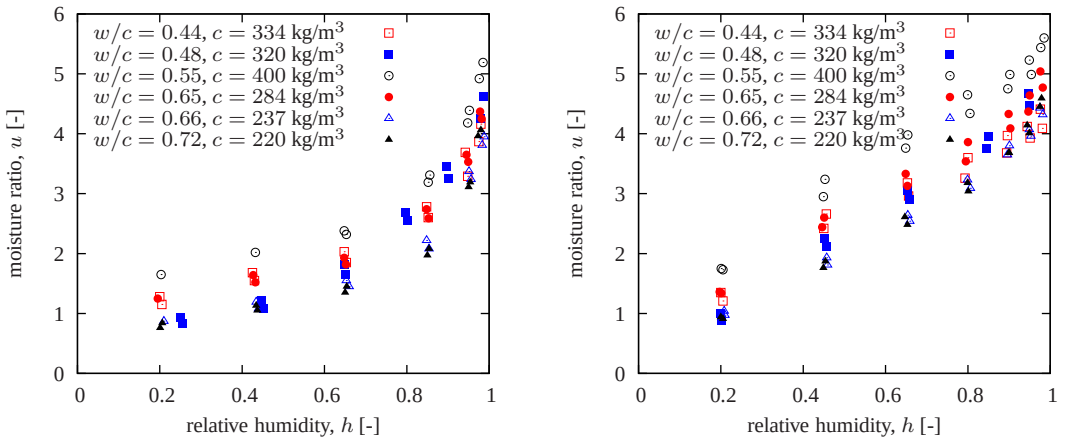

Figure 5.3: (a) sorption and (b) desorption isotherms (expressed as moisture ratio) for different concrete mixtures; data taken from [58].

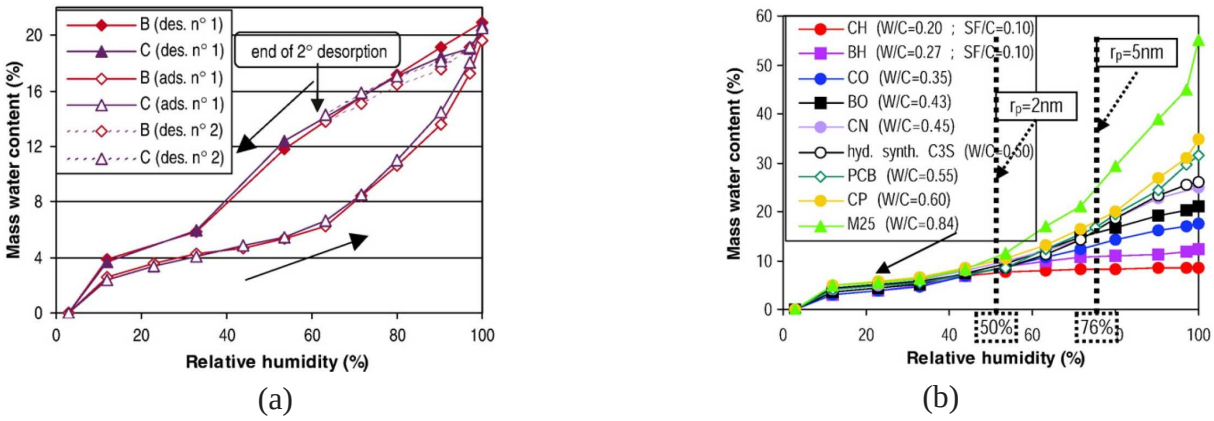

Figure 5.4: Sorption isotherms (expressed as mass water content per dry hydrated cement paste) for (a) concrete "B" and cement paste "C" with the same water-to-cement ratio (b) desorption isotherms for concretes, mortars and pastes of different composition; all isotherms determined using saturated salt solution method; figures adapted from [8].

Figure 5.3 shows sorption and desorption isotherms for concretes of various compositions. The desorption isotherms are in the range 40% – 98% almost straight. Higher cement content seems to outweigh the effect of water-to-cement ratio as in 5.1b.

As documented in [8], the most important aspect is the pore-size distribution related to the volume of hydrated cement paste. Figure 5.4a shows that almost identical sorption isotherms are obtained for cement paste and concrete if the water-to-cement ratio is the same and when the mass of absorbed water is related to the mass of hydrated cement paste. The pore structure (determined by concrete mixture) appears to be the most influencing factor for the capillary condensation region, while for the lower relative humidity the sorption isotherms are almost identical and independent of the composition, see Fig. 5.4b.

The shape of the desorption isotherm is dramatically different for ordinary and high-performance concrete, compare almost straight line for ordinary concrete Fig. 5.5a, b with HPC in Fig. 5.5c,

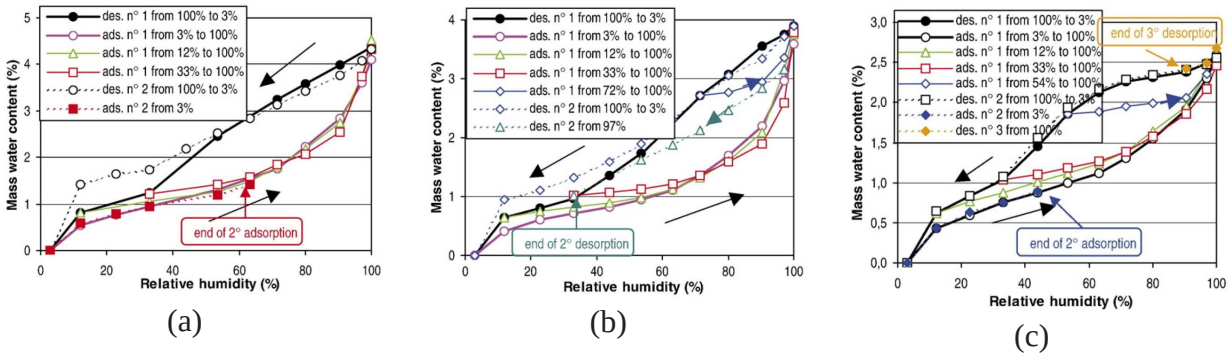

Figure 5.5: Sorption isotherms (expressed as mass water content per dry hydrated cement paste) for (a) concrete with $w/c = 0.45$, $c = 400$ kg/m^3, (b) concrete with $w/c = 0.43$, $c = 353$ kg/m^3, (c) high performance concrete with $w/c = 0.27$, $c = 421$ kg/m^3, $f_{cm} = 115.5$ MPa, and with added silica fume; figures adapted from [8].

where the concave part indicates on the smaller amount of pores with bigger radius.

Most of the the examples in this work study concrete drying, therefore the desorption isotherm, especially in the range from 50% to 100% relative humidity, is of major importance.

5.1.2 Formulae for sorption isotherms of concrete

A large variety of models for sorption isotherms has been published in the literature. Isotherm proposed by Langmuir, its improved version by Brunauer, Emmett, Teller (BET equation) or Dent give good agreement with the experimental data for concrete only at lower relative humidites.

Ricken isotherm [67] is widely used for sorption of porous building materials. It is expressed by equation

$$w = w_0 - \frac{\ln(1-h)}{d} \tag{5.6}$$

where w and w_0 is the moisture content and moisture content at zero relative humidity and d is a parameter with units [m^3/kg]. Note that for $h = 1$ this isotherm gives an infinite moisture content.

Künzel [67] proposes a following relation

$$w = w_f \frac{(b-1)h}{b-h} \tag{5.7}$$

where w and w_f is the moisture content and moisture content at free saturation and b is a dimensionless fitting parameter greater than 1.

Another expression for the sorption/desorption isotherm according to [52] reads:

$$u = u_h \left(1 - \frac{\ln h}{A}\right)^{-1/n} \tag{5.8}$$

where u is the moisture ratio. u_h is maximum hygroscopically bound water by adsorption, and A and n are constants obtained by fitting. This expression for sorption isotherm is used also in the material catalogue [58].

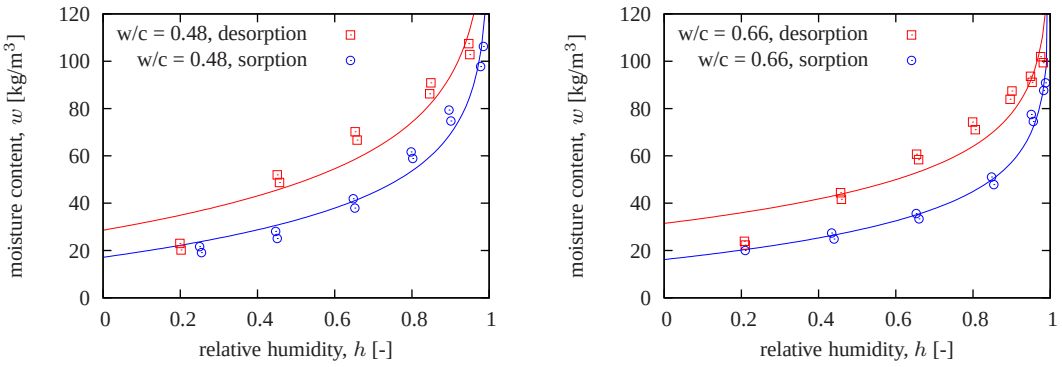

(a) (b)

Figure 5.6: Fit of experimental data from [58] using equation (5.6); (a) $\rho = 2300$ kg/m^3, w/c = 0.48, cement content 320 kg/m^3, desorption: $w_0 = 28.593$kg/m^3, $d = 0.0353$ m^3/kg, sorption: $w_0 = 17.149$kg/m^3, $d = 0.0353$ m^3/kg; (b) $\rho = 2300$ kg/m^3, w/c = 0.66, cement content 237 kg/m^3, desorption: $w_0 = 31.447$ kg/m^3, $d = 0.0494$ m^3/kg, sorption: $w_0 = 16.18$ kg/m^3, $d = 0.0559$ m^3/kg.

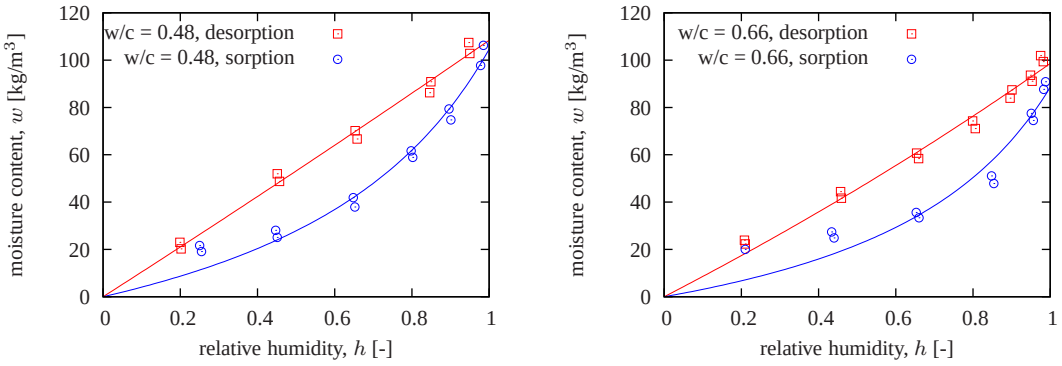

(a) (b)

Figure 5.7: Fit of experimental data from [58] using equation (5.7); (a) $\rho = 2300$ kg/m^3, w/c = 0.48, cement content 320 kg/m^3, desorption: $w_f = 108.406$kg/m^3, $d = 26.392$, sorption: $w_f = 104.643$kg/m^3, $d = 1.56932$; (b) $\rho = 2300$ kg/m^3, w/c = 0.66, cement content 237 kg/m^3, desorption: $w_f = 98.588$ kg/m^3, $d = 6.999$, sorption: $w_f = 88.579$ kg/m^3, $d = 1.492$.

The BSB isotherm [44] is an improved version of the famous BET isotherm. It is expressed in terms of the moisture ratio

$$u(h) = \frac{CkV_m h}{(1-kh)(1+(C-1)kh)} \tag{5.9}$$

where V_m is the monolayer capacity, k is a parameter within the range $0 < k < 1$. Parameter C depends on the absolute temperature T and on the difference between the heat of adsorption and condensation. Empirical formulae for estimation of the parameters can be found in [92]. Note that these formulae hold quite accurately for the cement paste only; a reduction of the moisture ratio is necessary when this isotherm should be applied to mortar or concrete.

In reference [92] the BSB isotherm is combined with the following permeability function

$$c(h) = \alpha_h + \beta_h \left[1 - 2^{-10^{\gamma_h (h-1)}}\right] \tag{5.10}$$

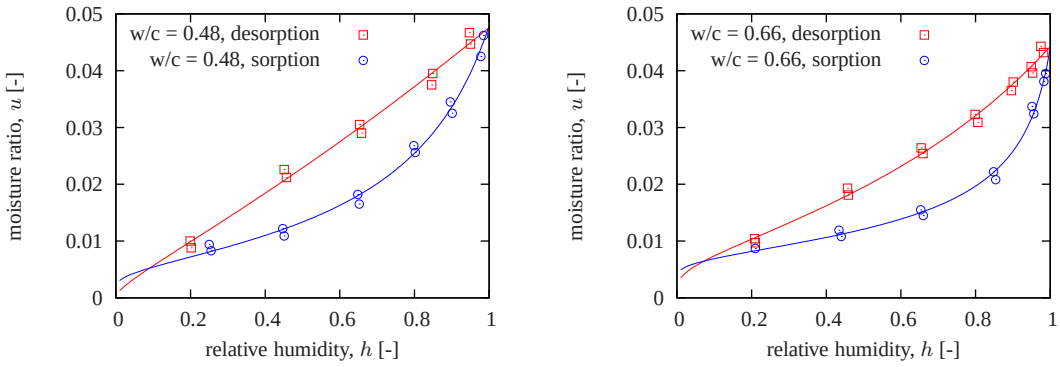

(a) (b)

Figure 5.8: Fit of experimental data from [58] using equation (5.8); (a) $\rho = 2300$ kg/m^3, w/c = 0.48, cement content 320 kg/m^3, desorption: $u_h = 0.0476$, $A = 4.830$, $n = 0.183$, sorption: $u_h = 0.0479$, $A = 0.214$, $n = 1.130$; (b) $\rho = 2300$ kg/m^3, w/c = 0.66, cement content 237 kg/m^3, desorption: $u_h = 0.0443$, $A = 0.825$, $n = 0.744$, sorption: $u_h = 0.044$, $A = 0.0534$, $n = 2.043$.

where α_h, β_h and γ_h are parameters that can be evaluated from the empirical mixture-based formulae. However, if those formulae are used outside the range of water-cement ratios for which they were calibrated, the permeability might become negative. Also the physical units are unclear.

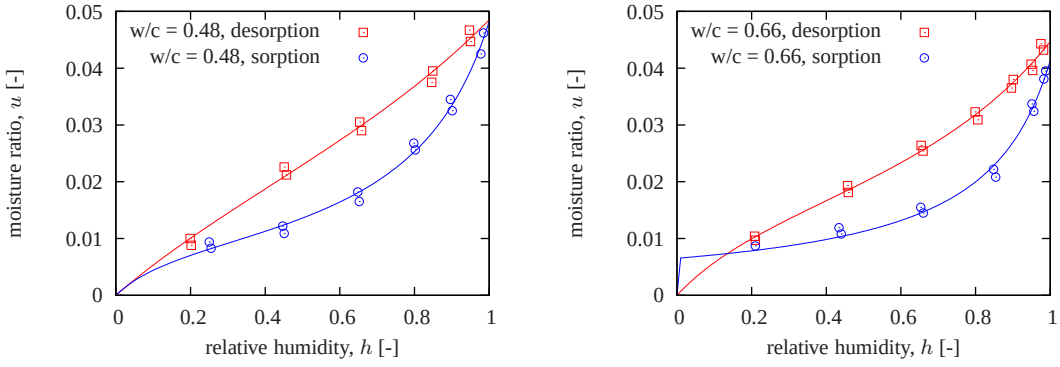

(a) (b)

Figure 5.9: Fit of experimental data from [58] using equation (5.9); (a) $\rho = 2300$ kg/m^3, w/c = 0.48, cement content 320 kg/m^3, desorption: $V_m = 0.0324$, $C = 3.638$, $k = 0.483$, sorption: $V_m = 0.00954$, $C = 8.371$, $k = 0.808$; (b) $\rho = 2300$ kg/m^3, w/c = 0.66, cement content 237 kg/m^3, desorption: $V_m = 0.0187$, $C = 6.153$, $k = 0.619$, sorption: $V_m = 0.00651$, $C = 2.084 \times 10^6$, $n = 0.8422$.

5.2 Model for nonlinear moisture transport in concrete – Bažant & Najjar (1972)

5.2.1 Governing equation

The presented material model results from the combination of two equations. The first one is the mass conservation equation

$$\frac{\partial w}{\partial t} = -\nabla \cdot J + S_w \tag{5.11}$$

where $\nabla\cdot$ is the divergence operator and J is the water mass flux density [kg/m^2·s] (mass of water passing through a unit area in unit time), and S_w is the moisture source or sink (due to chemical reactions) [kg/m^3·s]. The second equation

$$J = -c(h,T)\nabla h \tag{5.12}$$

relates the flux J to the gradient of a potential, which is in this case the pore relative humidity h. In this equation ∇h is the gradient of relative humidity and c is a temperature- and humidity-dependent coefficient called moisture permeability [kg/m·s]. Combining these two equations and omitting the moisture sink S_w, one gets

$$\frac{\partial w}{\partial t} = \nabla \cdot (c(h,T)\nabla h) \tag{5.13}$$

Assuming that the desorption isotherm has a constant slope, $k = \mathrm{d}w/\mathrm{d}h$ [kg/m^3] (often called "moisture capacity"), equation (5.13) can be modified to

$$\frac{\partial h}{\partial t} = \nabla \cdot (C(h,T)\nabla h) \tag{5.14}$$

where $C = c/k$ is the moisture diffusivity [m^2/s]. For concrete and other cementitious materials the dependence of diffusivity on relative humidity is highly nonlinear. According to [39] it can be approximated by

$$C(h) = C_1 \left(\alpha_0 + \frac{1-\alpha_0}{1+\left(\frac{1-h}{1-h_c}\right)^n} \right) \tag{5.15}$$

where C_1 is the moisture diffusivity at full saturation [m^2/s], α_0 is the ratio between the minimum diffusivity at very low saturation and maximum diffusivity at full saturation, h_c is a parameter that corresponds to the relative humidity in the middle of the transition between low and high diffusivity, and exponent n controls the shape of that transition.

The fib Model Code 2010 [48] provides default values of parameters: $\alpha_0 = 0.05$, $h_c = 0.8$, $n = 15$. The maximum diffusivity C_1 [m^2/s] can be estimated from the mean compressive strength f_{cm} [MPa]

$$C_1 = \frac{10^{-8}}{f_{cm} - 8} \tag{5.16}$$

5.2.2 Boundary conditions

The Dirichlet boundary condition, prescribing the value of environmental relative humidity h_{env} on the surface, is not very realistic. Reference [39] recommends to add to all exposed (drying)

surfaces the so-called "equivalent surface thickness" of 0.75 mm. This should correctly capture the effect of additional diffusion resistance of the surface.

Another approach used e.g. in [87] postulates a mixed boundary condition relating the moisture flux on the boundary to the difference between the relative humidity on the boundary and in the environment,

$$J/k = f \cdot (h_{env} - h) \tag{5.17}$$

where f is the surface factor [m/s] (0.75 - 7.5 mm/day according to [87]). In the case of a non-linear isotherm the moisture capacity and permeability cannot be lumped together and replaced by diffusivity. In such a case, the mixed boundary condition reads

$$J = \bar{f} \cdot (h_{env} - h) \tag{5.18}$$

where $\bar{f}$ is in [kg/(m^2 day)].

5.2.3 Experimental data and results from literature

Two sets of experimental data (originally published in [4] and [5]) related to 1-D diffusion were taken from [39]. In Fig. 5.10 dots denote experimentally measured data, dashed lines correspond to the best fit with the linear theory (constant diffusivity) and the results obtained with the Bažant-Najjar model are drawn using solid lines.

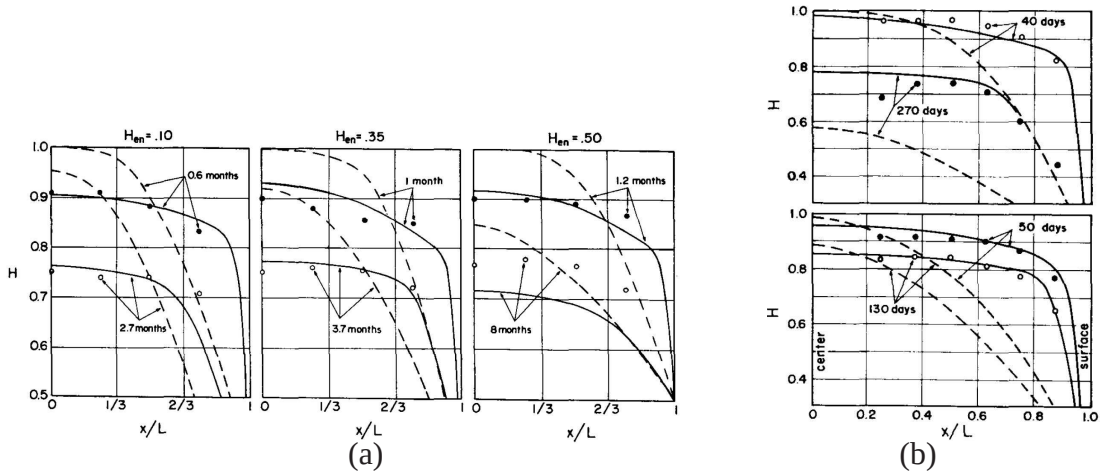

Figure 5.10: Distribution of the relative humidity in (a) three different drying specimens 6 in. (125.4 mm) thick exposed to $h_{env} = 0.1$, 0.35 and 0.5; (original Fig. 7 from [39], experimental data from [5]); (b) in one drying specimen 12 in. (304.8 mm) thick, $h_{env} = 0.1$ (original Fig. 8 from [39], experimental data from [4]).

The thesis of Nilsson [73] contains four data sets of measured relative humidity in drying specimens. In the experiment, prismatic specimens with four sealed sides (aluminum sealing) were used. The effective thickness of the specimens (i.e. the distance between the opposite drying surfaces) was 160 mm. Before drying at $h_{\rm env} = 40\%$ all specimens were cured under sealed conditions. The third set of experimental data exhibits a non-monotonous behavior (see Fig. 5.12c) and the fourth one used concrete with a very high water-to-cement ratio, hence only the first two sets are used in the present simulations (Fig. 5.12a, b). Unfortunately no

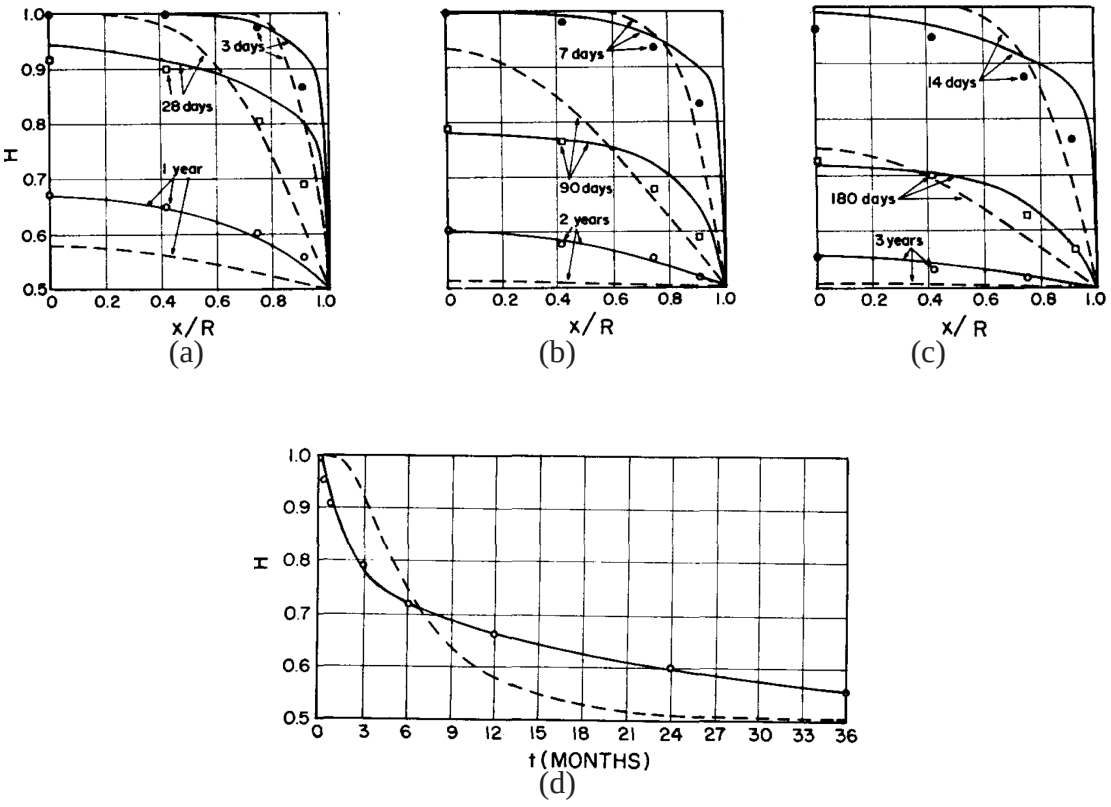

Figure 5.11: Computed distribution of the relative humidity and experimentally measured data (a)–(c) and the development of relative humidity in time (d) in drying cylinders of diameter 6 in. (125.4 mm) exposed to $h_{env} = 0.5$; solid line represents the optimal fit using non-linear diffusion theory, dashed line corresponds to the best fit according to linear diffusion; (original Figs. 9 and 10 from [39], experimental data from [60]).

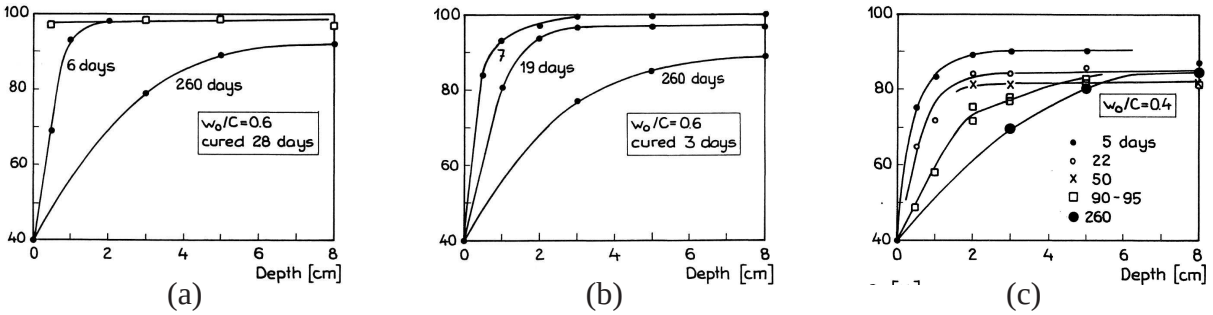

Figure 5.12: Measured relative humidity in concrete specimens with (a) w/c ratio 0.6, cement content 325 kg/m^3, cured 28 days, (b) w/c ratio 0.6, cement content 325 kg/m^3, cured 3 days, and (c) w/c 0.4, cement content 490 kg/m^3, cured 3 days; original Fig. 9.5 in [73].

information of the concrete strength is available, therefore it is not possible to determine the maximum diffusivity according to (5.16).

Kim and Lee [65] studied drying on prismatic specimens with all sides sealed except one; the effective thickness was 400 mm. Concretes of three compositions were used in the study.

The first composition (L) had w/c = 0.68 and 28-day compressive strength $f_c = 22$ MPa, the second one (M) w/c = 0.4 and $f_c = 53$ MPa, and the last one (H) w/c = 0.28 and $f_c = 76$ MPa. The specimens were demolded after the first day and were water-cured until the beginning of the experiment, i.e. until the age of 3 or 28 days. During drying the relative humidity of the environment was approx. 50%. Only the concrete of the first composition (L) (Fig. 5.13) is used in the study. Modeling of drying of the other two would be too inaccurate due to a high drop of relative humidity caused by self-desiccation. In order to compensate for the (measured) drop in relative humidity due to self-desiccation the authors of [65] used a somewhat incorrect procedure to recover the measured data of drying specimens. This was done simply by adding the difference between drying and self-desiccation to the actually measured data. This procedure leads to a considerable change (increase) of the gradient of relative humidity near the drying surface.

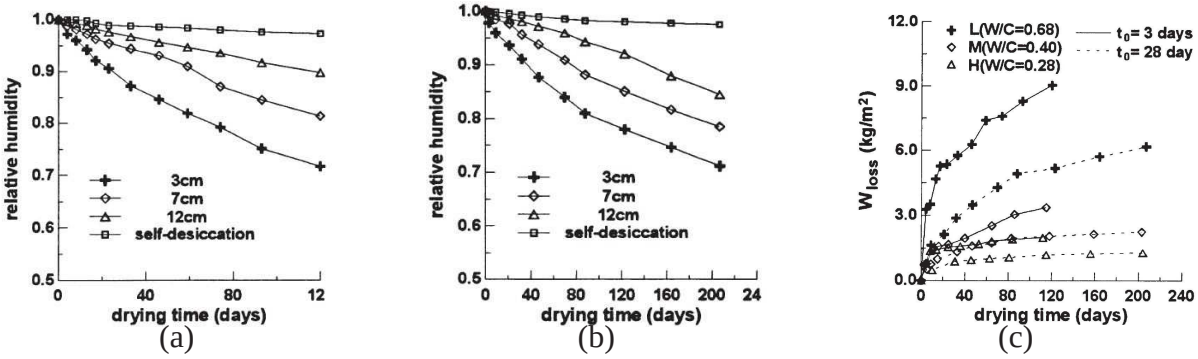

Figure 5.13: Measured relative humidity in specified depths from surface of drying specimens and relative humidity drop due to self-desiccation for (a) L cured 3 days, (b) L cured 28 days and (c) measured water mass loss per unit drying surface; pictures adapted from [65].

5.2.4 Numerical simulations

The aim of the numerical simulations presented in this Section was to revise the values of parameters of the model based on Bažand and Najjar [39], to assess the fib recommendations, and to examine the influence of the boundary conditions.

The solution of the diffusion equation (5.14) with the formula for diffusivity (5.15)) was implemented for 1D and axial symmetry in the Matlab environment. The solution utilized the "factory" bvp4c solver. For verification, the problem was also implemented into the FE package OOFEM which allows for more general simulations. However, the simulations in 1D and axial symmetry are fully sufficient to capture all presented experiments.

In order to find the best combination of parameters of formula (5.15) to match the experimentally measured data, the problem has been solved for all reasonable combinations of parameters and the error (sum of squares) of the solution has been assessed.

First, the recommended values of parameters from [39] have been used to check the difference between the original solution published by Bažant and Najjar (Figures 7 and 8 in [39], see Fig. 5.10) and the new solution computed by the present author (solid red lines in Figs. 5.14 and 5.17a). These values of parameters are listed in Tabs. 5.1 and 5.2 in columns labeled Bažant. For the first case (Fig. 5.10a and Fig. 5.14), these solutions differ, but not as dramatically as

for the second case (Fig. 5.10b and Fig. 5.17a). For the first case the overall fit seems to be even better than in the original paper. The recommended set of parameters for the second case does not give a good agreement with the experimental data—the diffusivity is too low. The optimal solutions are drawn in Fig. 5.14 and 5.17a in green (Dirichlet b.c.) and blue (mixed b.c.) lines. The corresponding sets of parameters are listed in Tabs. 5.1 and 5.2. Comparing the newly found parameters with the old ones, the biggest difference is in the value of the maximum diffusivity C_1, which almost doubled in the first case and increased five times in the second case.

Table 5.1: Recommended [39] and optimized parameters related to Fig. 5.14

parameter / variant	Bažant	Dirichlet b.c.	mixed b.c.	linear diffusion
α_0 [-]	0.05	0.05	0.05	-
h_c [-]	0.75	0.8	0.75	-
n [-]	16	16	16	-
C_1 [mm^2/day]	38.2	60	70	8
f [mm/day]	-	-	1	-

Table 5.2: Recommended [39] and optimized parameters related to Fig. 5.17

parameter / variant	Bažant	Dirichlet b.c.	mixed b.c.
α_0 [-]	0.05	0.05	0.1
h_c [-]	0.75	0.8	0.8
n [-]	16	10	10
C_1 [mm^2/day]	18.7	90	100
f [mm/day]	-	-	0.5

Table 5.3: Recommended [39] and optimized parameters related to Fig. 5.11

parameter / variant	Bažant	best fit	fit based on last 4 measurements
α_0 [-]	0.025	0.002	0.02
h_c [-]	0.792	0.85	0.775
n [-]	6.	3.	5.
C_1 [mm^2/day]	23.9	50.	31.

Figure 5.17b shows the time evolution of the relative water loss for the best (red) and 49 next best combinations (black). For these combinations the difference between the experimental data and the solution is almost the same, however, the sets of parameters differ considerably, see Fig. 5.17c. The optimized range of parameters (50 best combinations of approx. 1500) remains quite wide (original: $\alpha_0 = 0.05 - 0.5$, $h_c = 0.6 - 0.9$, $n = 10 - 16$, $C_1 = 15 - 90$ mm^2/day; optimized: $\alpha_0 = 0.05 - 0.1$, $h_c = 0.7 - 0.8$, $n = 10 - 16$, $C_1 = 40 - 90$ mm^2/day).

The best fits of Nilsson's data are shown in Fig. 5.2.4. The relative humidity is captured correctly even in the core of the specimen at early ages. This has been made possible by the initial condition reflecting the drop of relative humidity due to self-desiccation. To fit the first experimental data set the following parameters have been used: $\alpha_0 = 0.4$, $h_c = 0.9$, $n = 20$, $C_1 = 6$ mm^2/day (Dirichlet b.c.) and $\alpha_0 = 0.3$, $h_c = 0.6$, $n = 16$, $C_1 = 3$ mm^2/day, $f = 5$

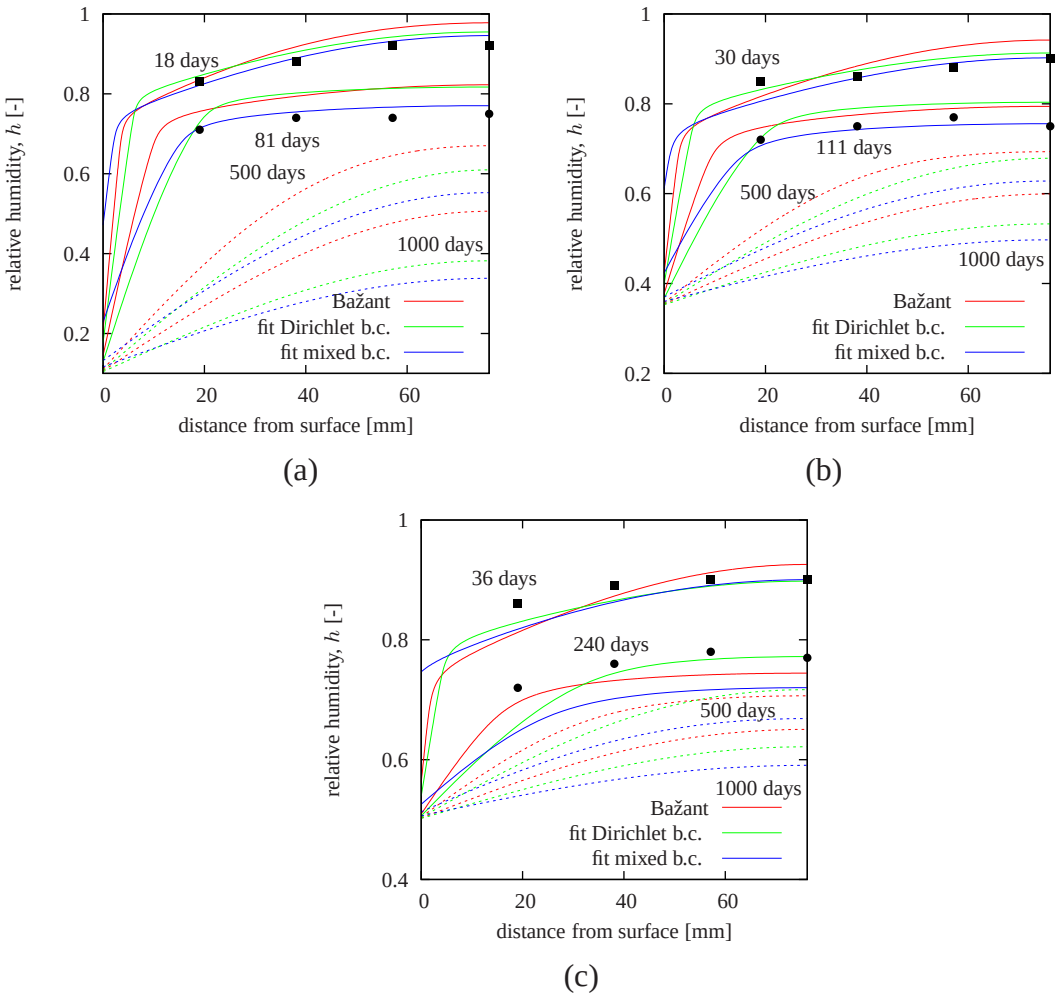

Figure 5.14: Fit of data from Bažant's Fig. 7 (Abrams & Orals): distribution of relative humidity over the cross section at specified times (and after 500 and 1000 days of drying) for (a) $h_{\text{env}} = 0.1$, (b) $h_{\text{env}} = 0.35$ and (c) $h_{\text{env}} = 0.5$.

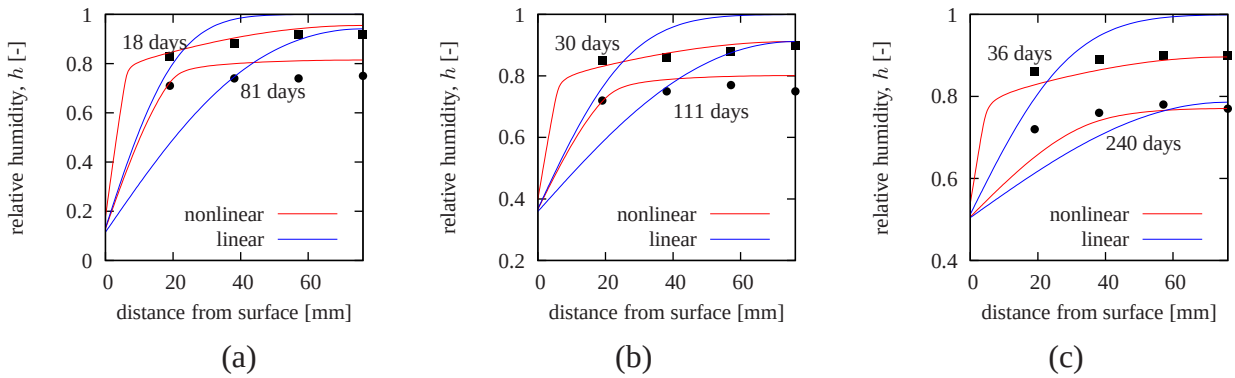

Figure 5.15: Fit of data from Bažant's Fig. 7 (Abrams & Orals): distribution of relative humidity over the cross section at specified times using linear and nonlinear diffustion at (a) $h_{\text{env}} = 0.1$, (b) $h_{\text{env}} = 0.35$ and (c) $h_{\text{env}} = 0.5$.

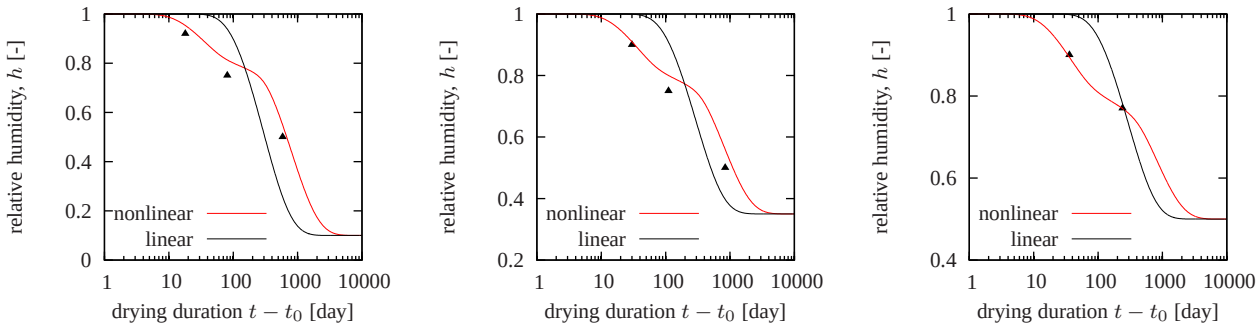

Figure 5.16: Fit of data from Bažant's Fig. 7 (Abrams & Orals) using linear and nonlinear diffusion theory: development of the relative humidity in the middle of the specimen for (a) $h_{\text{env}} = 0.1$, (b) $h_{\text{env}} = 0.35$ and (c) $h_{\text{env}} = 0.5$.

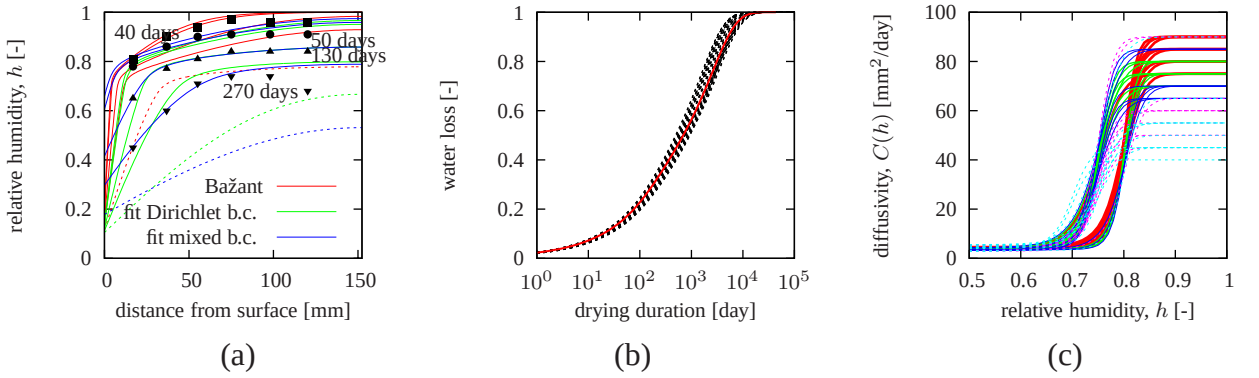

Figure 5.17: (a) Fit of data from Bažant's Fig. 8 (Abrams & Monfore): distribution of relative humidity over the cross section at specified times (and at 1000 days of drying), (b) computed moisture loss expressed as a fraction of the total loss, and (c) diffusivity functions for the best 50 combinations (the thicker the line, the smaller the error).

mm/day (mixed b.c.). The second set of experimental data has been best fit with $\alpha_0 = 0.3$, $h_c = 0.7$, $n = 6$, $C_1 = 5$ mm^2/day (Drichlet b.c.) and $\alpha_0 = 0.3$, $h_c = 0.7$, $n = 10$, $C_1 = 6$ mm^2/day, $f = 1$ mm/day (mixed b.c.). It is clear that these values differ considerably from those in Tab. 5.1; the values of maximum diffusivity are about 10× to 30× smaller. Also, the diffusivity functions do not exhibit a pronounced difference between low and high humidity (the minimum diffusivity is 30% or 40% of the maximum value, instead of the recommended value of 5% or 10%).

Neither the parameters recommended by fib nor the parameters from [65] give a satisfactory agreement with the experimental data; see Fig. 5.21a and Fig. 5.22a. In these figures the difference between the calculated profiles of relative humidity is almost inobservable, because these two sets of parameters share all values except maximum diffusivity C_1, which differs very slightly (see Tabs. 5.4 and 5.5). Keeping all parameters except C_1 fixed to their values recommended by fib, it has been found that values of $C_1 = 64$ mm^2/day (see solid lines Fig. 5.21b) and 83 mm^2/day (see solid lines Fig. 5.22b) give the smallest error. However, the agreement with the experimental data is not deemed to be good, especially for the data points near surface. Dashed lines in Fig. 5.21b show the solution which has been obtained by optimizing all the

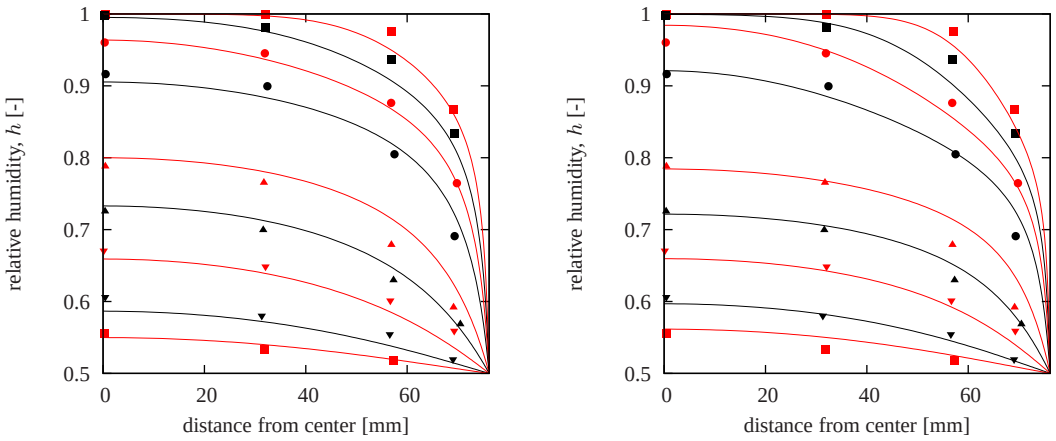

Figure 5.18: Fit of data from Bažant's Fig. 9 (Hanson): distribution of relative humidity over the cross section at specified times taking into account (a) all measurements (b) considering only the data from last 4 humidity profiles.

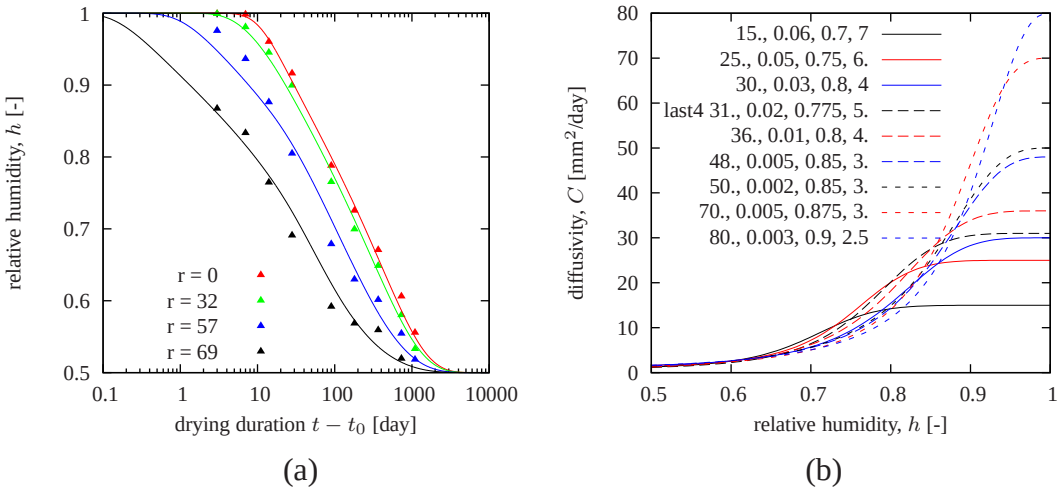

Figure 5.19: Fit of data from Bažant's Figs. 9 and 10 (Hanson): (a) development of the relative humidity at specified points in time, (b) diffusivity functions which give approximately similar error.

parameters.

Definitely the best fit has been obtained with mixed boundary conditions (and not with Dirichlet b.c. as in previous cases), see Figs. 5.21c and 5.22c. The self-desiccation has been treated in two different ways: it has been reflected either by the initial condition at the beginning of the simulation, or by a slightly more complicated procedure applied during whole computation. This procedure consists of the following steps: 1) fitting the time evolution of self-desiccation with a power function (in both cases: $0.035(1 - \exp(-0.05t^{0.65}))$); 2) evaluating the increment of this function in every time step and then subtracting it from the computed solution. Such a procedure is not perfect (the same value is subtracted from all points of the cross section, independently of the actual relative humidity), but it should be more realistic than the method used in [65].

The development of shrinkage and its final magnitude is closely related to the time evolution

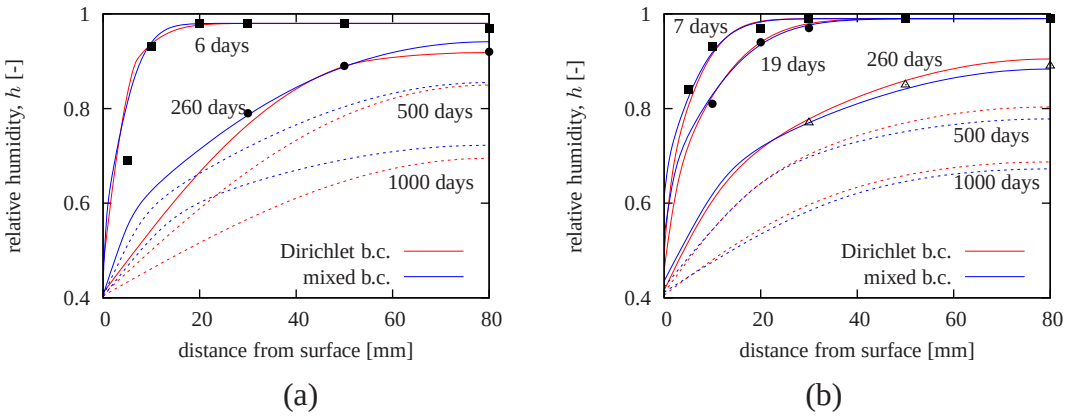

Figure 5.20: Fit of Nilsson's data at specified times and at 500 and 1000 days of drying.

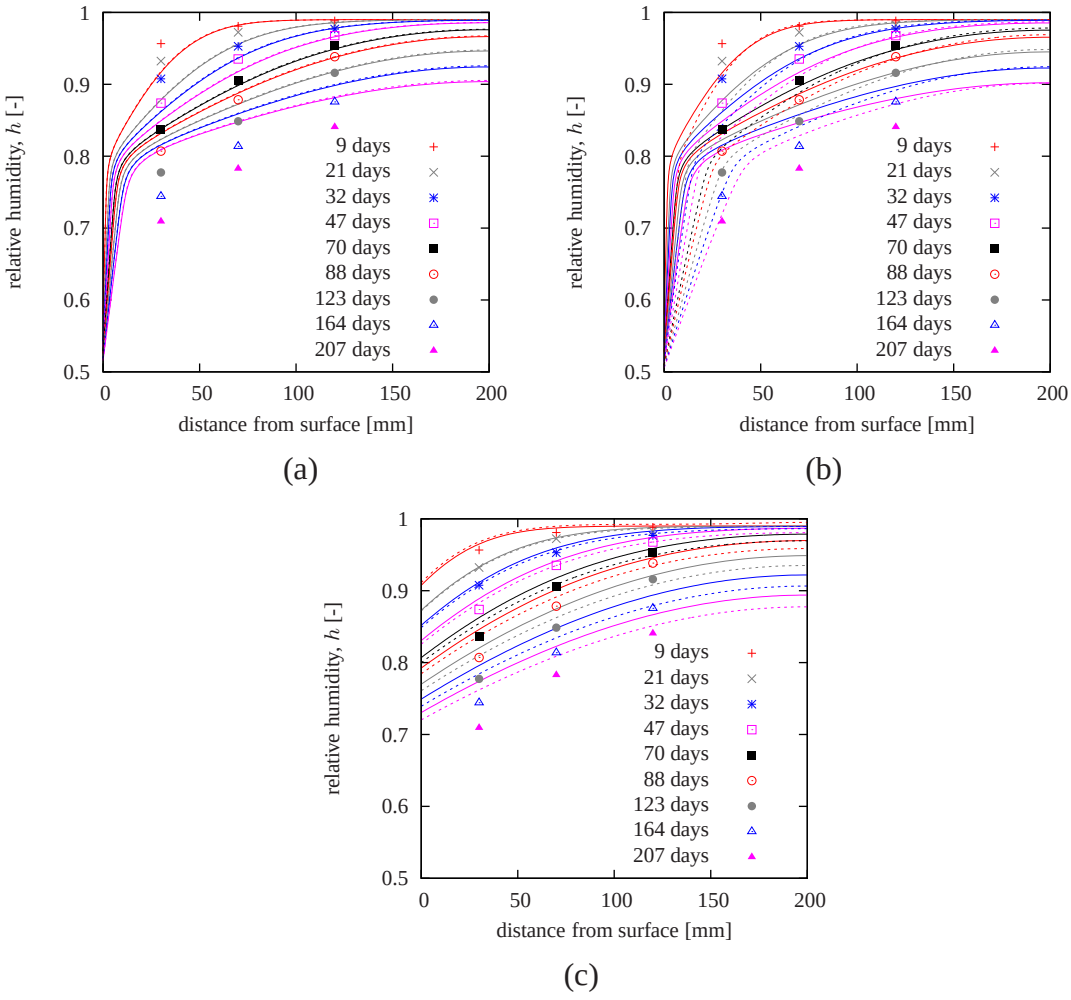

Figure 5.21: Evolution of relative humidity in time (Kim-Lee, "L", curing time 28 days) (a) Dirichlet b.c.; solid lines: parameters from [65]; dashed lines: parameters according to fib; (b) Dirichlet b.c.; solid lines: optimized value of C_1, other parameters according to fib; dashed lines: best fit; (c) mixed b.c.; desiccation reflected by initial condition (solid lines) or by a function (dashed lines).

Table 5.4: Kim-Lee, "L", curing time 28 days, variants related to Fig. 5.21

parameter / variant	(a) solid	(a) dashed	(b) solid	(b) dashed	(c) solid	(c) dashed
α_0 [-]	0.05	0.05	0.05	0.2	0.05	0.1
h_c [-]	0.8	0.8	0.8	0.8	0.6	0.6
n [-]	15	15	15	20	16	16
C_1 [mm^2/day]	62.88	61.71	64	55	75	75
f [mm/day]	-	-	-	-	0.5	0.5

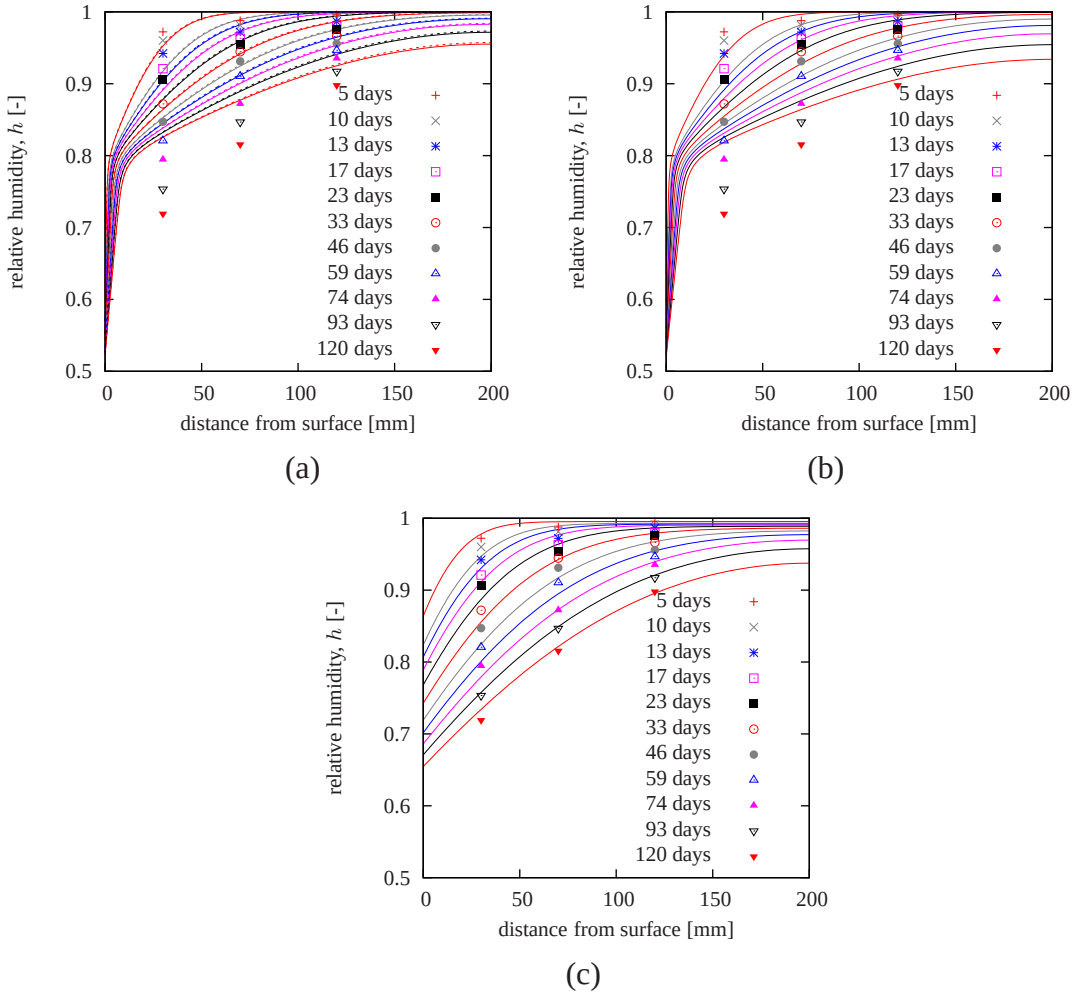

Figure 5.22: Evolution of relative humidity in time (Kim-Lee, "L", curing time 3 days) (a) Dirichlet b.c.; solid lines: values from [65], dashed lines: values according to fib; (b) Dirichlet b.c.; optimized value of C_1 with other parameters according to fib; (c) mixed b.c.; desiccation described by a function.

of water loss and to the total content of evaporable water. Therefore, to guarantee a realistic prediction of shrinkage, it is vital to be able to accurately simulate the development of moisture loss. The moisture loss can be computed either by time integration of the moisture flux at the boundary or by subtracting total moisture content at given time from its initial value at the onset of drying. Fig. 5.23 shows the experimentally measured data and the computed water loss for some previously mentioned cases. Note that the slope of the desorption isotherm is assumed

Table 5.5: Kim-Lee, "L", curing time 3 days, variants related to Fig. 5.22

parameter / variant	(a) solid	(a) dashed	(b)	(c)
α_0 [-]	0.05	0.05	0.05	0.05
h_c [-]	0.8	0.8	0.8	0.5
n [-]	15	15	15	14
C_1 [mm^2/day]	63.6	61.71	83	55
f [mm/day]	-	-	-	1

to be constant, equal to 100 kg/m^3. This value works only as a scalar multiplier, while the computed shapes remain the same. Fig. 5.23a shows that a more accurate development of water loss has been obtained with Dirichlet boundary conditions and that the shape of the moisture loss curve computed using the mixed boundary conditions is initially too flat and in the main phase of drying too steep. For the shorter curing period the experimental data are far from any computed solution (see Fig. 5.23b).

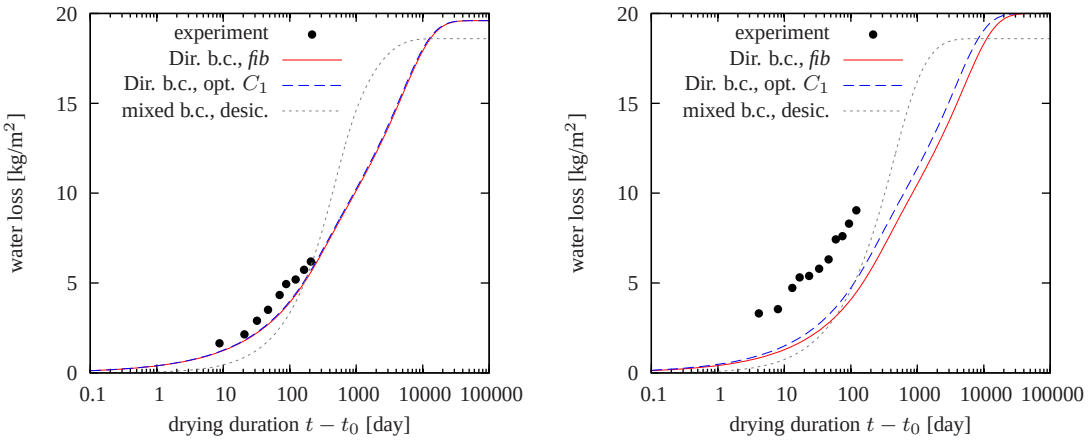

(a) (b)

Figure 5.23: Time evolution of water loss per square meter of drying surface, assumed slope of desorption isotherm is the same for all data series: 100 kg/m^3, (a) Kim-Lee, "L", curing time 28 days, (b) Kim-Lee, "L", curing time 3 days.

5.2.5 Conclusion

The material model based on [39] has been successfully implemented in the Matlab environment and also into the FE package OOFEM. It has been found that values of parameters published in the original papers [39] and [65] give different results from those published. The recommendation of parameters in [48] is too simplistic and gives a poor agreement with experimental measurements. The model proposed in [39] is almost insensitive to the specific choice of some parameters, namely to the exponent n. The best agreement with experimental data has been obtained when using the mixed boundary conditions instead of the Dirichlet b.c.. The assumption of a linear isotherm might be sufficient when modeling the time development of relative humidity in the specimen, but it seems that it is necessary to use a more general model when the moisture loss is of interest, too.

5.3 Heat transport in concrete

5.3.1 Governing differential equations and boundary conditions

Neglecting that the temperature gradient causes also migration of water, the heat transport in concrete can be described by two following equations.

$$q = -\lambda(h,T)\nabla T \tag{5.19}$$

$$\rho c\frac{\partial T}{\partial t} = -\nabla\cdot q + Q \tag{5.20}$$

The first one is well-known Fourier equation where the heat flux q [W/m^2] is equal to the temperature gradient multiplied by thermal conductivity λ [W/m·K] and flows in the opposite direction. The second equation describes the energy balance. Here the time derivative of temperature is proportional to the sum of the divergence of the heat flux and the rate of internal heat generation per unit volume Q [W/m^3]. The proportionality factor is the specific heat c [J/kg·K] multiplied by the material density ρ [kg/m^3].

There are four basic types of boundary conditions: Dirichlet boundary conditions prescribing temperature on part of boundary Γ_T,

$$T(\boldsymbol{x}) = \bar{T}(\boldsymbol{x}) \quad \text{for} \quad \boldsymbol{x}\in\Gamma_T \tag{5.21}$$

Neumann boundary conditions prescribing flux on part of boundary $\Gamma_{\bar{q}}$,

$$\boldsymbol{n}\cdot q(\boldsymbol{x}) = \bar{q}_n(\boldsymbol{x}) \quad \text{for} \quad \boldsymbol{x}\in\Gamma_{\bar{q}_p} \tag{5.22}$$

mixed boundary condition

$$\boldsymbol{n}\cdot q(\boldsymbol{x}) = \alpha(\boldsymbol{x})(T(\boldsymbol{x}) - T_{\text{env}}(\boldsymbol{x})) \quad \text{for} \quad \boldsymbol{x}\in\Gamma_{\bar{q}_c} \tag{5.23}$$

where α [W/m^{2}K] is the convective heat transfer coefficient and T_{env} is the temperature of the environment, and the radiation (Newton) boundary condition

$$\boldsymbol{n}\cdot q(\boldsymbol{x}) = \sigma\psi(T(\boldsymbol{x}) - T_\infty(\boldsymbol{x}))^4 \quad \text{for} \quad \boldsymbol{x}\in\Gamma_{\bar{q}_r} \tag{5.24}$$

with the Stefan–Boltzmann constant $\sigma = 5.670\times10^{-8}$ [W/m^2·K^4], emissivity ψ (0.–1.), and the temperature of the source T_∞.

5.3.2 Thermal conductivity of concrete

The thermal conductivity λ [W/m·K] depends mainly on the concrete composition (type of aggregates and density), degree of saturation and temperature, and for most common structural concretes it is in the range 1.4 – 3.6 W/m·K [72]. Water has higher conductivity than air and therefore more saturated concrete has also higher conducitivity; this becomes pronounced in case of light-weight concretes. However, in experimental measurements, it is easier to measure thermal diffusivity and from that compute thermal conductivity.

5.3.3 Thermal diffusivity of concrete

Thermal diffusivity δ [m^2/s] is defined as

$$\delta = \frac{\lambda}{c\rho} \tag{5.25}$$

and its typical values are in the range 0.002 to 0.006 m^2/h [72].

5.3.4 Specific heat of concrete

This material property depends mainly on the moisture content and on the density of concrete. Specific heat grows with increasing moisture content and with decreasing density. For ordinary concrete it is in the range from 840 to 1170 J/kg·K [72].

5.4 Coupled heat and moisture transport in Concrete – Künzel (1995)

The material model for simultaneous heat and moisture transport proposed by Künzel [67] was developed for the building materials in general, not particularly for concrete. The model should provide quite accurate solution to problems of a common engineering practice, while the governing equations still remain quite simple and the number of input parameters is manageable. The material model uses two state variables, from which all other can be derived: temperature T and relative humidity h.

The mechanism of moisture transport is the combination of the water vapor diffusion driven by the pressure differences and described by Fick's law (larger pores) and the liquid water conduction through micropores and capillary pores governed by Darcy's law, and the surface diffusion in larger pores, which is caused by the gradient in relative humidity.

The model is based on two balance equations, one for heat and the other for moisture. The first one reads

$$\frac{\partial H}{\partial t} = -\nabla \cdot q + Q \tag{5.26}$$

where H [J/m^3] is the total enthalpy, q [W/m^2] is the heat flux density, and Q [W/m^3] is heat source or sink. The total enthalpy H is composed of the moisture enthalpy H_w [J/m^3] and the enthalpy of the dry material H_d [J/m^3].

$$H = H_w + H_d \tag{5.27}$$

The moisture enthalpy is described by

$$H_w = \left((w - w_{frozen})\, c_w + w_{frozen} c_e - h_e \frac{\mathrm{d}w_{frozen}}{\mathrm{d}T} \right) T \tag{5.28}$$

where w [kg/m^3] is the total water content, w_{frozen} [kg/m^3] content of frozen water, c_w [J/kg·K] specific heat capacity of liquid water, c_e [J/kg·K] specific heat capacity of ice, h_e [J/kg] specific melting enthalpy. In most cases (temperatures above melting point) this equation can be simplified to

$$H_w = w c_w T \tag{5.29}$$

Enthalpy of the dry building material is defined as

$$H_d = \rho_d c_d T \tag{5.30}$$

with the bulk density of the dry building material ρ_d [kg/m^3], and the specific heat capacity of the dry building material c_d [J/kg· K].

The heat flux obeys the Fourier law

$$q = -\lambda \nabla T \tag{5.31}$$

where λ [W/m·K] is thermal conductivity of the moist building material defined as

$$\lambda = \lambda_0(1 + b \cdot w/\rho_s) \tag{5.32}$$

with the thermal conductivity of dry building material λ_0 [W/m·K] and the thermal conductivity supplement defined as percentual increase in conductivity per one mass percent of moisture b [%/%].

The enthalpy source term Q covers only vapor diffusion with the simultaneous phase transition (condensation/evaporation)

$$Q = -h_v \nabla \cdot J_v \tag{5.33}$$

where h_v [J/kg] is the latent heat of phase change ($h_v = 2500$ kJ/kg = evaporation enthalpy of pure water, the sorption enthalpy can be neglected in most cases) and J_v [kg/m^2·s] is the vapor diffusion flux density. It can be determined from

$$J_v = -\delta_p \nabla p = -\frac{\delta}{\mu} \nabla p \tag{5.34}$$

where δ_p [kg/m·s·Pa] is the water vapor permeability of the building material, δ [kg/m·s·Pa] is the water vapor permeability in air, μ is the water vapor diffusion resistance factor, and p [Pa] is the water vapor partial pressure

$$p = p_{sat} h \tag{5.35}$$

The water water vapor permeability in air can be approximately expressed (standard DIN 52615) as

$$\delta = 2.0 \times 10^{-7} T^{0.81} / P_L \tag{5.36}$$

where P_L [Pa] is ambient air pressure, 101325 Pa and temperature T is here in Kelvin.

The saturation vapor pressure p_{sat} [Pa] can be estimated from empirical relationship as a function of temperature

$$p_{sat} = 611 \exp\left(\frac{aT}{T_0 + T}\right) \tag{5.37}$$

with $a = 22.44$ and $T_0 = 272.44$ °C if $T < 0$ °C and $a = 17.08$ and $T_0 = 234.18$ °C if $T \geq 0$ °C.

The vapor diffusion flux density J_v appears also in the second (moisture balance) equation

$$\frac{\partial w}{\partial t} = -\nabla \cdot (J_w + J_v) + S_w \tag{5.38}$$

where S_w [kg/m^3 s] is the moisture source or sink and J_w [kg/m^2·s] is the liquid transport flux density expressed as

$$J_w = -D_h \nabla h \tag{5.39}$$

with the liquid conduction coefficient D_h [kg/m · s].

After substituting some of these equations into the main balance equations (5.26) and (5.38) one gets

$$\frac{\mathrm{d}H}{\mathrm{d}T} \cdot \frac{\mathrm{d}T}{\mathrm{d}t} = \nabla \cdot (\lambda \nabla T) + h_v \nabla \cdot (\delta_p \nabla (h p_{sat})) \tag{5.40}$$

$$\frac{\mathrm{d}w}{\mathrm{d}h} \cdot \frac{\mathrm{d}h}{\mathrm{d}t} = \nabla \cdot (D_h \nabla h + \delta_p \nabla (h p_{sat})) \tag{5.41}$$

which can be easily solved using the FE method. In these two equations $\mathrm{d}H/\mathrm{d}T$ corresponds to the heat storage capacity of the moist building material (obtained simply by differentiating equations (5.29) and (5.30) with respect to temperature) and $\mathrm{d}w/\mathrm{d}h$ is the moisture capacity of the building material (i.e. derivative of the sorption isotherm). The liquid conduction coefficient D_h can be replaced by $D_w\,\mathrm{d}w/\mathrm{d}h$, where D_w [m^2/s] is the capillary transport coefficient. The capillary transport coefficient can be estimated (for $w \leq w_f$) from

$$D_w = 3.8\left(\frac{A}{w_f}\right)^2 1000^{\frac{w}{w_f}-1} \tag{5.42}$$

where A is the water absorption coefficient.

At constant temperature the equation (5.41) can be rewritten to

$$\frac{\mathrm{d}w}{\mathrm{d}h}\cdot\frac{\mathrm{d}h}{\mathrm{d}t} = \nabla\cdot\left[\left(D_w\frac{\mathrm{d}w}{\mathrm{d}h}+\delta_p p_{sat}\right)\nabla h\right] \tag{5.43}$$

The typical value of the water vapor diffusion factor μ for concrete is 210–260 and the reasonable value of the water absorption coefficient A is about 0.1–1. kg·m^{-2}·day$^{-0.5}$.

The dependence of moisture diffusivity on relative humidity is shown in Fig. 5.24 for Bažant-Najjar model (with $C_1 = 30$ mm^2/day and the other parameters according to fib) and for Künzel's model (with linear isotherm and the other parameters used in Chapter 8).

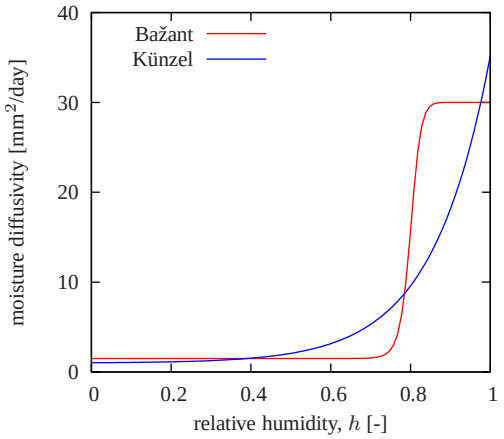

Figure 5.24: Comparison of the moisture diffusivity according to Bažant and Najjar ($C_1 = 30$ mm^2/day, $\alpha_0 = 0.05$, $h_c = 0.8$ and $n = 15$) with Künzel's model ($T = 20°$C, $\mu = 400$, $A = 0.3$ kg·m^{-2} day$^{-0.5}$, linear isotherm, $w_f = 100$ kg/m^3).

6 MPS: Numerical Simulations and Model Deficiencies

In this section, the experimental data from the literature are compared to the results obtained with MPS theory, which reduces to the standard B3 model in the special case of basic creep. The material model was implemented into the finite element package OOFEM [76, 77, 78], which was used to run all the numerical computations.

All examples concerning drying and/or thermally induced creep have been run as a staggered problem, with the heat and/or moisture transport analyses preceding the mechanical analysis. The available experimental data contained the mechanical strains (due to elasticity and creep), with the thermal and shrinkage strains subtracted.

In the experiments, shrinkage and thermal strains were measured separately on load-free specimens and were subtracted from the strain of the loaded specimen under the same environmental conditions. It should be noted that even after subtraction of shrinkage and thermal strain, the evolution of mechanical strain described by MPS theory is affected by humidity and temperature. Attention is focused here on the mechanical strain, composed of the first three contributions to the total strain and a cracking unit as shown in Fig. 4.1; these units are stress-dependent.

In the examples presented in Sections 6.1 and 6.2 the specimens were sealed, the elevated temperature was kept constant during the entire experiment and its distribution was assumed to be uniform over the cross section of the specimen. Under such conditions, it is sufficient to run the numerical simulation for one material point only.

On the other hand, a more complex approach is necessary to simulate the experiments from Sections 6.3, 6.4, 6.6, and a virtual experiment from Section 6.5 where the specimens are subjected to drying at constant room temperature. The well-known model proposed by Bažant and Najjar which was presented in Section 5.2 is used in the simulations of moisture transport.

In experiment presented in Section 6.7, the specimens were subjected to one or more thermal cycles and some of them also to drying. The heat and moisture transport processes are considered to be completely independent. This can be justified by the fact that by the time of the first temperature change all the specimens had already attained moisture equilibrium. Again, the Bažand and Najjar model is used to simulate the moisture diffusion. Although the temperature in this experiment was not constant in time, it was not necessary to solve it. Due to the experimental setup (small sample thickness and slow temperature variation) it was sufficient to prescribe the same temperature uniformly over the whole cross section.

6.1 Experiments of Kommendant, Polivka and Pirtz (1976)

6.1.1 Experimental setup

The research report [66] studied concrete creep at elevated temperatures. Two concrete mixtures have been examined. Since the purpose of the concrete was the same (atomic power plants), also the composition of these two mixtures was very similar; the main difference was the used aggregates (both calcitic dolomites and dolomitic limestones). The two concretes were named after the origin of the aggregates. The same cement (Portland type II, low alkali) was used in both mixtures. Both compositions contained also water reducing agents and retarding admixtures.

The Berks concrete mixture contained: 418.86 kg/m^3 of cement, 159.59 kg/m^3 of water (w/c = 0.381), 726 kg/m^3 of sand, and 1091 kg/m^3 of aggregates (a/c = 4.34). The 28-day

compressive strength of moist cured specimens was 45.2 MPa. The York concrete mixture had a higher cement content 448.52 kg/m^3, quantities of the remaining ingredients are similar: 172.05 kg/m^3 of water (w/c = 0.384), 741 kg/m^3 of sand, 1066 kg/m^3 of aggregates (a/c = 4.03). Even though the cement content was higher, the 28-day compressive strength was comparable: 45.9 MPa.

All the experiments were done on 60 cylindrical specimens 6×16 inches (15.24×40.46 cm) which were sealed against the moisture with loss butyl rubber sealing. For every age at loading and temperature the creep was measured on 3 specimens, autogenous shrinkage on 2 and drying shrinkage (irrelevant in this study) on one.

The specimens were cured at 23°C. 5 days prior to loading the temperature started increasing at a constant rate of 13.33°C/day until the target value 43 or 71°C was reached.

The specimens were loaded by compressive stress 30%/45%/60% of strength reached at the time of loading (28, 90 or 270 days). The concrete creep is assumed to be linear only at stress levels below 40% of the compressive strength which makes only the results obtained at the lowest stress level suitable for this study. The compressive stress was the same for the specimens loaded at the age of 28 and 90 days, 2100 psi (14.48 MPa) the stress applied on the specimen at the age of 270 days was 2400 psi (16.55 MPa).

In some of the experiments the strain was measured also after unloading. In one particular experiment (Berks concrete loaded at the age of 270 days), the temperature was raised from 23°C to 43°C at the age of 544 days.

All figures in this Section show the evolution of the compliance function or mechanical strain. A closer look at Fig. 6.1 indicates that the average value of the 3 measurements can be misleading and can lead to misinterpretation of the physical mechanism. Therefore all figures in this section show the individual measurements (3 creep specimens for every setup) compensated for the thermal strain and the average value of the autogenous shrinkage.

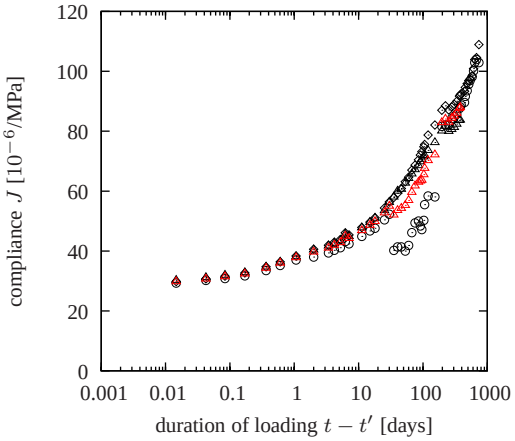

Figure 6.1: Evolution of mechanical strain for Berks concrete placed in 71°C and loaded at the age of 28 days. Black color shows the experimental measurements on 3 specimens and red color their average incorrectly indicating on higher creep rate at the later phase. The average was used in [15].

6.1.2 Numerical simulations

It is assumed that in the distribution of relative humidity, temperature and stress is uniform in the whole specimen. This assumption enables to run all the computations on just one finite element.

First, it is necessary to calibrate parameters of the basic creep q_1–q_4 on the data measured at room temperature, then it is possible to modify the recommended values of the activation energies (3 parameters) and finally to tune up the value of μ_S which matters only at variable temperature.

The parameters of the B3 model can be estimated from the composition of concrete mixture and the compressive strength using the empirical formulae: $q_1 = 18.8559$, $q_2 = 122.8909$, $q_3 = 0.7511$, $q_4 = 7.2670$ (all in 10^{-6}/MPa) for Berks concrete and $q_1 = 18.7116$, $q_2 = 125.4213$, $q_3 = 0.7875$, $q_4 = 7.6533$ (all in 10^{-6}/MPa) for York concrete. For Berks concrete the reference [15] recommends these values: $q_1 = 20.0$, $q_2 = 70.0$, $q_3 = 5.6$ and $q_4 = 7.0$, all in 10^{-6}/MPa).

As shown in Figures 6.2 and 6.3 with the set of empirically estimated parameters, the effect of aging is highly overestimated. Even with the recommended parameters [15] the computed compliance for the age at loading $t' = 270$ days underestimates the experimental data for the loading durations $t - t'$ longer than 3 days. For the shorter loading durations the data are not captured accurately for any age at loading. Since the concrete composition of both mixtures is very similar, it can be expected that also the optimum set of parameters of the compliance function should be similar. Indeed, with the values $q_1 = 14$, $q_2 = 60$, $q_3 = 16$, $q_4 = 6$ (all in 10^{-6}/MPa) the compliance functions match the experimental data of both concrete compositions very well.

The reference [15] presented only two figures with Kommendant's data. Both of them showed the compliance increase at constant elevated temperatures for the fixed age at loading ($t' = 28$ and 90 days) such as in Fig. 6.4. For the longer loading durations the creep rate is correct; the error stems from the region of the shorter loading durations, approximately $t - t' < 10$ days. If the data series with the same temperature are plotted together (see Fig. 6.5) instead of the same age at loading, the experimental data clearly show that with increasing temperature the effect of aging diminishes while in simulations it persists.

However, this problem can be easily alleviated if the simulation does not start at the age of loading, but 5 days earlier when the temperature actually started increasing. The temperature changes prior to loading increase the microprestress (resulting in the lower viscosity of the aging dashpot and its higher compliance) which does not have time to fully relax until loading. On the other hand the response becomes sensitive to the choice of parameter μ_S. The influence of parameter μ_S on compliance is shown in Fig. 6.6, for $\mu_S = 0$ the behavior is similar as before (it is not exactly the same because the equivalent times are different). With the increasing value of μ_S, the influence of aging significantly decreases. (The effect of aging is still the same but it becomes negligible comparing to additional compliance caused by the temperature changes.) The best agreement (comparing these four values) is found with $\mu_S = 8.75 \times 10^{-5}$ MPa^{-1}day^{-1}. Ten times higher value of $\mu_S = 8.75 \times 10^{-4}$ MPa^{-1}day^{-1} that works best in Section 6.7 gives here too high initial compliance.

The results that are shown in Figures 6.7–6.10 have been obtained with the original version of the MPS model with adjusted parameters of the basic creep $q_1 = 14$, $q_2 = 60$, $q_3 = 16$, $q_4 = 6$ (all in 10^{-6}/MPa), with parameter controlling increase in compliance caused by temperature changes $\mu_S = 8.75 \times 10^{-5}$ MPa^{-1}day^{-1}, and with default values of the activation energies.

The agreement with the experimental data is deemed to be very good. For the highest temperature $T = 71°\mathrm{C}$ the model gives an opposite trend than the experiment but this behavior can be hardly taken as a disadvantage of the material model. In Figs. 6.7b and 6.8b the measured compliance of the specimens loaded at the age $t' = 28$ days is smaller or equal than for $t' = 90$ and $t' = 270$ days, while the MPS model gives the expected trend: lower compliance of more mature specimens.

The fit of the experimental data can be further improved by modifying the recommended values of the activation energies that have been used so far. This is shown in Fig. 6.11 for the York concrete and the highest temperature $T = 71°\mathrm{C}$. Since all specimens are almost fully hydrated, change in the activation energy Q_E/R controlling the equivalent hydration time t_e would not change anything. On the other hand if the activation energy Q_S/R which determines the rate of the viscous process is increased from 3000 K to 4500 K and Q_R/R, which is associated with the rate of viscoelastic process from 5000 K to 6000 K the fit becomes more accurate.

Figures 6.12 and 6.13 show further verification of the MPS theory on Kommendant's experimental data where the measurements continued after full unloading. There are 5 different data series for Berks concrete and 6 for York concrete. In one case (red curve in Fig 6.12c) the temperature was raised during the experiment from 23°C to 43°C. In all examined cases the experimentally measured and the computed strain recovery after unloading matches very well. This means that the transient thermal creep is correctly modeled by a rheological unit (aging dashpot) which remains deformed after unloading.

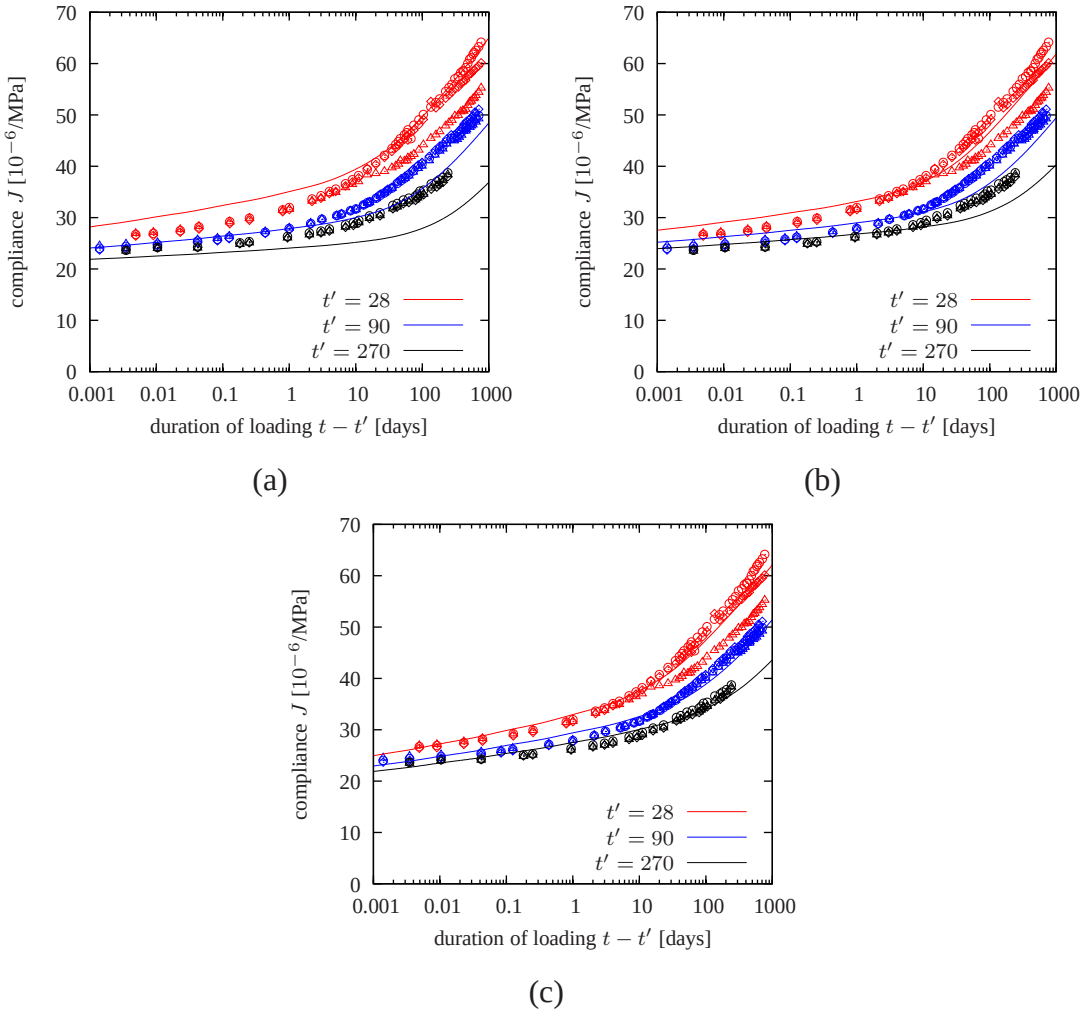

Figure 6.2: Berks concrete: experimentally measured and computed compliance functions for three different ages at loading and room temperature (a) material parameters estimated from concrete mixture $q_1 = 18.86$, $q_2 = 122.89$, $q_3 = 0.75$, $q_4 = 7.27$ (all in 10^{-6}/MPa), (b) parameters from [15] $q_1 = 20$, $q_2 = 70$, $q_3 = 5.6$, $q_4 = 7$ (all in 10^{-6}/MPa), (c) optimized parameters $q_1 = 14$, $q_2 = 60$, $q_3 = 16$, $q_4 = 6$ (all in 10^{-6}/MPa).

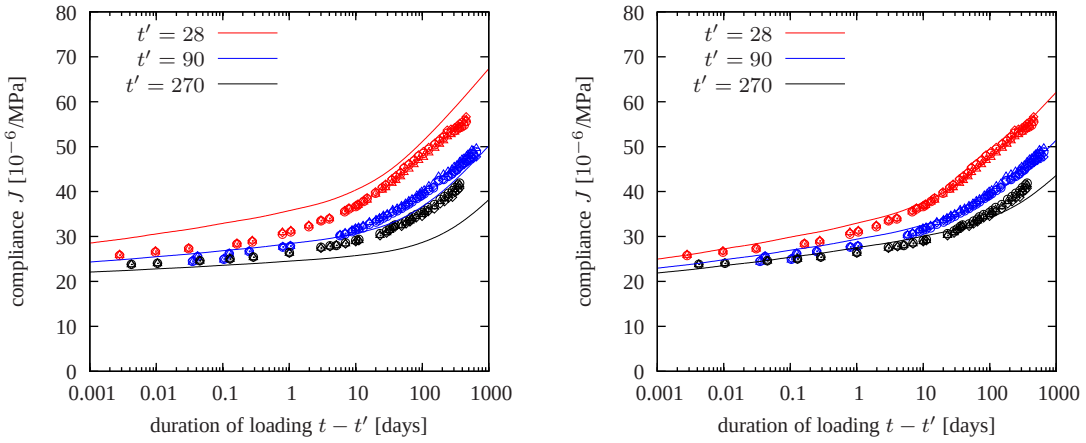

Figure 6.3: York concrete: experimentally measured and computed compliance functions for three different ages at loading and room temperature (a) material parameters estimated from concrete mixture $q_1 = 18.7116$, $q_2 = 125.4213$, $q_3 = 0.7875$, $q_4 = 7.6533$ (all in 10^{-6}/MPa), (b) optimized parameters $q_1 = 14$, $q_2 = 60$, $q_3 = 16$, $q_4 = 6$ (all in 10^{-6}/MPa).

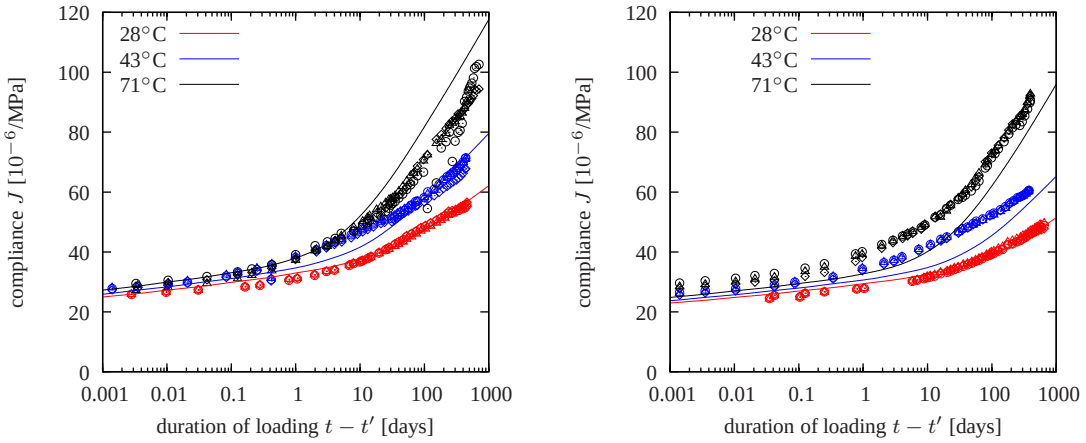

Figure 6.4: York concrete: experimentally measured and computed compliance functions for three different levels of temperature, age at loading (a) $t' = 28$ days, (b) $t' = 90$ days. Temperature was constant throughout the simulation.

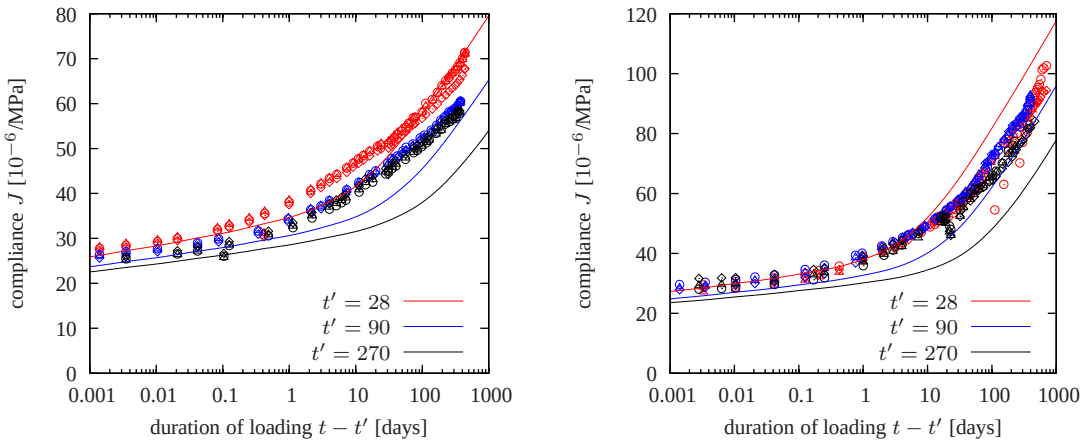

Figure 6.5: York concrete: experimentally measured and computed compliance functions for three different ages at loading, (a) $T = 43°\mathrm{C}$, (b) $T = 71°\mathrm{C}$. Temperature was constant throughout the simulation.

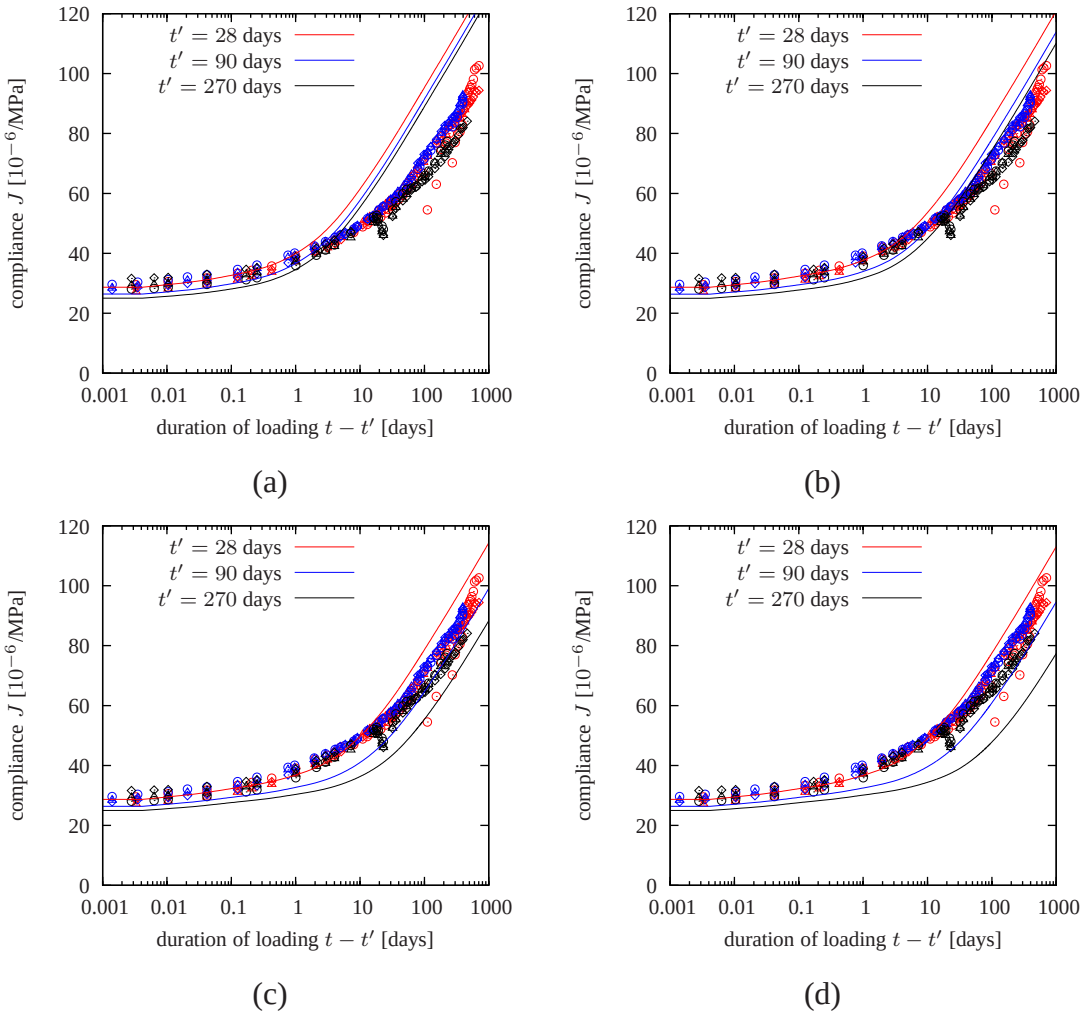

Figure 6.6: York concrete: experimentally measured and computed compliance functions for three different ages at loading and (a) $\mu_S = 8.75 \times 10^{-4}$ MPa^{-1}day^{-1}, (b) $\mu_S = 8.75 \times 10^{-5}$ MPa^{-1}day^{-1}, (c) $\mu_S = 8.75 \times 10^{-6}$ MPa^{-1}day^{-1}, (d) $\mu_S = 0$ MPa^{-1}day^{-1}.

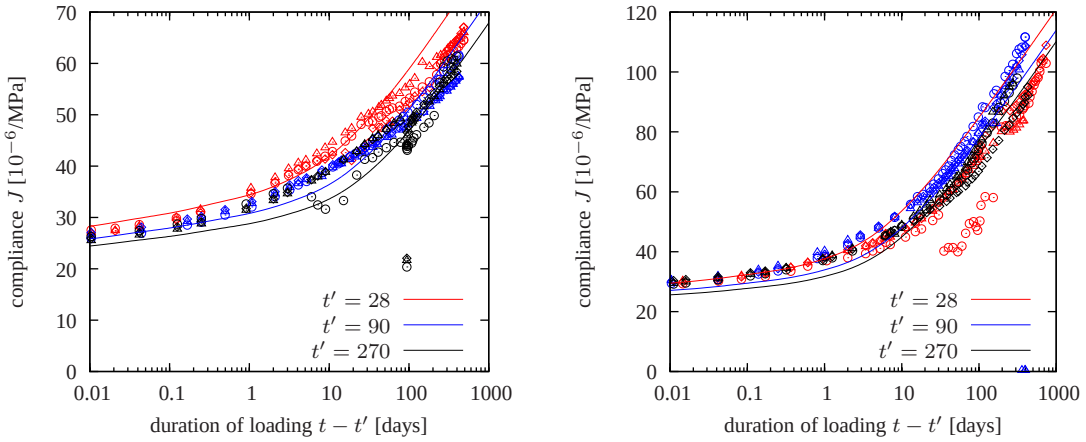

Figure 6.7: Berks concrete: experimentally measured and computed compliance functions for three different ages at loading and temperature (a) $T = 43°\mathrm{C}$, (b) $T = 71°\mathrm{C}$.

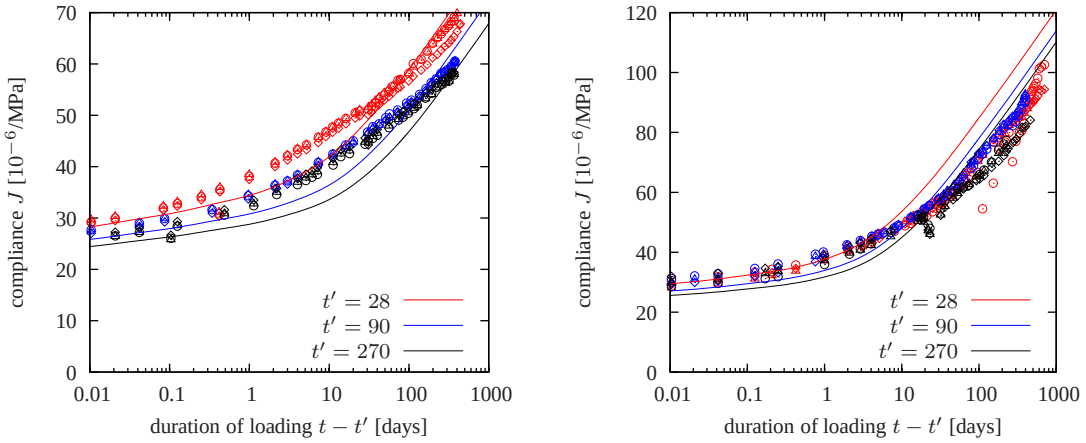

Figure 6.8: York concrete: experimentally measured and computed compliance functions for three different ages at loading and temperature (a) $T = 43°\mathrm{C}$, (b) $T = 71°\mathrm{C}$.

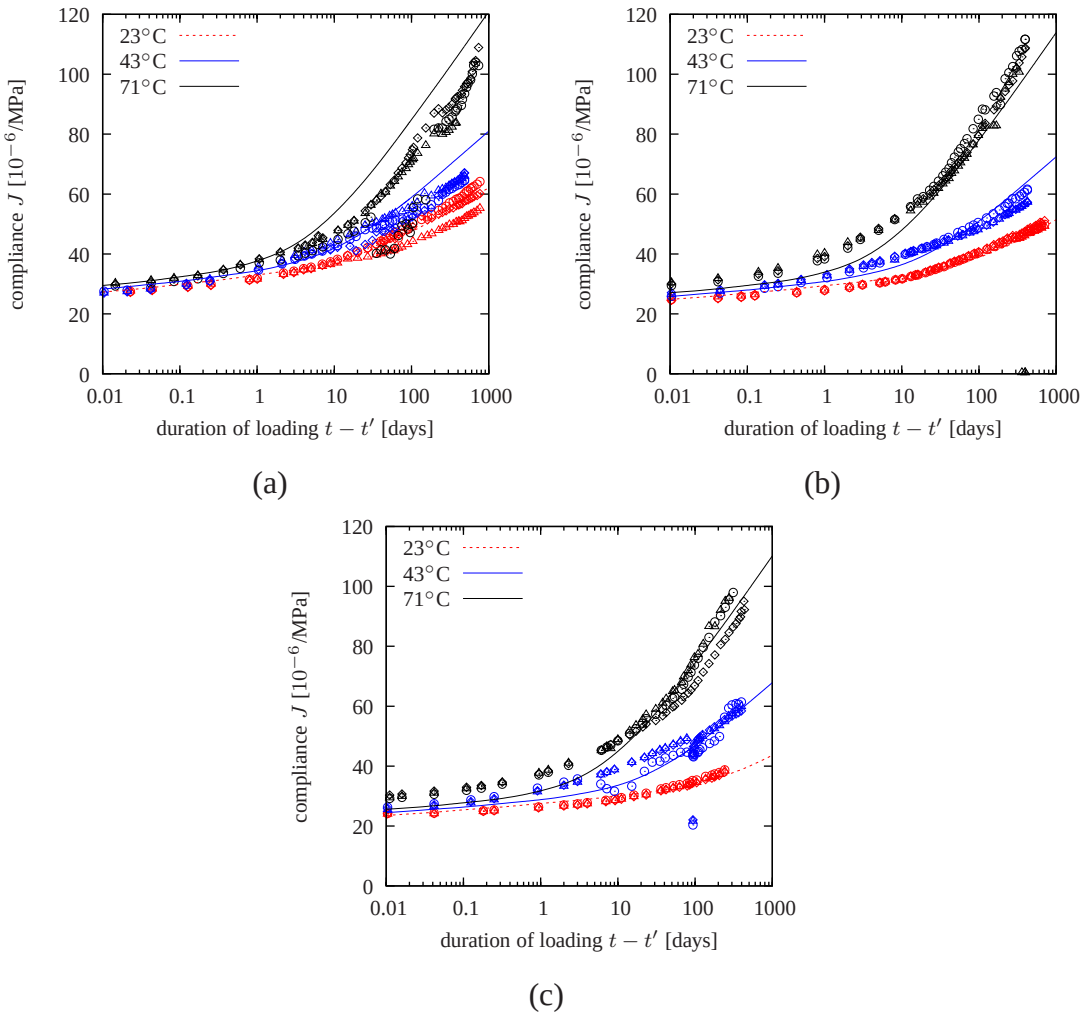

Figure 6.9: Berks concrete: experimentally measured and computed compliance functions for (a) $t' = 28$, (b) $t' = 90$, (c) $t' = 270$ days.

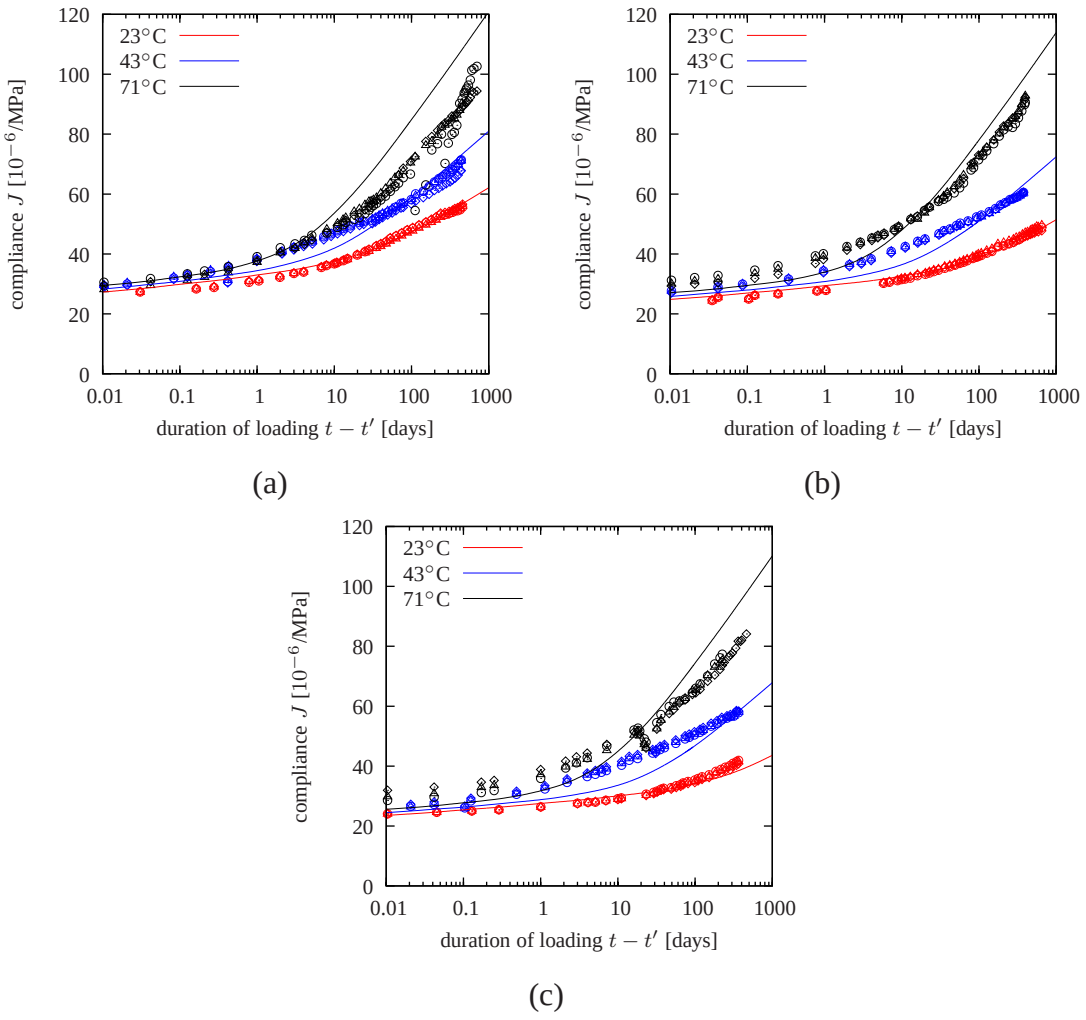

Figure 6.10: York concrete: experimentally measured and computed compliance functions for (a) $t' = 28$, (b) $t' = 90$, (c) $t' = 270$ days.

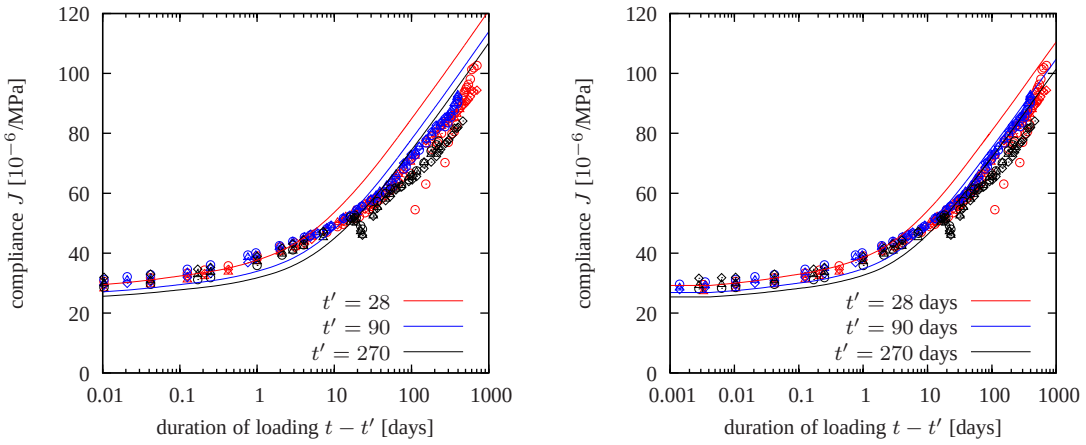

Figure 6.11: York concrete: experimentally measured and computed compliance functions for three different ages at loading and $T = 71°\mathrm{C}$. MPS model with (a) default values of activation energies $Q_R/R = 5000$ K and $Q_S/R = 3000$ and (b) adjusted activation energies to achieve an optimum fit: $Q_R/R = 6000$ K and $Q_S/R = 4500$ K.

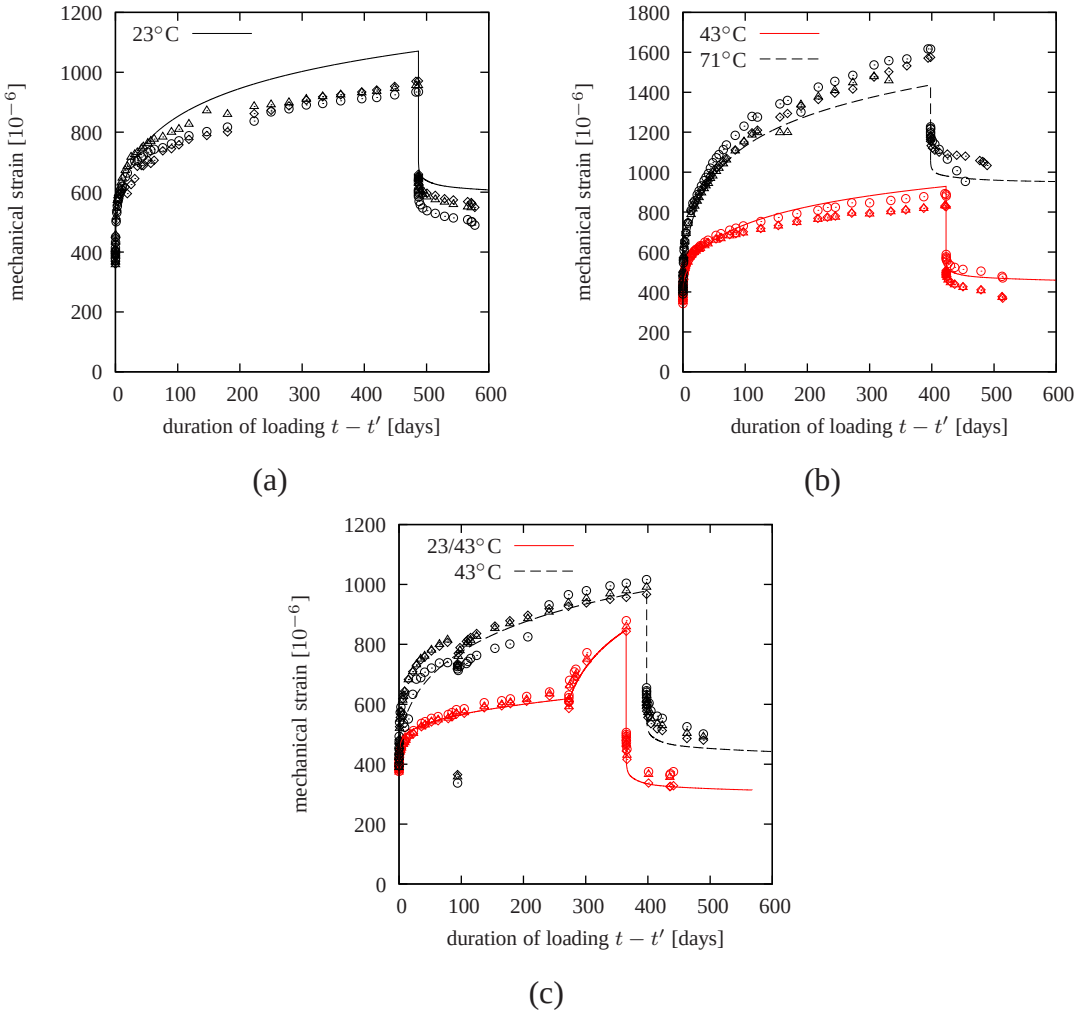

Figure 6.12: Experimental data (concrete with Berks aggregates) and results of numerical simulations using MPS theory: evolution of mechanical strain for loading and full unloading, age at loading (a) $t' = 28$ days, (b) $t' = 90$ days, (c) $t' = 270$ days.

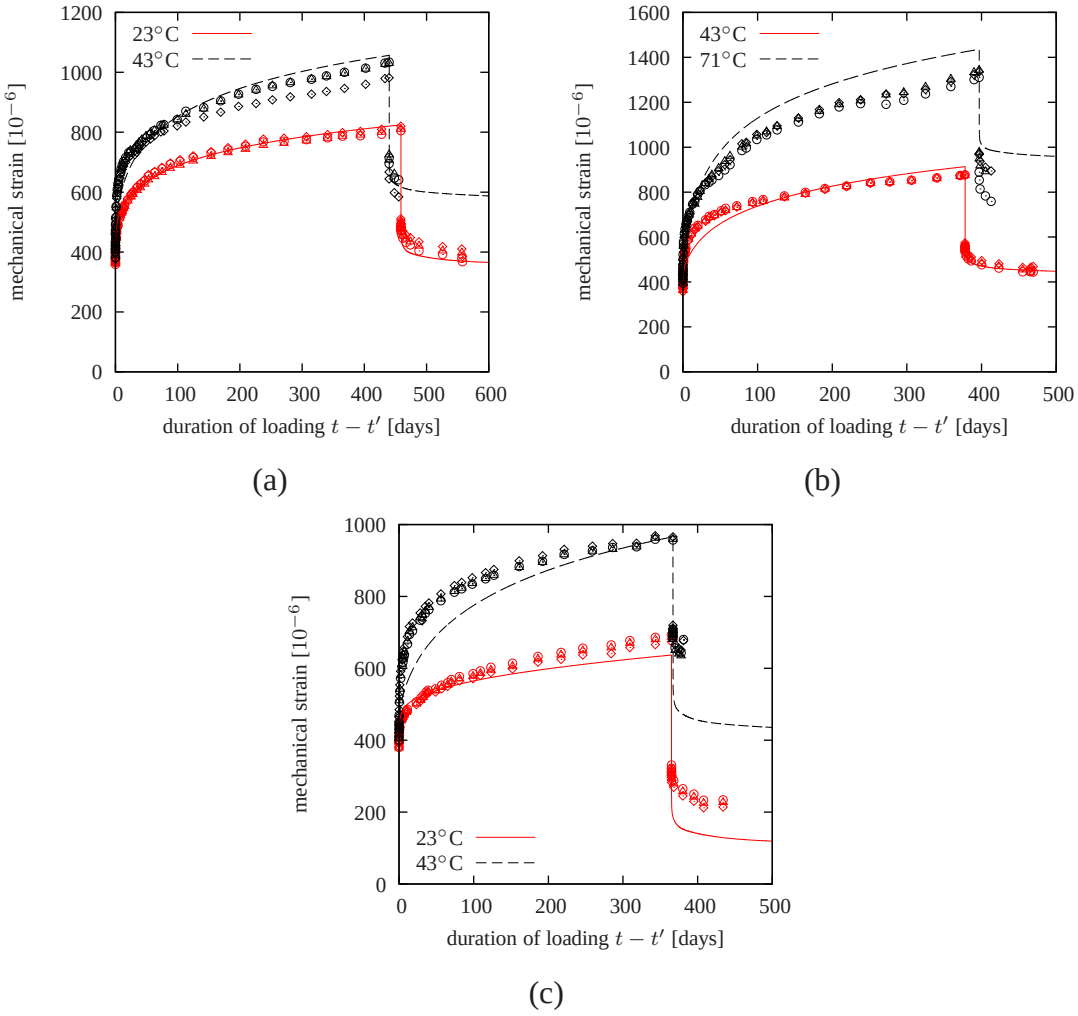

Figure 6.13: Experimental data (concrete with York aggregates) and results of numerical simulations using MPS theory: evolution of mechanical strain for loading and full unloading, age at loading (a) $t' = 28$ days, (b) $t' = 90$ days, (c) $t' = 270$ days.

6.2 Experiments of Nasser and Neville (1965)

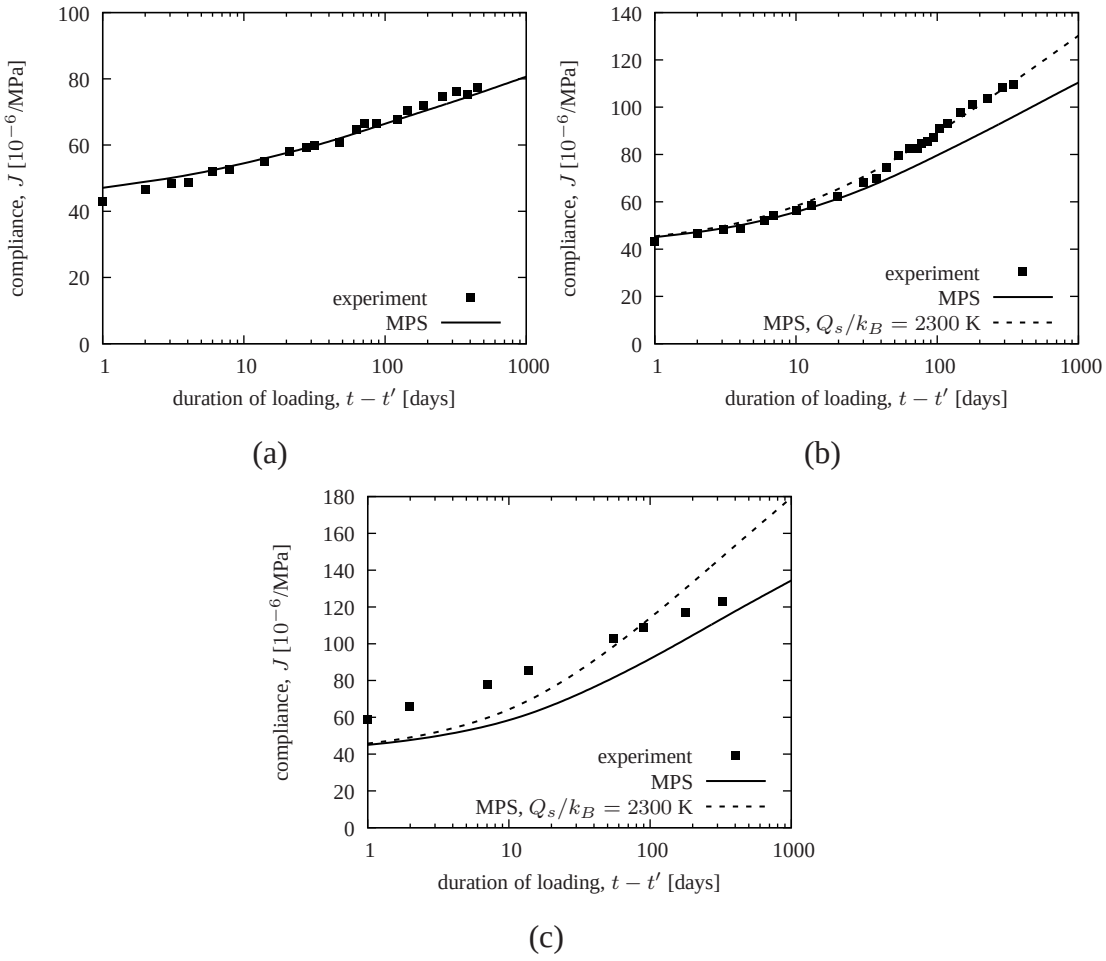

Figure 6.14: Experimental data (Nasser and Neville) and compliance functions computed using MPS theory for temperatures (a) 21°C, (b) 71°C, (c) 96°C.

6.2.1 Experimental setup

Nasser and Neville [71] studied the creep of cylindrical concrete specimens subjected to three different levels of temperature. In their experiments, all specimens were sealed in water-tight jackets and placed in a water bath in order to guarantee a constant temperature. At the age of 14 days the specimens were loaded to 35%, 60% or 69% of the average compressive strength at the time of loading; unfortunately, only the lowest load level is in the range in which concrete creep can be considered as linear.

6.2.2 Numerical simulations

Paper [71] does not contain enough information to allow the parameters of B3 model/MPS theory to be predicted, but the values $q_1 = 15$, $q_2 = 80$, $q_3 = 24$ and $q_4 = 5$ (all in 10^{-6}/MPa)

published in [15] provide a good agreement at room temperature, see Figure 6.14a.

For the higher temperature, T = 71°C, the agreement is good up to 20 days at loading, but afterwards the computed creep rate is too low (see the dashed curve in Fig. 6.14b). A remedy can be sought in modifying the activation energy. Reduction of Q_S/R from the default value 3000 K to the adjusted value of 2300 K leads to an excellent fit (see the solid curve in Fig. 6.14b). Unfortunately, the prediction for the highest temperature (T = 96°C, is improved only partially - see Fig. 6.14c).

The changes in activation energy have no influence on the results when the temperature is close to the room temperature. Before loading, the specimens had been subjected to an environment at the given temperature, which accelerated the hydration processes in concrete, i.e. increased the maturity of concrete. In other words, the higher the temperature, the lower the initial compliance. On the other hand, for longer periods of loading the higher temperature accelerates the rate of bond breakages, which accelerates creep. This justifies the shape of the obtained curve for the medium temperature, which is different from the one published in [15], where the initial compliance for this temperature was higher than for the room temperature.

6.3 Experiments of Bryant and Vadhanavikkit (1987)

6.3.1 Experimental setup

Reference [45] presents shrinkage and creep data measured on prismatic specimens. Effects of the specimen size, shape and age at loading on creep and shrinkage have been examined.

All specimens were made of the same concrete mixture containing 390 kg/m^3 of ordinary Portland cement, 183 kg/m^3 of water (w/c = 0.47), 1667 kg/m^3 of coarse aggregates, and 318 kg/m^3 of sand (a/c = 5.09). The concrete mixture contained no additives. The 28-day compressive strength determined on cylinders 150×300 mm was 50.1 MPa, and the modulus of elasticity 29.8 GPa.

All specimens were cast in open plywood molds; after the initial set, the specimens were covered with a damp burlap. The mold was removed after two days and the specimens were moved to a room with controlled environment. The relative humidity $h_{\rm env} = 95\%$ was dropped to $h_{\rm env} = 60\%$ after 6 days. The temperature was kept throughout the experiment at 20°C. The creep specimens were loaded by external or internal bars causing a compressive stress of 7 MPa. Creep and shrinkage strains were monitored using 200 mm long demountable mechanical gage. The initial strain readings were taken on day 8 before the humidity was lowered.

There were two major groups of the experimental specimens subjected to drying. The specimens in one of the groups are referred to as the "prisms" the other as "slabs". The "prisms" had sealing only on the bases, the "slabs" on two additional sides, which forced the drying to be one-dimensional.

All faces of the companion sealed specimens, 4 faces of the "slab" specimens, and 2 parallel faces of the prismatic specimens were sealed with a 0.035 mm thick aluminum foil. The sealing had failed after approximately 300 days. This failure had a significant impact on sealed specimens (failure is accompanied by sudden increase in creep rate and shrinkage) but only a partial effect on slab segments which had by the time of sealing failure already partially dried out. All sealed specimens were 150×150×600 mm, the drying specimens (prisms and slabs) D×D×4D with D = 100, 150, 200, 300 or 400 mm.

The experimental results of the basic creep are presented in Fig. 6.15, for shrinkage in Fig. 6.16, and for the drying creep in Figs. 6.17 and 6.18.

6.3.2 Numerical simulations

First, it was essential to specify the values of the material parameters q_1–q_4 controlling the basic creep. The first estimate was provided by the empirical formulae of the B3 model which use the compressive strength and the composition of concrete mixture. However, this prediction overestimates the effect of aging and also gives too small viscoelastic compliance (see Fig. 6.15a). In order to get an acceptable agreement with the experimental data, it was necessary to modify the parameters q_1–q_3 while parameter q_4 controlling long-time creep was kept at its original value (see Fig. 6.15b for the improved fit; predicted and adjusted values of the parameters q_1–q_4 are listed in Table 6.1).

Next, it was needed to fit 4 parameters of the Bažant-Najjar model for moisture transport [39], one shrinkage parameter k_{Sh}, one drying creep parameter μ_S, and finally 2 parameters controlling cracking G_f and f_t.

It has been found that in this case the exact values of the cracking parameters (tensile strength and fracture energy) do not matter (if they are within a reasonable range character-

Table 6.1: Values of parameters – structural analysis

	basic creep (all values in $\times 10^{-6}$				MPS		fracture	
	q_1 MPa^{-1}	q_2 MPa^{-1}	q_3 MPa^{-1}	q_4 MPa^{-1}	μ_S MPa^{-1}day^{-1}	k_{Sh} –	f_t MPa	G_F N/m
Bryant	9	75	28	6.5	5×10^{-6}	0.00195	2	100
predict.	18	108	1.5	6.5				

istic of the given concrete class). What plays a significant role is whether or not the cracking is assumed – see Fig. 6.19 for comparison. If cracking is neglected, the shrinkage deformation grows faster and reaches a higher final value. On the other hand the compliance is higher if cracking is assumed; the reason is that the compliance is computed as a difference of the total deformation and shrinkage strains divided by the compressive stress. Therefore a smaller value of the shrinkage strain is subtracted from the total strain and this results in a higher compliance.

Since no information on humidity profiles or water loss were available, the only option how to determine parameters of the Bažant-Najjar model was to exploit the assumption of the MPS theory postulating the proportionality of the humidity change and shrinkage strain at the material point level. The approximate values of parameters can be then obtained inversely by fitting the experimentally measured shrinkage curves. A trial-and-error procedure was used to calibrate these values and k_{Sh} on shrinkage data of a 150 mm thick slab (thick black line in Fig. 6.16a). The following values of the Bažant-Najjar moisture diffusion model were used: $C_1 = 40 \times 10^{-6}$ m^2/day, $\alpha_0 = 0.18$, $h_C = 0.75$, $n = 10$. The remaining gray curves show (except the last data point in 200 mm, 300 mm and 400 mm series) that with these parameters the agreement with the rest of the experimental data is excellent. Still reasonable is the fit of the shrinkage data of prismatic specimens – see Fig. 6.16b. The measured value of shrinkage at the age of 2000 days of larger specimens is lower than modeled. (An approximate value of μ_S can be used in this set of simulations, because shrinkage development is not sensitive to that value. Parameter μ_S replaces the product $c_0 c_1 q_4$.)

Finally, the remaining parameter μ_S controlling the magnitude of the drying creep was calibrated to give the best possible agreement with the experimental measurements on a 150 mm thick drying slab (gray long-dashed line in Fig. 6.17a). It seems that the "final" value of the drying creep is captured correctly, even though the drying creep seems to be significantly delayed; this delay is in the remaining cases even more pronounced. However, the time delay of the drying creep is not the biggest disadvantage. What is striking is that the final value of the drying creep is incorrectly scaled with specimen size. The smaller the specimen size the smaller the final value of the drying creep, which contradicts the experimental observations – see Figs. 6.17a and b. To show this behavior in more detail, the basic creep has been subtracted from the total compliance and the resulting drying creep and cracking strain are plotted in Fig. 6.20. In this figure the red curve corresponds to the smallest specimen size and the blue to the largest.

Creep of partially predried slabs and prisms is shown in Fig. 6.18. In the first case (drying slabs, Fig. 6.18a), the magnitude of the drying creep seems to be captured correctly. In the latter case (drying prisms, Fig. 6.18b) the drying creep is underestimated (approx 1/2–2/3 of the correct value). Naturally–in both cases the more predried the specimen, the smaller the time delay between the experimental and the numerically obtained values.

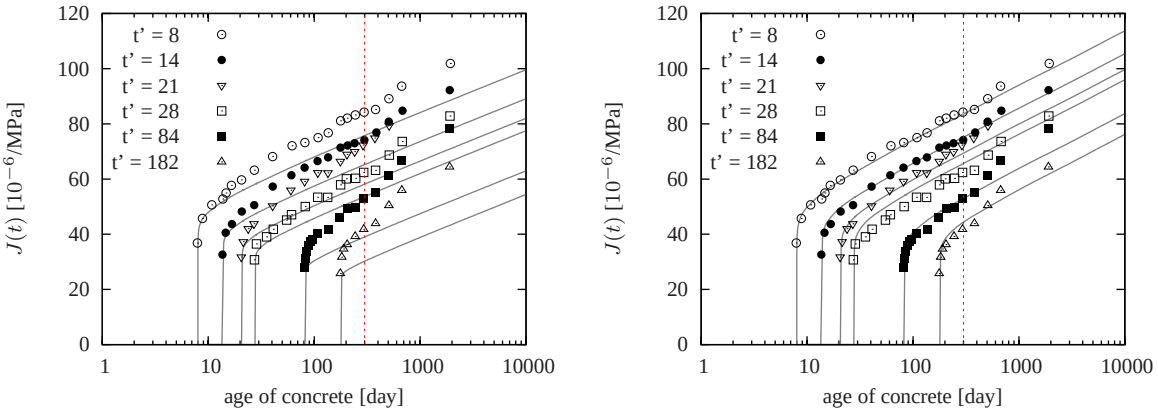

Figure 6.15: Time development of basic creep for different times at loading t' with (a) parameters predicted from concrete composition, (b) optimized set of parameters; dashed line indicates the approximate time of the sealing failure (experimental data from [45]).

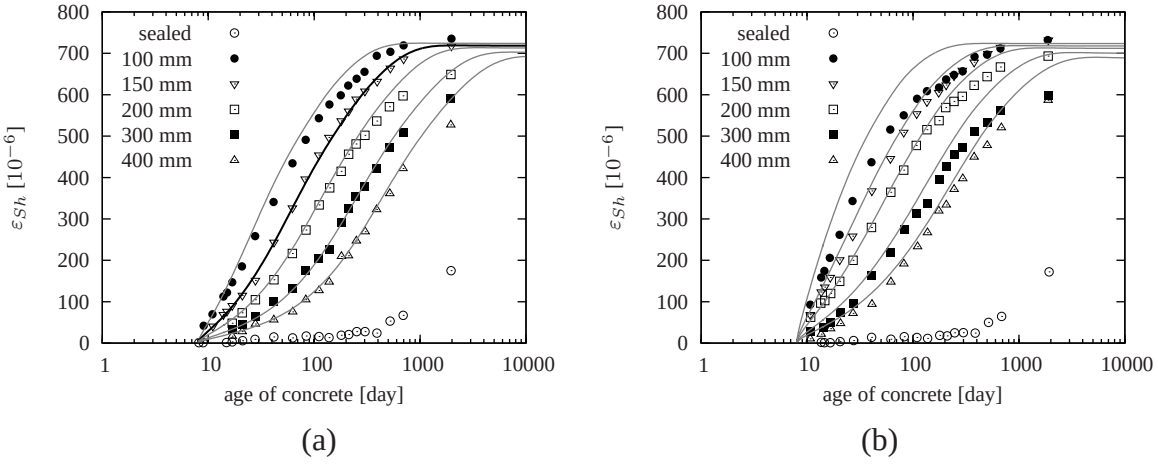

Figure 6.16: Time development of shrinkage strains measured on (a) slabs and (b) prisms, $t_0 = 8$ days; lines correspond to the results of FE simulations, points are experimental measurements [45].

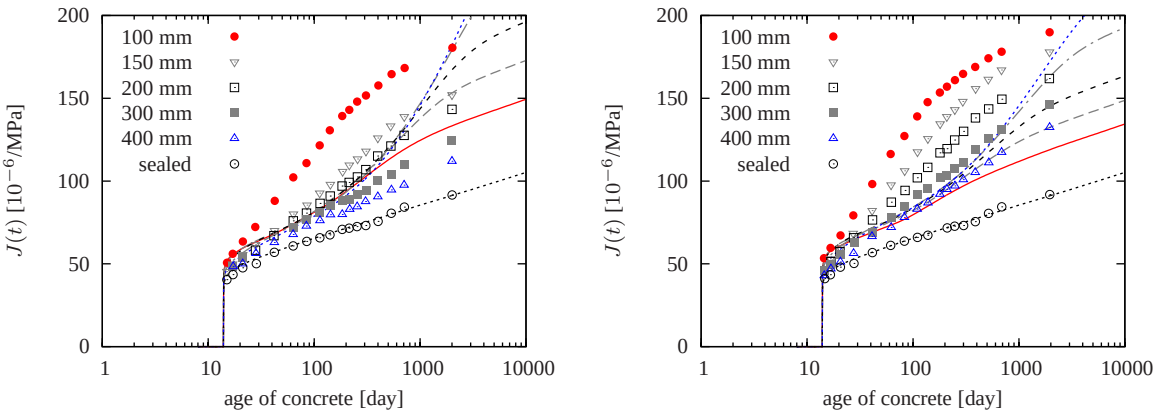

Figure 6.17: Compliance of drying (a) slabs and (b) prisms of various thicknesses, $t_0 = 8$ days, $t' = 14$ days, lines correspond to the results of FE simulations, points are experimental measurements [45].

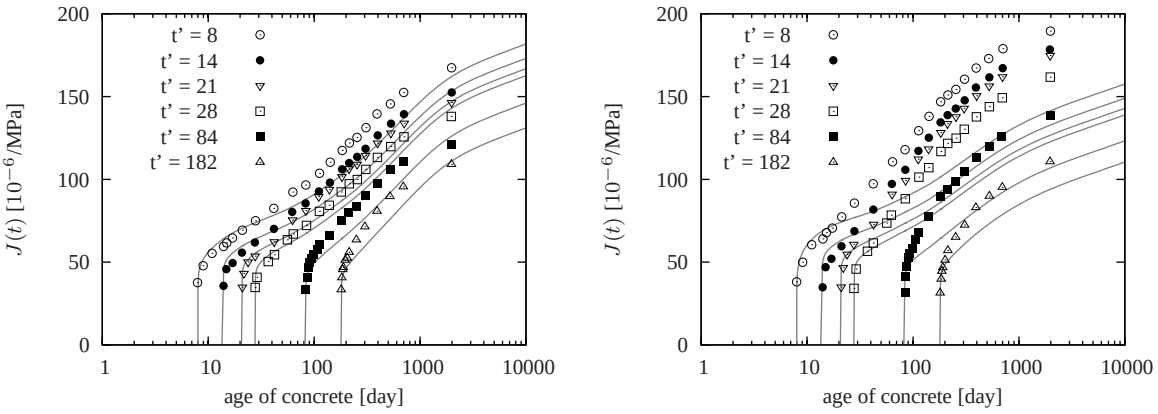

Figure 6.18: Compliance of drying (a) slabs 150 mm thick and (b) prisms 150×150 mm loaded at different ages t', for $t_0 = 8$ days, lines correspond to the results of FE simulations, points are experimental measurements [45].

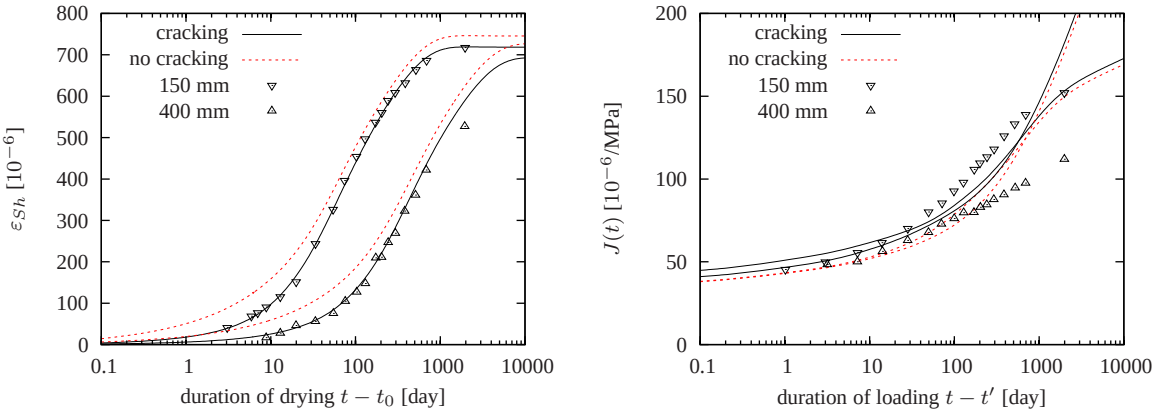

(a) (b)

Figure 6.19: Comparison of results of FE simulations of drying slabs with/without cracking: (a) shrinkage, (b) compliance, $t_0 = 8$ days, $t' = 14$ days.

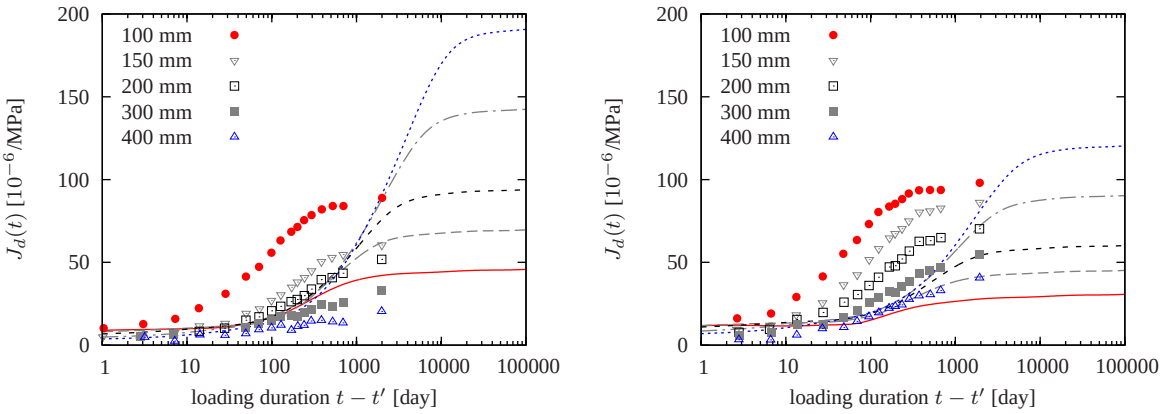

(a) (b)

Figure 6.20: Drying component of compliance of (a) slabs and (b) prisms, $t_0 = 8$ days, $t' = 14$ days, lines correspond to the results of FE simulations, points are experimental measurements [45].

6.4 Experiments of Keeton (1965)

6.4.1 Experimental setup

The technical report [64] presents the shrinkage and creep data measured on cylinders of three different sizes and stored at different levels of relative humidity.

The specimens were removed from the steel mold after one day; then they were cured for 7 days at 100% relative humidity. The height of each cylinder was 3× its diameter. Strain measurements were made in the central portion of the height of the specimens.

The exact concrete composition is somewhat unclear. The specified cement content was 452.4 kg/m^3, 1689.9 kg/m^3 of aggregates and 206.95 kg/m^3 of water, which corresponds to $w/c \approx 0.46$, but the report specifies this ratio to be 0.32. After 28 days of curing at $h_{\text{env}} = 100\%$, the compressive strength was 45.16 MPa and Young's modulus 27.23 GPa.

6.4.2 Numerical simulations

The same fitting procedure as in Section 6.3 was applied also in the case of Keeton's data. Parameters of the Bažant-Najjar transport model and the shrinkage coefficient k_{Sh} were calibrated to match experimental data measured on 4-in diameter cylinder exposed to drying at 50% relative humidity (middle line in Fig. 6.21b). Shrinkage at $h_{\text{env}} = 50\%$ of 3-in (Fig. 6.21a) and 6-in (Fig. 6.21c) cylinders is also captured correctly, but in all cases the shrinkage at lower relative humidity ($h_{\text{env}} = 20\%$) is overestimated and shrinkage at higher relative humidity ($h_{\text{env}} = 75\%$) is underestimated.

The following values of parameters of the Bažant-Najjar moisture diffusion model were used: $C_1 = 60 \times 10^{-6}$ m^2/day, $\alpha_0 = 0.04$, $h_C = 0.8$ and $n = 6.0$. The structural analysis used following values of parameters: $q_1 = 14$, $q_2 = 200$, $q_3 = 4$, $q_4 = 8$ all in $\times 10^{-6}$ MPa^{-1}, $\mu_S = 3 \times 10^{-6}$ MPa^{-1}day^{-1}, $k_{Sh} = 0.0022$, $f_t = 2$ MPa, $G_F = 100$ N/m.

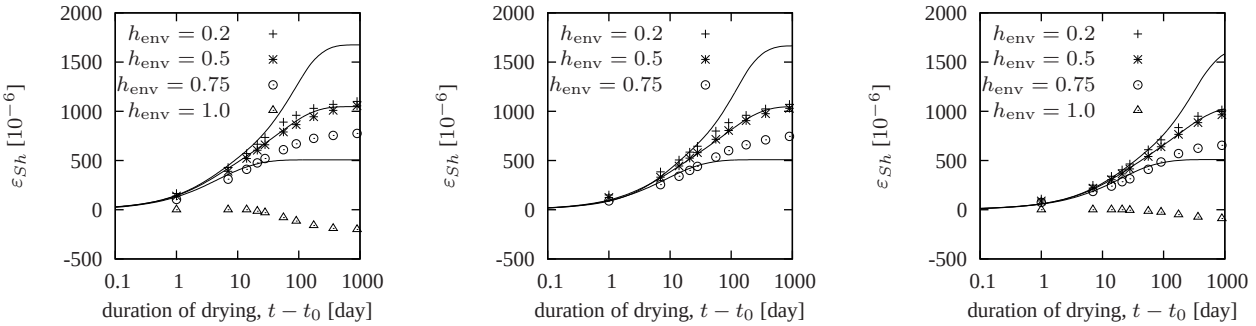

Figure 6.21: Time development of shrinkage strains of concrete cylinders exposed to different relative humidities, $t_0 = 8$ days, (a) D = 3 in, (b) D = 4 in, (c) D = 6 in; lines correspond to the results of FE simulations, points are experimental measurements [64].

6.5 Response to cyclic humidity

In most of the concrete structures, concrete is subjected to changes in relative humidity and temperature. Due to the relatively low moisture diffusivity, daily changes in relative humidity affect only a very thin surface layer, while the annual cycles penetrate deeper. Not only concrete exposed to ambient conditions, but also the laboratory specimens undergo humidity and temperature fluctuations, although these changes are smaller. Even when the specimen is placed at a climate chamber, the relative humidity and temperature inevitably oscillate (e.g. in [6] the relative humidity was 50 ± 4 % and temperature 23 ± 1.7 °C).

For these reasons, the material model describing creep and shrinkage should give similar results for constant relative humidity and temperature as well as for slightly fluctuating/cyclic conditions. Sudden changes should of course lead to an increase in creep rate, but the effect of further cycling should be damped (see e.g. experimental results in [79] or [51]).

Fig. 6.22 shows shrinkage and compliance response of 100 mm thick wall to cyclic relative humidity as modeled by the MPS theory. The curing time was 7 days, the initial humidity was 95% and the amplitude 2.5%. Prescribed cyclic humidity with period T applied at the boundary was described by the cosine function (with mean 92.5%). The values of the material parameters are almost identical to those from Section 6.3. In Fig. 6.22, the curve with $T = 0$ corresponds to prescribed humidity starting from 95% linearly decreasing to 92.5% within 0.25 day and then kept constant.

This figure shows that although the magnitude of the prescribed relative humidity was very small, the increase in creep deformation is substantial, reaching almost 1.5× the compliance without cycles after one year of loading.

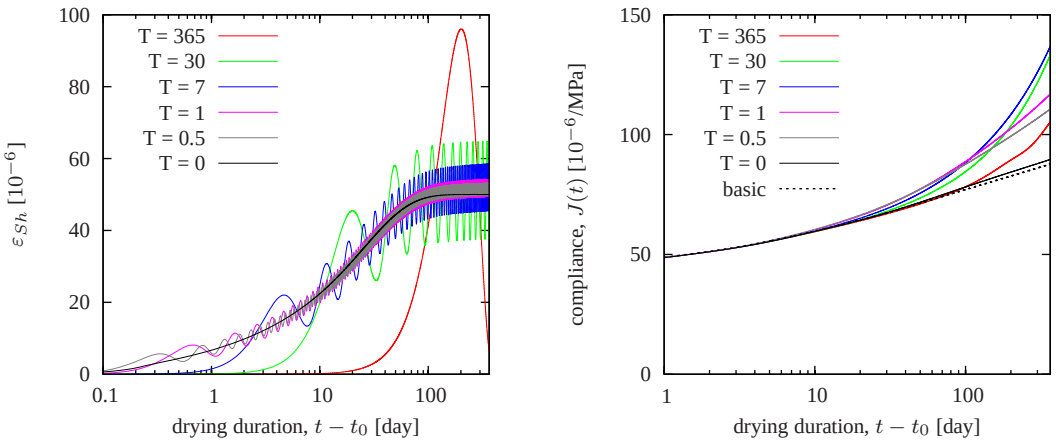

Figure 6.22: Response to cyclic humidity of period T prescribed at the boundary of a wall with thickness 100 mm, $t_0 = 7$ days: (a) shrinkage, (b) compliance.

6.6 Experiments of Pickett (1942)

6.6.1 Experimental setup

Gerald Pickett was probably the first one, who documented [79] the influence of drying on concrete creep. In his experiments, concrete beams ($51 \times 51 \times 864$ mm) were subjected to sustained three- and four-point bending. The actual span was 813 mm. In case of three-point bending, the central load was 24.95 kg (or 22.68 kg), and in the four-point bending configuration, two loads of 19.05 kg were placed at quarter-span. The concrete mixture was following: $w/c = 0.5$, $(a + s) : c = (2.42 + 2.08) : 1$.

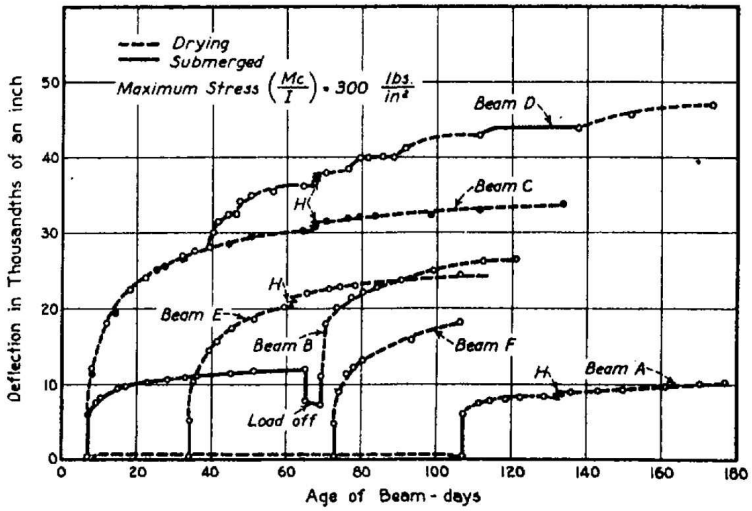

Figure 6.23: Pickett's data (original figure from [79]) measured on prismatic concrete beams subjected to bending, points denoted "H" are related to short-time failure of air-conditioning, which led to temporary decrease in relative humidity from 50% to 30%

The loading and curing history was different for every specimen; some specimens were kept submerged in water and some were exposed to drying at 50% relative humidity. Additionally, some drying specimens experienced one drying and wetting cycle due to the short-time failure of the air-conditioning; this led to temporary decrease in relative humidity from 50% to 30% (approx. one day). This point is marked in Fig. 6.23 by "H".

The beam denoted as "B" was loaded in three-point bending while being submerged in water. This specimen was unloaded after 58 days of loading, and after additional four days it was reloaded to the same level and exposed to drying. Beam "C" was loaded and subjected to drying. Beam "D" was first loaded in three-point bending, which was after 28 days of loading replaced with four-point bending, having a similar effect on vertical deflection. This beam was first drying, but later was subjected to drying and wetting cycles, which resulted into additional increase in creep rate. Specimens "E" and "F" were cured for 34 and 73 days, and afterwards were loaded and exposed to drying.

6.6.2 Numerical simulations

In the numerical simulations, first, the set of parameters for basic creep q_1–q_4 was needed. This set corresponds to creep of sealed specimens, but only data for water immersed specimen (data

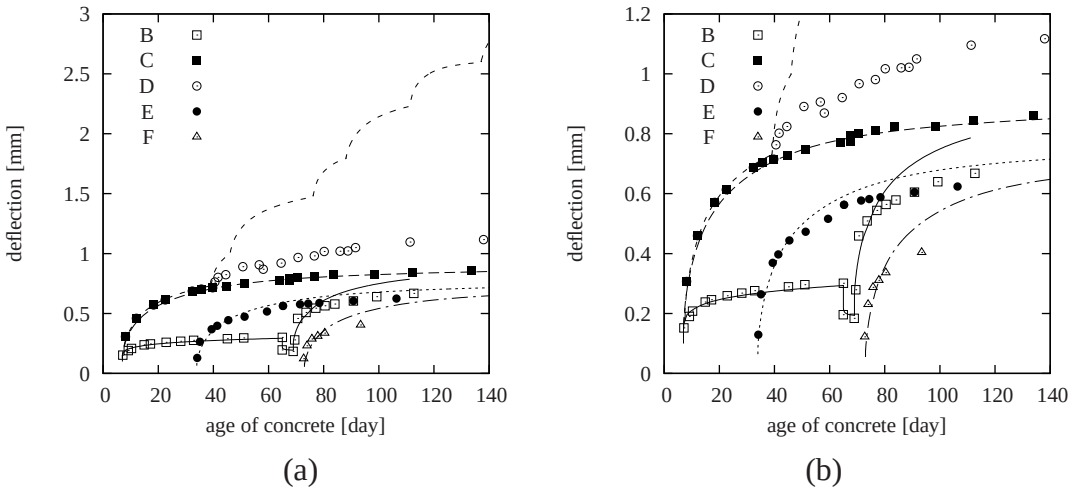

Figure 6.24: Experimental and computed time evolution of vertical deflection (a) in full view (b) in detail.

series "B") were available. First attempt to determine these values was based on empirical formulae recommended by the B3 model. The predicted values needed to be modified. Since the relation between vertical deflection and compliance function is known, this optimization could be done on one material point and not on the whole 3D computational model. Next, the parameter μ_S of the MPS theory and the parameters of the moisture analysis, which precedes the mechanical problem were adjusted in order to match data series "C". Note, that the exact value of the shrinkage factor k_{sh} is not important because drying is the same from all sides, and so the shrinkage strains do not cause deflections.

The results of all numerical simulations are shown in Fig. 6.24. For the sealed specimen ("B") the loading and unloading is captured correctly, but the drying creep after reloading is overestimated.

The experimentally measured data of specimens loaded at the onset of drying ("C", "E", "F") show considerable decrease in compliance due to aging. The first data series "C" served for calibration of parameters, but also the second one "E" is captured almost correctly. For the last one ("F"), the compliance is overestimated.

The computed final deflection for the cyclic drying and wetting cycles (data series "D") overestimates the experimentally measured data approximately 2.5×. Similar problem arises if the change in relative humidity due to air-conditioning failure is considered.

6.7 Experiments of Fahmi, Polivka and Bresler (1972)

6.7.1 Experimental setup

In the experiments reported in [51], all specimens had the shape of a hollow cylinder with inner diameter of 12.7 cm, outer diameter of 15.24 cm and height of 101.6 cm. The weight ratio of the components of the concrete mixture was water : cement : aggregates $= 0.58 : 1 : 2$. The average 21-day compressive strength measured on cylinders 76 by 152 mm was 40.3 MPa. Using the CEB-FIP recommendations [50], the 28-day strength can be estimated as 42.2 MPa. The experiment was performed for four different histories of loading, temperature and relative humidity. The loading programs of the first two specimens are summarized in Table 6.2, the other two loading programs with cyclic thermal loading are specified in Tables 6.3.

Table 6.2: Testing programs of the sealed (Data set #1) and drying (Data set #2) specimen with one temperature cycle

time duration [day]	T [°C]	RH [%]	σ [MPa]	time duration [day]	T [°C]	RH [%]	σ [MPa]
21	23	100	0	18	23	100	0
37	23	98	-6.27	14	23	50	0
26	47	98	-6.27	37	23	50	-6.27
82	60	98	-6.27	108	60	50	-6.27
10	23	98	-6.27	10	23	50	-6.27
25	23	98	0	25	23	50	0

Table 6.3: Testing programs of the sealed (Data set #3) and drying (Data set #4) specimen subjected to several temperature cycles; Asterisks denote a section which is repeated five times

time duration [day]	T [°C]	RH [%]	σ [MPa]	time duration [day]	T [°C]	RH [%]	σ [MPa]
21	23	100	0	18	23	100	0
37	23	98	-6.27	14	23	50	0
9	40	98	-6.27	37	23	50	-6.27
5	60	98	-6.27	14	60	50	-6.27
14	23	98	-6.27	14	23	50	-6.27
7*	60	98	-6.27	7*	60	50	-6.27
7*	23	98	-6.27	7*	23	50	-6.27
40	23	98	0	40	23	50	0

6.7.2 Numerical simulations

The four parameters of the B3 model describing the basic creep, q_1, q_2, q_3 and q_4, were determined from the composition of the concrete mixture and from the compressive strength using empirical formulae according to [13] (the cement content was assumed to be 500 kg/m^3). The

result of this prediction exceeded expectations; only minor adjustments were necessary to get the optimal fit (see the first part of the strain evolution in Figure 6.25a). The following values were used: $q_1 = 19.5$, $q_2 = 160$, $q_3 = 5.25$ and $q_4 = 12.5$ (all in 10^{-6}/MPa). They differ significantly from the values recommended in [15], $q_1 = 25$, $q_2 = 100$, $q_3 = 1.5$ and $q_4 = 6$, which do not provide satisfactory agreement with experimental data.

Beside the exponent p with standard value 2, the MPS theory reformulated in terms of viscosity (Section 4.2) uses only one additional parameter, μ_S, which was varied until the best fit with experimental data was obtained. All other parameters were initially set according to standard recommendations.

A really good fit of the first experimental data set (at 98% relative humidity, i.e., $h = 0.98$) was obtained for $\mu_S = 875 \times 10^{-6}$ MPa^{-1}day^{-1}; see Fig. 6.25a. The agreement is very satisfactory, except for the last interval, which corresponds to unloading. It is worth noting that the thermally induced part of creep accounts for more than a half of the total creep (compare the experimental data with the solid curve labeled as *basic* in Fig. 6.25 a.

In order to obtain an accurate creep evolution for loading history #2 (drying and one thermal cycle) it was first necessary to calibrate parameters of the Bažant-Najjar model for moisture diffusion. Even though the distribution of relative humidity across the section was not measured, the parameters were successfully identified from the time evolution of shrinkage and thermal strains of the unloaded companion specimen (Fig. 6.26). Parameters n, h_c and α_0 were set to their default values according to *fib* recommendations [48]. The best agreement was reached with maximum diffusivity $C_1 = 25$ mm^2/day, shrinkage parameter $k_{sh} = 0.0039$, and coefficient of thermal expansion $\alpha_T = 8 \times 10^{-6}$ K^{-1}. Unfortunately, with default values of the other parameters, the value of μ_S calibrated on data set #1 could not be used to fit the experimental data set #2, because it would have led to a gross overestimation of the creep (see the solid curve in Fig. 6.25b). However, it is possible to accurately reproduce the experimental data if the default values of parameters α_r and α_s are adjusted to 0.01 and 1.0 respectively (dashed curve in Fig. 6.25b). Parameters α_s and α_r control the effect of reduced humidity on the rate of microprestress relaxation and the rate of bond breakages, and the modification has no effect on the response of sealed specimens.

For the last two testing programs with several temperature cycles, described in Table 6.3, the agreement between the experimental and computed data is reasonable only until the end of the second heating cycle (solid curves in Fig. 6.27. For program #3, the final predicted compliance exceeds the measured value almost twice (Fig. 6.27 a)), for program #4 almost five times with the default values of parameters α_r and α_s (solid curve in Fig. 6.27 b)) and twice with the values which were previously optimized in the loading history #2 (dashed curve in Fig. 6.27 b)). In order to obtain a better agreement, parameter μ_S would have to be reduced, but this would result into a dramatic underestimation of the creep in the first two testing programs. The experimental data show that the temperature cycles significantly increase the creep only in the first cycle; during subsequent thermal cycling their effect on creep diminishes. Therefore it could be beneficial to enhance the material model by adding a certain internal variable keeping track of the temperature history, which would improve the behavior under cyclic thermal loading, while the response to sustained loading would remain unchanged.

Another deficiency of the model is illustrated by the graphs in Fig. 6.28. They refer to the first set of experiments. As documented by the solid curve in Fig. 6.25a, a good fit was obtained by setting $\mu_S = 875 \times 10^{-6}$ MPa^{-1}day^{-1}, assuming that the relative pore humidity is 98%. The pores are initially completely filled with water; however, even if the specimen is

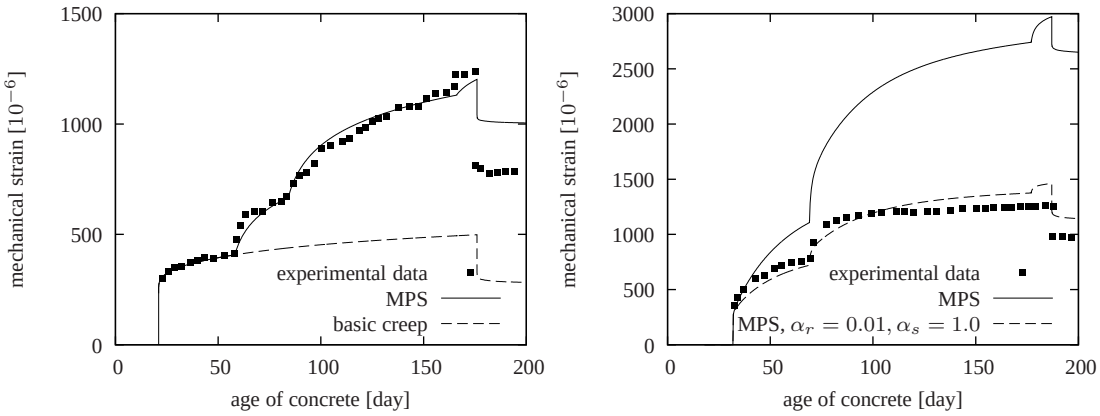

Figure 6.25: Mechanical strain evolution for (a) sealed specimens, with relative pore humidity assumed to be 98%, loaded by compressive stress 6.27 MPa at time $t' = 21$ days, and (b) drying specimens at 50% relative environmental humidity, loaded by compressive stress 6.27 MPa at time $t' = 32$ days.

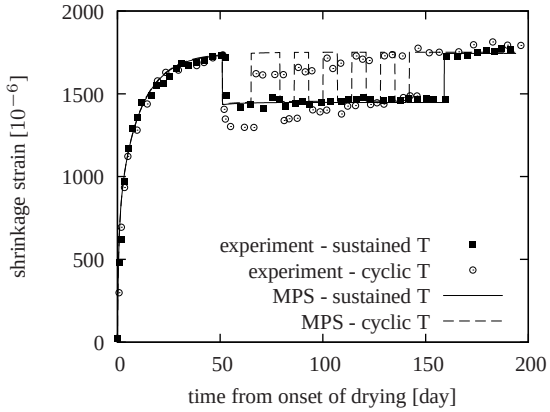

Figure 6.26: Shrinkage strain evolution for specimens drying at 50% relative environmental humidity.

perfectly sealed, the relative humidity decreases slightly due to the water deficiency caused by the hydration reaction. This phenomenon is referred to as self-desiccation.

The problem is that the exact value of pore relative humidity in a sealed specimen and its evolution in time are difficult to determine without additional equations describing the underlying chemical reactions. In simple engineering calculations, a constant value of 98% is often used for sealed conditions. Unfortunately, the response of the model is quite sensitive to this choice, and the creep curves obtained with other assumed values of pore relative humidity in the range from 95% to 100% would be substantially different; see Figure 6.28. The source of this strong sensitivity is the assumption that the instantaneously generated microprestress is proportional to the absolute value of the change of $T \ln h$; see the right-hand side of (4.18), which is reflected in the second term on the left-hand side of (4.19).

At (almost) constant humidity h, the time derivative of $T \ln h$ is simply $\dot{T} \ln h$, which is very sensitive to the specific value assigned to h in a sealed specimen. For instance, if the assumed humidity is changed from 98% to 96%, this term is doubled, which has the same effect as if the

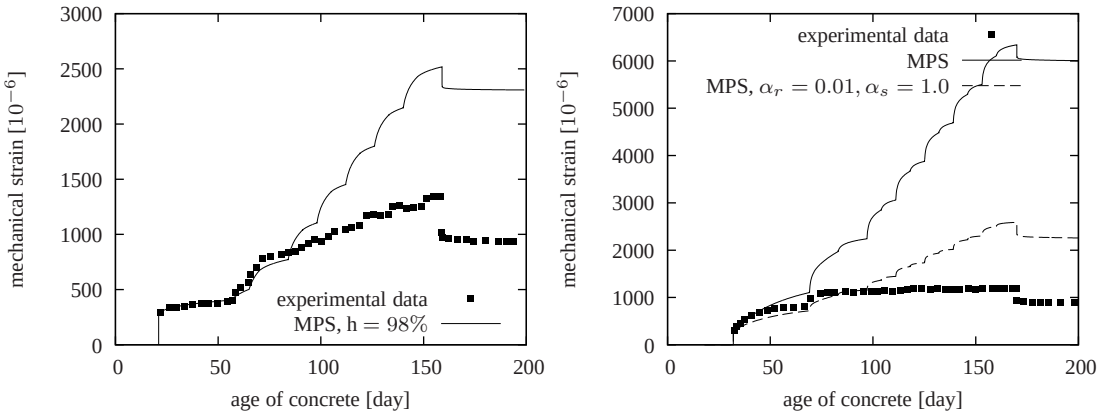

Figure 6.27: Mechanical strain evolution under cyclic variations of temperature for (a) sealed specimens, with relative pore humidity assumed to be 98%, loaded by compressive stress 6.27 MPa at time $t' = 21$ days, and (b) drying specimens at 50% relative environmental humidity, loaded by compressive stress 6.27 MPa at time $t' = 32$ days.

assumed humidity were kept the same but parameter μ_S were doubled.

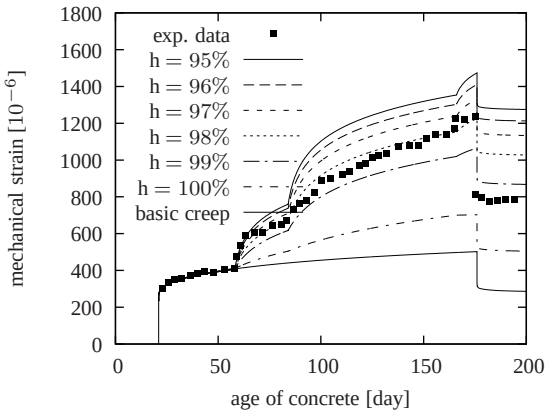

Figure 6.28: Mechanical strain evolution for sealed specimens, loaded by compressive stress 6.27 MPa from age 21 days, with the assumed relative humidity in the pores varied from 95% to 100% and with parameter $\mu_S = 875 \times 10^{-6}$ MPa^{-1} day^{-1}.

6.7.3 Summary

Classical experimental data from the literature have been compared with the results of the numerical simulations which used the original Microprestress-solidification theory as a material model. These data comprised concrete creep at constant elevated and monotonic temperature, creep of mortar at cyclic temperature (+drying), and a thorough study on concrete creep at drying and shrinkage at room temperature.

The performance of the Microprestress-solidification theory as a material model used for simulating concrete creep at elevated and/or variable temperature can be summarized as follows.

- The MPS theory performs well for standard sustained levels of temperature and load levels within the linear range of creep.
- In order to achieve a realistic prediction of creep at elevated temperature, the complete temperature history must be modelled. The model is sensitive not only to the level of temperature but also to heating or cooling rate.
- Very good agreement with the experimental data for unloading indicates that the transient thermal creep deformation is permanent and has been correctly assigned to a rheological unit (aging dashpot) which does not deform after unloading.
- At higher temperatures (above 70°C) the experimental data are reproduced with somewhat lower accuracy, even at lower temperatures the activation energies might need to be properly adjusted.
- For sealed specimens subjected to variable temperature, the results predicted by the original MPS theory turn out to be very sensitive to the assumed value of relative pore humidity (which is below 100% due to self-desiccation).
- Numerical simulations have also revealed that the original MPS theory grossly overestimates creep when the specimen is subjected to the cycles of temperature or relative humidity.

The originally proposed microprestress-solidification theory has been found unsuitable for modeling of drying creep and shrinkage under general conditions. The main deficiencies are summarized with decreasing order of importance.

- The modeled drying creep is too delayed behind experiments. Experiments reported in [45], [64], [43], [42] and many other papers indicate that shrinkage and drying creep occur simultaneously.
- The drying creep as modeled by the MPS theory conctradicts the experiments (see also Fig. 6.29). Using MPS, the drying creep of large specimens is several times bigger than for small specimens.
- Drying creep is strongly influenced even by small fluctuations in relative humidity. Not only the amplitude, but also the frequency of these fluctuations matters.
- A linear relationship between humidity and shrinkage rates seems to be too simplistic, shrinkage at different levels of relative humidity is not captured correctly, e.g. [64].

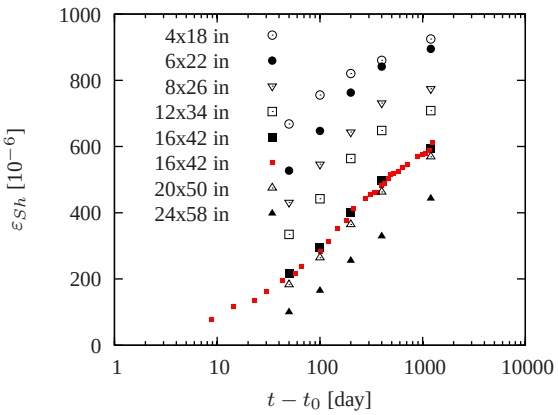

Figure 6.29: Time development of shrinkage strains in experiment conducted by Hansen and Mattock [59]. Experiment used cylindrical specimens with diameter 4–24 in. (101.6–609.6 mm), the concrete mixture contained 5.44 bags/yd^3 of Type III cement (303.38 kg/m^3), 28-day compressive strength was 6000 psi (41.4 MPa). The specimens were cured for 8 days in the fog room; afterwards, they were transferred to the laboratory with $h_{\text{env}} = 50\%$ and $T = 70$ F (21.1 °C). Unfortunately, only few data points are available to the author (complete data series are presented in the Appendix stored at ACI headquarters).

- The current model does not take into account swelling, e.g. [64].
- If the shrinkage development is calibrated on small specimens, then the prediction on large members tends to be overestimated [45], [59].
- The material model does not provide enough parameters to fully calibrate the shrinkage and drying creep behavior (only one parameter for each affecting the magnitude).

7 MPS: Improvement and Validation

7.1 Cyclic temperature & sensitivity to "choice" of relative humidity reached after self-desiccation

As a simple remedy to overcome the problems mentioned in Section 6.7, the governing equation of the flow term viscosity (4.21) is replaced by

$$\dot{\eta} + \frac{1}{\mu_S T_0} \left| T\frac{\dot{h}}{h} - \kappa_T \dot{T} \right| (\mu_S \eta)^{\frac{p}{p-1}} = \frac{\psi_S}{q_4} \tag{7.1}$$

with

$$\kappa_T = \begin{cases} k_{Tm} & \text{if } T = T_{max} \text{ and } \dot{T} > 0 \\ k_{Tc} & \text{if } T < T_{max} \text{ or } \dot{T} \leq 0 \end{cases} \tag{7.2}$$

in which k_{Tm} [-] and k_{Tc} [-] are new parameters and $T_{\max}$ is the maximum temperature attained in the previous history of the material point.

Formula (7.2) is constructed such that, during monotonic heating, factor κ_T remains constant and equal to parameter k_{Tm}, which replaces $-\ln h$ in the original equation (4.21). In this way, the sensitivity to the specific choice of h under sealed conditions is eliminated and parameter k_{Tm} can be determined from the creep test under sealed conditions with monotonically increasing temperature. For $k_{Tm} = 0.02$, the solid curve nicely fitting the experimental results in 7.1(a) is obtained, independently of the assumed pore relative humidity.

Parameter k_{Tc} affects the behavior under non-monotonic temperature evolution. It is motivated by the idea that the amount of new microprestress generated by repeated temperature cycles is reduced, because the material is going through the states that have been attained before. The optimal value of k_{Tc} can be determined by fitting the third testing program in 7.2(a).

For sealed specimens and monotonous thermal loading, only the product $\mu_S k_{Tm}$ matters, and so the good fit in 7.2(a) could be obtained with different combinations of μ_S and k_{Tm}.

The results are shown in Fig. 7.1 for sustained thermal loading (testing programs 1 and 2) and in Fig. 7.2 for cyclic thermal loading (testing programs 3 and 4). In these figures, the solid curves labeled as *MPS* represent the best fit obtained with the standard microprestress-solidification theory, default values of activation energies and adjusted values of parameters $\alpha_r = 0.01$ and $\alpha_s = 1.0$. Dashed curves in Figs. 7.1b and 7.2b labeled as *improved MPS*, $k_{Tc} = k_{Tm}$ correspond to the improved MPS theory with the newly introduced parameter k_{Tm} and with $\alpha_r = 0.01$ and $\alpha_s = 1.0$, but without parameter k_{Tc} influencing creep under non-monotonic temperature (or, equivalently, with $k_{Tc} = k_{Tm}$). The product $\mu_S \times k_{Tm}$ is the same but a better agreement was obtained when the value of k_{Tm} was reduced to 0.017 and μ_S was increased to 1040×10^{-6} MPa^{-1} day^{-1}. These dashed lines are not shown in Figs. 7.1a and 7.2a because they would coincide with the solid lines. The best agreement with experimental data is obtained with the same values but additionally with constant $k_{Tc} = 0.001$; these results are plotted in Figs. 7.1 and 7.2 by short-dashed lines. In 7.1a, only a small change can be observed compared to the original MPS; these differences arise when the temperature evolution ceases to be monotonous. Fig. 7.2 shows a substantial improvement for the cases of cyclic thermal loading.

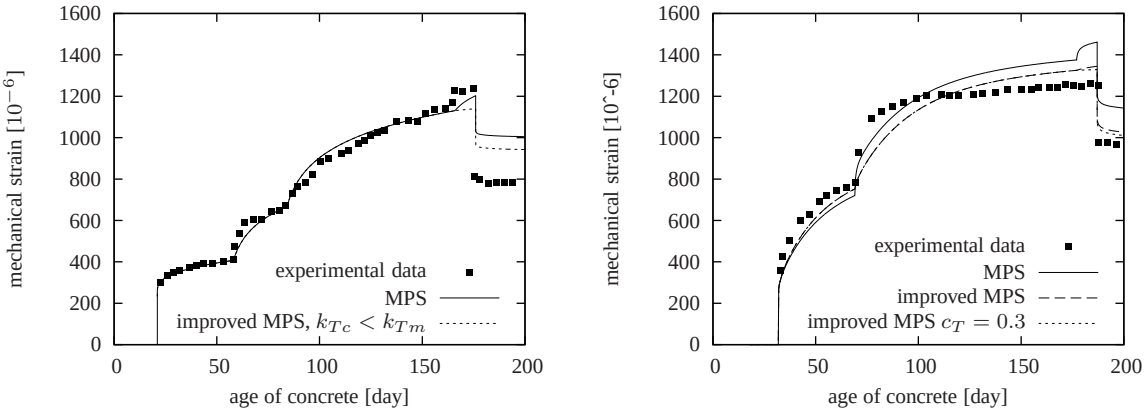

Figure 7.1: Mechanical strain evolution for (a) sealed specimens loaded by compressive stress 6.27 MPa at time $t' = 21$ days, and (b) drying specimens loaded by compressive stress 6.27 MPa at $t' = 32$ days.

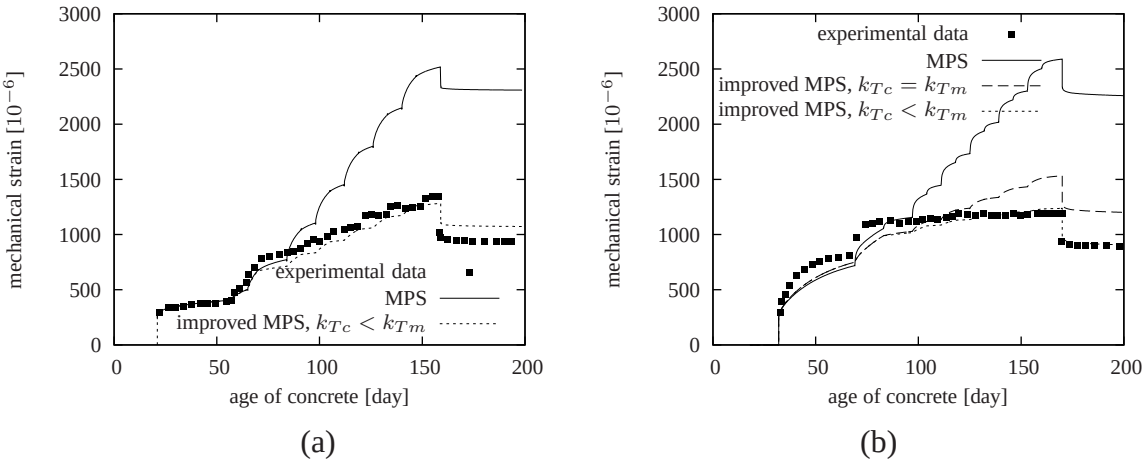

Figure 7.2: Mechanical strain evolution under cyclic variations of temperature for (a) sealed specimens loaded by compressive stress 6.27 MPa at time $t' = 21$ days, and (b) drying specimens loaded by compressive stress 6.27 MPa at time $t' = 32$ days.

7.2 Delay of the drying creep after shrinkage, size effect on drying creep and shrinkage

This section presents one of the possible solutions leading to elimination of problems which were addressed in Section 6.3. This solution leads not only to the **correct size effect on drying creep** but also to **reduction of the time delay between the drying creep and shrinkage**. On the other hand the proposed method shatters the physical motivation of the Microprestress theory.

To focus merely on the problems associated with the size effect on drying creep, the equation governing the viscosity evolution (4.21) can be under constant temperature $T = T_0$ rewritten in a simple form

$$\dot{\eta} + k_3 \Big| \frac{\dot{h}}{h} \Big| \eta^{\tilde{p}} = \frac{\psi_S}{q_4} \tag{7.3}$$

with newly introduced parameters

$$\tilde{p} = p/(p-1) \tag{7.4}$$

$$k_3 = \mu_S^{\frac{1}{p-1}} \tag{7.5}$$

The role of parameter $\tilde{p}$, in particular its influence on the "size effect on drying creep", can be elucidated using a simplified one-point calculation. Instead of simulating the whole specimen with nonuniform drying, we can focus on the evolution of the average humidity in the specimen. Obviously, the average humidity decreases faster in a small specimen than in a large one, but the final value is always the same (equal to the ambient humidity $h_{\rm env}$). To facilitate the numerical treatment, consider a drying process in which $\ln h$ decreases in a linear fashion from 0 (initial full saturation is assumed) to $\ln h_{\rm env}$ during a time interval from t_0 to t_1. The fraction $\dot{h}/h$ is then constant and equal to $\ln h_{env}/(t_1 - t_0)$, and equation (7.3) has a constant coefficient at $\eta^{\tilde{p}}$. By separation of variables it can be converted to

$$\frac{\mathrm{d}\eta}{\frac{\psi_S}{q_4} - k_3 \frac{|\ln h_{\rm env}|}{t_1 - t_0} \eta^{\tilde{p}}} = \mathrm{d}t \tag{7.6}$$

Setting for simplicity $\psi_S = 1$ and taking into account the initial condition $\eta(t_0) = t_0/q_4$, the solution can be written as

$$\int_{t_0/q_4}^{\eta(t)} \frac{\mathrm{d}\eta}{\frac{1}{q_4} - k_3 \frac{|\ln h_{\rm env}|}{t_1 - t_0} \eta^{\tilde{p}}} = t - t_0 \tag{7.7}$$

The integral can be evaluated analytically for $\tilde{p} = 0.5$, 1, 2 and 4.

After that, the drying creep compliance can be computed as

$$J_d(t, t_0) = \int_{t_0}^{t} \frac{\mathrm{d}s}{\eta(s)} - q_4 \ln \frac{t}{t_0} \tag{7.8}$$

Here it is assumed that the load is applied at the onset of drying, i.e., at $t = t_0$. The last term on the right-hand side (with a negative sign) corresponds to the contribution of the dashpot to the basic creep compliance.

The following figures present the behavior for three different histories of relative humidity. Until the age of $t_0 = 10$ days the humidity is kept constant and equal to 1, then it starts decreasing with a constant rate $\mathrm{d}(\ln h(t))/\mathrm{d}t = \mathrm{const}$ until the relative humidity of the environment

$h_{\text{env}} = 0.5$ is reached, and after that it remains constant. For the fastest process the final relative humidity is reached at time $t_1 = 100$ days. Processes labeled as "normal" and "slow" attain that level of relative humidity at the age of $t_1 = 1000$ and $t_1 = 10000$ days respectively. The evolution of relative humidity for these three studied cases is shown in Fig. 7.3.

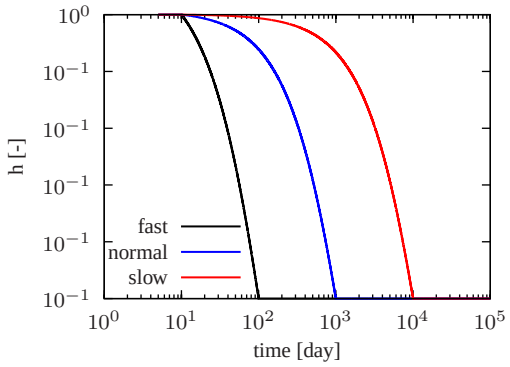

Figure 7.3: Evolution of relative humidity for three studied processes, plotted in semilogarithmic scale. Logarithm of humidity evolves at a constant rate.

The numerically calculated flow-term viscosity for $\tilde{p} = 2$, 1 and 0.5 is shown Fig. 7.4; for the corresponding compliance calculated according to equation (7.8) see Fig. 7.5. The presented results were obtained with $q_4 = 7 \times 10^{-6}$/MPa and with $k_3 = 10^{-6}$ MPa·day for $\tilde{p} = 2$, with $k_3 = 10$ for $\tilde{p} = 1$, and with $k_3 = 3 \times 10^4$ MPa$^{0.5}$·day$^{0.5}$ for $\tilde{p} = 0.5$.

As seen in Fig. 7.4, for the standard value of $\tilde{p} = 2$ the biggest decrease in viscosity happens in the slowest drying process; the viscosity grows with a decreasing rate (in the log-log scale) until about 1000 days and then until the end of drying at 10,000 days it remains almost constant. For $\tilde{p} = 1$ the decrease is more or less the same independently of the drying rate. For $\tilde{p} = 0.5$ the rate of the slow process remains almost unchanged (in the log-log scale), while for the fastest drying it drops significantly.

The ultimate drying compliance is independent of the drying rate only if $\tilde{p} = 1$. For $\tilde{p} > 1$ a higher compliance is reached with a lower drying rate, and finally for $\tilde{p} < 1$ the faster the drying rate the higher the ultimate drying compliance.

The influence of the parameter $\tilde{p}$ on the time delay of the drying creep after shrinkage is shown in Fig. 7.6 which shows the normalized evolution of shrinkage and drying creep. Reduction of the parameter $\tilde{p}$ from its recommended value 2 to 0.5 leads to substantial decrease in the time lag. The experimental data indicate that these processes occur simultaneously.

The following Section shows that the same trends hold also for non-uniform humidity distribution over the specimen cross-section and for a constitutive model where the deformation of the dashpot is just a part of the total deformation.

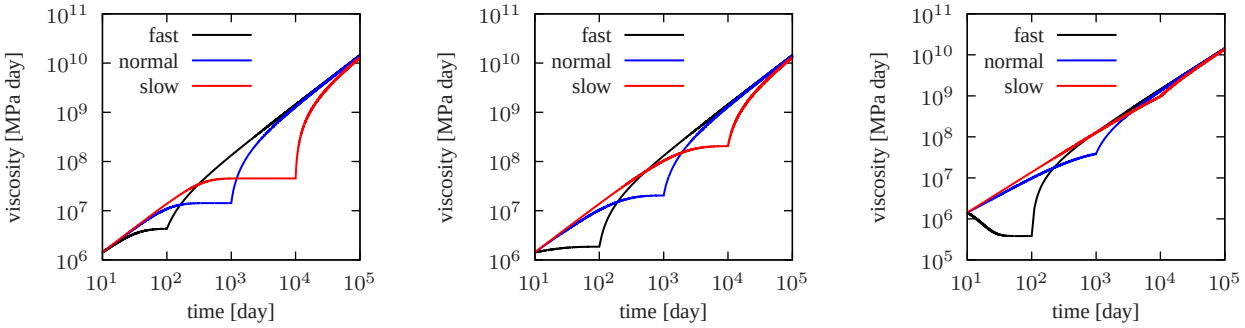

Figure 7.4: Evolution of flow-term viscosity (in log-log scale) for (a) $\tilde{p} = 2 =$ value recommended in original MPS model, (b) $\tilde{p} = 1$, and (c) $\tilde{p} = 0.5$.

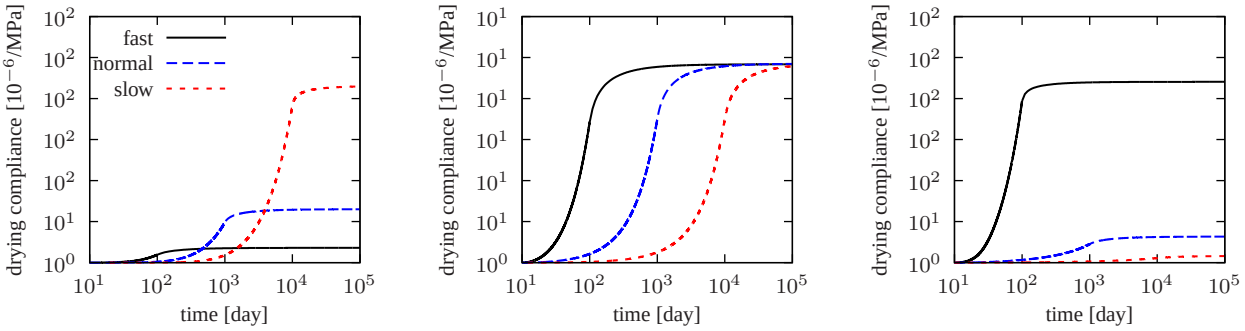

Figure 7.5: Evolution of drying creep compliance (in log-time scale) for (a) $\tilde{p} = 2$ - value recommended in original MPS model, (b) $\tilde{p} = 1$, and (c) $\tilde{p} = 0.5$.

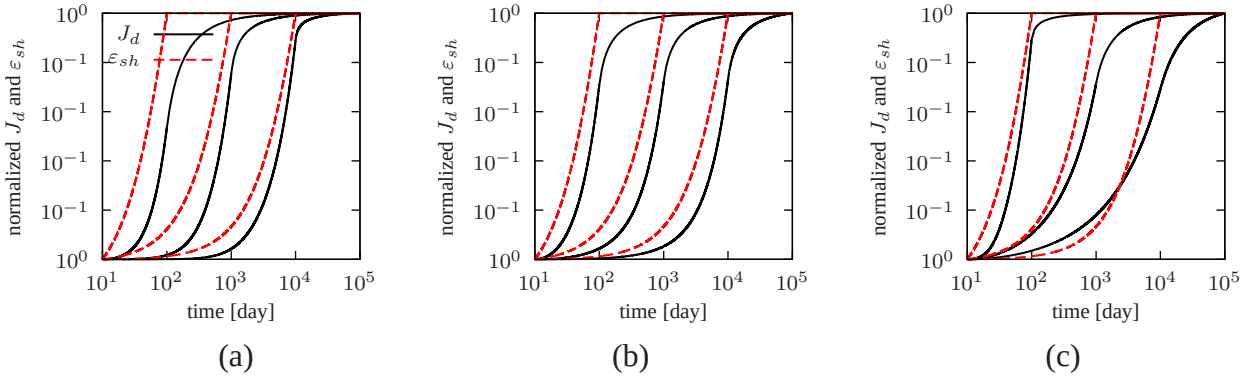

Figure 7.6: Evolution of normalized shrinkage and drying creep compliance (in log-time scale) for (a) $\tilde{p} = 2$ - value recommended in original MPS model, (b) $\tilde{p} = 1$, and (c) $\tilde{p} = 0.5$.

7.2.1 Validation by experimental data: Bryant and Vadhanavikkit (1987)

Experimental data indicate that the parameter $\tilde{p}$ should probably be chosen less than one because the measured "ultimate" drying creep decreases with increasing specimen size (and the drying time).

The conclusion of the simplified one-point calculation can be verified by finite element simulations of the nonuniformly drying loaded specimens of different sizes. The data in Fig. 7.7 were obtained with $\tilde{p} = 0.6$, which gave the best fit of Bryant's data, but which corresponds to $p = -1.5$, for which the original equations of the MPS theory lose their physical meaning.

The main deficiency of the proposed modification is that the model gives too low compliance of predried specimens loaded long after the onset of drying (lines $t' = 84$ and $t' = 182$ in Fig. 7.8). This difference does not necessarily mean that the proposed creep model is incorrect, the difference the measured and computed deformation can possibly origin from crack closure.

Figure 7.9 only confirms that with the exponent $\tilde{p} = 1$ or $p = \infty$ which influences only the viscosity of the aging dashpot (the flow term), the overall ultimate creep compliance is the same independently of the specimen size.

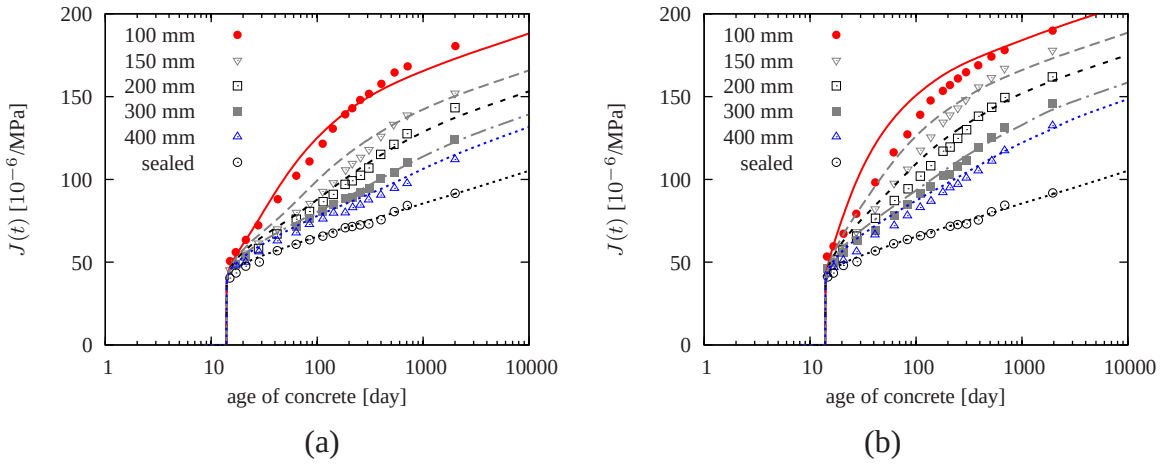

Figure 7.7: Creep compliance curves measured by Bryant and Vadhanavikkit (1987) on (a) drying slabs and (b) drying prisms of different sizes and their fits by the MPS theory with parameters $\tilde{p} = 0.6$, $\mu_S = 2 \times 10^{-10}$ MPa^{-1}day^{-1}.

7.2.2 Revalidation: Fahmi, Polivka and Bresler (1972)

Fahmi's experiment used only specimens of one size (wall thickness), therefore the size-effect of specimen size on drying creep and shrinkage remains unknown. For this reason the validation uses parameter $\tilde{p} = 1$, i.e. $p = \infty$ for which the size effect should be negligible. This choice brings about another advantage: the governing equation can be solved analytically so the viscosity increment is obtained directly.

Figures 7.10 and 7.11 support the idea of the nonstandard choice of parameter p. Comparing the present results with the numerical results presented in Section 7.1 (with $p = 2$), the agreement became far better, especially in the case when the specimens are drying.

The value of the shrinkage parameter k_{sh} had to be increased to 0.0045. This is caused by the reduced delay of the drying creep leading to higher short-term compliance. If the value of

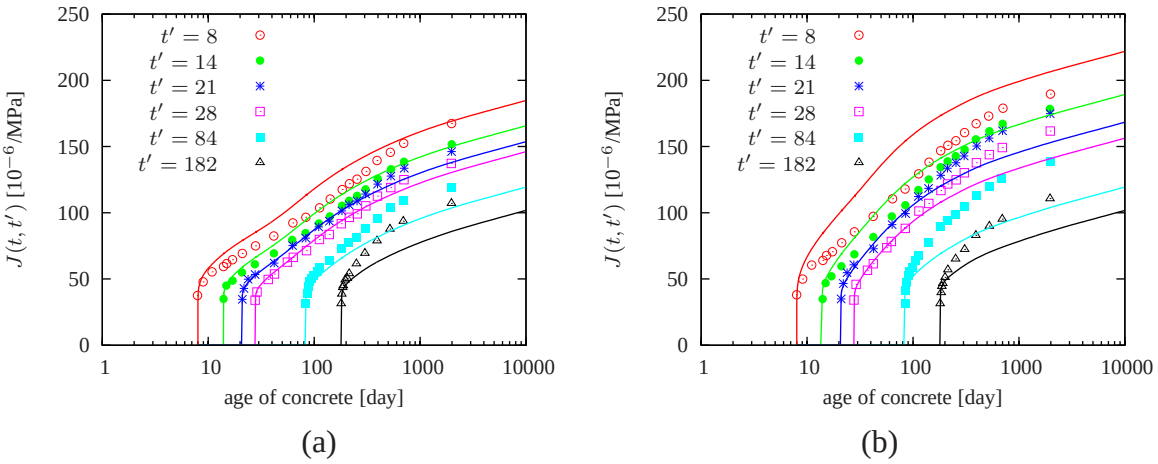

Figure 7.8: Creep compliance curves measured by Bryant and Vadhanavikkit (1987) on predried (a) slabs and (b) prisms and their fits by the MPS theory with parameters $\tilde{p} = 0.6$, $\mu_S = 2 \times 10^{-10}$ MPa^{-1}day^{-1}. Specimens were drying from the age $t_0 = 8$ days and were loaded at different ages t'.

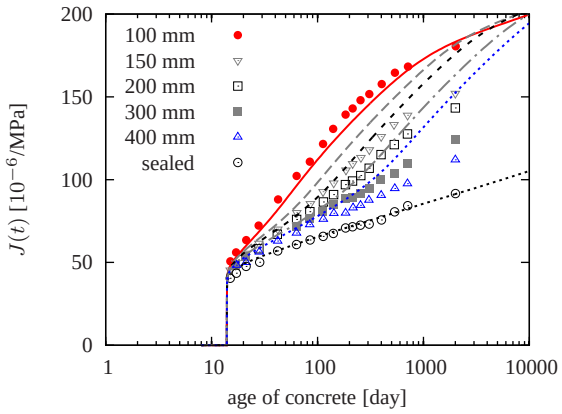

Figure 7.9: Creep compliance curves measured by Bryant and Vadhanavikkit (1987) on drying slabs of different sizes and their fits by the MPS theory with parameters $\tilde{p} = 1.0$, $k_3 = 35$.

k_{sh} was not increased, the overall shrinkage would underestimate the experimental data. Results of the shrinkage simulations are shown in Fig. 7.12.

Similarly to simulations in Section 7.1, recommended values of parameters α had to be changed in order to achieve an optimum fit. The present values are $\alpha_R = 0.01$, $\alpha_S = 0.6$ and α_E remains unchanged (recommended value). With the recommended values (and fixed values of other parameters) the simulations would overestimate creep of drying specimens as shown in Fig. 7.13. Results of the simulations with constant relative humidity do not change.

7.3 Conclusion

For sealed specimens subjected to variable temperature, the results predicted by the original MPS theory turn out to be very sensitive to the assumed value of relative pore humidity (which is below 100% due to self-desiccation). Numerical simulations have also revealed that the original MPS theory grossly overestimates creep when the specimen is subjected to cyclic temperature.

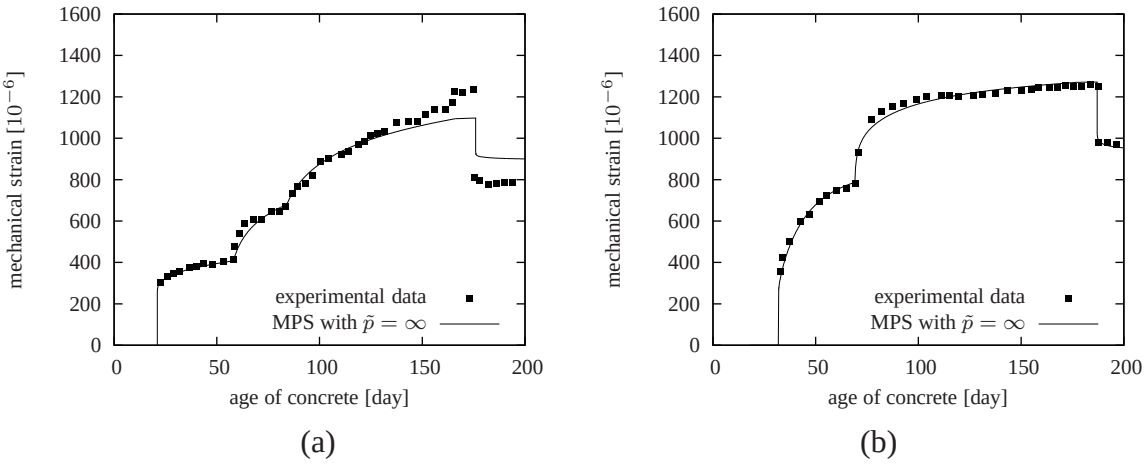

Figure 7.10: Mechanical strain evolution for (a) sealed specimens loaded by compressive stress 6.27 MPa at time $t' = 21$ days, and (b) drying specimens loaded by compressive stress 6.27 MPa at time $t' = 32$ days; $\tilde{p} = 1$, $k_3 = 90$, $k_{Tm} = 0.2889$, $k_{Tc} = 0.017$, $\alpha_R = 0.01$, $\alpha_S = 0.6$, $k_{sh} = 0.0045$.

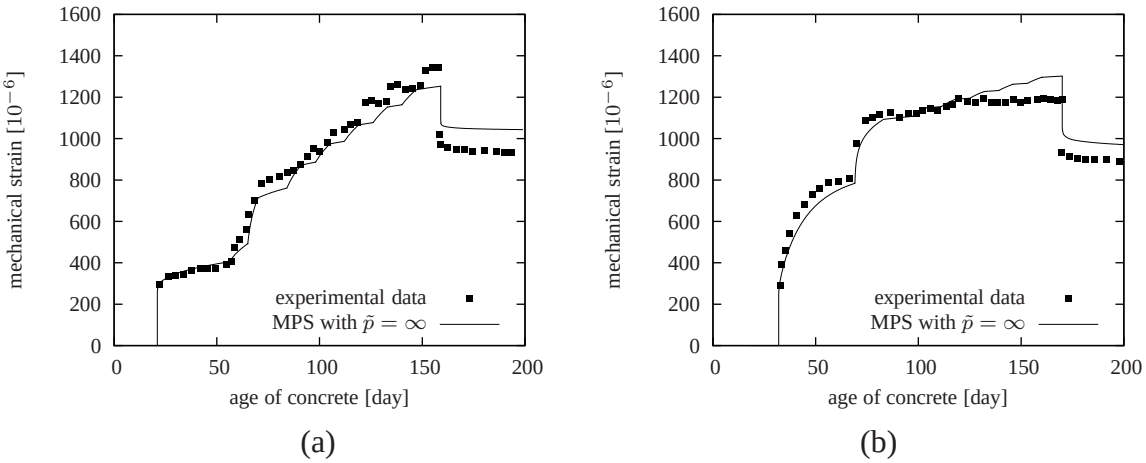

Figure 7.11: Mechanical strain evolution under cyclic variations of temperature for (a) sealed specimens loaded by compressive stress 6.27 MPa at time $t' = 21$ days, and (b) drying specimens loaded by compressive stress 6.27 MPa at time $t' = 32$ days; $\tilde{p} = 1$, $k_3 = 90$, $k_{Tm} = 0.2889$, $k_{Tc} = 0.017$, $\alpha_R = 0.01$, $\alpha_S = 0.6$, $k_{sh} = 0.0045$.

In order to overcome these deficiencies, a modified version of the model has been proposed and successfully validated. Excessive sensitivity to the specific choice of pore relative humidity in a sealed specimen has been eliminated. Also, it has become easier to calibrate the model because thermal and moisture effects on creep are partially separated. New parameters k_{Tm} and k_{Tc} have been introduced in order to reduce the influence of subsequent thermal cycles on creep. This modification does not affect creep tests in which the evolution of temperature is monotonous.

It has been found that the opposite size effect on drying creep is associated with the value of exponent $\tilde{p}$ in the governing equation for viscosity. If the recommended value $\tilde{p} = 2$ is changed to $\tilde{p} = 1$, the size effect is eliminated. For $\tilde{p} < 1$ the size effect on drying creep agrees with the experimental data, however, with this value the original theoretical justification of the MPS

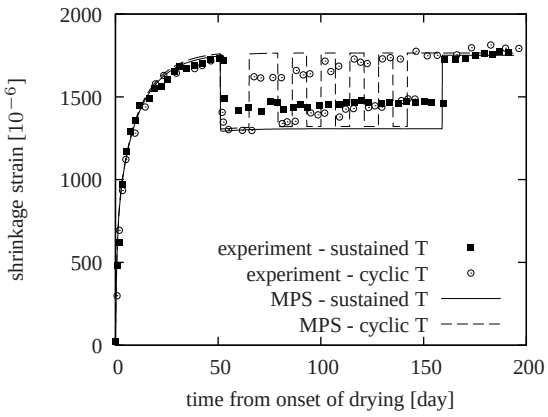

Figure 7.12: Shrinkage strain evolution for specimens drying at 50% relative environmental humidity; $\tilde{p} = 1$, $k_3 = 90$, $k_{Tm} = 0.2889$, $k_{Tc} = 0.017$, $\alpha_R = 0.01$, $\alpha_S = 0.6$, $k_{sh} = 0.0045$.

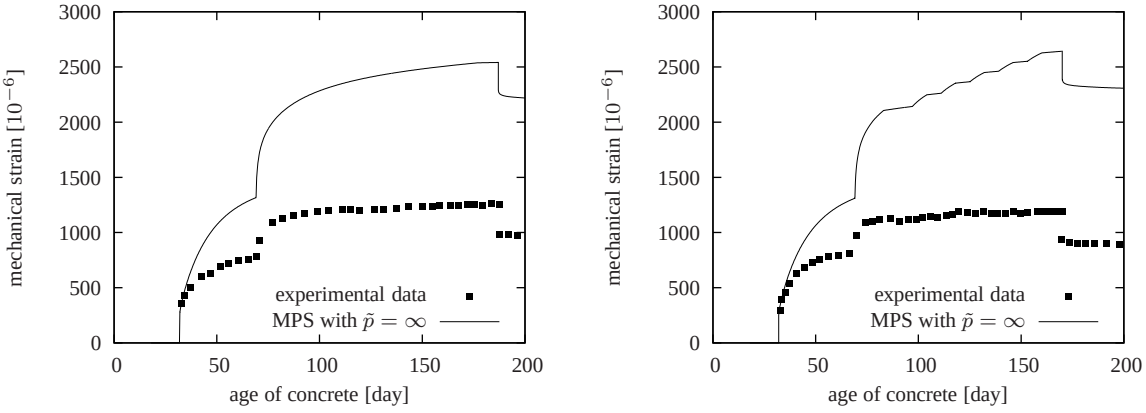

Figure 7.13: Mechanical strain evolution of drying specimens under (a) sustained and (b) cyclic temperature loading; specimens loaded by compressive stress 6.27 MPa at time $t' = 32$ days; $\tilde{p} = 1$, $k_3 = 90$, $k_{Tm} = 0.2889$, $k_{Tc} = 0.017$, $\alpha_R = \alpha_S = 0.1$, $k_{sh} = 0.0045$.

model is lost.

8 Shrinkage updating

This section first summarizes the key steps of the shrinkage-updating procedure first presented in [10]. The goal is to improve the initial prediction of the B3 model by utilizing the short-time shrinkage and water loss measurements. The capabilities of this method are then demonstrated on the experimental data of Granger [57] and Aguilar [6] and certain deficiencies are pointed out.

8.1 Measuring water loss to improve shrinkage prediction

The methodology offered in [10] for updating of the shrinkage prediction based on short-time measurements is due to the ill-possedness of the problem different from the creep updating procedure.

The creep updating procedure presented also in [10] uses two correcting parameters p_1 and p_2, which are solved from the following two equations of the least-square linear regression.

$$p_2 = \frac{\sum_{i=1}^{n} F_i J_i - n\bar{F}\bar{J}}{\sum_{i=1}^{n} F_i^2 - n\bar{F}^2} \tag{8.1}$$

$$p_1 = \bar{J} - p_2\bar{F} \tag{8.2}$$

where F is the predicted compliance function (e.g. model B3 or B4), J is the measured compliance function, $F_i = F(t_i, t_i')$, $J_i = J(t_i, t_i')$, n is the number of measured values, $\bar{J} = \sum_i J_i/n$ is the mean of the measured compliances and $\bar{F} = \sum_i F_i/n$ is the mean of the predicted compliances. The corrected compliance function is then computed as

$$J_{\text{impr}}(t, t') = p_1 + p_2 F(t, t'). \tag{8.3}$$

If the similar procedure was used for a shrinkage updating, the parameter p_1 would possess the meaning of the shrinkage strain that occurred before the first reading and similarly to the previous case, p_2 would be the scaling parameter. However, if the shrinkage experiment is performed properly and the first reading is done right after the onset of drying, p_1 must be zero.

The shrinkage evolution can be conveniently described by function [10]

$$\varepsilon_{sh}(t) = \tanh\sqrt{\frac{t}{\tau_{sh}}}\varepsilon_{sh}^{\infty}(h_{\text{env}}) \tag{8.4}$$

or its older version [29]

$$\varepsilon_{sh}(t) = \sqrt{\frac{t}{t+\tau_{sh}}}\varepsilon_{sh}^{\infty}(h_{\text{env}}). \tag{8.5}$$

Both equations possess an intrinsic time, the shrinkage half-time τ_{sh}. The second parameter is the ultimate shrinkage at given relative humidity. The shrinkage halftime is both the structural and material property. It grows with square of the effective thickness of the structural member or specimen and with decreasing diffusivity. The highly nonlinear concrete diffusivity also indicates that the shrinkage halftime should increase with decreasing ambient relative humidity. The ultimate shrinkage is mainly a material property, but the experiments indicate that it slightly decreases with specimen size.

On contrary to creep, to identify the correct values of these two parameters from the short time shrinkage measurements is next to impossible. This is demonstrated in Fig 8.1a; the two functions with shrinkage halftimes 100 and 300 days and significantly different ultimate values are almost indistinguishable during the first 50 days of drying. Comparing to creep, higher initial shrinkage does not necessarily mean that its final value (or its value after a certain period) would be higher than of a different concrete which initially exhibits lower shrinkage, Fig 8.1b.

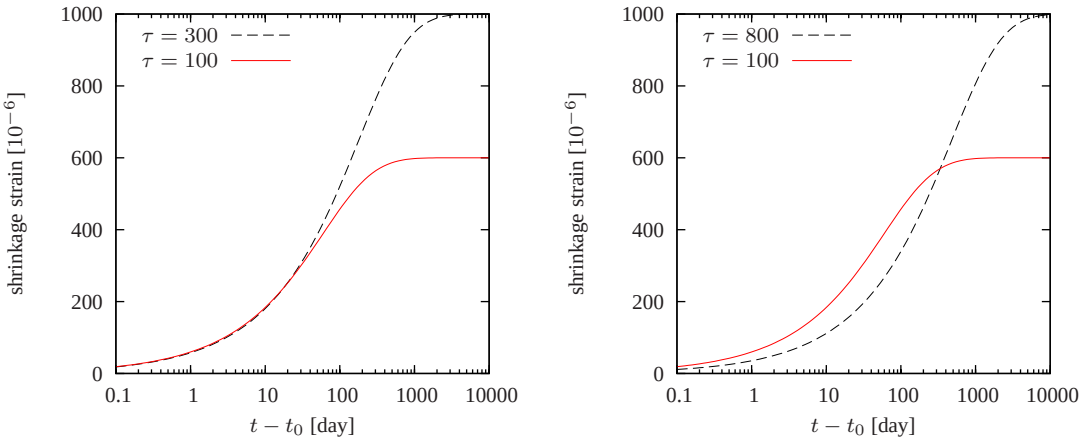

Figure 8.1: Illustration of two shrinkage histories (a) with almost identical values during the first 50 days of drying but with different ultimate values, (b) giving misleading initial assumption of the ultimate value.

The shrinkage updating procedure proposed in [10] stems from the similarity between the shrinkage and the drying process; both can be described with the function of the same form. They occur almost simultaneously and their relationship only slightly differs from linear. If the final value of the moisture loss at given humidity $\Delta w_\infty(h_{\rm env})$ is known, the drying halftime τ_w can be then fitted/optimized based on the short time measurements. Provided that there exists the link between the shrinkage and drying halftime, τ_{sh} can be computed in the next step. As the final step, the ultimate shrinkage is determined using least-squares fitting, keeping the previously computed value of τ_{sh} fixed.

The ultimate value of water loss is affected mainly by the relative humidity of the ambient environment, amount of water and of cementitious materials in concrete mixture, degree of hydration and the type of concrete curing. If one knows the total amount of evaporable water $\Delta w_\infty(h_{\rm env} = 0)$, the moisture loss can be for a specified relative humidity computed from the (measured or assumed) desorption isotherm. In case of water/moist curing the only possibility how to determine $\Delta w_\infty(h_{\rm env} = 0)$ is to oven-heat the specimen to 105–110 °C and to measure the weight difference. If no additional water was added during curing (specimen was sealed), then it can be roughly estimated based on concrete composition as

$$\Delta w_\infty(0) = w - 0.2(c + \text{silica fume} + \text{filler}) \tag{8.6}$$

which approximates the final value of the chemically bound water to be equal to 20% of the weight of the cementitious materials. According to [72], the chemically bound water is 0.18–0.26 of the cement content, the typical value is 0.25.

An excellent description of the relationship between the shrinkage and relative humidity (A.43) is obtained with a cubic function. From the reasoning that the evolution of shrinkage and moisture loss is similar, the original methodology recommended a cubic isotherm. The expression for the moisture loss reads

$$\Delta w_\infty(h_{\rm env}) \approx \eta \left[1 - (h_{\rm env}/0.98)^3\right] \Delta w_\infty(0) \tag{8.7}$$

where $\eta \approx 0.75 - 0.85$; this isotherm gives no moisture change for $h_{\rm env} = 0.98$.

However, such nonlinear behavior is more common for sorption isotherms, the desorption isotherms are in the range from 0.2–0.98 often almost linear. Since the shrinkage is related to moisture decrease, a desorption (linear) isotherm should be used. The formula for the weight loss due to drying then changes to

$$\Delta w_\infty(h_{\rm env}) \approx \eta \, (1 - h_{\rm env}) \, \Delta w_\infty(0) \tag{8.8}$$

In case of the linear isotherm, the parameter η can be bigger, $\eta \approx 0.8 - 1.0$. Both isotherms related to equations (8.7) and (8.8) are shown in Fig. 8.2. The formulations are not realistic in the range for $h_{\rm env} = 0 - 0.2$, but in reality it is not usually the case.

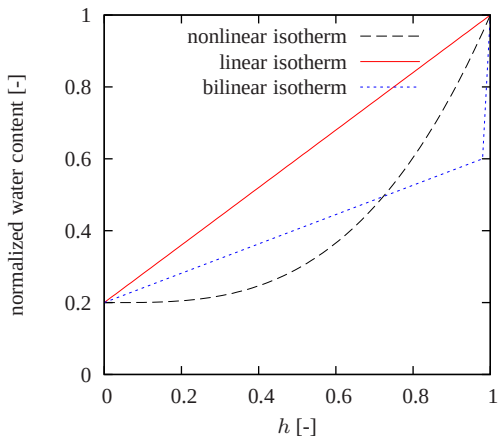

Figure 8.2: Isotherms associated with equations (8.7) and (8.8)

The recommended procedure [11], [13], [22] can be subdivided into two parts, first it is necessary to achieve an accurate shrinkage prediction of the experimental specimen and then to update the parameters of the B3 model which will be used for the real structure.

I Measure the final water loss for $h_{\rm env} = 0$ using oven-drying or calculate it using equation (8.6).

II Determine the terminal moisture loss for the average ambient relative humidity from equation (8.7) or (8.8).

III Calculate the auxiliary values

$$\psi_i = \left(\frac{\Delta w_i}{w_\infty(h_{\rm env})} \right)^2 \tag{8.9}$$

where w_i is the measured moisture loss, which should be spaced approximately evenly in the scale of $\log(t - t_0)$.

IV Evaluate the water-loss halftime

$$\tau_w = \frac{\sum_i \hat{t}_i \psi_i}{\sum_i \psi_i^2} \tag{8.10}$$

where $\hat{t}$ is the duration of drying.

V Improve the prediction of the shrinkage halftime

$$\tau_{sh} = 1.25\tau_w \tag{8.11}$$

VI Calculate the scaling parameter p_3

$$p_3 = \frac{\sum_i \varepsilon'_{sh,i} \bar{\varepsilon}_{sh,i}}{\sum_i \bar{\varepsilon}^2_{sh,i}} \tag{8.12}$$

where $\varepsilon'_{sh,i}$ denotes the measured shrinkage strain at time t_i and $\bar{\varepsilon}_{sh,i}$ is the computed shrinkage strain at the same time using

$$\bar{\varepsilon}_{sh}(t) = -\varepsilon^{\infty}_{sh} k_h \tanh \sqrt{\frac{t - t_0}{\tau_{sh}}} \tag{8.13}$$

In the last equation the values of $\varepsilon^{\infty}_{sh}$ and k_h are computed using formulas in Section A.9.

VII Improve the predicted value of ultimate shrinkage at given relative humidity

$$\varepsilon^{\infty}_{sh} = p_3 \bar{\varepsilon}^{\infty}_{sh} \tag{8.14}$$

Now using the improved shrinkage halftime τ_{sh} and the ultimate shrinkage at given relative humidity $\varepsilon^{\infty}_{sh}$ two more general parameters of the B3 model are updated.

I The first parameter linked to concrete diffusivity is computed from the updated shrinkage halftime, shape factor k_s and the effective thickness D.

$$k_t = \frac{\tau_{sh}}{(k_s D)^2} \tag{8.15}$$

II The second parameter is the generalized shrinkage magnitude

$$\varepsilon^{\infty}_{s} = \frac{\varepsilon^{\infty}_{sh}}{0.57514\sqrt{3 + \frac{14}{t_0 + \tau_{sh}}}} \tag{8.16}$$

8.2 Experiments of Granger (1995)

Granger's Ph.D. thesis [57] studies creep and shrinkage of concrete used in six French nuclear power plants. Experimental data are provided for basic creep, autogenous shrinkage, drying shrinkage and water loss. Experimental data for drying creep are missing; Granger presents merely the results of numerical simulations.

For the present purpose only the experimental data linking the moisture loss and the drying shrinkage, see Fig 8.3, are important. Shrinkage was measured on concrete cylinders exposed to $h_{\mathrm{env}} = 50\%$ after 28 days, until then the specimen was sealed. The cylinders were 1 m in height (0.5 m gauge length) and 16 cm in diameter, the top and bottom surfaces were kept sealed throughout the experiment.

The composition of the concrete mixture is specified in Table 8.1, however, the composition is ambiguous, different sand and filler dosages are presented in two different parts of [57]. The water in Table 8.1 represents total water in the concrete mixture, including water in aggregates.

Table 8.1: Granger: Concrete properties and composition

	Chooz	Penly	Flamanville	Paluel	Civaux B11	Civaux BHP
cement [kg/m^3]	350	350	375	375	350	266
water [kg/m^3]	190	202	180	180	195	161
admixtures [kg/m^3]		1.15	1.5	1.56	1.225	9.98
gravel [kg/m^3]	1130	1012	1040	1048	1100	1133
sand (page 88) [kg/m^3]	792.93	591.47	743.16	709	629.18	637.33
filler (page 88) [kg/m^3]	42.93	60.53	51.84	63	142.82	201.67
sand (page 53) [kg/m^3]	750	702	795	722	772	782
filler (page 53) [kg/m^3]		50		50		57
silica fume [kg/m^3]						40.3
air entrainer [kg/m^3]	0.9	3	1.1	2.1	2.9	1.9
w/c [-]	0.54	0.58	0.48	0.48	0.56	0.61
$f_{c,28}$ [MPa]	43.5	34.3	64.5	40.2	53.4	43
$f_{c,365}$ [MPa]	47.9	40.6	75.7	49	61.2	53.6
E_{28} [GPa]	38.6	36.2	36.7	33.7	31.9	38.4
E_{365} [GPa]	40.8	39.5	39.5	36.4	37.3	44

8.3 Numerical simulations - Granger

This section does not intend to demonstrate the performance of the methodology presented in the first part of this chapter, the main goal is to critically assess crucial point of the methodology and to stress out its deficiencies identified in the individual steps of the algorithm. The results presented in this section use the concrete mixtures specified on page 88 (not 53) of [57].

In the computations, the split of the total deformation between the autogenous and the drying shrinkage is neglected. The whole deformation is attributed to the drying shrinkage. This is justified by the fact that on the beginning of the experiment the specimens were already 28 days old and by that time the autogenous shrinkage has reached more than half of the ultimate value, see Fig. 8.3 d. From the six compositions, the biggest increase after the age of 28 days was approximately 50×10^{-6} which is negligible compared to the value of the drying shrinkage, and additionally, the decrease in relative humidity due to drying would diminish the additional autogenous shrinkage. Also the water-to-cement ratio w/c in Tab. 8.1 indicates that the ultimate value of the autogenous shrinkage should be quite small.

8.3.1 Prediction of the ultimate water loss

To start with, let us take a closer look at the proposed function for the development of the water loss (8.17) if it is capable of properly capturing the experimentally measured data (Fig. 8.3a) in the whole time range of drying.

$$\Delta w(t) = \tanh \sqrt{\frac{t}{\tau_w}} \Delta w_\infty(h_{\text{env}}) \tag{8.17}$$

The fitting was performed in Matlab using non-linear least squares optimization. The smallest error evaluated in terms of RMS was obtained when the ultimate water loss $\Delta w_\infty(h_{\text{env}})$ was

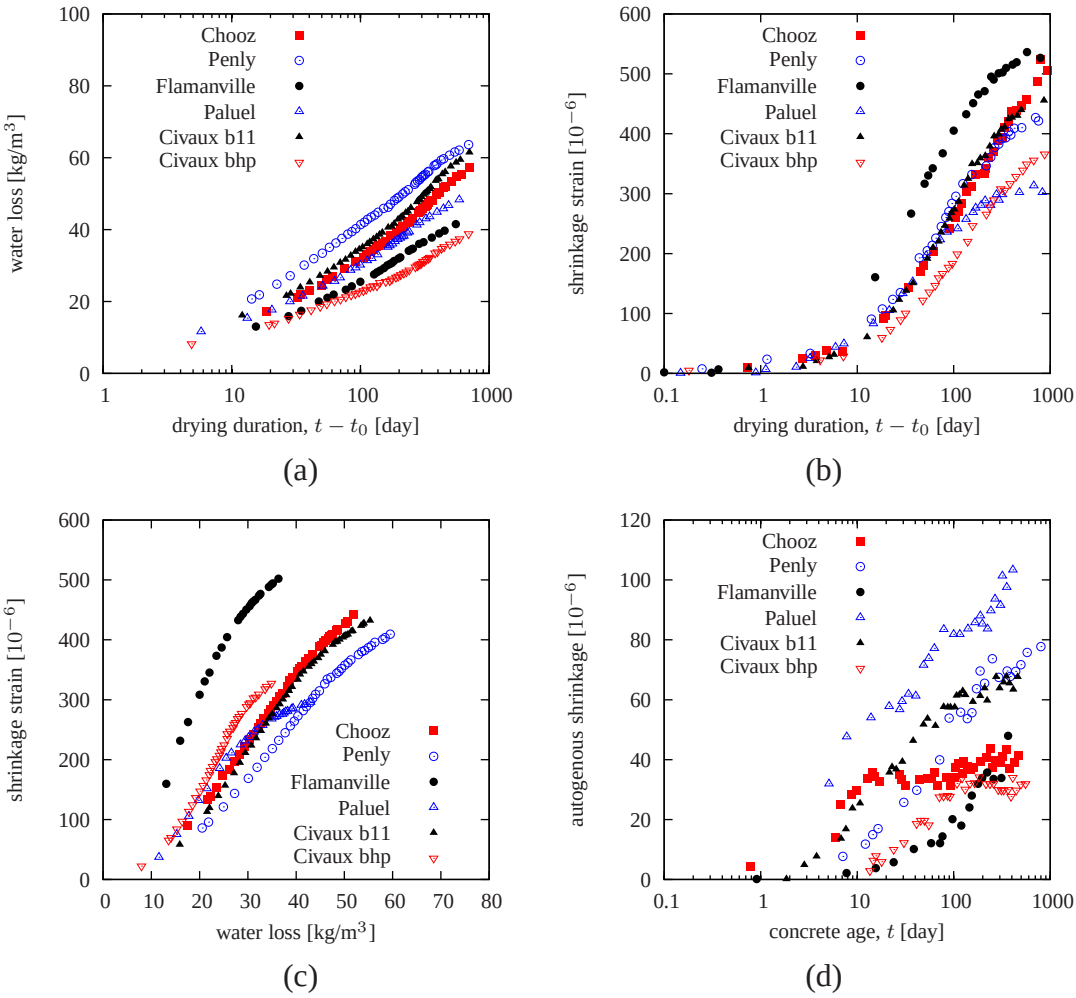

Figure 8.3: Granger's data: development of (a) water loss (b) shrinkage (c) relationship between shrinkage and water loss and (d) autogenous shrinkage

set to 1.05 of the highest value of the corresponding data series reached so far. The concrete strength and the water-to-cement ratio influencing the diffusivity is similar for all compositions. It can be expected that by the end of the experiment the concrete samples have dried to the same degree; for this reason the same factor 1.05 was used in all six cases. The results are shown in Fig. 8.4a. The experimental data are systematically underestimated during the first 100 days of drying and tend to be overestimated in the latter stage of drying, also the final rate seems to be incorrect. The power 0.5 in (8.17) must not be changed, because it origins from the diffusion theory.

Better agreement is obtained when the experimental data are shifted downwards. The optimum value of this shift that works for this case is 5.0 kg/m^3, see Fig. 8.4b for the improved fit. Now the asymptotic value was set as 1.15 of the maximum reached value. The reason the original function (8.17) did not work is that it possesses only one intrinsic time τ_w, but in reality the process is more complex. Even though the specimens were not submerged in water during curing, the first period of drying is dominated by the fast emptying of the large capillary pores and the second one by much slower moisture diffusion. In order not to shift the experimental data, it is wiser to incorporate the faster process into the equation (8.17) by splitting the to-

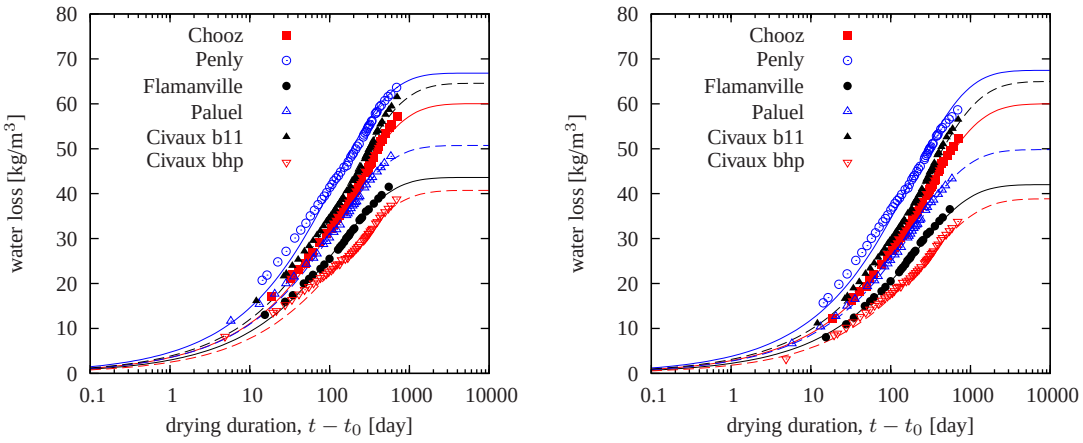

Figure 8.4: Optimum fits of the (a) original (b) vertically shifted (-5.5 kg/m^3) water loss data using equation (8.17).

tal moisture loss into two components, whose proportion is controlled by one parameter. The proposed function reads

$$\Delta w(t) = \left[(1-\alpha_w)\tanh\sqrt{\frac{t}{\tau_w\gamma_w}} + \alpha_w \tanh\sqrt{\frac{t}{\tau_w}}\right]\Delta w_\infty(h_{\text{env}}) \tag{8.18}$$

Parameter α_w controls the proportion between the slow and the fast drying process, while γ_w provides the information about their rate. Another function with the same asymptotic behavior at the early stage of drying and the same number of parameters is given by

$$\Delta w(t) = \left[(1-\alpha_w)\left(1-e^{-\sqrt{\frac{t}{\tau_w\gamma_w}}}\right) + \alpha_w\left(1-e^{-\sqrt{\frac{t}{\tau_w}}}\right)\right]\Delta w_\infty(h_{\text{env}}) \tag{8.19}$$

To tell which one is better based on Granger's data is almost impossible. Function with $\tanh$ (8.18) ends more rapidly compared to function (8.19) which terminates more smoothly, see Fig 8.5. These fits were obtained with fixed values of parameters α_w and γ_w, in case of equation (8.18) $\alpha_w = 0.85$ and $\gamma_w = 0.025$ and in case of (8.19) $\alpha_w = 0.93$ and $\gamma_w = 0.05$. In both cases the best agreement was reached with the ultimate shrinkage equal to 1.22 of the maximum reached value.

Another aspect is the prediction of the ultimate moisture loss at environment of given relative humidity. Publications [11], [13] recommend to use the nonlinear isotherm (8.7) together with (8.6). The result (Fig. 8.6a) overestimates the expected values by approx 10 kg/m^3. On the other hand the linear isotherm (8.8) recommended in [22], which is more realistic for desorption, gives together with (8.6) approximately 60% of the expected value (Fig. 8.6b). Figure 8.6c shows the results when only cement is assumed in (8.6) and 10% instead of 20% of cement is the chemically bound water, see Fig. 8.6d. This led to improvement, but the amount of chemically bound water is unrealistically small.

Substantial improvement is attained when the bilinear isotherm (such as in Fig. 8.2) is used. In case of Granger's data the initial drop from 100% to 98% relative humidity is associated with the decrease in water content equal to 15% of water added into the concrete mixture (about

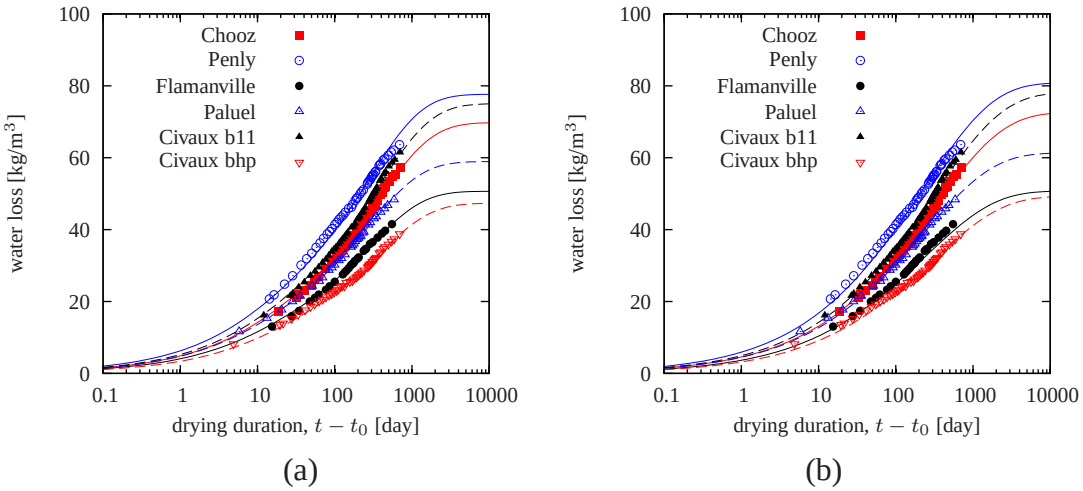

Figure 8.5: Optimum fits of the original water loss data using (a) equation (8.18), (b) equation (8.19).

25 kg/m^3) and when the filler content was ommited from (8.6) – Fig. 8.6e. To spread the terminal values further apart the (purely heuristic) correcting term multiplying the drop in moisture content can be introduced; the final form would then become $0.15w(w-130)/50$. The result of the last improvement shown in Fig. 8.6f matches well the assumed ultimate value. The slope of the sorption isotherm on the interval 0–0.98 is on average approximately 80 kg/m^3, which is possible, but it is lower than the typical value 100 kg/m^3. The need for the bilinear isotherm is also justified by the proposed changes to the water-loss function.

8.3.2 Shrinkage prediction/updating

In order to correctly extrapolate shrinkage from the short-term measurements and the shrinkage halftime derived from water-loss halftime, it is vital that the shrinkage function matched the data accurately in the whole time range, but especially in the first part. If the shrinkage function did not capture the shrinkage data correctly, an accurate extrapolation would be the result of sheer luck.

An optimum fit (in terms of RMS error) of the shrinkage data (all measured points were considered) using the equation (8.4) was obtained when the ultimate shrinkage $\varepsilon_{sh}^{\infty}$ was equal to 105% of the maximum reached value in the corresponding data series. The resulting fits are shown in Fig. 8.7a. In these fits the experimental data are up to approximately 50 days (in case of Civaux BHP up to 100 days) overestimated, which means that if the short-time measurements contained only these points, the final extrapolation would strongly underestimate the shrinkage development and its final value. Fig. 8.7b shows the detail (first 100 days of drying) of Fig. 8.7a plotted with respect to $\sqrt{t-t_0}$. In this time scale, the measured data strongly deviate from a straight line which indicates that they do not follow the same asymptotic behavior (for the early drying times) as was expected.

Smaller initial shrinkage can be attributed either to surface cracking or to the initial period of drying which is associated with a high decrease in water content but only small decrease in relative humidity which causes shrinkage.

For this reason the originally proposed exponent 0.5 in (8.4) is replaced with a parameter

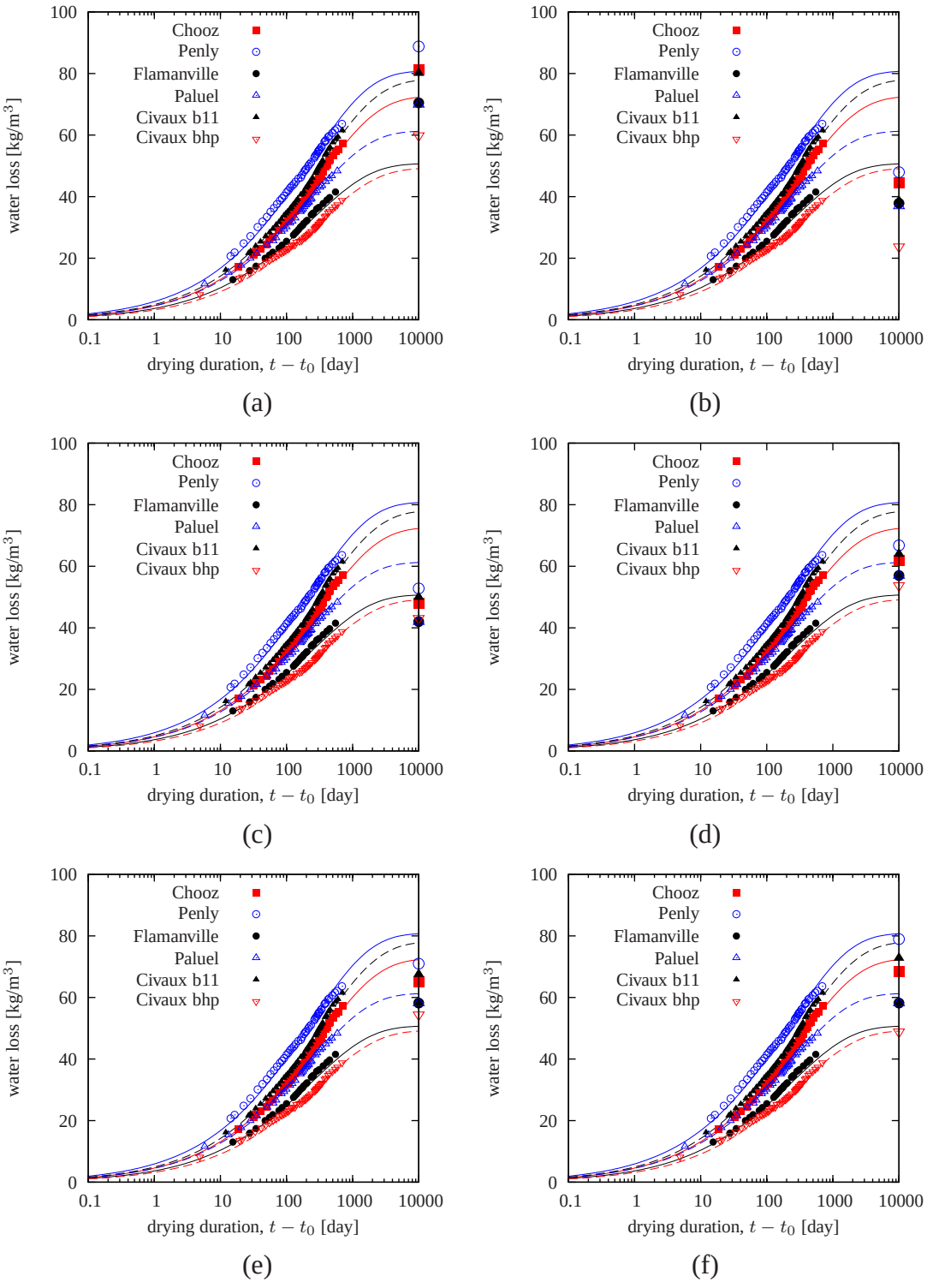

Figure 8.6: Experimentally measured water loss and its computed ultimate value (represented by points at 10,000 days) using (a) nonlinear isotherm (8.7), (b) linear isotherm (8.8), (c) linear isotherm, only cement is considered as cementitious material in (8.6), (d) linear isotherm, water consumed by hydration is equal to $0.1c$, (e) bilinear isotherm, only cement and silica fume are considered as cementitious materials in (8.6) , (f) bilinear isotherm + correction

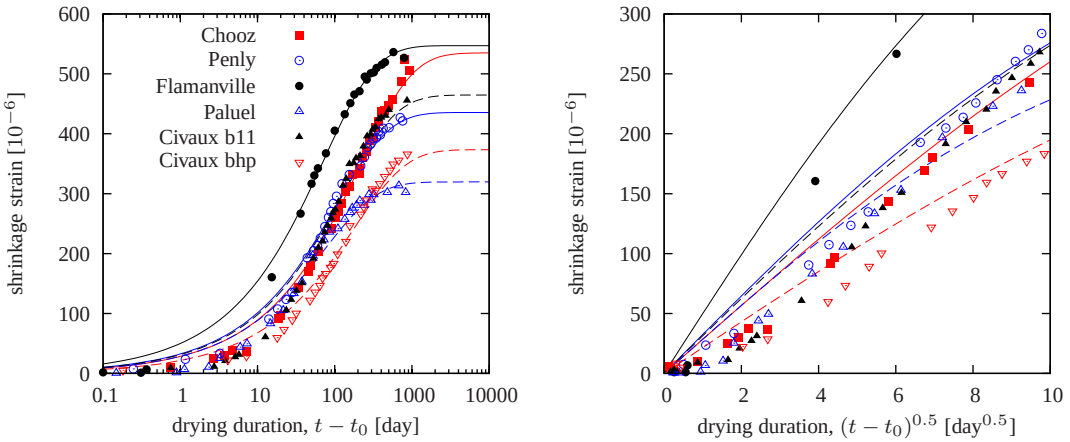

Figure 8.7: Optimum fits of the shrinkage data using function 8.4 plotted (a) in semilogarithmic scale (b) with respect to $(t-t_0)^{0.5}$ (shown only first 100 days)

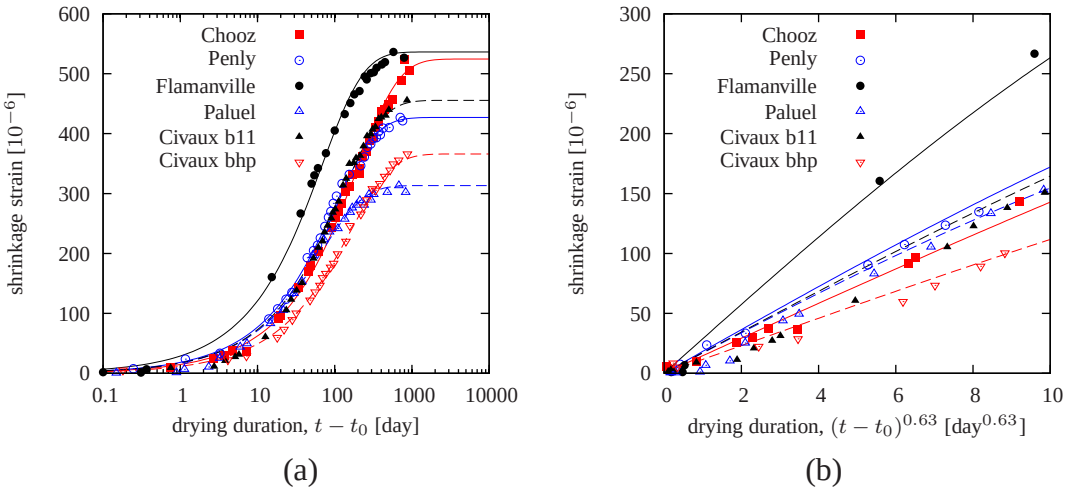

Figure 8.8: Optimum fits of the shrinkage data using function 8.20 with $p_{sh} = 0.63$ plotted (a) in semilogarithmic scale (b) with respect to $(t-t_0)^{0.63}$ (shown only first 38 days)

p_{sh}

$$\varepsilon_{sh}(t) = \varepsilon_{sh}^{\infty}(h_{\text{env}}) \tanh\left(\frac{t}{\tau_{sh}}\right)^{p_{sh}} \tag{8.20}$$

and in case of Granger's data its optimum value is found to be 0.63. Now the smallest error is reached with the ultimate shrinkage $\varepsilon_{sh}^{\infty}$ being equal to the corresponding maximum attained shrinkage strain; the results are shown in Fig. 8.8.

Similarly to the water loss, even now we cannot be certain with the suitability of the chosen shrinkage function. Fig. 8.10 illustrates the normalized functions (8.20) and

$$\varepsilon_{sh}(t) = \left(\frac{t}{t+\tau_{sh}}\right)^{q_{sh}} \varepsilon_{sh}^{\infty}(h_{\text{env}}) \tag{8.21}$$

with exponents $p_{sh} = 0.5$, $q_{sh} = 0.5$ and with the shrinkage halftime adjusted such that the half of the ultimate value is reached at 100 days of drying. Up to 300 days the curves almost cannot

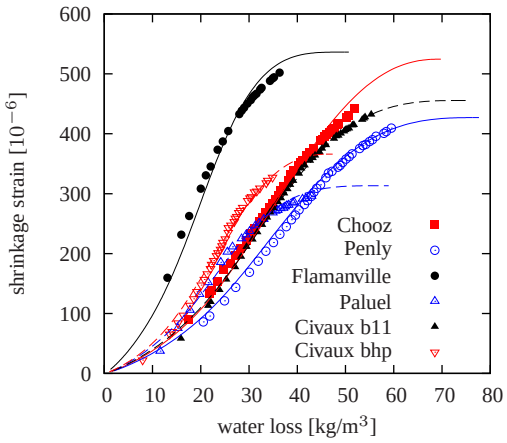

Figure 8.9: Dependence of shrinkage strain on water loss (fits from Figs. 8.8 and 8.5(a))

be distinguished.

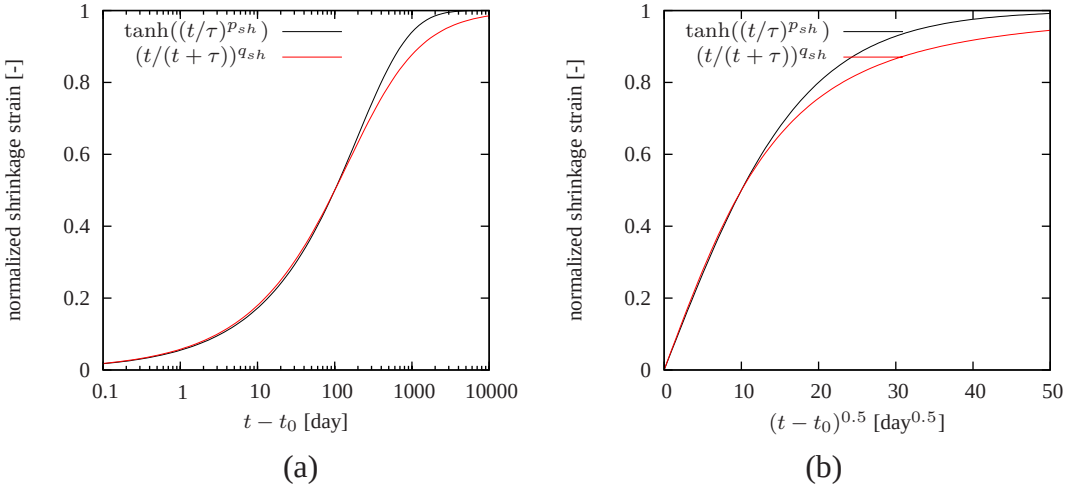

Figure 8.10: Illustration of two different shrinkage functions which are almost indistinguishable from each other except for very long times which are not covered by experiments (a) in logarithmic time scale (b) plotted with respect to $\sqrt{t - t_0}$. In both cases $p_{sh} = q_{sh} = 0.5$.

To preserve a good agreement of these two functions in case of a non-traditional value of exponent p_{sh} in (8.20) the exponent in (8.21) must be different as illustrated in Fig. 8.11. Of course, the early asymptotics then do not match.

Figure 8.12a shows the relationship between the shrinkage and drying halftime. Using the originally proposed functions for water loss and shrinkage (8.17) and (8.4) the mean of the ratio between the shrinkage and water-loss halftime was found to be 0.86 instead of 1.25. The only difference was the applied constraint on the ultimate values of the water loss and shrinkage. If this constraint was not used, the ultimate value could be in some cases lower than the actually measured value. This would be associated with faster drying and hence smaller drying halftime τ_w. This hypothesis was then verified and indeed, the mean ratio of τ_{sh}/τ_w was 1.23, see Fig. 8.12b. This phenomenon is rather striking because from the visual point of view, the quality of the fits was very similar. This also justifies the original motivation of this methodology

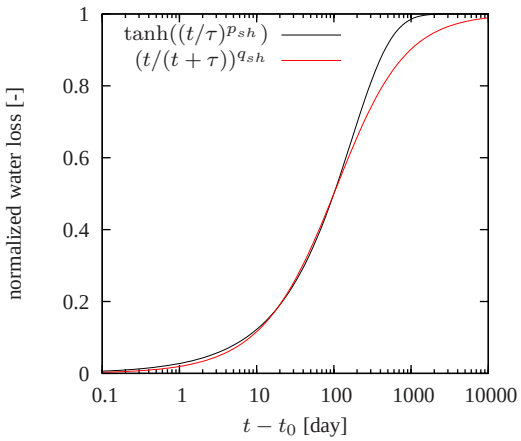

Figure 8.11: Illustration of two different shrinkage functions plotted in logarithmic time scale; the functions use non-traditional exponents, $p_{sh} = 0.65$, $q_{sh} = 0.8$. In both cases the value 0.5 is reached at 100 days.

illustrated in Fig. 8.1a, without the ultimate value, it is almost impossible to determine the halftime. Even though the processes in this case were considered to be nearly finished, still the ultimate values were unclear. As shown later, the error in the assumed ultimate value is several times multiplied in terms of the halftimes.

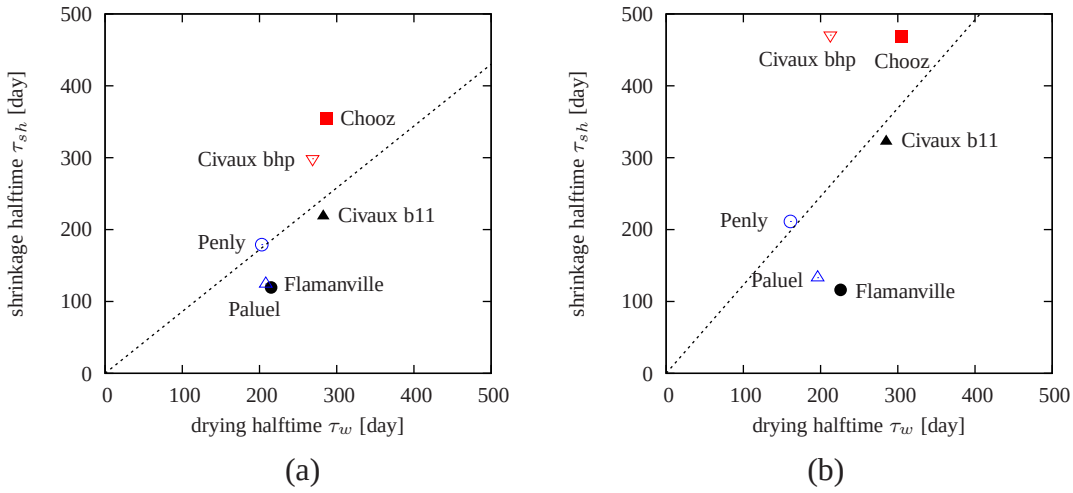

Figure 8.12: Relationship between the shrinkage and drying halftimes obtained from fitting considering all measured points. Water loss and shrinkage was fitted with the originally proposed functions (8.17) and (8.4), (a) the ultimate shrinkage and water loss was set to 1.05 multiple of the maximum value reached so far (b) no constraint on the ultimate values.

Figure 8.13 shows the relationship between the shrinkage and drying halftime for the standard value of exponent $p_{sh} = 0.5$ and for its adjusted value $p_{sh} = 0.63$. In both cases the fitting of the moisture loss as well as shrinkage covered all measured data, not just the portion. Again, the data do not exhibit a uniform trend, but as a gross approximation a linear relationship can be assumed; on average $\tau_{sh} = 0.37\tau_w$ for $p_{sh} = 0.5$ and $\tau_{sh} = 0.31\tau_w$ for $p_{sh} = 0.63$.

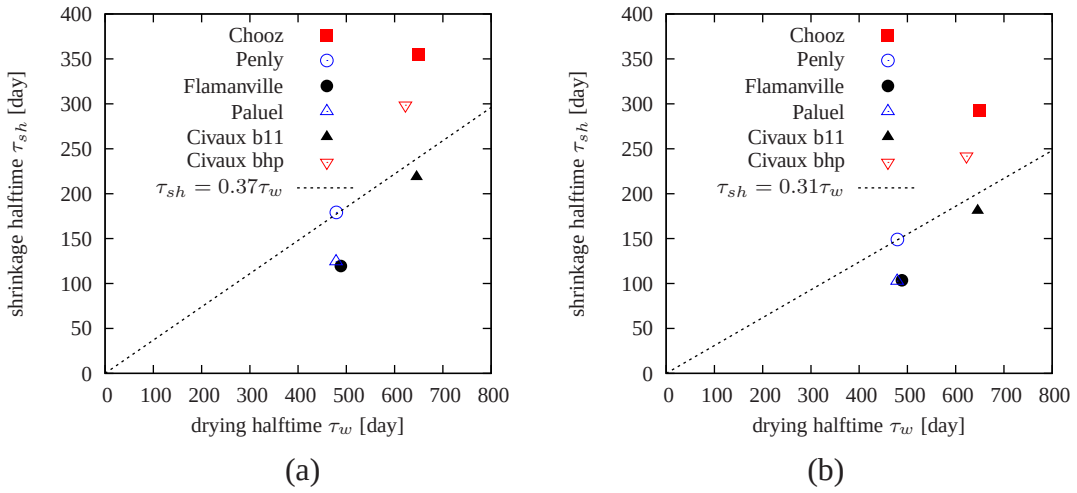

Figure 8.13: Relationship between the shrinkage and drying halftimes obtained from fitting considering all measured points. Water loss was fitted with function (8.18) and shrinkage with (8.20), (a) $p_{sh} = 0.5$ and (b) $p_{sh} = 0.63$

Now let us explore the influence of the error caused by the wrongly estimated final value of the mass of evaporable water at given relative humidity on the drying halftime. The error can origin either in desorption isotherm or in estimating of the evaporable water content at zero relative humidity (oven drying or simplified approach using concrete composition).

Figure 8.14a demonstrates that the dependence of the relative error of the drying halftime τ_w on Δw_∞ is almost independent of the particular data series and is mainly the property of the given function. Also the time range and the number of the data points used does not make much difference, the results in Fig. 8.14a were computed using the data from the first 60 days of the experiment. The slope at $\Delta w_\infty = 1$ is approximately 4, which means that 10% error in the estimated evaporable water leads to 40% error in the drying halftime τ_w, which cannot be revealed compared to the experimental data as demonstrated on an example for Chooz concrete in Figure 8.14b. There, the curve for the optimum value of Δw_∞ and its 0.9 and 1.1 multiple coincide up to 400 days - even though they were optimized only based on the data from the first 60 days.

It can be expected that the reversed procedure used in the prediction of the ultimate shrinkage ε_{sh}^∞ from the shrinkage halftime τ_{sh} would lead to error decrease. The input error is caused not only by incorrectly estimated drying halftime τ_w, but also by the relationship between τ_{sh} and τ_w. The error reducing ratio is approximately 1:0.5 for exponent $p_{sh} = 0.63$ (Fig. 8.15a) and 1:0.4 for $p_{sh} = 0.5$ (Fig. 8.15b).

If the shrinkage function could properly represent both short and long-time shrinkage, then the final shrinkage would be almost independet of the duration of the experiment used for calibration, this is illustrated in Figure 8.16 where almost the same result is obtained for 30, 60 and 90 days long experiment. Also up to several times longer duration of drying it is impossible to detect that the shrinkage time was estimated incorrectly.

On the other hand when the shrinkage function does not match the experimental data in the whole time range, the predicted final shrinkage is strongly dependent not only on the duration of the short-time experiment, but also on the distribution of the data points. Here, such function is represented by the standard $\tanh(\sqrt{t - t_0})$. As was earlier pointed out in Fig. 8.7, when the

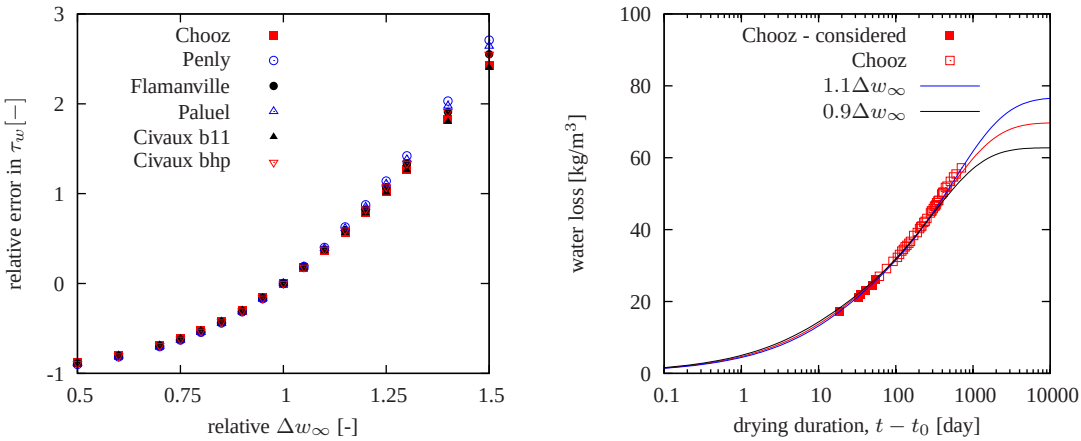

(a) (b)

Figure 8.14: (a) Influence of incorrectly assumed amount of evaporable water Δw_∞ on error in water-loss halftime τ_w, (b) example of estimating τ_w from Δw_∞ and short time measurements (60 days) using equation (8.18).

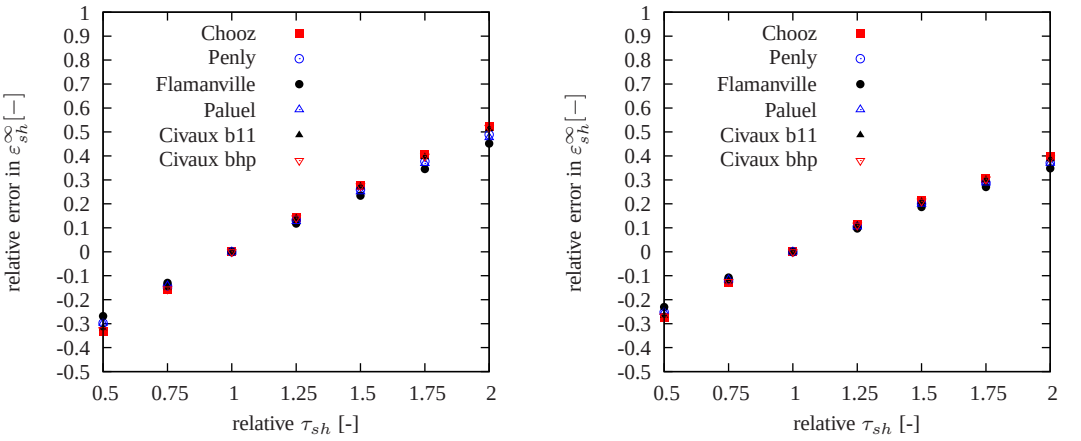

(a) (b)

Figure 8.15: Influence of incorrectly assumed shrinkage halftime τ_{sh} on error in the ultimate shrinkage value using equation (8.20) with (a) $p_{sh} = 0.63$, (b) $p_{sh} = 0.5$.

function is tuned up to match the long-term data, the experimental values of the short-time drying are overestimated. Therefore, if the shrinkage prediction was based on the early data and the shrinkage halftime, the final value would be underestimated as shown in Figures 8.17a–8.19a. The longer the duration of the short-time experiment, the better the fit. Faster convergence can be obtained when only the last measured point is used because the other points won't "spoil" the fit, see Figs. 8.17b–8.19b.

8.3.3 Conclusions - Granger's data

- The function describing water loss in time should be modified because it gives poor agreement with the experimental data in the early period of drying. It should be extended with another term – such as in equations (8.18) or (8.19) – which would correspond to water

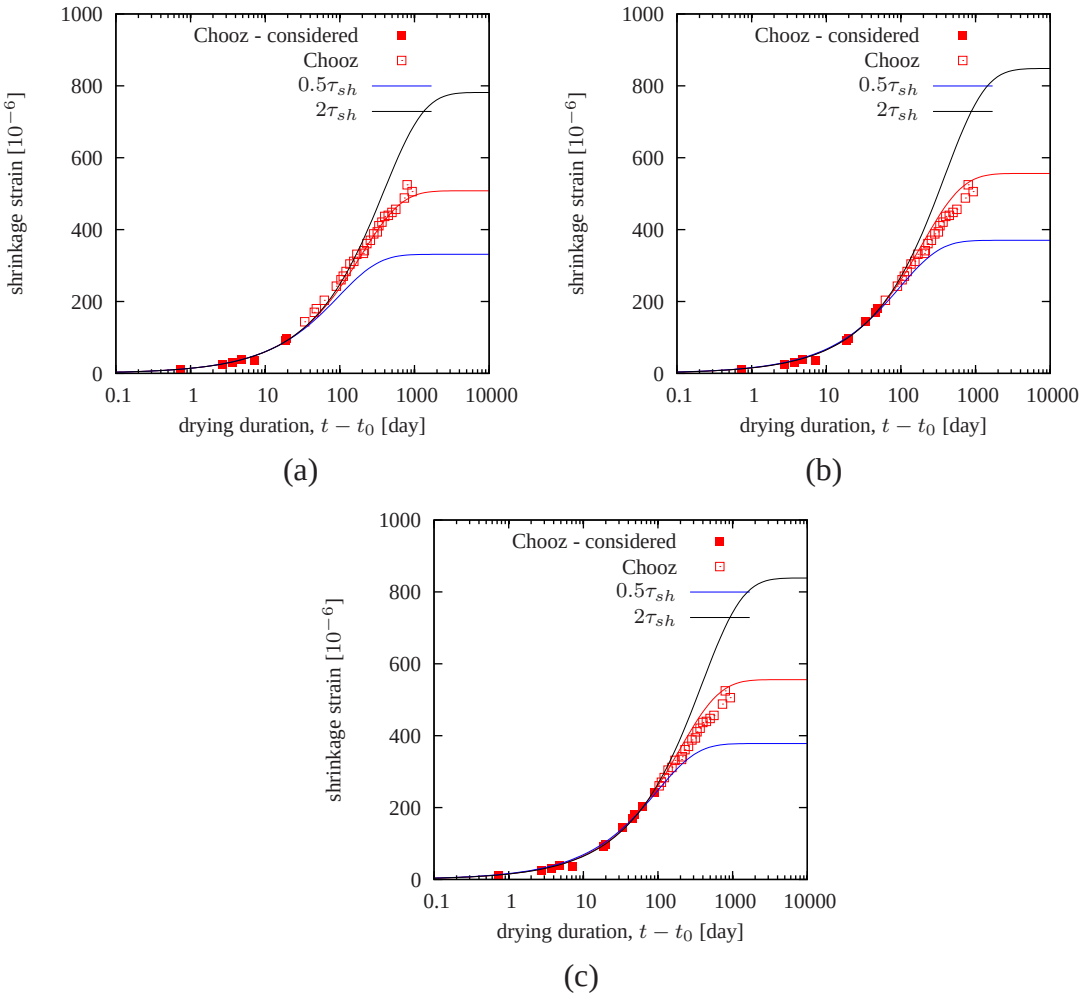

Figure 8.16: Shrinkage prediction based on computed shrinkage halftime and all data from short time measurements (a) 30 days, (b) 60 days, (c) 90 days, in all cases the fitting used equation (8.20) with $p_{sh} = 0.63$.

loss associated with emptying of large pores filled with water. This additional term is necessary not only for concrete that was cured in water, but also for sealed specimens.

- Granger's data indicate that having a certain experience, it is possible to predict the final value of the moisture loss from composition of the concrete mixture. The nonlinear (cubic) isotherm tends to overestimate the assumed ultimate value, while the linear isotherm reaches only 60% of the expected value. The best agreement is reached with the bilinear desorption isotherm.

- The originally proposed relationship between the halftimes $\tau_{sh} = 1.25\tau_w$ was found to be unrealistic. The shrinkage and drying halftimes are very sensitive to data, especially at the later stage. It was shown that even small changes can lead to completely different ratio. Different ratios are found for functions that match the data better than the recommended functions (8.4) and (8.17). The linear relationship between τ_{sh} and τ_w is in any case very simplistic and can lead to considerable errors.

  As an example consider that the final water loss at given relative humidity Δw_∞ was

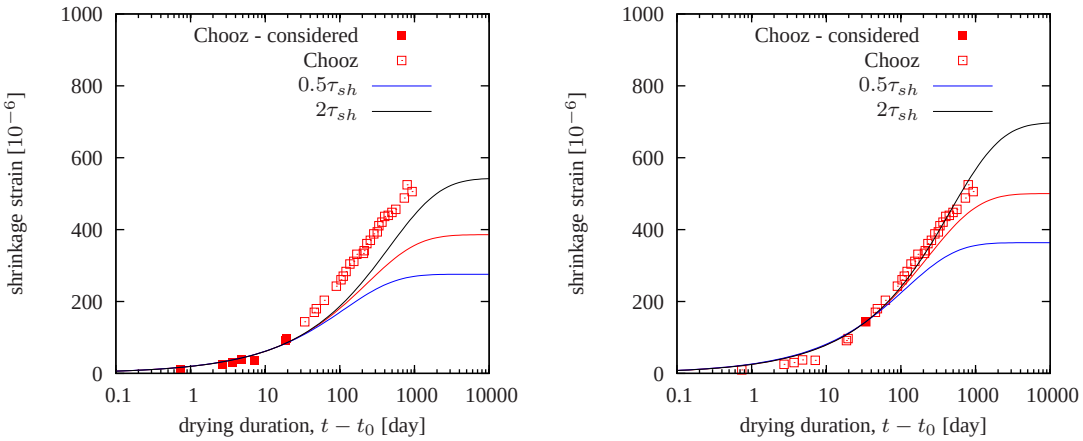

Figure 8.17: Shrinkage prediction using equation (8.20) with $p_{sh} = 0.5$ and based on computed shrinkage halftime and (a) all data until 30 days of drying (b) one measurement at 34 days.

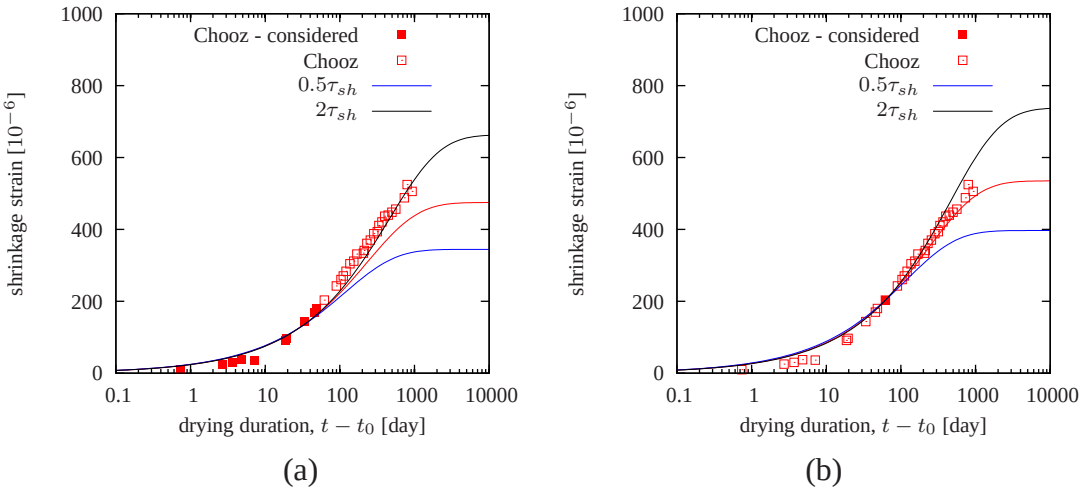

Figure 8.18: Shrinkage prediction using equation (8.20) with $p_{sh} = 0.5$ and based on computed shrinkage halftime and (a) all data until 60 days of drying (b) one measurement at 62 days.

estimated 10% higher than the actual value. Using least squares, the computed drying halftime τ_w is 40% higher than the actual (see Fig. 8.14). Even when the shrinkage halftime τ_{sh} could be computed with 100% accuracy from τ_w, the value of the final shrinkage $\varepsilon_{sh}^{\infty}$ would be 20% overestimated (considering also that the shrinkage function correctly captures the data in the whole range, see Fig. 8.15). Taking into account the error induced by assuming on the linear realtionship between τ_w and τ_{sh} the error would be comparable to (maybe even exceed) the original (blind) prediction. For the B3 model [13] coefficient of variation is 34%.

Considering the scatter shown in Figs. 8.12 and 8.13, estimation of τ_{sh} from τ_w is literally impossible.

- The correct value of the shrinkage halftime and a proper form of a shrinkage function are necessary for the correct shrinkage prediction. Having these two conditions fulfilled,

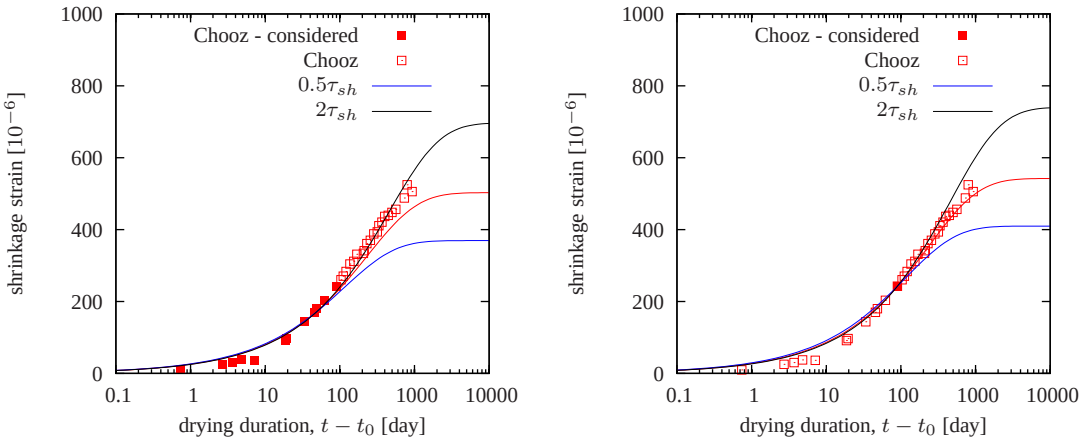

Figure 8.19: Shrinkage prediction using equation (8.20) with $p_{sh} = 0.5$ and based on computed shrinkage halftime and (a) all data until 90 days of drying (b) one measurement at 90 days.

the shrinkage can be predicted from experiment of very limited duration. With correct shrinkage halftime and a function which does not decribe well the initial period of drying, it is better to use only the last measured point.

- The shrinkage data from the first 10 days of drying should be neglected.

8.4 Experiments of Aguilar (2005)

Extensive study published in the Ph.D. thesis of Aguilar [6] contains a broad set of experimental data on shrinkage and moisture loss of concrete prisms. The main aim was to analyze the influence of concrete mixture on drying shrinkage, because the local Chilean aggregates cause larger creep than usual (600–1300$\times 10^{-6}$), see Fig. 8.20. Many different concrete compositions were tested from which 94 were selected for the analysis.

The variations in concrete composition comprised: different cement types (Portland, Portland pozzolan coarse and Portland pozzolan fine cement), 2 types of aggregates (limestone/siliceous), maximum nominal aggregate size (20/40 mm), water content to obtain 60/120 mm slump, admixtures (no admixtures, water reducing agents, expansive and shrinkage reducing admixtures, gypsum, ice), and of course different dosages of the constituents. Even though the compositions were often quite different, the intended specific strength was 30 MPa.

Two specimen sizes were used in the study: rectangular prisms 100$\times$100$\times$500 mm (according to DIN standard) and 75$\times$75$\times$285 mm (according to ASTM standard). Three specimens were prepared from each composition and size. Weight loss and shrinkage were measured on the same specimens. Length changes (shrinkage) were measured both on the lateral surface and between the specimen bases.

The specimens were cast into standardized molds from which they were removed 24 hours ($\pm$2 hours) after casting. Just before the first reading, they were submerged into water for 30-60 minutes in order to attain temperature stability. Before the measurement, the surface was wiped with a cloth to remove excessive water. After the first reading, the prisms were returned for curing into the lime water where they were kept for another 6 days. Afterwards, the specimens were again superficially wiped and measured. The specimens were stored in a room with controlled environment: 50$\pm$4% relative humidity and 23$\pm$1.7°C. No sealing was used, the specimens were drying from all sides. The readings were done 1, 2, 5, 6, 7, 8, 14, 15, 21, 22, 28, 56, 83, 90, 112, 224, 360, 448, 540, 630, 720 and 1350 days from the end of curing. Finally, the specimens were oven-dried at 110°C and the final weight was recorded.

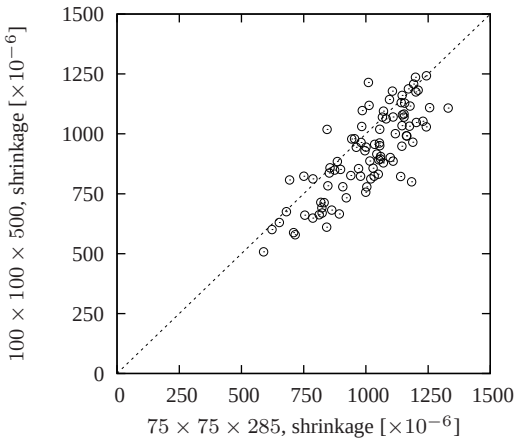

Figure 8.20: Maximum shrinkage measured on specimens of two different sizes, each point represents the average of three measurements.

- Since no reading was done before the first water bath, no information is available on the amount of imbibed water or the initial swelling deformation.

- The wiping with the cloth is a somewhat unclear procedure. This procedure was tried by the present author on a prismatic mortar specimen $4\times4\times16$ cm, every wiping removed water equal approximately to 0.5% of the specimen mass, while the surface looked still the same (darkish color of a moist concrete).

- The autogenous shrinkage was not recorded, in some cases it can represent a substantial part of the deformation.

- Regarding the oven-drying, it was not specified, what was the criterion to terminate the drying. According to a private communication with the author of [6], the specimens were oven-dried for about 4 days. The specimen could be crushed in order to speed up the drying process, in reality they were kept intact.

- It can be expected that the smaller specimens will exhibit bigger scatter - comparing the ratio of the maximum aggregate size 4 cm to the dimensions of the specimen with the shorter edge length 7.5 cm and gage length 28.5 cm. For this reason the computations are primarily fit to the data of the bigger specimens, $100 \times 100 \times 500$ mm.

8.5 Numerical simulations - Aguilar

The following simplifying assumptions have been used:

- Volume of the individual specimen was calculated as its weight right after demolding (and 1 hour water bath) divided by the fresh concrete density.

- Weight loss is always considered with respect to the state at the age of 7 days, i.e. right after water curing. Corresponding moisture ratio is obtained as a weight divided by the actual specimen volume.

8.5.1 Prediction of water loss

Similarly to the study of Granger's data, the water-loss data are analyzed first and the shrinkage data are investigated afterwards.

Comparing to the previous study, Aguilar examined specimens of two sizes. Thanks to the oven-drying at the end of the experiment, there is the opportunity to assess the relative ultimate water loss. If the difference in the measured moisture content turns out to be similar for both sizes, the specimens have dried either completely or to a similar degree.

Figure 8.21 shows the relationship between the ultimate water loss per unit volume measured on large and small specimens. The specimens were first dried at 50% relative humidity (Fig. 8.21a) and then the same specimens were transferred into an oven (Fig. 8.21b). No correction factors multiplying the ultimate values are used in this plot.

In Fig. 8.21a the points are nicely centered around the diagonal, which implies that in the end of the experiment a similar portion of the moisture has dried out both from small and large specimens. This suggests that the specimens are nearly dry or have dried approximately similarly.

However, the points in Fig. 8.21b are centered rather in the upper-left portion of the figure, which means that in the end of oven-drying a bigger portion of water has evaporated from the bigger specimens than from the smaller samples. This behavior cannot be reasonably explained.

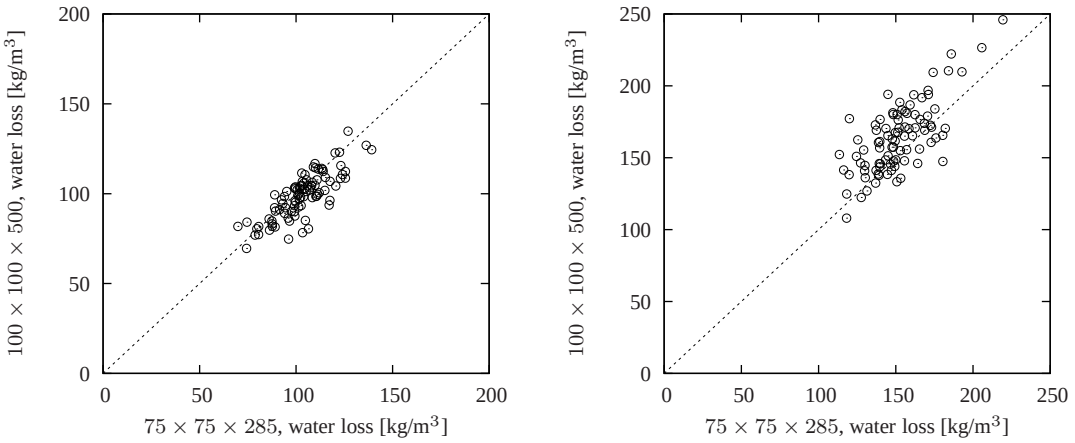

Figure 8.21: Ultimate measured water loss of specimens of two different sizes (a) dried at $h_{\mathrm{env}} = 0.50$, (b) oven-dried. Each point represents the average of three measurements.

In Figure 8.22 the measured water lost by oven drying is plotted against the amount calculated based on concrete composition. It was assumed that the specimen has not dried completely, so the plotted data represent the measured data multiplied by the factor $k_{oven} = 1.05$. From the concrete composition the water loss was estimated using following formula which gives quite reasonable agreement:

$$\Delta w_\infty(h_{\mathrm{env}} = 0) = w + w_{\mathrm{additives}} + w_{\mathrm{aggregates}} + w_{\mathrm{absorbed,1h}} + w_{\mathrm{absorbed,6d}} - \alpha_c c \qquad (8.22)$$

where w is the amount of water prescribed in the concrete composition, $w_{\mathrm{additives}}$ is the weight of additives (the same density as water is assumed), $w_{\mathrm{aggregates}}$ is the amount of water in the aggregates which were not completely dry, $w_{\mathrm{absorbed,1h}}$ is the water imbibed by the specimen after demolding during 1 hour in the water bath and $w_{\mathrm{absorbed,6d}}$ is the water consumed during curing. The initially absorbed water $w_{\mathrm{absorbed,1h}}$ can be only roughly estimated and there is no check that the value is correct. The selected value of the surface absorption 0.02 ml/(m^2 s) is rather small, but considering that the concrete is highly saturated, it was found to be adequate. The amount of imbibed water is then $w_{\mathrm{absorbed,1h}} = 0.02 \times 10^{-3} \times 3600 \times S/V$ which is 3.2 kg/m^3 for larger specimens and 4.3 kg/m^3 for smaller specimens. The amount of chemically bound water is proportional to cement weight, with the proportionality factor α_c. First, the value 0.2 that worked best in case of Granger's data can be used as the first approximation.

The standard deviation of the relative error between the computed and measured water loss for the bigger specimens is approximately 11.8%. The mean relative error for the smaller specimens is 9.4%.

Figure 8.23 suggests that perhaps a different parameter α_c should be used for different cement types. The chemically bound water is comparable for the Portland and the fine pozzolan cement, while the coarse pozzolan cement binds lower amount of water (during the limited time before the decreased relative humidity stops the hydration).

For the 50% relative humidity, the computed weight loss based on concrete composition

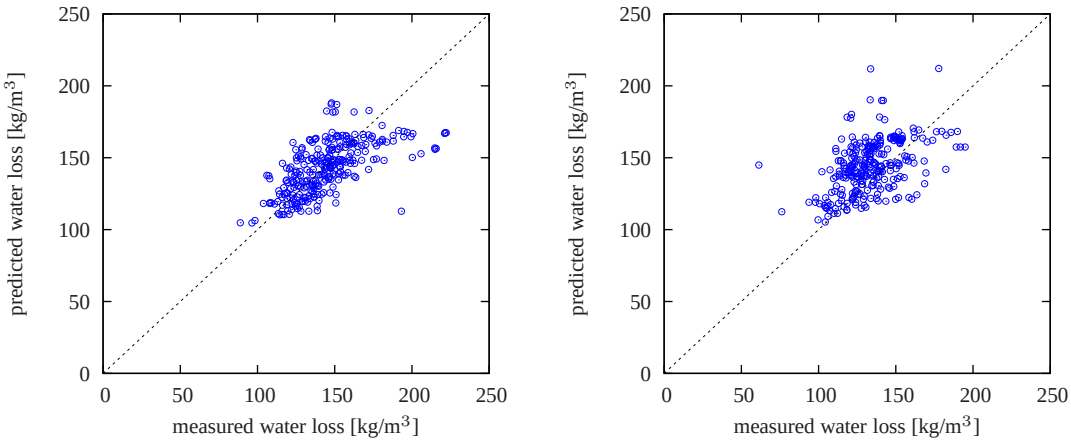

Figure 8.22: Comparison of the measured and computed amount of evaporable water lost by oven drying for specimens with the edge length (a) 100 mm, (b) 75 mm.

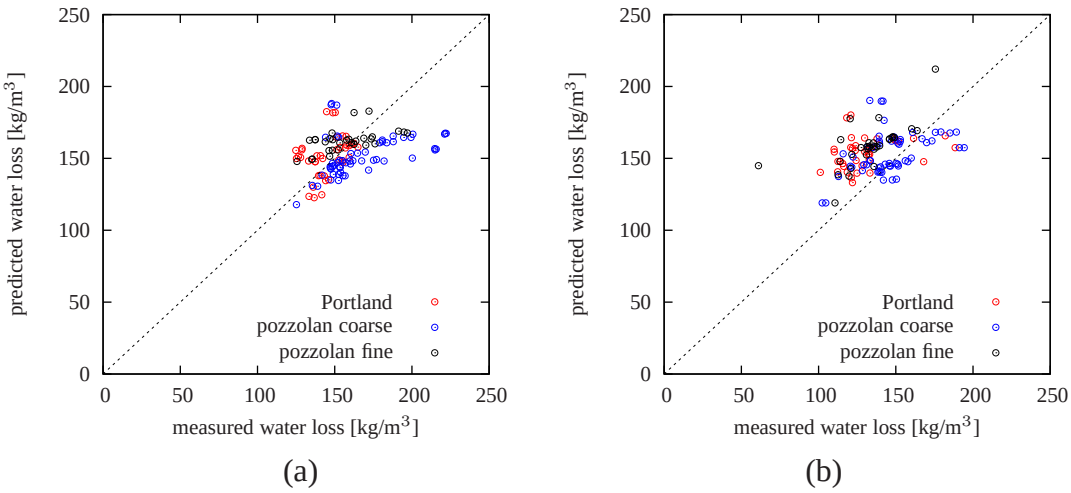

Figure 8.23: Comparison of the measured and computed amount of evaporable water lost by oven drying for specimens with the edge length (a) 100 mm, (b) 75 mm. Only the concretes without admixtures are considered, the behavior depends on the cement type.

was estimated using the following equation

$$\Delta w_\infty(h_{\text{env}} = 50\%) = \eta(1. - h_{\text{env}})(w + w_{\text{additives}} + w_{\text{aggregates}} - \alpha_c c - w_{\text{large pores}}) + \\ + w_{\text{absorbed,1h}} + w_{\text{absorbed,6d}} + w_{\text{large pores}} \tag{8.23}$$

with parameter $\eta = 0.8$ related to the slope of the desorption isotherm in interval 0–0.98. The value of the moisture content stored in the large pores $w_{\text{large pores}}$ can be determined when the sorption isotherm is known which is not the present case. Now it can be only roughly estimated; it will be probably related to the amount of water in the concrete mixture, because the higher the amount of water leads to the bigger the portion of the large pores. The smallest error was achieved with $w_{\text{large pores}} = k_w \times (w + w_{\text{additives}} + w_{\text{aggregates}})$ and $k_w = 0.26$, the average value of $w_{\text{large pores}}$ is 55 kg/m^3. The slope of the desorption isotherm up to 98% relative humidity is then $\eta(w + w_{\text{additives}} + w_{\text{aggregates}} - \alpha_c c - w_{\text{large pores}})$ which is on average only 60 kg/m^3.

Comparison between the measured and the moisture loss computed from composition is shown in Fig. 8.24. Similarly to the previous case the measured value was multiplied by factor $k_{oven} = 1.05$.

For the bigger specimens (Fig. 8.24a) the data points are nicely centered around the diagonal (standard deviation of the relative error $\sigma = 9.3\%$), for the smaller specimen the agreement is still satisfactory, but the cluster of points is somewhat tilted.

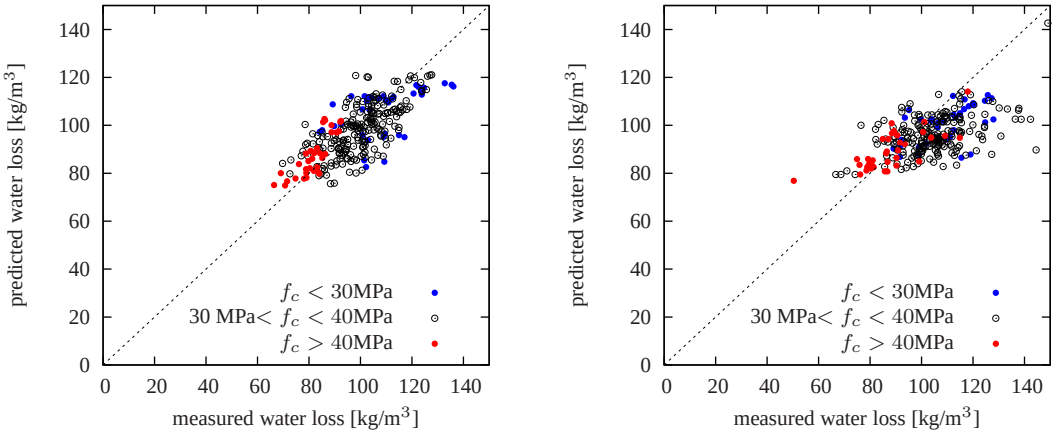

Figure 8.24: Comparison of the measured amount of evaporable water lost by drying at $h_{\text{env}} = 50\%$ and the amount computed based on concrete composition for specimens with the edge length (a) 100 mm, (b) 75 mm.

Utilizing the information from the oven-drying experiment, the moisture loss can be computed as

$$\Delta w_\infty(h_{\text{env}} = 50\%) = \eta(1. - h_{\text{env}})(k_{oven}\Delta w - w_{\text{large pores}} - w_{\text{absorbed,1h}} - w_{\text{absorbed,6d}}) + \\ + w_{\text{absorbed,1h}} + w_{\text{absorbed,6d}} + w_{\text{large pores}} \tag{8.24}$$

where Δw is the difference between the moisture content in the end of curing and after oven-drying.

The results of the prediction based on oven heating is shown in Fig. 8.25. For the bigger specimens the error is comparable to the methodology based on composition (now $\sigma = 8.9\%$), but for the smaller specimens the inclination from the diagonal becomes even more apparent.

In order to make the average slope of the desorption isotherm more realistic, the following adjustments of the parameters were done. First the amount of chemically bound water captured by parameter α_c is reduced from 0.2 to 0.15. This can be explained by shorter curing period (only 7 days before the onset of drying). Next, the parameter relating the amount of large pores to water in composition is set to $k_w = 0.15$ which makes the average of the moisture content represented by the large pores equal to 30 kg/m^3. Then the parameter relating the slope of the desorption isotherm to the amount of evaporable water η was increased to 0.9. Finally the values measured by oven-drying were multiplied by $k_{oven} = 1.2$ instead of 1.05.

The errors are comparable to the previous set of parameters, but now the average slope of the desorption isotherm is 105.8 kg/m^3. The results are shown in Figures 8.26–8.29

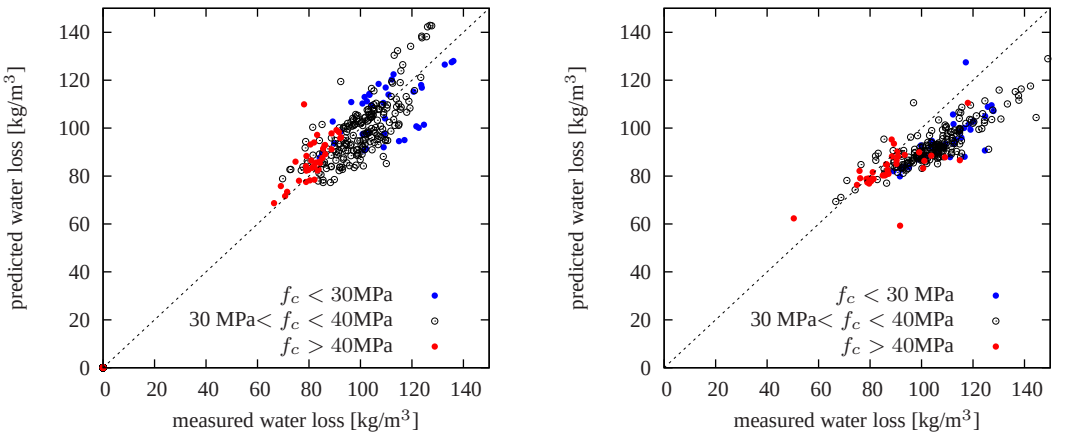

Figure 8.25: Comparison of the measured amount of evaporable water lost by drying at $h_{\mathrm{env}} = 50\%$ and the amount computed based on the oven-drying experiment for specimens with the edge length (a) 100 mm, (b) 75 mm.

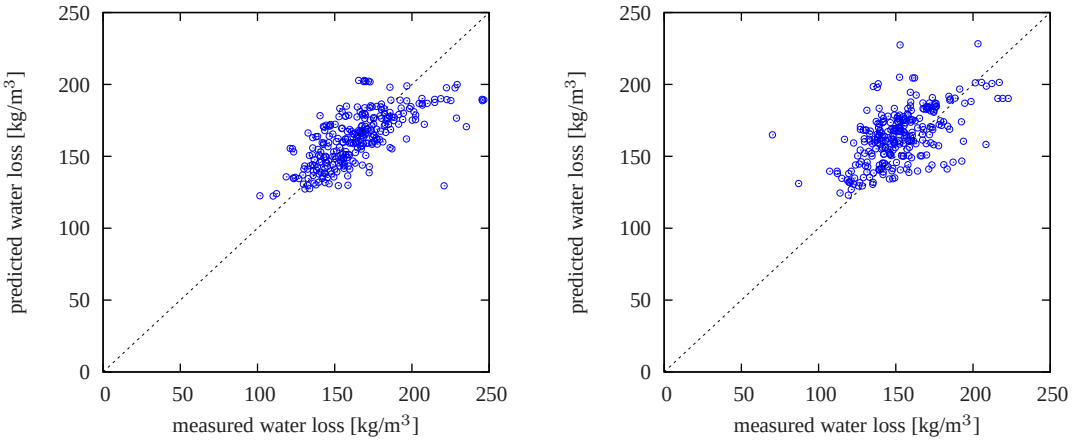

Figure 8.26: Comparison of the measured and computed amount of evaporable water lost by oven drying for specimens with the edge length (a) 100 mm, (b) 75 mm ($\alpha_c = 0.15$, $k_w = 0.15$, $\eta = 0.9$, $k_{oven} = 1.2$).

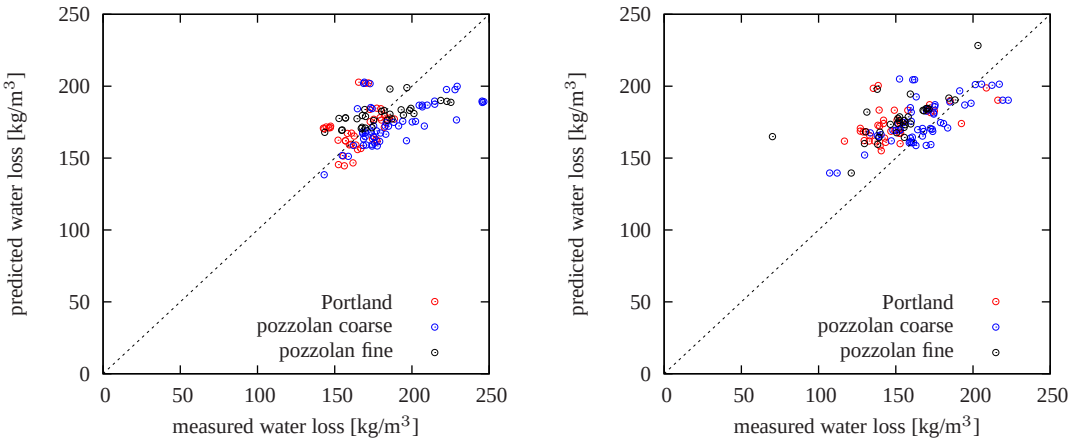

Figure 8.27: Comparison of the measured and computed amount of evaporable water lost by oven drying for specimens with the edge length (a) 100 mm, (b) 75 mm. Only the concretes without admixtures are considered, the behavior depends on the cement type ($\alpha_c = 0.15$, $k_w = 0.15$, $\eta = 0.9$, $k_{oven} = 1.2$).

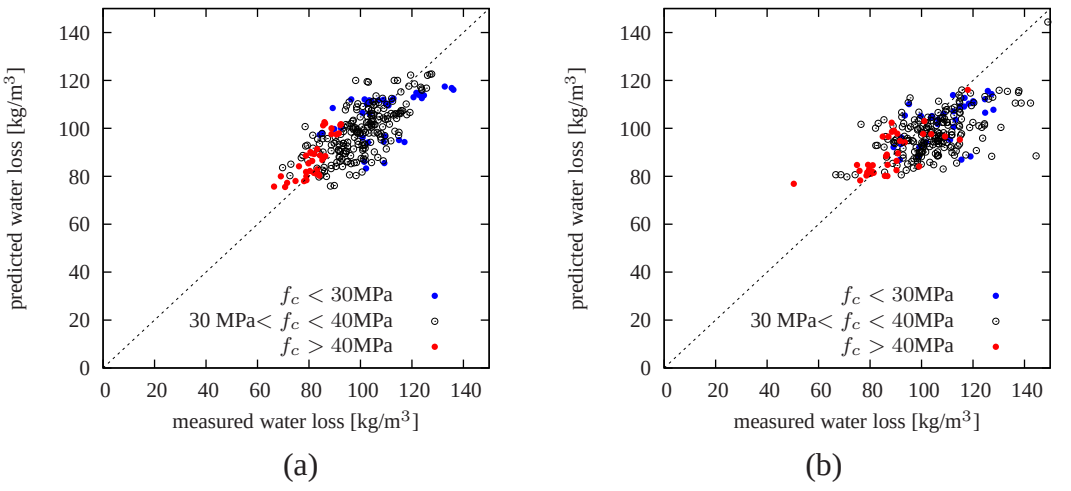

Figure 8.28: Comparison of the measured amount of evaporable water lost by drying at $h_{\mathrm{env}} = 50\%$ and the amount computed based on concrete composition for specimens with the edge length (a) 100 mm, (b) 75 mm ($\alpha_c = 0.15$, $k_w = 0.15$, $\eta = 0.9$, $k_{oven} = 1.2$).

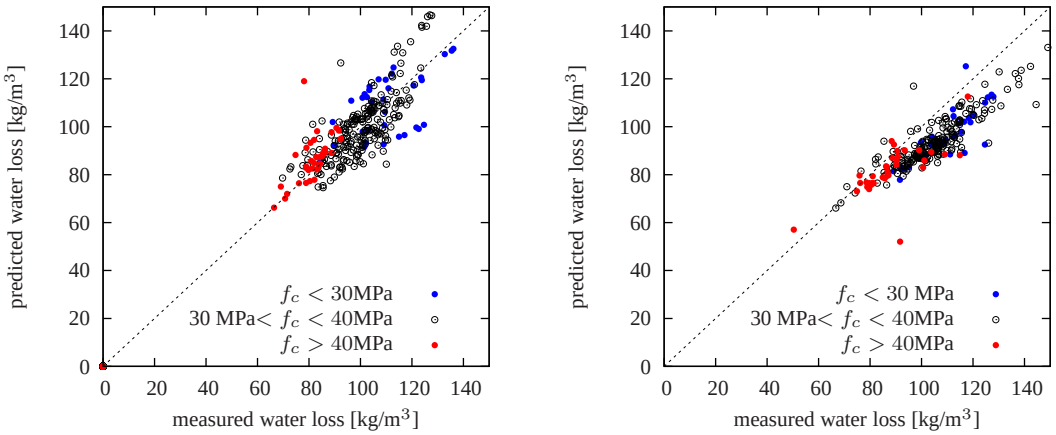

Figure 8.29: Comparison of the measured amount of evaporable water lost by drying at $h_{\mathrm{env}} = 50\%$ and the amount computed based on the oven-drying experiment for specimens with the edge length (a) 100 mm, (b) 75 mm ($\alpha_c = 0.15$, $k_w = 0.15$, $\eta = 0.9$, $k_{oven} = 1.2$).

8.5.2 Relationship between shrinkage and moisture loss

This section aims to reveal whether or not there exists a link between the drying halftime and the shrinkage halftime. The big scatter in the previous section could have two main sources: first, the effective thickness was quite big compared to Aguilar's specimens (uncertainty in the ultimate value causes error in halftime), and second, only six compositions with different additives and admixtures were used. In Aguilar's study there are 42 compositions without any admixtures.

Due to the fact that all the specimens were water-cured, it is inevitable to use a function (8.18) which splits the total water loss into two components with two different characteristic times. Shrinkage can be fitted with (8.20), first with $p_{sh} = 0.5$. All the data points are used in the fitting. All the parameters were kept unconstrained. The result of such optimization is shown in Fig. 8.30. The mean of the ratio between the ultimate water loss $\Delta w_\infty(h_{\text{env}})$ and the maximum reached value was 1.02 and between the ultimate shrinkage ε_{sh}^∞ and the maximum reached value 0.9997. The relationship between the drying and shrinkage halftime is quite wide-spread (standard deviation of the ratio $\tau_{sh,i}/\tau_{w,i}$ is 0.27). Maybe a clearer trend could be obtained if the parameters in (8.18) and (8.20) were subsequently constrained.

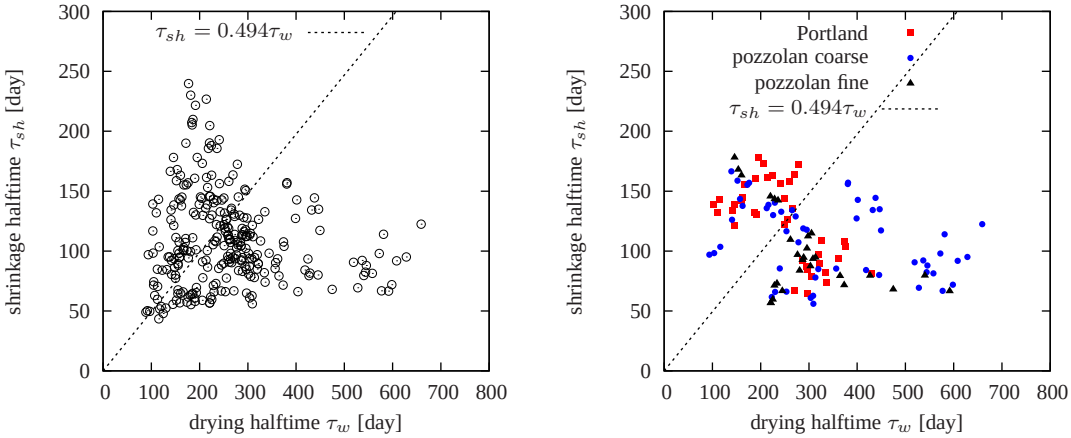

Figure 8.30: Relationship between the ideal shrinkage halftimes and the corresponding water-loss halftimes for (a) all concretes (b) only concretes without admixtures. All parameters are kept free except $p_{sh} = 0.5$ (according to Bažant). Mean error (RMS) of the shrinkage fits is 39.6×10^{-6} and water loss fits 1.27. Mean of the individual ratios $\tau_{sh,i}/\tau_{w,i}$ is 0.494, standard deviation 0.265.

First, the ratio between the ultimate water loss and its maximum was fixed to 1.02 and the ratio between the ultimate shrinkage and its maximum value to 1.0. As could be expected, the mean error increased (RMS: shrinkage 41.2×10^{-6}, water loss 1.32), but the standard deviation of the ratios $\tau_{sh,i}/\tau_{w,i}$ decreased to 0.206 with the mean value 0.472.

Next the ratio between the water-loss halftimes was set to 0.03 (RMS: water loss 1.57, mean of $\tau_{sh,i}/\tau_{w,i}$ is 0.492, standard deviation 0.226) and finally the last remaining parameter α_w was set to 0.6. Interestingly, the mean of the ratio $\tau_{sh,i}/\tau_{w,i}$ changed only by 12% and the standard deviation reduced to 60% of the original one. But even now, as presented in Fig. 8.31, the scatter is still huge.

The same fitting procedure was then repeated: motivated by the fitting of Granger's data also the exponent p_{sh} in (8.20) was subject to optmization. Figure 8.32 shows the ratios when all

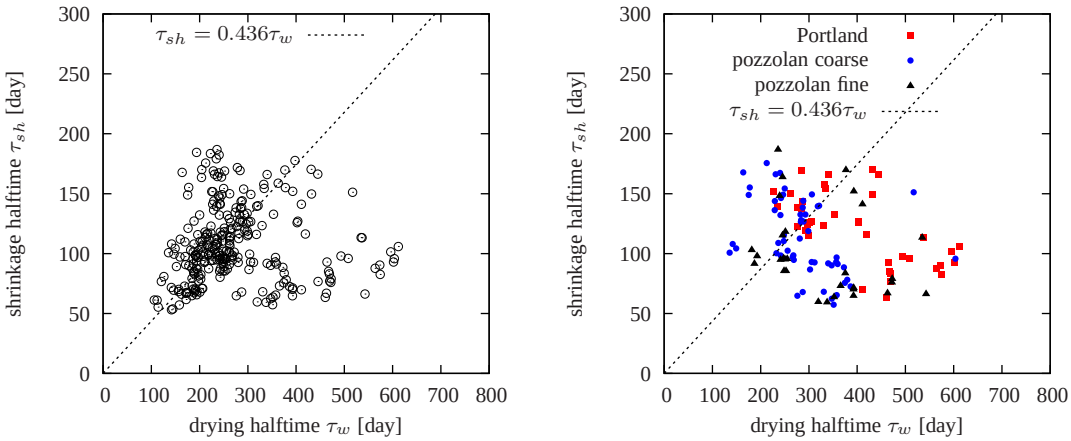

(a) (b)

Figure 8.31: Relationship between the ideal shrinkage halftimes and the corresponding water-loss halftimes for (a) all concretes (b) only concretes without admixtures. $p_{sh} = 0.5$, $\Delta w_\infty : \max(\Delta w) = 1.02$, $\gamma_w = 0.03$, $\alpha_w = 0.6$, $\varepsilon_{sh}^\infty : \max(\varepsilon_{sh}) = 1.0$. Mean error (RMS) of the shrinkage fits is 41.2×10^{-6} and water loss fits 1.96. Mean of the individual ratios $\tau_{sh,i}/\tau_{w,i}$ is 0.436, standard deviation 0.161.

parameters were kept unconstrained. Note the considerable reduction in the shrinkage error and the standard deviation of $\tau_{sh,i}/\tau_{w,i}$ compared to Fig. 8.30. Although the error of the shrinkage fits decreased, the mean of the ratio between the ultimate and maximum reached shrinkage is only 0.9672 with standard deviation 0.0209. This suggests that the function (8.20) is not suitable even with non-standard value of the exponent p_{sh}.

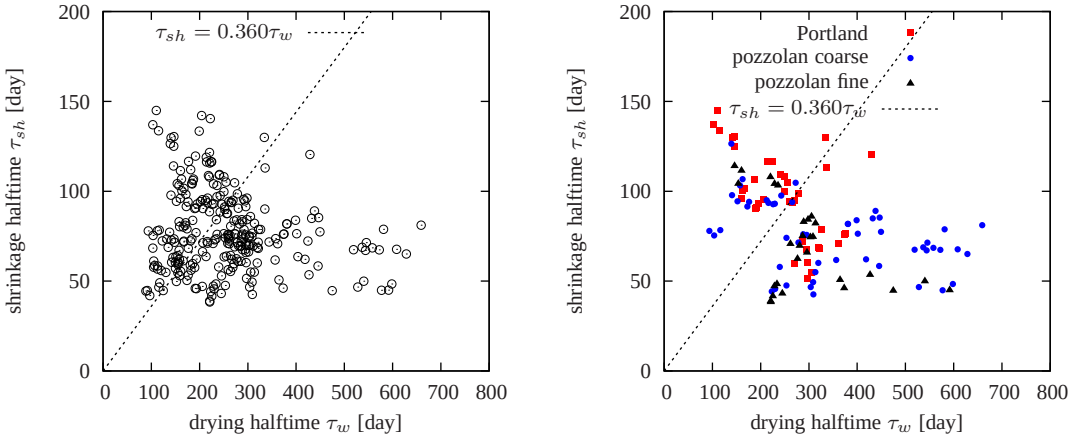

(a) (b)

Figure 8.32: Relationship between the ideal shrinkage halftimes and the corresponding water-loss halftimes for (a) all concretes (b) only concretes without admixtures. All parameters are kept free. Mean error (RMS) of the shrinkage fits is 24.8×10^{-6} and water loss fits 1.26. Mean of the individual ratios $\tau_{sh,i}/\tau_{w,i}$ is 0.360, standard deviation 0.195.

Smaller error in the shrinkage fits as well as the ratio between the ultimate shrinkage and the maximum reached value is obtained with function (8.21). In case of Granger's data the difference between the functions (8.20) and (8.21) could not be recognized because the exper-

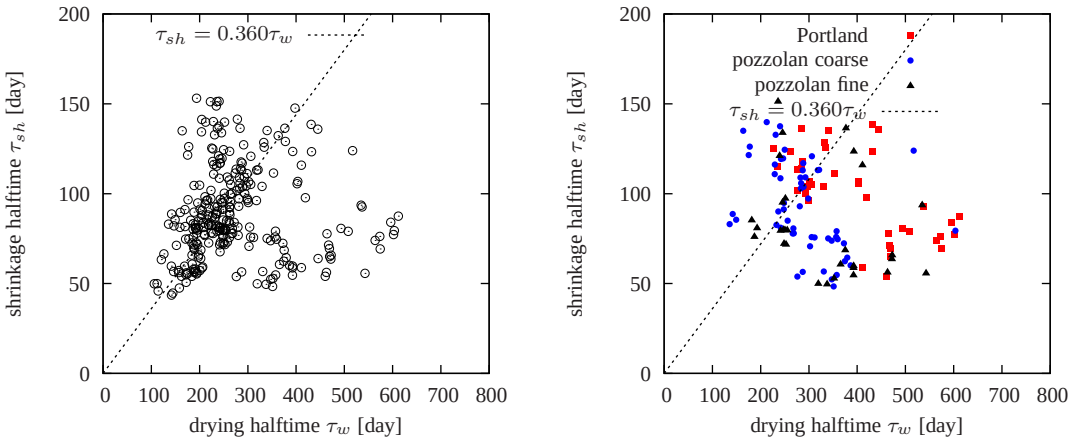

(a) (b)

Figure 8.33: Relationship between the ideal shrinkage halftimes and the corresponding water-loss halftimes for (a) all concretes (b) only concretes without admixtures. $\Delta w_\infty : \max(\Delta w) = 1.02$, $\gamma_w = 0.03$, $\alpha_w = 0.6$, $p_{sh} = 0.6$, $\varepsilon_{sh}^\infty : \max(\varepsilon_{sh}) = 1.0$. Mean error (RMS) of the shrinkage fits is 34.8×10^{-6} and water loss fits 1.96. Mean of the individual ratios $\tau_{sh,i}/\tau_{w,i}$ is 0.360, standard deviation 0.131.

iment did not last long enough. Aguilar's data indicate that the shrinkage evolution terminates more smoothly than it is described with $\tanh$ function, see Fig. 8.10. The obtained relationship between the halftimes is shown in Figure 8.34 which almost cannot be distinguished from Fig. 8.33 except for the different scale on the vertical axis.

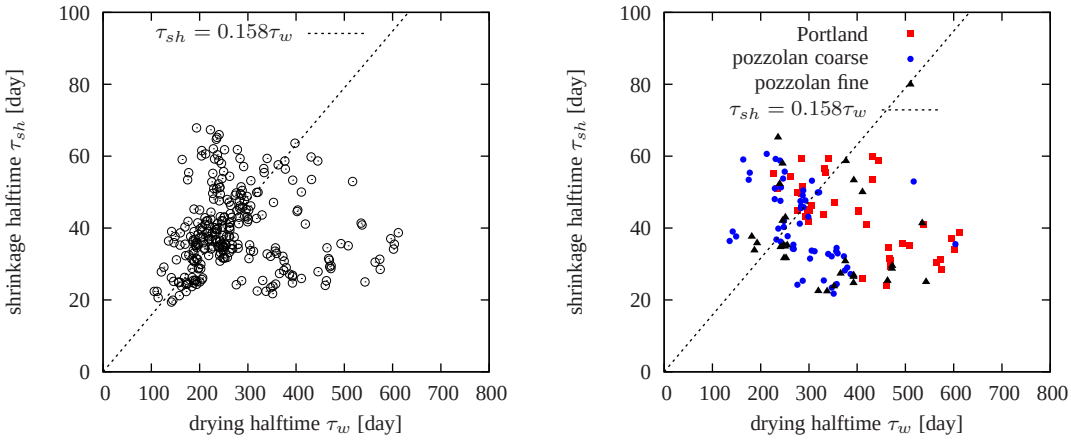

(a) (b)

Figure 8.34: Relationship between the ideal shrinkage halftimes and the corresponding water-loss halftimes for (a) all concretes (b) only concretes without admixtures. Shrinkage is described with function (8.21). $\Delta w_\infty : \max(\Delta w) = 1.02$, $\gamma_w = 0.03$, $\alpha_w = 0.6$, $q_{sh} = 0.86$, $\varepsilon_{sh}^\infty : \max(\varepsilon_{sh}) = 1.03$. Mean error (RMS) of the shrinkage fits is 28.1×10^{-6} and water loss fits 1.96. Mean of the individual ratios $\tau_{sh,i}/\tau_{w,i}$ is 0.158, standard deviation 0.0575.

When the same procedure is applied to the data measured on smaller specimens, the agreement is worse than expected, see Fig. 8.35. The ratio between the halftimes almost doubled and the errors increased too.

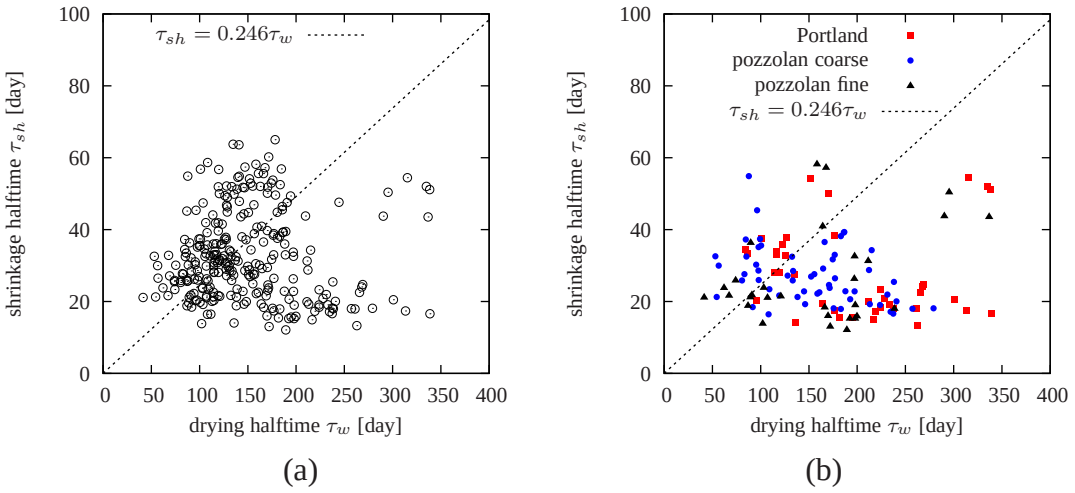

Figure 8.35: Relationship between the ideal shrinkage halftimes and the corresponding water-loss halftimes for (a) all concretes (b) only concretes without admixtures. Shrinkage is described with function (8.21), smaller specimens. $\Delta w_\infty : \max(\Delta w) = 1.01$, $\gamma_w = 0.03$, $\alpha_w = 0.6$, $q_{sh} = 0.86$, $\varepsilon_{sh}^\infty : \max(\varepsilon_{sh}) = 1.01$. Mean error (RMS) of the shrinkage fits is 33.4×10^{-6} and water loss fits 2.18. Mean of the individual ratios $\tau_{sh,i}/\tau_{w,i}$ is 0.246, standard deviation 0.116.

According to the diffusion theory, the drying halftime should be proportional to the square of the effective thickness, D. In this case the ratio $D_{100}^2 : D_{75}^2 = 1.88$, so the halftimes should be in also this ratio. As shown in Fig. 8.36, the error probably stems from shrinkage, not from the moisture loss, because the average ratio of the drying halftimes determined by fitting is $\tau_{w,100} : \tau_{w,75} = 1.8$ which is only slightly different from the ideal value 1.88, while the ratio of the drying halftimes (even though the exponent p_{sh} was equal 0.5) is 1.23. The scatter is in both figures quite large.

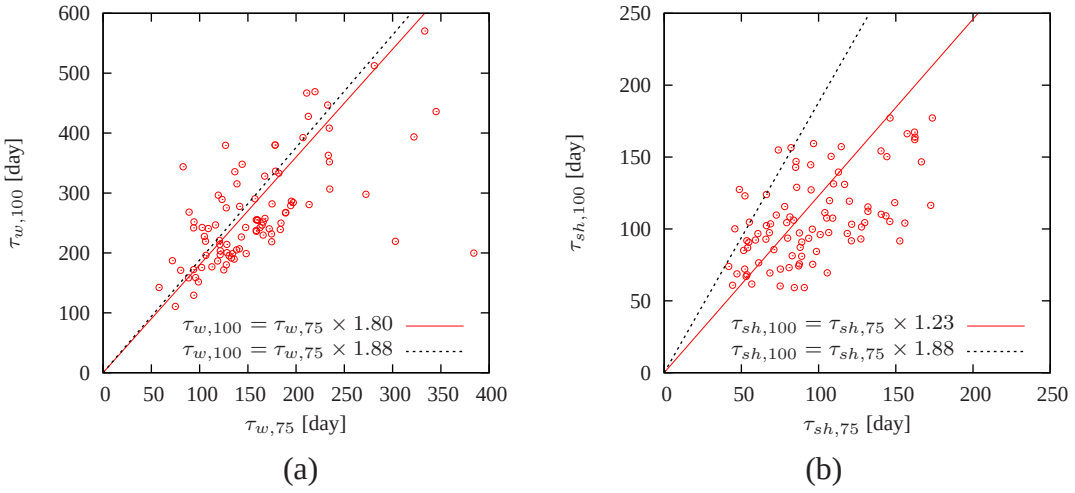

Figure 8.36: Relationship between the ideal (a) water-loss halftimes and (b) shrinkage halftimes identified by fitting using equations (8.18) and (8.20) with exponent $p_{sh} = 0.5$.

8.5.3 Conclusions - Aguilar's data

- Prediction of the ultimate water loss of the drying concrete specimen can be computed using two methods providing comparable accuracy. The first one uses concrete composition, the second one makes use of the results of the oven-drying experiment.
- Comparable results of the predicted moisture loss can be obtained with different values of parameters (α_c, k_{oven}, η, k_w). Some combinations provide good agreement with the measured data but lead to unrealistic values of some material properties (such as moisture capacity).
- Aguilar's shrinkage data indicate that the shrinkage function with $\tanh$ (8.20) is not suitable, the function terminates too rapidly. Considerably smaller error is reached with the function (8.21). In both cases the exponents p_{sh} and q_{sh} are higher than the recommended value 0.5.
- The relationship between the water-loss halftime and the shrinkage halftime exhibits large scatter.
- The water-loss halftimes identified from Aguilar's data are scaled correctly with the specimen size. This is not true for shrinkage halftimes; it can be caused by the specimen size, which is quite small compared to the maximum aggregate size.

8.6 Numerical modeling in OOFEM

The objective of this section is to prove not only the validity of the simplifying assumptions made in this previous sections but also to check that the measured data can be obtained with the combination of Künzel's (transport) and MPS (structural analysis) models. The validation is done in terms of finite element analysis in program OOFEM. The first data series of the thesis [57] [6] was selected as an example.

8.6.1 FE simulations of Granger's experiment

Although the Granger's Ph.D. thesis provides the basic creep data, the values of the basic creep parameters q_1–q_4 were computed from concrete composition using the formulae of the B3 model. The reason is that the resulting shrinkage (measured/computed on stress-free specimens) is insensitive to these values. For the "Chooz" composition with $f_c = 43.5$ MPa, $c = 350$ kg/m^3, w/c = 0.54 and $a/c = 5.617$ the parameters are $q_1 = 19.22$, $q_2 = 116.28$, $q_3 = 2.87$, $q_4 = 6.07$ all in 10^{-6}/MPa. Since the size effect on drying creep is not known, it is better to stick to the "safe" value of the exponent $\tilde{p} = 1$ which gives the same drying creep independently of the specimen size. Parameter $k_3 = 35$ is taken from fitting of Bryant's data. The remaining fitting parameter in the structural analysis is the shrinkage coefficient k_{sh}.

In the analysis presented in Section 8.3.1, the total amount of evaporable water at zero relative humidity for the "Chooz" composition was estimated as $190 - 0.2 \times 350 = 120$ kg/m^3, the assumed amount of water accumulated in large pores as $0.15 \times 190 \times (190 - 130)/50 = 34.2$ kg/m^3 and the amount of evaporable water at 50% relative humidity $0.8 \times (1 - 0.5) \times (120 - 34.2) + 34.2 = 68.52$ kg/m^3. The slope of the desorption isotherm is then $0.8 \times (120 - 34.2) = 68.64$ kg/m^3. The isotherm and the results are presented in Figs. 8.37 and 8.38, the

used parameters are listed in Tables 8.2 and 8.3. In all alternatives, the desorption isotherm is bilinear with the breaking point at $h = 0.98$

For the first set of parameters (labeled OOFEM #1), the evolution of water loss is captured correctly, but the shrinkage is too delayed behind the experiment. This is caused by the initial high moisture capacity – during drying the moisture content decreases rapidly, but the change in shrinkage strain is linked to change in relative humidity, which initially decreases very slowly.

In the next step the moisture capacity on interval $h = (0 - 0.98)$ was increased from 68.6 to 80 kg/m^3, keeping the same free saturation moisture content. The behavior improved, but in order to obtain a realistic shrinkage evolution it was necessary to replace the original highly nonlinear isotherm with almost linear one (OOFEM #3) with slope 115 kg/m^3. Qualitatively the same results are obtained when the isotherm is shifted upwards 17.5 kg/m^3 (OOFEM #4). The increased amount of evaporable water 137.5 kg/m^3 then corresponds to smaller amount of the chemically bound water expressed by parameter $\alpha_c = 0.15$.

Even though the slope of the isotherm increased, the amount of water that evaporates at $h_{\text{env}} = 0.5$ decreased to 62.5 kg/m^3, however, the agreement with the experimental data is still very good, see Fig. 8.37b.

For every isotherm it was necessary to properly adjust the shrinkage constant, k_{sh}, to correctly capture the ultimate shrinkage value. The value of k_{sh} had to be biggest for the highly nonlinear isotherm which led to the slowest decrease in relative humidity (and shrinkage). The slow rate of drying was accompanied with substantial relaxation. Therefore a large value of the shrinkage constant was necessary to achieve the correct shrinkage deformation.

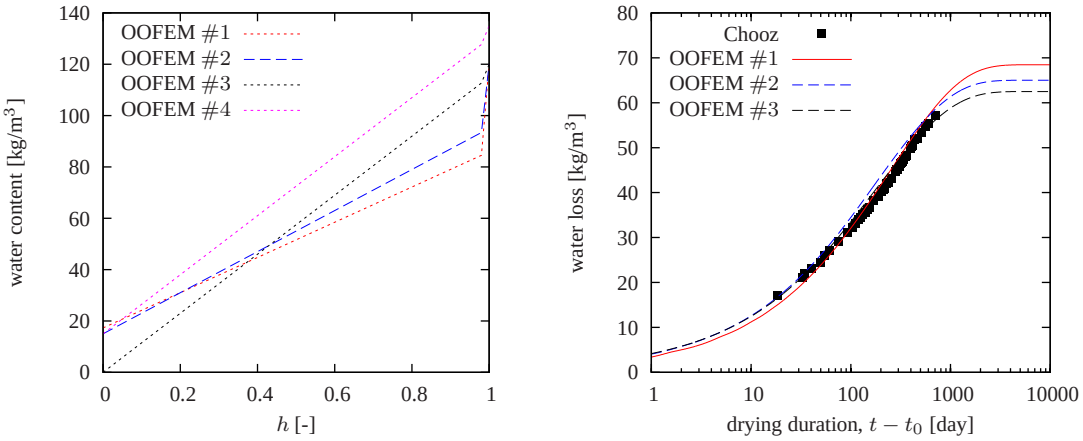

(a) (b)

Figure 8.37: (a) Alternatives of the desorption isotherm used in simulations, (b) comparison of the Granger's experimental data with numerical simulations in OOFEM: water loss in time.

Figure 8.39 shows the updated results from Section 8.3.1. However, the fits with the analytical functions (8.18) or (8.19) became poor.

8.6.2 FE simulations of Aguilar's experiment

The first concrete in Aguilar's thesis had compressive strength $f_c = 37.$ MPa, the concrete composition consisted of 414.8 kg/m^3 of cement, 19.4 kg/m^3 of water in aggregates, 192.2

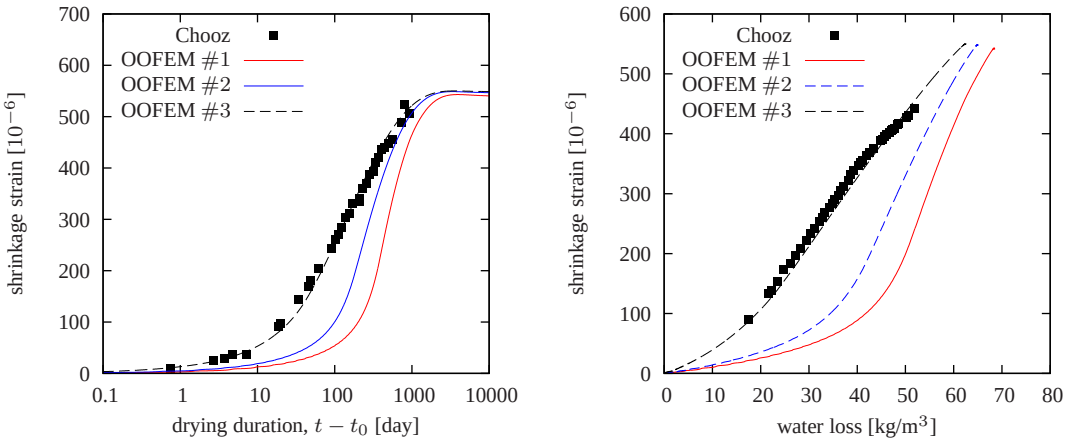

Figure 8.38: Comparison of Granger's experimental data with numerical simulations in OOFEM (a) shrinkage strain in time, (b) shrinkage strain vs. water loss.

Table 8.2: Granger's experiment: summary of the input material parameters: diffusion

		OOFEM #1	OOFEM #2	OOFEM #3	OOFEM #4
$w(0)$	[kg·m^{-3}]	17.3	15	0	17.5
k	[kg·m^{-3}]	68.6	80	115	115
w_f	[kg·m^{-3}]	120	120	120	137.5
μ	[-]	500	450	400	400
A	[kg·m^{-2} day$^{-0.5}$]	0.3	0.35	0.35	0.35

Table 8.3: Granger's experiment: values of shrinkage constant

		OOFEM #1	OOFEM #2	OOFEM #3	OOFEM #4
k_{sh}	[-]	0.0015	0.0014	0.0013	0.0013

kg/m^3 of additionally added water, and 1808.9 kg/m^3 of aggregates. The resulting water-to-cement ratio (computed from the added water only) was 0.4634 and aggregate-to-cement ratio 4.361. Using the B3 formulae, the basic creep parameters can be estimated as $q_1 = 20.84$, $q_2 = 146.44$, $q_3 = 1.96$, $q_4 = 7.24$, all in 10^{-6}/MPa. The MPS parameters are taken the same as in the last section, $\tilde{p} = 1$ and $k_3 = 35$.

This section presents only the data and simulations of the bigger specimens ($100 \times 100 \times 500$ mm), the results of the smaller sample of the same composition are omitted because the size-effect on shrinkage does not hold in case of Aguilar's data.

For the first concrete mixture, the amount of water consumed during the 6-day curing period was 11.85 kg/m^3, adding the water imbibed during the 1-hour bath just after demolding this makes approximately 15 kg/m^3. Based on the concrete composition, the amount of chemically bound water is $0.15 \times 414.8 = 62.2$ kg/m^3, and the amount of evaporable water at $h_{\text{env}} = 0$ is $226.6 - 62.2 = 164.4$ kg/m^3. Water occupying large pores represents $0.15 \times (192.2 + 19.4) =$

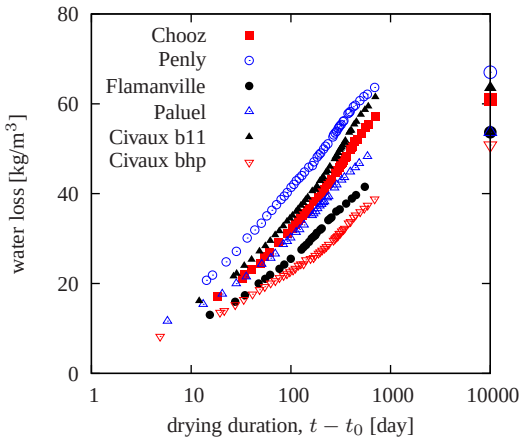

Figure 8.39: Experimentally measured water loss (Granger's data) and the updated ultimate value (represented by points at 10,000 days) using bilinear isotherm, only cement and silica fume are considered as cementitious materials in (8.6), $\eta = 1.0$ in (8.8) and the water content assigned to large pores is computed as $0.035 \times w$.

31.7 kg/m^3. The slope of the desorption isotherm can be computed as $0.9 \times (164.4 - 31.7) = 106$ kg/m^3 and the amount of evaporable water at $h_{\text{env}} = 0.5$ is $0.5 \times 106 \times (164.4 - 31.7) + 31.7 + 15 = 99.6$ kg/m^3

The input parameters are summarized in Tables 8.4 and 8.5, the results are shown in Figs. 8.40 and 8.41.

In the analysis of moisture transport, the problem appears right away. Künzel's model is not capable of simulation in the region above free saturation. If the total amount of evaporable water 164 kg/m^3 is assigned to the free saturation water content w_f, the drying process is with the normal values of material parameters too slow compared to the experimental data, see the red curve in Fig. 8.40.

In the experiment, the concrete loses already 20 kg/m^3 after one day of drying. Most of this amount is the water which soaked into the concrete during the water bath and occupies the large pores where it is not strongly bound and can easily leak out. For this reason, in the following simulations the amount of absorbed water 15 kg/m^3 is subtracted from the experimental data and in the presented plots this value is added to the computed values.

In the following simulations the sorption isotherms are constructed such that the total water loss (from $h = 1.0$ to $h = 0.5$) is 95 kg/m^3 which is equal to the 1.02 multiple of the experimentally measured value.

For this concrete the experimentally measured content of evaporable water (by oven-drying) was 142 kg/m^3, in the previous Section the "real" total content of evaporable was found to be 1.2 multiple of the measured value, which makes approx 170.5 kg/m^3. For this reason in the parameter sets #3 and #5 the water content is set to a higher value.

Similarly to the findings in Section 8.6.1, the straighter the isotherm and the higher its slope, the better the agreement of the MPS model with the measured shrinkage data.

Figures 8.42, 8.43 and 8.44 show the comparison between the measured and the computed values of the total (oven-drying) or partial (drying at 50% h_{env}) amount of evaporable water. In these figures, the experimentally measured ultimate values of water loss determined by oven-drying were multiplied by 1.25, the values measured by drying at 50% h_{env} by 1.02. The water

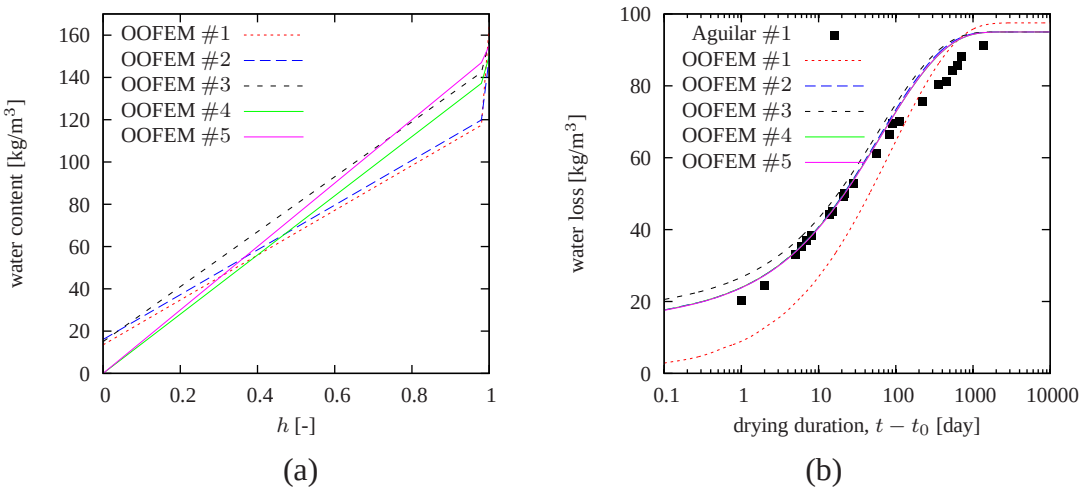

Figure 8.40: (a) Alternatives of the desorption isotherm used in simulations, (b) comparison of the Aguilar's experimental data with numerical simulations in OOFEM: water loss in time.

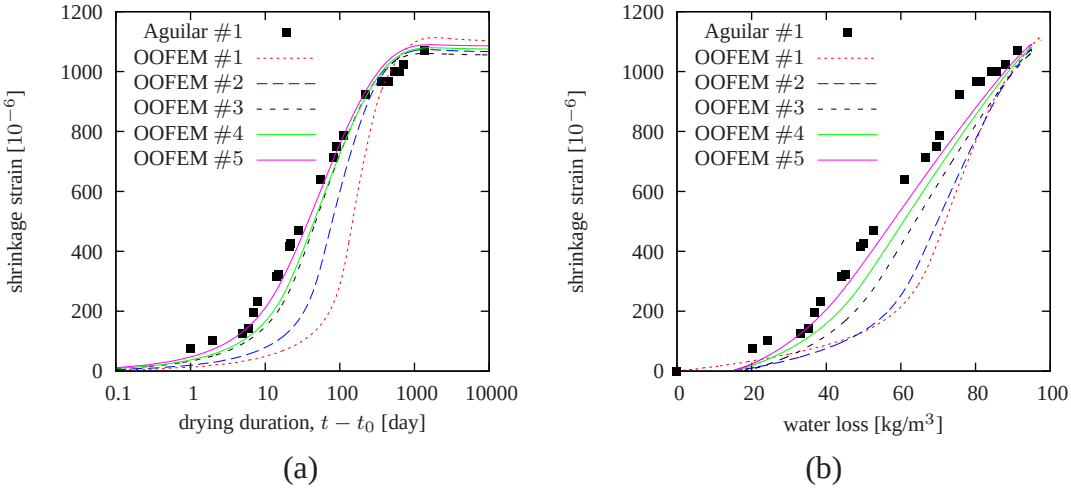

Figure 8.41: Comparison of Aguilar's experimental data with numerical simulations in OOFEM (a) shrinkage strain in time, (b) shrinkage strain vs. water loss.

in larger pores is computed as $0.035 \times w$ and the chemically bound water as $0.13 \times c$. The desorption isotherm is in all cases bilinear and the intersection with the vertical axis is at the origin ($\eta = 1$). The results are qualitatively comparable with those in Figures 8.26 8.29 and 8.28 which were computed with different input parameters.

8.6.3 Conclusions: FE simulations in OOFEM

The finite element simulations in program OOFEM have revealed that the experimentally measured water loss data can be fitted with almost any isotherm provided that the difference between the moisture content at free saturation w_f and the content $w(h_{\text{env}})$ matches the asymptotic value of moisture loss. However, the shape of the desorption isotherm drastically influences the development of relative humidity which is the driving force of shrinkage. Highly nonlinear isotherms led to significant delay in the computed evolution of shrinkage compared to the experiment. In

Table 8.4: Summary of the input material parameters: diffusion

		OOFEM #1	OOFEM #2	OOFEM #3	OOFEM #4	OOFEM #5
$w(0)$	[kg·m^{-3}]	13.5	16	15	0	0
k	[kg·m^{-3}]	106	106	130	140	150
w_f	[kg·m^{-3}]	164	149 (+15)	157 (+18)	150 (+15)	155 (+15)
μ	[-]	500	500	500	500	500
A	[kg·m^{-2} day$^{-0.5}$]	0.5	0.5	0.5	0.5	0.5

Table 8.5: Summary of the input material parameters: MPS

		OOFEM #1	OOFEM #2	OOFEM #3	OOFEM #4	OOFEM #5
k_{sh}	[-]	0.0032	0.0027	0.0025	0.0025	0.0025

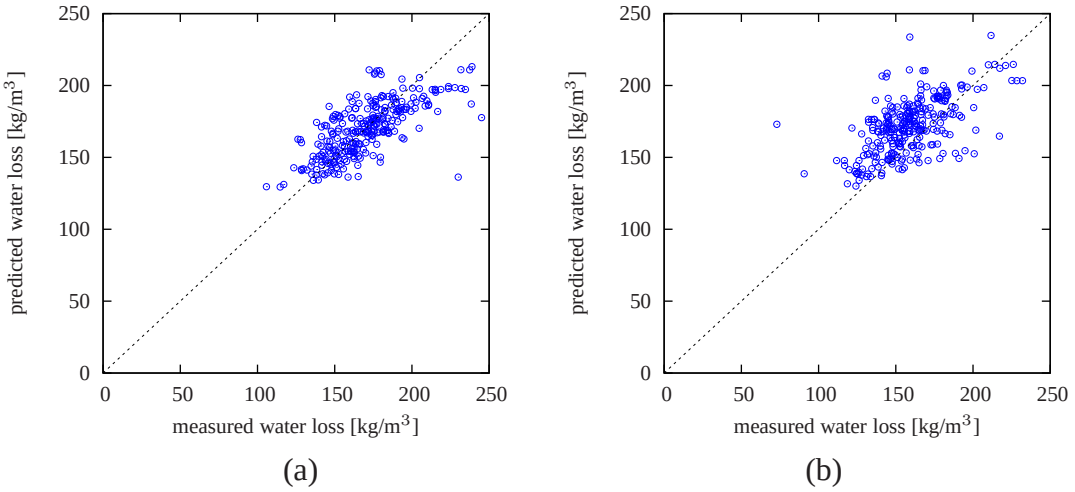

Figure 8.42: Comparison of the measured and computed amount of evaporable water lost by oven drying for specimens with the edge length (a) 100 mm, (b) 75 mm ($\alpha_c = 0.13$, $k_w = 0.035$, $\eta = 1.0$, $k_{oven} = 1.25$).

order to match the shrinkage data, the desorption isotherm had to be almost straight.

The slope of the desorption isotherm (moisture capacity) identified in simulations of Aguilar's data is very steep; the average is 149 kg/m^3, which is far above the typical value 100 kg/m^3.

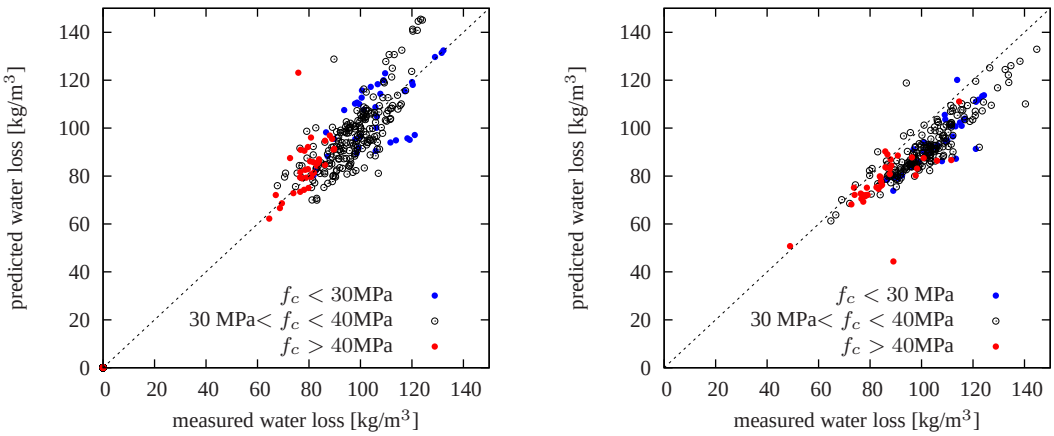

Figure 8.43: Comparison of the measured amount of evaporable water lost by drying at $h_{\mathrm{env}} = 50\%$ and the amount computed based on the oven-drying experiment for specimens with the edge length (a) 100 mm, (b) 75 mm ($\alpha_c = 0.13$, $k_w = 0.035$, $\eta = 1.0$, $k_{oven} = 1.25$).

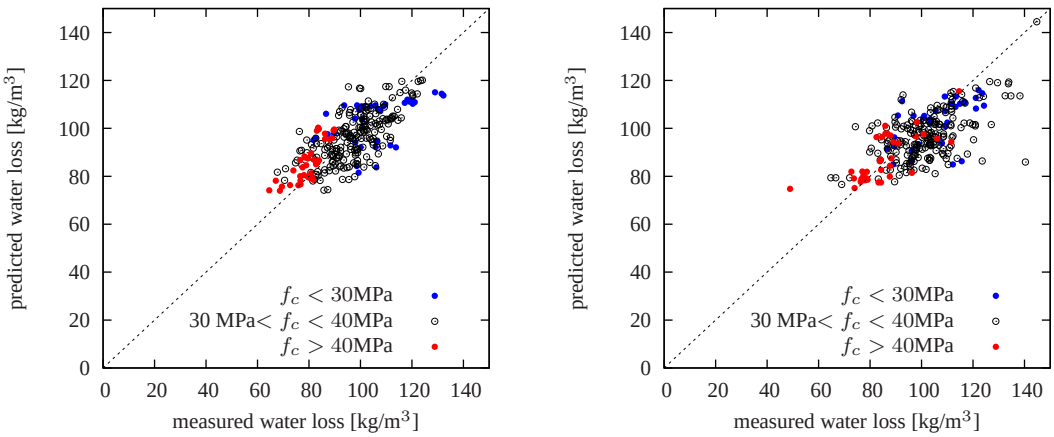

Figure 8.44: Comparison of the measured amount of evaporable water lost by drying at $h_{\mathrm{env}} = 50\%$ and the amount computed based on concrete composition for specimens with the edge length (a) 100 mm, (b) 75 mm ($\alpha_c = 0.13$, $k_w = 0.035$, $\eta = 1.0$, $k_{oven} = 1.25$).

8.7 Concluding recommendations

- The original function for water loss (8.17) should be replaced with a more complex one (8.18) combining the fast and slow processes, this is inevitable for specimens stored underwater or moist cured. However, it should be used also for sealed samples.
- The shrinkage function (8.20) should be replaced with (8.21) which does not end so suddenly. This could not be analyzed from Granger's experiment because it terminated too early. The optimum value of exponents p_{sh} and q_{sh} is bigger than 0.5.
- The ratio between the drying halftime and shrinkage halftime does not exhibit a uniform trend.
- The predicted shrinkage magnitude based on concrete composition should be preserved and changed only when necessary. The originally recommended methodology can improve as well as deteriorate the blind prediction.
- The dependence of shrinkage on moisture loss is far from linear, more suitable is a "S"-shaped curve having three distinct parts:
  - substantial moisture loss and minor shrinkage strain - this part corresponds to emptying of large capillary pores
  - approximately linear relationship between shrinkage and moisture loss
  - very slow moisture loss leading to almost no shrinkage strain
- The experimental data were successfully fitted in the finite element calculations exploiting MPS and Künzel's models. In the MPS model, the highly nonlinear desorption isotherm leads to considerable time delay of shrinkage behind the experimental data. To eliminate this delay, the isotherm needs to be adjusted, preserving the ultimate amount of water loss at given relative humidity. However, such isotherm is almost linear and its slope is very steep.
- Clearer conclusions can be made if the following conditions are met
  - the specimens are sealed during curing and absolutely no water is added
  - more specimens with different sizes are created from the same concrete mixture
  - the specimens are crushed and oven-dried at the end of an experiment
  - the desorption isotherm is experimentally measured

9 Application

This chapter presents one real-world application of the Microprestress-solidification theory and of Künzel's model for moisture transport.

The studied structure is a floor made of reinforced concrete cast on a foundation slab; it is located in the new laboratory hall of the UCEEB (University Centre for Energy Efficient Buildings) in Buštěhrad, Czech Republic.

The slab is 100 mm thick and is reinforced with two layers of the welded reinforcing mesh ⌀6/100/100 mm. The thickness of the top concrete cover is 30 mm and the bottom 15 mm. In order to prevent random shrinkage cracks, the top half of the slab was cut at the age of 4 days. The distance between the cuts is in the examined part between 2.8 and 3.8 meters. The floor is separated from the foundation slab with a plastic foil.

It was expected that the asymmetric drying (from the top surface only, the bottom is assumed to be perfectly sealed) would lead to warping (curling). Due to the non-uniform shrinkage (over the thickness) the edges and corners of the cut segments would rise. If the self-weight was neglected the curvature would be constant, for this reason the vertical deflection should grow with the square of the distance from the center of the segment.

The question was what should be the optimum spacing of the cuts. The longer the distance between the cuts the bigger can be the deflection. A heavy load placed on the corner of the lifted slab could cause cracks in the top surface. On the other hand, more cuts cost more money (after 3 months the cuts are filled with silicone sealing) and reduce the durability.

9.1 Experimental setup

The preliminary FE computations which studied only the symmetric quarter of the slab without the self-weight, the maximum deflection of the 3×3 meters slab was estimated as 4–9 mm after 50–150 days of drying depending on the input parameters. Due to the big differences it was decided that the evolution of the deflections of the newly made floor would be recorded and the FE model would be recalibrated to get more experience and to be able to predict the behavior of slabs with different dimensions. The recorded deflections would be supplemented with the shrinkage and water loss measurements on specimens made of the identical concrete mixture (same batch).

9.1.1 Concrete mixture specifications, floor fabrication

The design recipe of the concrete mixture contained 340 kg/m^3 of cement (CEM II/A-M - 42.5 Čížkovice), max 178 kg/m^3 of water, 840 kg/m^3 of fine aggregates 0–4 mm (Černuc, natural aggregates), 190 kg/m^3 of coarse aggregates 4–8 mm (Zlosyň, natural crushed aggregates), 190 kg/m^3 of coarse aggregates 8–16 mm (Černuc, natural crushed aggregates). The resulting water-to-cement ratio was 0.52 and aggregates-to-cement ratio 5.28. During concreting the composition was found unsuitable and the biggest aggregates 8/16 were removed and replaced with the finer fraction of the aggregates 4/8. Some of the concrete physical properties were tested but so far the results have not been provided to the present author despite numerous promises.

The concrete floor was cast on November 28$^{\text{th}}$, 2013. Owing to the high water-to-cement ratio, the size of the maximum aggregates and superplasticizer, the concrete mixture was very

liquid. After the initial set, the surface was smoothed down making it very compact and glossy.

No curing was used. During concreting the temperature could be around $5°C$.

After 4 days the floor was cut with a circular saw, the depth of the cut was half of the thickness (50 mm). A very simplified diagram of the cut pattern is shown in Fig. 9.4. Approximately 3 months after casting the cuts were filled with silicone sealing and the surface was penetrated.

The temperature and relative humidity was measured only at 2 to 14-day intervals. The measurements for the first 75 days are shown in Fig.9.1, then the thermo and hygrometer was stolen. Afterwards the relative humidity is assumed to be constant - 50% (end of the heating period).

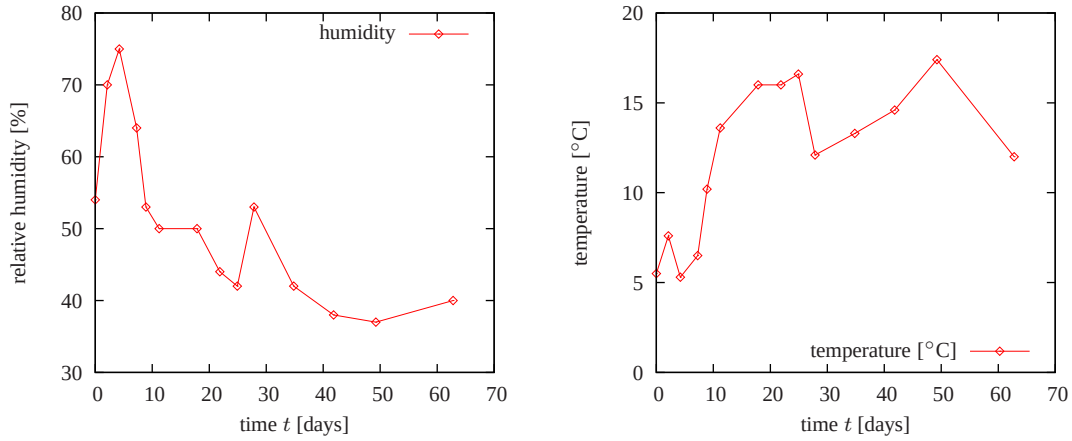

(a) (b)

Figure 9.1: Recorded evolution of (a) relative humidity and (b) temperature. Time $t = 0$ corresponds to December 5th 2013.

9.1.2 Measurements of vertical deflections

The red-drawn portion of the slab in Fig. 9.4 was selected for the measurements of the vertical deflections. One of the reasons was its advantageous position - it is in the corner of the laboratory and no separating walls or heavy equipment were to be placed there in the following months. It is also one of the largest slabs in the whole laboratory.

The vertical deflections were measured at four corners of the slab (points 1, 2, 3, 4) relatively with respect to the center S. The round-headed bolts were used for the measuring points, they were glued into the holes drilled 10 cm from the edges. This distance could not be smaller because of the risk that the corner spalls off during drilling; the concrete was young at that time.

The vertical deflections were determined using the very precise leveling method (accuracy 0.01 mm). Zero reading was done on December 5^{th} 2013, the last one on April 4^{th} 2013. The results are shown in Fig.9.2. The highest value exhibits the point #2, the smallest value point #4 which is in the corner of the room. The deflections of the points #1 and #3 are almost equal and coincide with the average deflection of all four points.

The highest average deflection was recorded on April 3^{rd}, 98 days after casting; in the last reading the deflection decreased.

Despite the promises, the floor slab was loaded many times. Probably the biggest load that occurred couple of times was by the high-lift truck (approximately 1.5 ton weight).

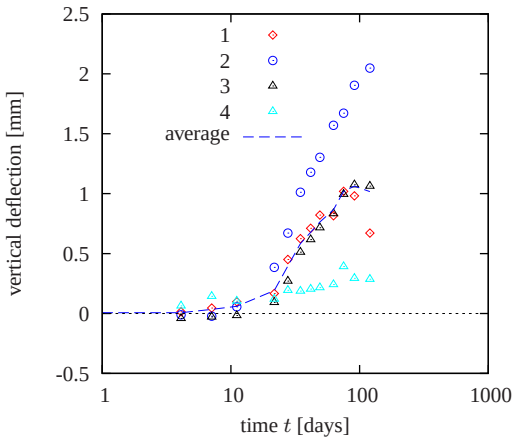

Figure 9.2: Measured vertical deflections of the concrete floor. Time $t = 0$ corresponds to December 5^{th} 2013.

9.1.3 Measurements of shrinkage and water loss

The measurement of shrinkage and water loss was carried out in order to inversely identify some basic material properties which can supplement the FE simulation of the drying concrete slab.

For this reason all the specimens were cast from the same batch as the floor and afterwards were stored in the same conditions (stored approximately 1 m next to the selected floor segment) as the floor except for the first week. The concrete floor was exposed to drying right after casting. In order not to miss the initial part of shrinkage or water loss while the specimens were still in mold or unprepared, it was attempted to keep them sealed as long as possible.

The specimens were designed such that the inverse analysis was as simple as possible; in this case the drying was intended to be unidirectional.

The shrinkage measurement was carried out on prismatic specimens fabricated from the same batch of concrete as the laboratory floor. Four different sets of three specimens were prepared. One set was intended for the measurement of autogenous shrinkage, the remaining three of different dimensions for drying shrinkage. The length of the specimens was approximately 900 mm, height 100 mm and thickness 52 mm (S), 76 mm (M) and 103 mm (L). On average, the displacements were measured over the length 770 mm.

The specimens for water-loss (weight loss) measurements were cast into the circular polythene tubes with inner diameter 100 mm. Again, three different sizes (heights) were prepared: 54 mm (S), 79 mm (M) and 101 mm (L).

All specimens were cast on November 28^{th} and covered with a plastic foil to prevent water loss from evaporation.

The prismatic specimens were demolded on December 2^{nd} and right after that were sealed with epoxy and one layer of glass fabric. The specimens for measuring the autogenous shrinkage were coated from all sides, the remaining 3 sets were sealed from four sides only, keeping the two lateral surfaces (with different mutual distance) uncovered. The cylindrical specimens were kept in mold (PE tube) throughout the experiment. The prismatic specimens were equipped with gages and the first reading was done on December 5^{th}.

The cylindrical specimens were stored horizontally (bases of the cylinder were vertical),

making the the effective drying length half of the specimen height. The weight was measured with a digital scale with the precision of 1 gram and maximum loading 5 kg.

The shrinkage strain was computed as the measured displacement divided by the gage length. The displacement was measured with the old-fashioned mechanical gages with 10 μm precision. The gages were attached to a circular steel rod (8 mm diameter) passing through the holes in a steel beam which was placed into a mold before concreting. Every specimen was equipped with two gages, one on each side (to eliminate the error from bending).

It must be noted that even though the place was called a laboratory hall, during the whole experiment it was still a construction site. Naturally, it was essential to have the specimens and the measuring method as robust as possible. Despite of that several gages were destroyed during unauthorized manipulation.

On February 6$^{\text{th}}$ one cylinder from each set was removed from the tube and was placed in the oven to dry at 105°C. After 6 days of drying the weight loss stopped evolving. Anyway, the measurement continued for additional 2 weeks.

Some photographs with brief commentary are presented in Appendix D.1.

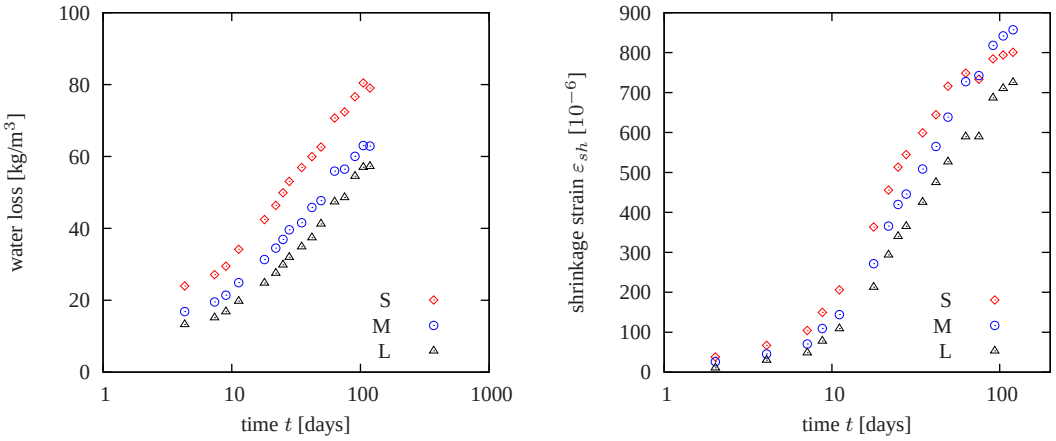

Figure 9.3: Recorded evolution of (a) water content and (b) shrinkage on small, medium and large sample. Time $t = 0$ corresponds to December 5th 2013.

9.2 Finite element simulations

9.2.1 Water loss & shrinkage

Before calculating the structural response of the drying floor slab, it was necessary to approach the calibration of the material parameters of the diffusion and the MPS model. As presented earlier, the material model based on the approach of Bažand and Najjar (Section 5.2) does not correctly capture the moisture loss of the young concrete since this concrete contains a bigger amount of free water which is lost rapidly. This cannot be realistically described with a linear isotherm which might be suitable for a mature concrete. For this reason all the presented simulations use the modified material model (moisture transport only, constant temperature is prescribed) based on Künzel, see Section 5.4.

Figure 9.4: Schematic representation of the laboratory floor geometry. Dimensions are in meters. The deflections were measured at points 1–4 and S. The 3D FE simulation modeled the upper right (red marked) portion of the slab. Vertical deflection in the 2D and 3D model was unified in the location labeled C.

The FE models for moisture loss consisted of one row of linear quadrilaterals, the mesh was denser near the drying surfaces (bases of the cylinder) and coarser in the core. The length of the FE mesh corresponded to the actual size of the experimental specimens. This problem was not solved in the staggered scheme because there was no need for the structural response.

The experimentally measured shrinkage data indicate that the properties of the sealing are not perfect. After approximately 10 days even the totally "sealed" specimen intended for the measurements of the autogenous shrinkage (and as a reference for the temperature compensation) started shrinking. After 100 days the measured strain was more than half of the drying shrinkage measured on the other specimens.

This resulted in changes in the FE models for the simulation of shrinkage which was originally planned to be only in 2D. All the models represented a symmetrical 1/4 of the cross-section. The model was 1 element thick (in the axial direction of the specimen) and again, towards the drying surfaces (or partially sealed), the finite element mesh was finer. The mesh for the diffusion was finer and more graded compared to the mesh for the structural analysis which was more uniform.

In the transport analysis, two different boundary conditions were used: one for the "normal" drying surface and the other for the "sealed" drying surface; both conditions were of the same type - the mixed condition relating the flux to the difference between h and h_{env}, see (5.18). In the axial direction of the beam the FE model was kept sealed.

In the structural analysis, the degrees of freedom normal to the planes of symmetry were constrained. The degrees of freedom normal to one of the surfaces representing the face of the cross-section were also constrained, on the opposite surface the master-slave condition was employed.

9.2.2 Water loss & shrinkage: calibration of material parameters

The material parameters were calibrated at the same time for both experiments. Similarly to the conclusions from Section 8, it was found that there exists a variety of combinations which give a reasonable agreement with the experimentally measured data of water loss. The main influencing factor is the shape of the sorption isotherm. A bilinear isotherm was used in all calculations. If the slope of the isotherm significantly differs from linear, the MPS model would give a considerable delay of shrinkage behind the experimental data.

The first measurement of both water loss and shrinkage was done approximately at the same time, at the age of 7 days. However, the drying of the specimens began at different times.

Until the first reading, the specimens for the measurement of the water loss were covered with a plastic foil. The sealing was not perfect, so the first experimental points are placed at $t - t_0 = 0.1$ day.

The situation with the shrinkage experiments is more complicated, the specimens were kept in mold for 4 days, the top surface was covered with a plastic foil, but again, the sealing was not perfect. Afterwards, the specimens were demolded and during approximately 8 hours the designated surfaces were sealed with epoxy. The specimens were instrumented after additional 3 days of drying. Therefore the FE analysis began at the age of 4 days but the first experimental data are placed at $t - t_0 = 3$ days.

The following boundary conditions were applied for the shrinkage specimens: during the first 8 hours of simulation the specimens were drying from all sides, after that the parameters were changed on the sealed surfaces.

The following values of the material parameters were used in the moisture transport analysis. The bilinear desorption isotherm shown in Fig. 9.5 is defined by $w(0) = 5$ kg·m^{-3}, the slope $k = 140$ kg·m^{-3} and the free water saturation $w_f = 160$ kg m^{-3}, the slope breaks at $h = 0.98$. The similar values of the Künzels model were used: the water vapor diffusion resistance $\mu = 400$ and the water absorption coefficient $A = 0.75$ kg·m^{-2} day$^{-0.5}$. On the exposed surfaces the surface factor was set to 10 kg/(m^2·day) and on the sealed surfaces to 0.03 kg/(m^2·day). The latter value was identified from the shrinkage evolution of the fully sealed specimen. The outer relative humidity h_{env} was prescribed accordingly to the measured values and after the theft the 50% relative humidity was assumed. As mentioned before, the temperature variations were not taken into account.

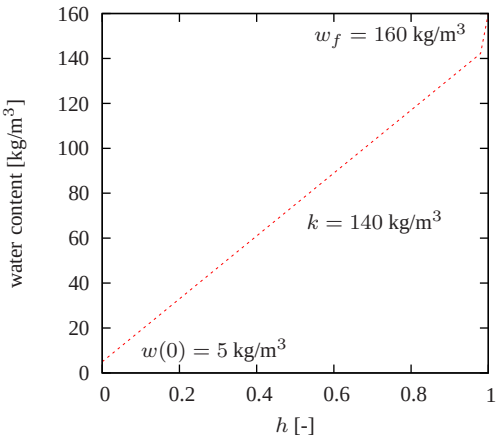

Figure 9.5: Sorption isotherm used in the FE simulation.

The structural analysis used the modified MPS model with no size effect on drying creep ($\tilde{p} = 1$); similarly to previous Chapter, the rate of the shrinkage strain ε_{sh} at the material point level is assumed to be proportional to the rate of relative humidity.

The basic-creep parameters q_1–q_4 were estimated (similarly to the previous sections) using the empirical formulae of the B3 model. The compressive strength was assumed to be $f_{cm} = 30$ MPa (high cement content but total absence of curing). The following values were used: $q_1 = 23.145$, $q_2 = 160.118$, $q_3 = 3.474$, $q_4 = 6.334$ all in 10^{-6}/MPa. The simulations of Bryant's experiment have revealed that the particular values of the tensile strength and fracture energy do not influence the results of the unloaded specimens subjected to drying, tensile strength f_t was set to 2.5 MPa and the fracture energy G_f to 100 N/m. The shrinkage is described with $k_{sh} = 0.0025$ and the drying creep with $k_3 = 50$. All other parameters (α_s, α_r, α_e) were set to their default values.

The results of the fitting are shown in Fig. 9.6 for water loss and in Fig. 9.7 for shrinkage. Not having the zero readings at the onset of drying, the experimental data were vertically shifted to match the simulations. The agreement with the experimental data is deemed to be very good in both cases. The average value of the moisture loss measured by oven drying was 160 kg/m^3; the results approach the value of 85 kg/m^3 which was computed as $160 - 15 - 0.5 \times 140$ where 15 is the moisture content of the isotherm above 98% relative humidity and 140 is the moisture capacity. Figure 9.6 suggests that the aggregates contained a considerable amount of water because $178 - 160 = 18$ kg/m^3 would correspond only to 5% of the cement weight.

The computed asymptotic value of shrinkage of the "sealed" specimen in Fig. 9.7 is higher

than the ultimate shrinkage of the drying specimens. This can be explained by the distribution of the relative humidity over the cross-section which is, compared to the other cases, more uniform. More uniform distribution of the relative humidity results in more uniform shrinkage eigenstrains and consequently in smaller magnitude of the self-equilibrated normal stresses, smaller relaxation and higher shrinkage.

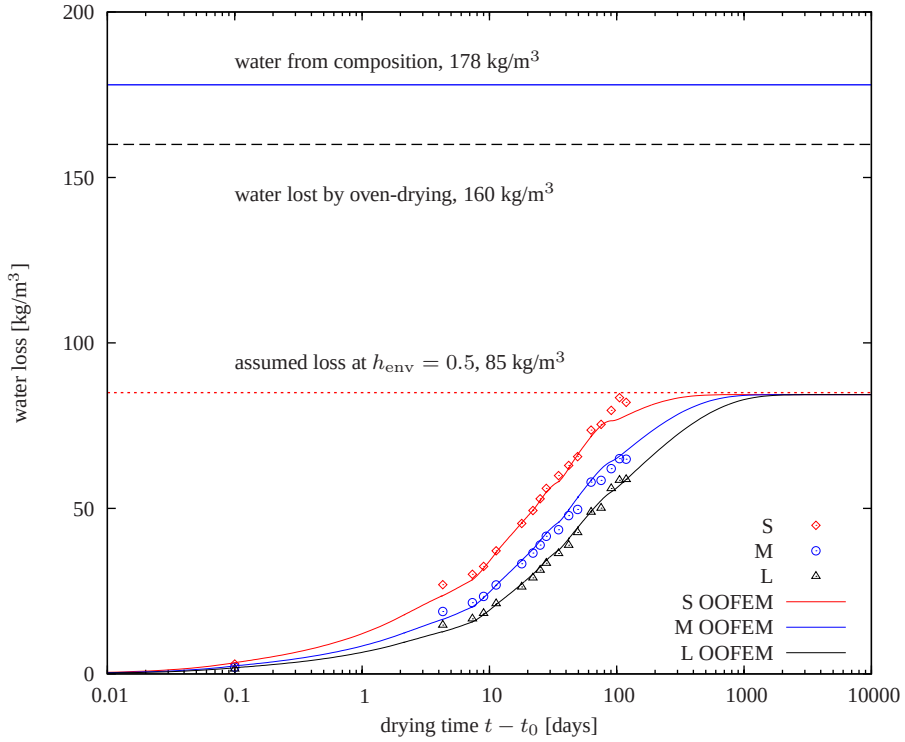

Figure 9.6: Comparison of the results obtained from FE simulations with the experimentally measured water loss. The drying began on December 5th. Labels “S”, “M” and “L” refer to specimen size.

9.2.3 2D model

Having the material parameters calibrated on the water-loss and shrinkage experiments, it is possible to approach the simulation of the drying floor slab.

The analysis starts with a simplified 2D model representing a section parallel to the cuts. In Fig. 9.4 it begins at point S and then it goes in the direction of point “C” until the edge. Point “C” is 100 mm from the edge. The length of the modelled slab is 1.5 m (average between 1.4 and 1.6 m).

The computational FE model for the structural analysis is shown in Fig. 9.8, the model consists of 180×12 plane stress elements, 360 truss elements and 181 contact 1D elements. The model for transport was composed of 50 quadrilateral elements ordered in a row; the problem could have been equivalently solved using 1D transport elements, 2D analysis was employed only to properly export the field of relative humidity.

The results (of the staggered analysis) were compared to the analysis run on a finer mesh and were found to be almost identical.

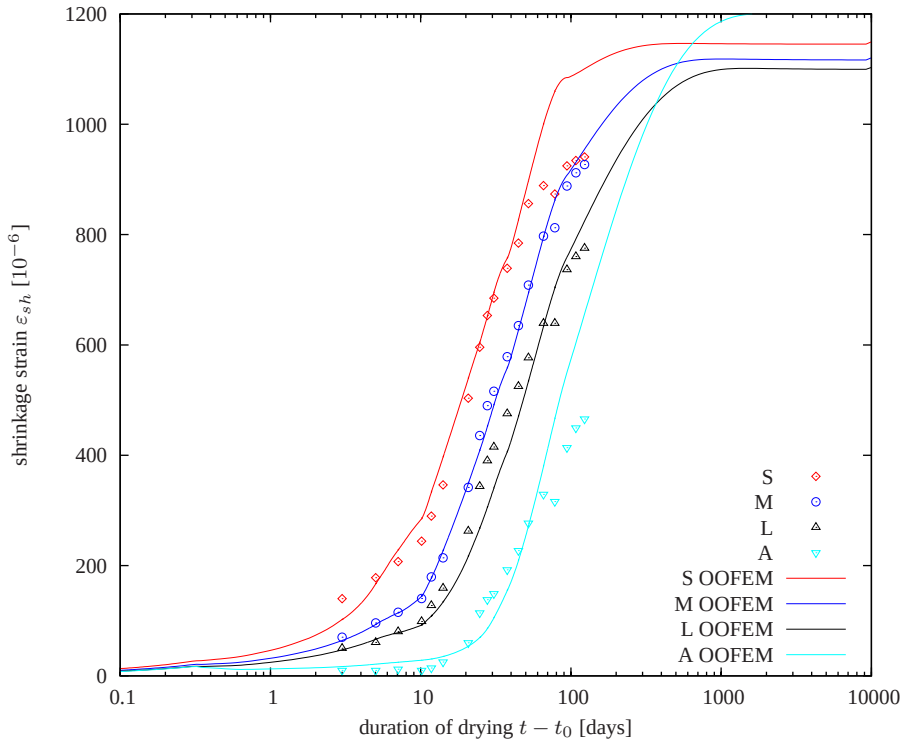

Figure 9.7: Comparison of the results obtained from FE simulations with the experimentally measured shrinkage strain. The drying began on December 2th. Labels “S”, “M” and “L” refer to specimens size, label “A” to specimen intended for the measurement of autogenous shrinkage.

The plane-stress idealization is in this case somewhat questionable. The real problem lies somewhere between plane strain and plane stress. Considering the application and restrictions of the isotropic damage model, plane stress is more suitable. (In the plane-strain configuration, the out-of plane stresses would cause a smeared damage in the whole slab and no localization could occur.)

Figure 9.4 shows the schematic description of the reference computational model labeled “A”. On the left edge (axis of symmetry), the horizontal degrees of freedom are restrained, on the lower half of the right edge the nodes share the same horizontal displacement (master-slave approach). The nodes on the lower edge are linked to the fully constrained nodes using 1-D contact elements transmitting only compression and having zero tensile stiffness. In this reference case, the reinforcing bars (2-D truss elements) are linked directly to the mesh nodes.

Regarding the material parameters, all values except for the tensile strength and fracture energy were taken from the previous section. In the simulations the tensile strength f_t was reduced to 1.5 MPa and the fracture energy G_f to 60 N/m. This should reflect the lower maturity of the material (the slab was not cured while the experimental specimens were at least sealed with a plastic foil) and the inevitable effects of the 1.5 ton vehicle and other live loads which are not considered in the analysis. It was also assumed that the perpendicular reinforcing bars act as a source of strain localization, to take this into account, both the tensile strength and fracture energy was reduced to one half in the finite elements 100 mm apart and approximately 35 mm from the top surface.

The behavior and the results of the numerical simulations are extremely sensitive to the

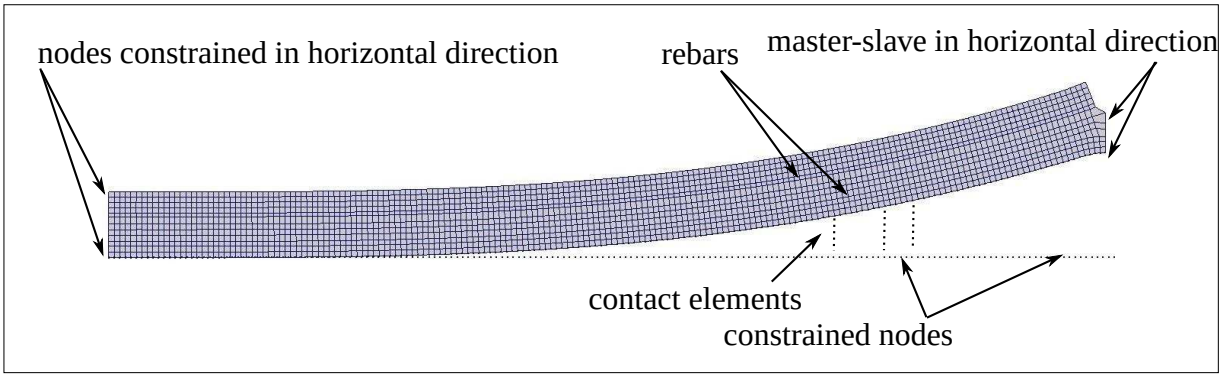

Figure 9.8: Deformed FE mesh of the 2D problem with 2534 nodes, 2160 plane-stress elements, 360 truss elements, 181 contact 1D elements.

choice of the boundary conditions. The comparison of the deflection at point "C" obtained with different versions of the computational model is shown in Fig. 9.9. The values of the material parameters for the moisture transfer as well as for the structural analysis were the same.

The following versions are presented:
"**A**" = reference case described above
"**B**" = "A", no body load
"**C**" = "A", the right edge is horizontally fully constrained
"**D**" = "C", bond-slip law between the reinforcement and concrete
"**E**","**E2**" = "A", force-displacement constitutive law on the right edge simulating friction forces.

From the presented cases, the biggest deflection (approximately 8.5 mm) was obtained in variant "C" which has horizontally restrained displacements on the right edge. The origin of such a high deflection is the very high axial force due to shrinkage and the asymmetric cut. The next attempt to reduce the deflection consisted in prescribing the bond-slip material law between the reinforcing bars and concrete. The simplified fib model (not taking into account the lateral stress) with the typical values for concrete was used. In this variant ("D") the deflection dropped to approximately 3 mm but it is still too much compared to the measurements. The most realistic models are probably the variants "A" (reference) and "E", "E2" where the vertical deflection is less than 1 mm. In these alternatives, the additional bond between the reinforcement and concrete does not make any difference.

The points in this figure represent the experimental measurements scaled by a ratio that was identified from the 3D analysis presented the in next Section. The measured deflections of the points 1, 2, 3 and 4 were scaled to 1/2, 1/3, 1/2 and 1, successively.

Some figures from the post-processing in program Paraview are shown in Appendix D.2.

Although the slab is loaded by its dead weight, the creep does not play a significant role in the time evolution of vertical deflection; the key aspect is the development of relative humidity and the relationship between relative humidity and shrinkage.

9.2.4 3D model

The experimentally measured vertical deflections at points 1–4 exhibit big differences although the distance from the center of the slab is the same. The deflections at points 1 and 3 are almost identical and they are very similar to the average deflection at points 2 and 4. It almost seems as

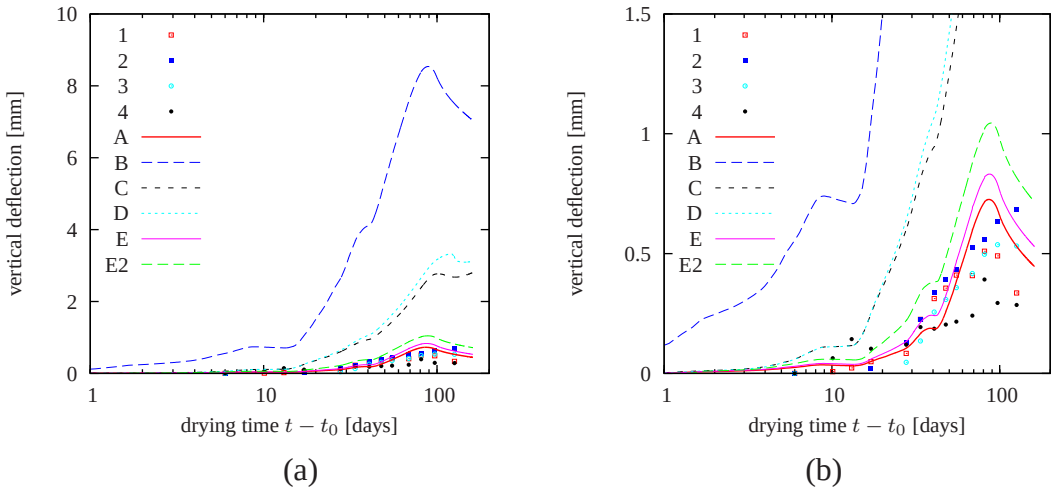

Figure 9.9: Vertical deflection at point "C" computed with different boundary conditions in 2D FE analysis, (a) deflections in range 0–10 mm, (b) detail; the points represent scaled experimentally measured deflections. The drying began on November 29th.

if the examined floor slab was tilted sideways. A 3D finite element model was created to clarify this assumption.

The model for the structural analysis is shown in Fig. 9.2.4, it represents the examined floor slab together with the side segments which are more narrow.

The model consists of more than 100.000 elements (114×120×5 layers, horizontal edge length is 33 mm). In order to save the computational time, the viscoelastic material without damage was used in some regions.

The boundary conditions are very similar to the setup in the reference 2D simulation. The right and the back (not visible) lateral surfaces in Fig. 9.2.4 are completely unconstrained, the nodes on the lower portion of the left and the front surfaces have constrained displacement normal to this surface (symmetry idealization).

The material properties are the same as in the previous section. The comparison of the results with the experimental data is shown in Figure 9.11. The amplitudes of the computed results approximately match the amplitude of the measured deflections but the time development is different. The vertical deflection at points 1, 3 and 4 is diminished by the weight of the side elements. The behavior is illustrated in the figures in Appendix D.2.

In the 3D FE simulation, the deflection starts growing after approximately 50 days of drying – not only too late compared to the experiments but also compared to 2D simulation. The absolute mesh size is not the source of problems, the 2D problem has been run with the same mesh size (5 layers of 45 elements, horizontal edge length 33 mm) and the results almost did not change. The problem apparently origins in the contact elements on the lower surface of the slab. In the analysis the slab is initially held and afterwards springs up, although the solution is converged. To make use of the 3D analysis which realistically describes the proportions of the deflections, the computed deflections at points 1–4 are related to the computed deflection at point C, as shown in Fig. 9.11b. After 50 days the ratio between the deflections is approximately 2:1 for points #1 and #3, 3:1 for point #2 and 1:1 for point #4.

Figure 9.12 shows the comparison of the measured and computed deflections. In this figure the computed deflections are taken from the 2D simulation and scaled according to the presented

ratios. Even now the computed deflection is lagging behind the experiments.

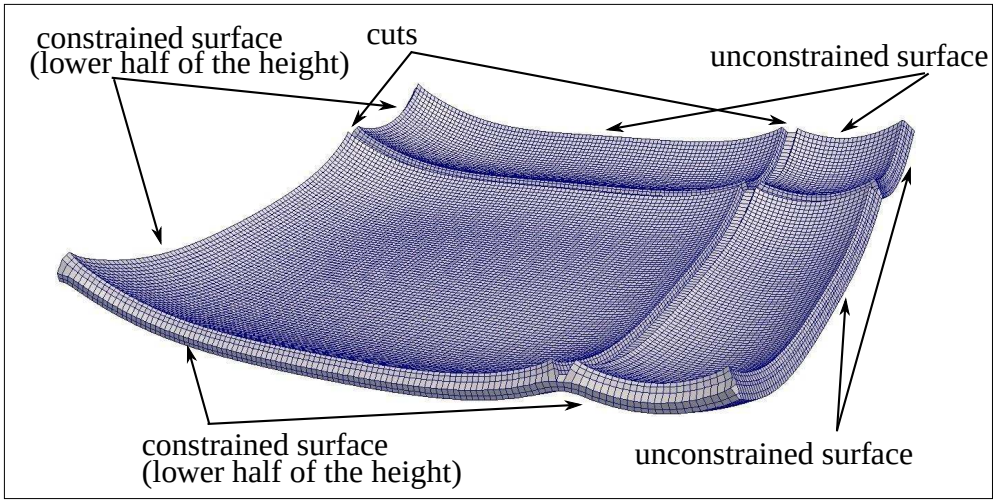

Figure 9.10: Deformed FE mesh of the 3D problem. In the horizontal direction the mesh size is uniform, $120 \times 114 \times 5$ volume elements, 97405 nodes and 100555 elements.

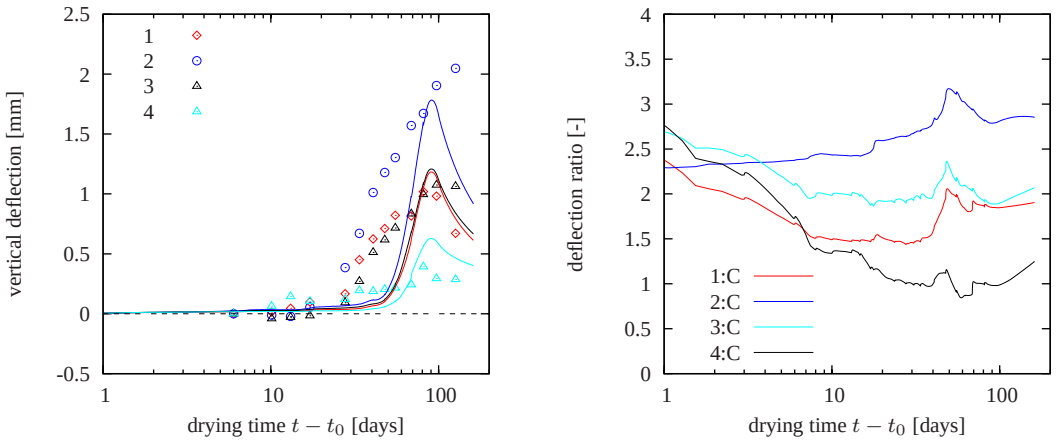

(a) (b)

Figure 9.11: (a) the experimentally measured deflections and the computed values from the 3D FE analysis, (b) ratios of the vertical deflections computed employing the 3D FE model. The location of point "C" is indicated in Fig. 9.4. The drying began on November 29th.

9.3 Conclusion

The presented example confirms the following conclusions drawn in the previous sections.

- Künzel's model can realistically describe the time evolution of water loss, however, the sorption isotherm giving very similar results is not unique.
- The MPS model can accurately describe shrinkage of the laboratory specimens, although the sorption isotherm has a unrealistically steep slope.

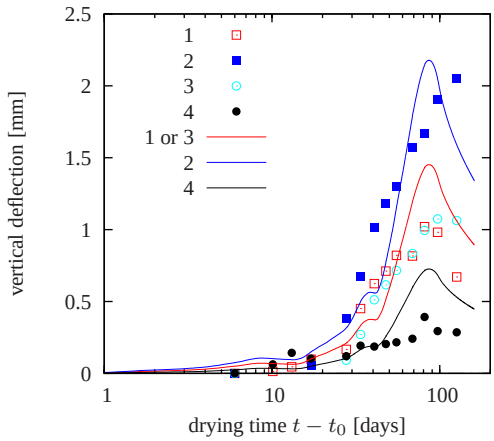

Figure 9.12: Comparison of the experimentally measured deflections with the scaled deflection from the 2D analysis. The drying began on November 29th.

- The FE simulations show a good agreement between the experimental and the numerical size effect on shrinkage and water loss.
- The results of the deflecting slab are too delayed behind the experiment. One of the possible reasons is the incorrect (linear) relationship between the shrinkage and humidity rate.

10 Summary and further work

The first part of this thesis provides a brief summary of the time-dependent processes specific for concrete. The attention is paid to concrete creep and shrinkage under variable temperature and humidity conditions. This behavior is documented by several examples (experimental results) found in the literature.

Solidification theory for basic creep of concrete and its extension for variable humidity and temperature called Microprestress-solidification (MPS) theory are introduced in Chapter 4. Both theories are physically based and are intended for the material point approach. It is shown that the microprestress can be completely eliminated from the formulation and that the governing equation can be formulated in terms of viscosity. The resulting model is still fully equivalent to the original one, but its structure becomes simplified, and the role of the model parameters becomes more transparent. Another benefit is the reduction of the number of independent model parameters.

The material model based on these theories has been successfully implemented into the OOFEM finite element package, and has been used in simulations of concrete creep at variable temperature and humidity. In Chapter 6, the classical experimental data from the literature have been compared with the results of the numerical simulations. These data comprised concrete creep at constant elevated and monotonically increasing temperature, creep of mortar at cyclic temperature (+drying), and a thorough study on concrete creep at drying and shrinkage at room temperature. The originally proposed microprestress-solidification theory has been found unsuitable for modeling of drying creep and shrinkage under general conditions. Several severe deficiencies of this model have been identified. Compared to the experiments, the original formulation of the MPS model exhibits the opposite size effect on drying creep, spurious sensitivity to the particular choice of relative humidity and excessive compliance during the repeated cycles of temperature and relative humidity.

Chapter 7 presents several modifications of the MPS material model, which have been introduced in order to overcome the above-mentioned deficiencies. Excessive sensitivity to the specific choice of relative humidity has been eliminated. Also, it has become easier to calibrate the model because thermal and moisture effects on creep are partially separated. A new variable has been introduced in order to reduce the influence of subsequent thermal cycles on creep. This modification does not affect creep tests in which the evolution of temperature is monotonous. However, problems regarding excessive creep prediction caused by humidity variations have not been resolved yet. It has been found that the size effect on drying creep is controlled by the value of exponent $\tilde{p}$ in the governing equation for viscosity. If the originally recommended value $\tilde{p} = 2$ is changed to $\tilde{p} = 1$, the size effect is eliminated. For $\tilde{p} < 1$ the size effect on drying creep agrees with the experimental data, however, with this value the original theoretical justification of the MPS model is lost. In order to take into account tensile cracking, the improved MPS model has been extended by a cracking unit, which is based on the isotropic damage model.

Chapter 5 presents a widely used material model proposed by Bažant and Najjar for moisture transport, a material model for heat transport, and finally, a material model proposed by Künzel for coupled heat and moisture transport. The material model based on Bažant and Najjar has been successfully implemented in the Matlab environment and into the FE package OOFEM. It has been found that values of parameters published in the original papers give different results from those published, and that the model is almost insensitive to the specific choice of some

parameters. The assumption of a linear isotherm is not appropriate when modeling the moisture loss.

The methodology for shrinkage updating based on short-term measurements of water loss and shrinkage was critically assessed in Chapter 8. It has been found that the key assumption of this approach – the linear relationship between the shrinkage halftime and water loss halftime – is not realistic. A small error made in the estimate of the ultimate water loss can lead to a big error in the prediction of the ultimate shrinkage.

Finally, in Chapter 9, the MPS model for concrete creep and Künzel's model for moisture transport are used in the analysis of a drying concrete floor in the laboratory hall in UCEEB, Buštěhrad, Czech Republic. The material parameters have been calibrated on the complementary experimental specimens for shrinkage and water loss. However, numerical results for the deflecting slab are too much delayed behind the experiment. One of the possible reasons is the incorrect (linear) relationship between the shrinkage and humidity rates.

In future work, the following major issues should be addressed:

- relationship between shrinkage and humidity
- localization of tensile cracking vs. increased compliance during drying
- elimination of material sensitivity to small variations in relative humidity and temperature

References

[1] Eugène Freyssinet en quelques ouvrages. http://www.efreyssinet-association.com/oeuvre/ouvrages.php, 2012.

[2] ACI Committee 209. *Prediction of Creep, Shrinkage, and Temperature Effects in Concrete STructures*. American Concrete Institute, 1997.

[3] ACI Committee 209. *Guide for Modeling and Calculating Shrinkage and Creep in Hardened Concrete*. American Concrete Institute, 2008.

[4] M.S. Abrams and G.E. Monfore. Application of a small probe-type relative humidity gage to research on fire resistance of concrete. *Journal of the Portland Cement Association Research and Development Laboratories*, 7:2–12, 1965.

[5] M.S. Abrams and D.L. Orals. Concrete drying methods and their effect on fire resistance. *Moisture of materials in relation to fire tests*, pages 52–73, 1965.

[6] C.P. Aguilar. *Estudio del comportamiento y desarrollo de una metodologia de prediccion de la retraccion hidraulica de hormigones, PhD. Thesis (in Spanish)*. Pontificia Universidad Catolica de Chile. Escuela de Ingenieria, 2005.

[7] M.S. Ahs. Sorption scanning curves for hardened cementitious materials. *Construction and Building Materials*, 22:2228–2234, 2007.

[8] V. Baroghel-Bouny. Water vapour sorption experiments on hardened cementitious materials; part I: Essential tool for analysis of hygral behaviour and its relation to pore structure. *Materials and Structures*, 37:414–437, 2007.

[9] Z.P. Bažant and A. Asghari. Computation of Kelvin-chain retardation spectra of aging concrete. *Cement and Concrete Research*, 4:797–806, 1974.

[10] Z.P. Bažant and S. Baweja. Creep and shrinkage prediction model for analysis and design of concrete structures - model B3. *Materials and Structures*, 28:357–365, 1995.

[11] Z.P. Bažant and S. Baweja. Justification and refinements of model B3 for concrete creep and shrinkage 2. updating and theoretical basis. *Materials and Structures*, 28:488–495, 1995.

[12] Z.P. Bažant and S. Baweja. Short form of creep and shrinkage prediction model B3 for structures of medium sensitivity. *Materials and Structures*, 29:587–593, 1996.

[13] Z.P. Bažant and S. Baweja. Creep and shrinkage prediction model for analysis and design of concrete structures: Model B3. *Adam Neville Symposium: Creep and Shrinkage - Structural Design Effects*, 2000.

[14] Z.P. Bažant, L. Cedolin, and G. Cusatis. Temperature effect on concrete creep modeled by microprestress-solidification theory. In F.-J. Ulm and F.H. Bažant, Z.P. andWittmann, editors, *Creep, Shrinkage and Durability Mechanics of Concrete and Other Quasi-Brittle Materials. Proceedings of the 5th International Conference CONCREEP 6, MIT, Cambridge*, pages 197–204, Amsterdam, 2001. Elsevier.

[15] Z.P. Bažant, L. Cedolin, and G. Cusatis. Temperature effect on concrete creep modeled by microprestress-solidification theory. *Journal of Engineering Mechanics*, 130 (6):691–699, 2004.

[16] Z.P. Bažant and J.-C. Chern. Double-power logarithmic law for concrete creep. *Cement and Concrete Research*, 14:793–806, 1984.

[17] Z.P. Bažant and J.-C. Chern. Log double power law for concrete creep. *ACI Journal*, 82:665–675, 1985.

[18] Z.P. Bažant and J.-C. Chern. Triple power law for concrete creep. *Journal of Engineering Mechanics*, 111:63–83, 1985.

[19] Z.P. Bažant, A.B. Hauggaard, and F. Ulm. Microprestress-solidification theory for concrete creep. I: Aging and drying effects. *Journal of Engineering Mechanics*, 123(11):1188–1194, 1997.

[20] Z.P. Bažant, A.B. Hauggaard, and F. Ulm. Microprestress-solidification theory for concrete creep. II: Algorithm and verification. *Journal of Engineering Mechanics*, 123(11):1195–1201, 1997.

[21] Z.P. Bažant, M.H. Hubler, and Y. Qiang. Excessive creep deflections: An awakening. *Concrete International*, 33(8):44–46, 2011.

[22] Z.P. Bažant and M. Jirásek. *Creep and Hygrothermal Effects in Concrete Structures*. Springer, in preparation.

[23] Z.P. Bažant and J.-K. Kim. Improved prediction model for time-dependent deformations of concrete: Part 2 - basic creep. *Materials and Structures*, 24:409–421, 1991.

[24] Z.P. Bažant and J.-K. Kim. Improved prediction model for time-dependent deformations of concrete: Part 3 - creep at drying. *Materials and Structures*, 25:21–28, 1992.

[25] Z.P. Bažant and J.-K. Kim. Improved prediction model for time-dependent deformations of concrete: Part 4 - temperature effects. *Materials and Structures*, 25:84–94, 1992.

[26] Z.P. Bažant and J.-K. Kim. Improved prediction model for time-dependent deformations of concrete: Part 5 - cyclic load and cyclic humidity. *Materials and Structures*, 25:163–169, 1992.

[27] Z.P. Bažant, J.-K. Kim, and L. Panula. Improved prediction model for time-dependent deformations of concrete: Part 1 - shrinkage. *Materials and Structures*, 24:327–345, 1991.

[28] Z.P. Bažant and E. Osman. Double power law for basic creep of concrete. *Materials and Structures*, 9(1):3–11, 1976.

[29] Z.P. Bažant, E. Osman, and W. Thonguthai. Practical formulation of shrinkage and creep of concrete. *Materials and Structures*, 9:395–406, 1976.

[30] Z.P. Bažant and L. Panula. Practical prediction of time-dependent deformations of concrete, part I: Shrinkage. *Materials and Structures*, 11:307–316, 1978.

[31] Z.P. Bažant and L. Panula. Practical prediction of time-dependent deformations of concrete, part II: Basic creep. *Materials and Structures*, 11:317–328, 1978.

[32] Z.P. Bažant and L. Panula. Practical prediction of time-dependent deformations of concrete, part III: Drying creep. *Materials and Structures*, 11:415–424, 1978.

[33] Z.P. Bažant and L. Panula. Practical prediction of time-dependent deformations of concrete, part IV: Temperature effect on basic creep. *Materials and Structures*, 11:424–434, 1978.

[34] Z.P. Bažant and L. Panula. Practical prediction of time-dependent deformations of concrete, part V: Temperature effect on drying creep. *Materials and Structures*, 12:169–174, 1979.

[35] Z.P. Bažant and S. Prasannan. Solidification theory for concrete creep. I: Formulation. *Journal of Engineering Mechanics*, 115(8):1691–1703, 1989.

[36] Z.P. Bažant and S. Prasannan. Solidification theory for concrete creep. II: Verification and application. *Journal of Engineering Mechanics*, 115(8):1704–1725, 1989.

[37] Z.P. Bažant and S.T. Wu. Rate-type creep law of aging concrete based on Maxwell chain. *Materials and Structures*, 7(37):45–60, 1974.

[38] Z.P. Bažant and Y. Xi. Continuous retardation spectrum for solidification theory of concrete creep. *Journal of Engineering Mechanics*, 121(2):281–288, 1995.

[39] Z. P. Bažant and L. J. Najjar. Nonlinear water diffusion in nonsaturated concrete. *Materials and Structures*, 5:3–20, 1972.

[40] Z. P. Bažant, E. Osman, and W. Thonguthai. Practical formulation of shrinkage and creep of concrete. *Materials and Structures*, 7:395–406, 1976.

[41] M. Briffaut, F. Bendoudjema, J.M. Torrenti, and G. Nahas. Concrete early age basic creep: experiments and test of rheological modelling approaches. *Construction and Building Materials*, 36:373–380, 2012.

[42] J.J. Brooks. 30-year creep and shrinkage of concrete. *Magazine of Concrete Research*, 57(9):545–556, 2005.

[43] J.J. Brooks and A.M. Neville. Estimating long-term creep and shrinkage from short-time tests. *Magazine of Concrete Research*, 27(90):3–12, 1975.

[44] S. Brunauer, J. Skalny, and E.E Bodor. Adsorption of nonporous solids. *Journal of Colloid and Interface Science*, 30(4):546–552, 1969.

[45] A. H. Bryant and C. Vadhanavikkit. Creep, shrinkage-size, and age at loading effects. *ACI Materials Journal*, 84:117–123, 1987.

[46] F. Dischinger. Untersuchungen über die Knicksicherheit, die elastische Verformung und das Kriechen des Betons bei Bogenbrücken. *Der Bauingenieur*, 18(33/34, 35/36, 39/40):487–520, 539–552, 595–621, 1937.

[47] Fédération Internationale du Béton. *Structural Concrete: Textbook on Behaviour, Design and Performance : Updated Knowledge of the CEB/FIP Model Code 1990*. Number vol. 1 in Bulletin (Fédération internationale du béton). International Federation for Structural Concrete, 1999.

[48] Fédération Internationale du Béton. *Model Code 2010*. Number vol. 55 in fib Bulletin. International Federation for Structural Concrete (fib), 2010.

[49] Fédération Internationale du Béton. *Model Code 2010*. Number vol. 65 in fib Bulletin. International Federation for Structural Concrete (fib), 2012.

[50] Comité Euro-International du Béton (CEB). *CEB-FIP Model Code 1990*. Number 213/214 in Bulletin (Fédération internationale du béton). Comité Euro-International du Béton (CEB), 1993.

[51] H.M. Fahmi, M. Polivka, and B. Bresler. Effects of sustained and cyclic elevated temperature on creep of concrete. *Cement and Concrete Research*, 2:591–606, 1972.

[52] P. Freiesleben Hansen. Coupled moisture/heat transport in cross sections of structures. *Beton og Konstruktionsinstituttet*, 1985.

[53] N.J. Gardner. Comparison and prediction provisions for drying shrinkage and creep of normal-strength concretes. *Canadian Journal for Civil Engineering*, 31(5):767–775, 2004.

[54] N.J. Gardner and M.J. Lockman. Design provisions for drying shrinkage and creep of normal-strength concrete. *ACI Materials Journal*, 98(2):159–167, 2001.

[55] N.J. Gardner and J.W. Zhao. Creep and shrinkage revisited. *ACI Materials Journal*, 90(3):236–246, 1993.

[56] D. Gawin, F. Pesavento, and B. A. Schrefler. Hygro-thermo-chemo-mechanical modelling of concrete at early ages and beyond. Part I: Hydration and hygro-thermal phenomena. *International Journal for Numerical Methods in Engineering*, 67:299–331, 2006.

[57] L. Granger. *Comportement differe du beton dans les enceintes de centrales nucleaires: analyse et modelisation, PhD. Thesis (in French)*. LCPC, Paris, France, 1995.

[58] K.K. Hansen. *Sorption Isotherms, A Catalogue*. Building Materials Laboratory, The Technical University of Denmark, 1986.

[59] T.C. Hansen and A.H. Mattock. Influence of size and shape of member on the shrinkage and creep of concrete. *Journal of the American Concrete Institute*, 62(2):267–290, 1966.

[60] J.A. Hanson. Effects of curing and drying environments on splitting tesile strength. *American Concrete Institute Journal*, 65:535–543, 1968.

[61] A. Hilaire, F. Bendoudjema, A. Darquennes, Y. Berthaud, and G. Nahas. Modeling basic creep in concrete at early-age under compressive and tensile loading. *Nuclear Engineering and Design*, 269:222–230, 2014.

[62] M. Jirásek and P. Havlásek. Accurate approximations of concrete creep compliance functions based on continuous retardation spectra. *Computers and Structures*, 135:155–168, 2014.

[63] M. Jirásek and P. Havlásek. Microprestress-solidification theory of concrete creep: Reformulation and improvement. *Cement and Concrete Research*, 60:51–62, 2014.

[64] Keeton. *Study of Creep in Concrete, Phase 1 (I-beam)*. U. S. Naval Civil Engineering Laboratory, Port Hueneme, California, 1965.

[65] J. K. Kim and C. S. Lee. Moisture diffusion of concrete considering self-desiccation at early ages. *Cement and Concrete Research*, 29:1921–1927, 1999.

[66] G.J. Kommendant, M. Polivka, and D. Pirtz. Study of concrete properties for prestressed concrete reactor vessels, final report - part II, creep and strength characteristics of concrete at elevated temperatures. *Rep. no. UCSESM 76-3 prepared for General Atomic Company*, 1976.

[67] H. Künzel. *Simultaneous Heat and Moisture Transport in Building Components*. IRB, Stuttgart, 1995.

[68] W.R. Lorman. The theory of concrete creep. *ASTM Proceedings*, 40:1082–1102, 1940.

[69] B.L. Meyers, D.E. Branson, and C.G. Chumann. Prediction of creep and shrinkage behavior for design from short term tests. *PCI Journal*, 17(3):29–45, 1972.

[70] M.A. Mukaddam and B. Bresler. *Behavior of Concrete Under Variable Temperature and Loading*. Department of Civil Engineering, University of California, Berkeley, California, 1970.

[71] K.W. Nasser and A.M. Neville. Creep of concrete at elevated temperatures. *ACI Journal*, 62:1567–1579, 1965.

[72] A.M. Neville. *Properties of concrete*. Wiley, 2011.

[73] L. O. Nilsson. *Hygroscopic Moisture in Concrete - Drying, Measurements & Related Material Properties*. Lund University, 1980.

[74] Japan Society of Civil Engineers (JSCE). *JSCE Guidelines for Concrete, Standard Specifications for Concrete Structures - 2007 "Design"*. Number 15 in JSCE Guidelines for Concrete. Subcommittee on English Version of Standard Specifications for Concrete Structures - 2007, Japan Society of Civil Engineers (JSCE), 2010.

[75] M. Omar, A. Loukili, G. Pijaudier-Cabot, and Y. Le Pape. Creep-damage coupled effects: Experimental investigation of bending beams with various sizes. *Journal of Materials in Civil Engineering*, 21(2):65–72, 2009.

[76] B. Patzák. OOFEM home page. http://www.oofem.org, 2000.

[77] B. Patzák and Z. Bittnar. Design of object oriented finite element code. *Advances in Engineering Software*, 32(10-11):759–767, 2001.

[78] B. Patzák, D. Rypl, and Z. Bittnar. Parallel explicit finite element dynamics with nonlocal constitutive models. *Computers Structures*, 79(26-28):2287–2297, 2001.

[79] G. Pickett. The effect of change in moisture-content on the creep of concrete under a sustained load. *Journal of the American Concrete Institute*, 38:333–355, 1942.

[80] S. E. Pihlajavaara. A review of some of the main results of a research on the ageing phenomena of concrete: effect of moisture conditions on strength, shrinkage and creep of mature concrete. *Cement and Concrete Research*, 4:761–991, 1974.

[81] N. Ranaivomanana, S. Multon, and A. Turatsinze. Basic creep of concrete under compression, tension and bending. *Construction and Building Materials*, 38:173–180, 2013.

[82] N. Ranaivomanana, S. Multon, and A. Turatsinze. Tensile, compressive and flexural basic creep of concrete at different stress levels. *Cement and Concrete Research*, 52:1–10, 2013.

[83] N. Reviron. *Etude du fluage des bétons en traction. Application aux enceintes de confinement des centrales nucléaires à eau sous pression, PhD. Thesis (in French)*. ENS Cachan, France, 2009.

[84] A.D. Ross. Concrete creep data. *Structural Engineer*, 15(8):314–326, 1937.

[85] P. Rossi, J.L. Tailhan, and F. Le Maou. Comparison of concrete creep in tension and in compression: Influence of concrete age at loading and drying conditions. *Cement and Concrete Research*, 51:78–84, 2013.

[86] P. Rossi, J.L. Tailhan, F. Le Maou, L. Gaillet, and E. Martin. Basic creep behavior of concretes investigation of the physical mechanisms by using acoustic emission. *Cement and Concrete Research*, 42:61–73, 2012.

[87] K. Sakata. A study on moisture diffusion in drying and drying shrinkage of concrete. *Cement and Concrete Research*, 13:216–224, 1983.

[88] K. Sakata. Prediction of concrete creep and shrinkage. In Z.B. Bazant and I. Carol, editors, *Proceedings of the 5th International RILEM Symposium, Barcelona, Spain*, pages 649–654, London, UK, 1993. E&F Spon.

[89] K. Sakata. Prediction of concrete creep and shrinkage. *Creep and Shrinkage of Concrete*, 31(5):767–775, 2004.

[90] J.L. Tailhan, C. Boulay, P. Rossi, F. Le Maou, and E. Martin. Compressive, tensile and bending basic creep behaviours related to the same concrete. *Structural Concrete*, 14(2):124–130, 2013.

[91] Český normalizační institut. *Eurokód 2: Navrhování betonových konstrukcí - Část 1-1: Obecná pravidla a pravidla pro pozemní stavby*. Český normalizační institut, 1996.

[92] Y. Xi, Z.P. Bažant, and H.M. Jennings. Moisture diffusion in cementitious materials. *Advanced Cement Based Materials*, 1(6):258–266, 1994.

A Material Models for Creep and Shrinkage (Cross-sectional Approach)

This section presents material models for concrete creep and shrinkage, which are used the so-called averaged cross-sectional approach. The aim was to capture the structure and properties of the best known models from the design codes and other recommendations as well as from the academic field. Attention is also paid to the historical development of some models, which revealed that some of the currently used formulae origin many decades ago. Special attention is paid to the influence of the variable enviornmental conditions.

A brief summary of the prediction models and the factors related to the ambient conditions that are considered in the models is listed in Table A.1.

All of the presented models except for one consider shrinkage to be bounded. The exception is the Gardner's model, which uses a logarithmic decay of shrinkage for long drying durations.

The basic creep is assumed to be bounded only in the design codes ACI, the first draft of *fib* Model Code 2010, SAK model and the very old models; the drying creep is bounded in all models.

The size and shape of the structural member is reflected using either the volume-to-surface ratio or the equivalent thickness. In order to capture the time evolution of shrinkage and drying of specimens with the same volume-to-surface ratio but with different geometry, the B3 model (and its ancestors) introduces a shape factor.

Table A.1: Summary of the material influencing factors and features

	curing duration	curing type	V/S	shape	h_{env}	h_{env} - cyclic creep	T - maturity	T - creep rate	T - creep amplitude	T - transient creep	T - drying/shrinkage rate	T - shrinkage magnitude	autogenous shrinkage
Branson		✓	✓		✓								
Pract. pred. (1976/78)	✓		✓	✓	✓		✓	✓	(✓)		✓		
Impr. pred. model (1991)	✓	✓	✓	✓	✓	✓	✓	✓	(✓)		✓		
B3	✓	✓	✓	✓	✓	✓	✓	✓	(✓)				(✓)
B3 - short			✓		✓								
GZ, GL 2000/4	✓		✓		✓								
Sakata	✓		✓		✓								
JSCE	✓		✓		✓		✓	✓	(✓)				✓
ModelCode			✓		✓		✓	✓	✓	✓	✓	✓	✓

A.1 Important models before 1970

Models presented in 1937 by Ross [84]

$$\varepsilon_c(\hat{t}) = \frac{\hat{t}}{a + b\hat{t}}\,\hat{\sigma} \tag{A.1}$$

and in 1940 by Lorman [68]

$$\varepsilon_c(\hat{t}) = \frac{m\hat{t}}{n + \hat{t}}\,\hat{\sigma} \tag{A.2}$$

used hyperbolic non-aging functions with several parameters. The two models are mentioned here, because after more than 30 years, improved, yet very similar formula was proposed by Branson, which is currently used in the design code ACI-209.

The so-called rate-of-creep model applied to concrete structures by Dischinger in 1937 [46], was probably the first one which simulated aging, i.e. smaller compliance for concrete loaded later. The creep coefficient is expressed by

$$\varphi(t) = \varphi_\infty\,[1 - \exp(-at)] \tag{A.3}$$

where a is a parameter and φ_∞ is the ultimate creep coefficient. For the rate-of-creep theory, the specific creep is defined as

$$C(t,t') = \frac{\varphi(t) - \varphi(t')}{E} \tag{A.4}$$

However, this model has two major disadvantages: firstly, this model fails to model creep recovery after unloading (caused by the same creep rate of "loading" and "unloading" compliance functions), and secondly, for very old concrete the model predicts zero creep, which is not observed in reality. The third disadvantage is the bounded creep.

A.2 Branson's formula (1971)

The prediction model proposed in the early 70's by Branson [69] is very important even nowadays, because it is embedded the core of the ACI-209 model codes. The paper proposes similar formula, only with different coefficients both for creep and drying shrinkage:

$$\varphi(\hat{t}) = \frac{\hat{t}^c}{d + \hat{t}^c}\,\varphi_u \tag{A.5}$$

$$\varepsilon_{sh}(\hat{t}) = \frac{\hat{t}^e}{f + \hat{t}^e}\,\varepsilon_{sh,u} \tag{A.6}$$

where φ is the creep coefficient (related to the instantaneous deformation, ε_{sh} is shrinkage, $\hat{t}$ is the duration of loading (drying), φ_u is the ultimate value of the creep coefficient ($\varepsilon_{sh,u}$ = ultimate shrinkage), and c, d, e and f are parameters. Optimization of these parameters to give the best fit of the measured data yielded to

$$\varphi(\hat{t}) = \frac{\hat{t}^{0.6}}{10 + \hat{t}^{0.6}}\,\varphi_u \tag{A.7}$$

$$\varepsilon_{sh}(\hat{t}) = \frac{\hat{t}}{35+\hat{t}}\,\varepsilon_{sh,u} \quad \text{moist curing} \tag{A.8}$$

$$\varepsilon_{sh}(\hat{t}) = \frac{\hat{t}}{55+\hat{t}}\,\varepsilon_{sh,u} \quad \text{steam curing} \tag{A.9}$$

If no measurements are done, $\varphi_u = 2.35$, $\varepsilon_{sh,u} = 800 \times 10^{-6}$ (moist cured), $\varepsilon_{sh,u} = 730 \times 10^{-6}$ (steam cured). The paper also proposes formulae for correction factors if loading age, humidity, thickness, slump, cement content, aggregates and air content differ from the reference state.

A.3 Double power law for basic creep of concrete (1976)

This material model for basic creep of concrete has been introduced in 1976 by Bažant and Osman [28]. This models should correctly reflect the effect of aging (dependence on t') as well as the dependence of creep on the load duration, i.e. on $t - t'$. The proposed compliance function reads

$$J(t,t') = \frac{1}{E_0}\left(1 + \varphi_1 (t')^{-m}\,(t-t')^{n}\right) \tag{A.10}$$

It contains only four parameters: exponents m and n controlling aging and shape of the compliance function, parameter φ_1 reflecting the magnitude of creep, and finally the instantaneous elastic modulus E_0. Values of these parameters can be obtained by optimization procedures leading to minimum error between the compliance functions and the experimentally measured data. Recommended values for exponents are $m = 1/3$ and $n = 1/8$. Development of the conventional elastic modulus in time can be obtained if one replaces the load duration $(t - t')$ by 0.001 day.

A.4 Practical formulation of shrinkage and creep of concrete (1976)

The main importance of the paper [29] is the development of formulae for shrinkage, which were with small modifications incorporated into the model B3 [10], one of the best prediction models for creep and shrinkage. The time development of shrinkage is described by equation

$$\varepsilon_{sh}(t,t_0) = \varepsilon_{sh,\infty} k_h S(t) \tag{A.11}$$

where

$$S(t) = \sqrt{\frac{t-t_0}{\tau_{sh}+t-t_0}} \tag{A.12}$$

$$\varepsilon_{sh,\infty} = \varepsilon_{s,\infty}\frac{E(7+600)}{E(t_0+\tau_{sh})} \tag{A.13}$$

$$k_h = 1 - 0.95 h_{\text{env}}^3 - 0.25 h_{\text{env}}^{200} \tag{A.14}$$

τ_{sh} is the shrinkage square half-time ($S^2(\tau_{sh}) = 0.5$), E(t) is the elastic modulus according to ACI. The shrinkage half-time depends not only on the shape and thickness of the drying specimen, but also on concrete diffusivity. It is defined by

$$\tau_{sh} = 600\,(k_s D/150)^2\,\frac{C_1^{ref}}{C_1(t_0)} \tag{A.15}$$

where D is the effective cross section thickness [mm], $D = 2v/s$ (v = volume, s = drying surface), k_s is the shape factor (slab 1.0, cylinder 1.15, square prism 1.25, sphere 1.3 and cube 1.55). The reference diffusivity $C_1^{ref} = 10$ mm^2/day and the maximum diffusivity at room temperature

$$C_1(t) = C_7 k'_T(0.05 + \sqrt{6.3/t}) \tag{A.16}$$

where C_7 is the diffusivity at the age of 7 days and k'_T is the temperature correction factor.

$$k'_T = \frac{T}{T_0} \exp\left(\frac{5000}{T_0} - \frac{5000}{T}\right) \tag{A.17}$$

Here, T is absolute temperature, T_0 is room temperature (both in Kelvin).

The compliance function proposed in this paper

$$J(t,t') = 1/E_0 + C_0(t,t') + C_d(t,t',t_0) - C_p(t,t',t_0) \tag{A.18}$$

has four constituents: part reflecting instantaneous deformation, part reflecting basic specific creep described by double power law and then drying specific creep (increase in creep when concrete is loaded and exhibits drying) and finally pre-dried specific creep (decrease in creep when loading already dry concrete).

A.5 Practical prediction of time-dependent deformations of concrete (1978)

A.5.1 Basic creep

Reference [31] modifies the original formula for basic creep [28] to following form

$$J(t,t') = \frac{1}{E_0}\left[1 + \left(\varphi_1(t')^{-m} + \alpha\right)(t-t')^n\right] \tag{A.19}$$

The same reference provides also empirical formulae for identification of parameters based on concrete composition and thus enabling "blind" prediction of creep. The input parameters are: compressive strength, water, cement, sand and gravel content, concrete density and cement class. To get the conventional static modulus (corresponding to ACI or CEB recommendations) the load duration should be taken $t-t' = 0.1$ day (not 0.001 day, which corresponds to normally measured elastic strains) and the dynamic modulus with $t - t' = 10^{-7}$ day.

A.5.2 Shrinkage

Reference [30] follows from the material model for shrinkage in [29] and proposes empirical formulae for the only two parameters: C_7 and $\varepsilon_{s,\infty}$ based on the concrete strength and composition.

A.5.3 Drying creep

The paper [32] provides slightly modified relations for the drying specific creep $C_d(t,t',t_0$ and for creep after drying $C_p(t,t',t_0$ first presented in (A.18) as well as empirical prediction formulae based on concrete mixture. The formulae describing specific drying creep are quite complex and read

$$C_d(t,t',t_0) = \frac{\varphi'_d}{E_0}(t')^{-0.5m} k'_h \varepsilon_{sh,\infty} S_d(t,t') \tag{A.20}$$

$$\varphi'_d = \left(1 + \frac{t' - t_0}{10\tau_{sh}}\right)^{-1/2} \varphi_d \tag{A.21}$$

$$k'_h = \left|h_0^{1.5} - h_{\text{env}}^{1.5}\right| \tag{A.22}$$

$$S_d(t, t') = \left(1 + \frac{10\tau_{sh}}{t - t'}\right)^{-c_d n} \tag{A.23}$$

Creep after drying is described by following equations

$$C_p(t, t', t_0) = c_p k''_h S_p(t, t') C_0(t, t') \tag{A.24}$$

with

$$S_p(t, t') = \left(1 + \frac{100\tau_{sh}}{t - t_0}\right)^{-n} \tag{A.25}$$

$$k''_h = h_0^2 - h_{\text{env}}^2 \tag{A.26}$$

It is interesting that value of the drying creep is linearly proportional to the ultimate shrinkage $\varepsilon_{sh,\infty}$. The time evolution equations (A.23) and (A.25) contain $10\tau_{sh}$ and $100\tau_{sh}$, respectively, instead of τ_{sh}. The reason is that the authors observed, that the drying creep is delayed approximately one decade in the log-scale and pre-dried creep two decades in the log-scale behind shrinkage.

A.5.4 Temperature effect on basic and drying creep

Reference [33] proposes formulae reflecting temperature effects on creep under sealed (no moisture transport) conditions and prediction formulae based on concrete composition. Elevated temperature results in two opposing effects; firstly, elevated temperature leads to thermally accelerated hydration reaction and thus to lower creep, and secondly, elevated temperature accelerates creep rate (Arrhenius concept). The governing equation (A.19) for the specific basic creep then changes to

$$C_0(t, t') = \frac{\varphi_T}{E_0} \left(t_e'^{-m} + \alpha\right) (t - t')^{n_T} \tag{A.27}$$

The creep acceleration is reflected by

$$\varphi_T = \varphi_1 \left(1 + C_T\right) \tag{A.28}$$

and the creep retardation by introducing the equivalent time

$$t'_e = \int_0^{t'} \exp\left(\frac{4000}{T_0} - \frac{4000}{T(t'')}\right) dt'' \tag{A.29}$$

Similar concept is used also for the drying creep [34], but the resulting formulae become even more complicated, because now also the drying process is influenced (accelerated) by elevated temperature. This results mainly in replacing expressions $\tau_{sh}/(t - t_0)$ by the "reduced time lag" $\Delta\tau$.

A.6 Log double power law for concrete creep (1985)

The material model called "Double-power logarithmic law for concrete creep" has been proposed in 1984 Bažant and Chern [16] and extended in 1985 to Log double power law [17]. The main reason for introduction of this model was systematic over-prediction of the basic creep for longer loading durations by the former model, the double power law. Both models are restricted only to basic creep, i.e. constant moisture content and temperature.

Double-power logarithmic law combines double power law (for shorter loading periods) with log law (for longer durations of loading). These two models are separated by the transition time, which depends not only on model parameters, but also on the age of loading. The compliance function corresponding to the log law turns suddenly into a straight line if it is plotted in a semi-logarithmic scale. The slope of this line is the same for all ages at loading.

The log double power law uses a transition between exponential shape and the straight line if the compliance is plotted in a semi-logarithmic scale, but now the transition is continuous and is directly embedded in the compliance function. The compliance function reads

$$J(t,t') = \frac{1}{E_0} + \frac{\psi_0}{E_0} \ln\left[1 + \psi_1 \left((t')^{-m} + \alpha\right)(t-t')^n\right] \tag{A.30}$$

However, both models exhibit unwanted properties such as divergence or change of sign of the relaxation function.

A.7 Triple power law for concrete creep (1985)

Triple power law proposed in 1985 by Bažant and Chern [18] does not provide more accurate fits of the experimentally measured data, but compensates several deficiencies of the previous models. First, the range of applicability is extended to very short loading durations. Comparing to the double-power logarithmic law, this model provides smoothness of the creep curves, even at the transition time. On the other hand, the compliance function is introduced in the rate form

$$\dot{J}(t,t') = \frac{\psi_1}{E_0} \frac{(t')^{-m} + \alpha}{(t-t')^{1-n}\,(t/t')^n} \tag{A.31}$$

This model is deemed to be unsuitable for the engineering practice, because when integrating this compliance function, one needs to evaluate the binomial integral.

A.8 Improved prediction model for time-dependent deformations of concrete (1991)

A.8.1 Basic creep

The physically-based material model for basic creep of concrete proposed by Bažant and Kim [23] in 1991 is based on five crucial ideas, which have been developed through the years based on observing experimental data.

- the short term creep curves have shape of $(t-t')^n$, so in semi-logarithmic scale the shape is exponential
- the basic creep is unbounded

- the long term creep curves approach function $\log(t-t')$, so in semi-logarithmic scale the shape approaches a straight line
- the higher the age at loading, t', the later occurs the transition from $(t-t')^n$ to $\log(t-t')$
- for the same duration of loading $t-t'$, the compliance decreases with $(t')^{-1/3}$

The compliance function presented in this paper splits the deformation into three parts: instantaneous (constant and non-aging), viscoelastic aging (solidifying) and finally long-term purely viscous part. It contains only four parameters q_1–q_4, which can be determined by linear regression. To determine their values (e.g. for "blind prediction"), one can use empirical formulae based on the concrete strength and the composition of concrete mixture. The compliance function is defined as

$$J(t,t',\sigma) = q_1 + F(\sigma)\left[q_2 Q(t,t') + q_3 \ln\left(1+t-t'\right) + q_4 \ln\left(\frac{t}{t'}\right)\right] \tag{A.32}$$

where $F(\sigma)$ is empirically based function introducing creep non-linearity for higher ratios compressive stress : compressive strength, and $Q(t,t')$ is a function related to aging.

It was shown that for short creep durations, this material model approaches the double power law, while for longer durations the logarithmic law. The compliance function does not exhibit divergence.

A.8.2 Shrinkage

Reference [27] presents modified shrinkage model based on [29] and [30]. The presented prediction formulae are almost identical (except proposed form of age-dependence) to those from model B3 published 4 years later. This model extends range of influencing parameters (from compressive strength and composition) to curing conditions and cement type. The main difference from the previous models is the function describing time evolution of shrinkage. Its form changed from (A.12) to

$$S(t) = \tanh\sqrt{\frac{t-t_0}{\tau_{sh}}} \tag{A.33}$$

Since this material model is physically based, this paper also reviews several underlying concepts.

- the shrinkage halftime τ_{sh} is proportional to square of the effective thickness D^2, which follows from the diffusion theory
- initial shape of the shrinkage function should be proportional to the square root of the drying period
- shrinkage is closely related to diffusion, and so depends on the volume-to-surface ratio corrected by a shape factor (solved also from the diffusion theory)
- microcracking caused by differential moisture distribution and shrinkage results in smaller amplitude of shrinkage comparing to specimens which dry and shrink uniformly
- temperature changes shrinkage rate, which obeys activation energy theory

A.8.3 Drying creep

The compliance function proposed in [24] has following additive form

$$J(t,t',\sigma) = q_1 + F(\sigma)\left(C_0(t,t') + C_d(t,t',t_0) + C_p(t,t',t_0)\right) \tag{A.34}$$

where, similarly to [32], $C_d(t,t',t_0)$ is the specific drying creep and $C_p(t,t',t_0)$ is the creep of pre-dried concrete. Only the formula for drying creep is shown here

$$C_d(t,t',t_0) = q_5 k'_h \varepsilon_{sh,\infty}\sqrt{S\left(\frac{t-t_0}{\tau_m}\right) - S\left(\frac{t'-t_0}{\tau_m}\right)} \tag{A.35}$$

where τ_m has similar meaning as the shrinkage halftime τ_{sh}, and $k'_h = h_0^3 - h_{\mathrm{env}}^3$. This approach does not hold if the specimen has already dried out before loading; in that case, the C_d and C_p is omitted and the basic creep is reduced by empirical factor $0.1 + 0.9 \times 0.98^2$.

The effects of cyclic environmental humidity can be taken into account according to [26]. All expressions in (A.34) remain unchanged, only the drying creep component is multiplied by correction factor κ, which depends on the period of humidity cycles, diffusivity (influencing so-called "penetration depth"), amplitude of the changing humidity h_{env}, and the effective thickness.

A.8.4 Temperature effects on creep

The proposed model [25] combines the basic [23] and drying [24] creep formulae with the refined concept from [34]. For both, basic and drying creep, the method is based on the activation energy concept. In case of the basic creep, the real age at loading t' is replaced by the equivalent age at loading t'_e,

$$t'_e = \int_0^{t'} \exp\left[\frac{U_h}{R}\left(\frac{1}{T_0} - \frac{1}{T(t'')}\right)\right] \mathrm{d}t'' \tag{A.36}$$

and the real load duration by the equivalent load duration:

$$t_T - t'_e = \int_t^{'t} \exp\left[\frac{U_0 + U_1 \ln\left(1 + t - t'\right)}{R}\left(\frac{1}{T_0} - \frac{1}{T(t'')}\right)\right] \mathrm{d}t'' \tag{A.37}$$

with reference temperature T_0 and absolute temperature T [K], R = gas constant, and U_* = activation energies. Similar methodology holds also for the temperature-influenced drying creep.

A.9 Creep and shrinkage prediction model for analysis and design of concrete structures - model B3 (1995)

Model B3 [10] represents the third major update to the previously published prediction models [30] [23] from the Northwestern University. The model uses split of the deformation into creep, shrinkage (swelling) and thermal part. The compliance function

$$J(t,t',\sigma) = q_1 + C_0(t,t') + C_d(t,t',t_0) \tag{A.38}$$

is additively subdivided into three parts, first one represents instantaneous deformation, the second one is the specific basic creep and the last one is additional specific drying creep. Nonlinearity caused by high stresses such as in the previous model [23] is omitted; the model is

restricted to stresses below $0.4f_{cm}$, where creep is assumed to be linear. The basic creep function is provided both by its rate form coming directly from the solidification theory [35] and by regular form, which is more suitable for structural engineers

$$C_0(t,t') = q_2 Q(t,t') + q_3 \ln\left(1 + (t-t')^n\right) + q_4 \ln\left(\frac{t}{t'}\right) \tag{A.39}$$

This equation is almost the same as (A.32), only the non-linear term $F(\sigma)$ vanished and exponent $n = 0.1$ appeared in the non-aging viscoelastic term.

This prediction model contains five basic parameters, q_1–q_5, which can be roughly estimated based on concrete mixture and concrete strength. Comparing these prediction formulae in this model with [23], one can observe huge simplification.

The formula for specific drying creep reads

$$C_d(t,t',t_0) = q_5\sqrt{\exp\left(-8H(t)\right) - \exp\left(-8H(t')\right)} \tag{A.40}$$

with

$$H(t) = 1 - (1 - h_{\text{env}})S(t) \tag{A.41}$$

$$S(t) = \tanh\sqrt{\frac{t-t_0}{\tau_{sh}}} \tag{A.42}$$

where τ_{sh} is the shrinkage half-time depending on the shape of the concrete member, its effective thickness, f_c and t_0.

The paper also advises to treat creep and shrinkage as statistical variables with COV 23% for creep and 34% for shrinkage. If the normal distribution is assumed, then e.g. parameters q_1–q_5 should be premultiplied by factors 1.45 or 0.55 to reflect the 95% or 5% confidence limits; shrinkage, compressive strength and relative humidity should be treated similarly.

Influence of constant elevated temperature on creep is treated by replacing age at loading t' by the "equivalent" age at loading t'_e and the stress duration $t - t'$ is replaced by the equivalent stress duration $t_T - t'_e$. This concept based on Arrhenius equations and activation energies should reflect higher hydration degree and higher creep rate at elevated temperature (at elevated temperature concrete behaves as if it was loaded later and for longer time).

A.9.1 Shrinkage

Development of shrinkage is described by

$$\varepsilon_{sh}(t,t_0) = -\varepsilon_{sh,\infty} k_h S(t) \tag{A.43}$$

where k_h is parameter depending on the environmental humidity h_{env}, ($k_h = 1 - h_{\text{env}}^3$ for $h_{\text{env}} \leq 0.98$ and $k_h = -0.2$ for $h_{\text{env}} = 1.$), and

$$\varepsilon_{sh,\infty} = \varepsilon_{s,\infty}\frac{E(7+600)}{E(t_0+\tau_{sh})} \tag{A.44}$$

with $\varepsilon_{s,\infty}$ defining the total amplitude of shrinkage if drying took place at $h_{\text{env}} = 0.$ and $E(t)$ is a function describing time evolution of the elastic modulus (according to ACI formula or it can be computed directly from the compliance function $E(t) = 1/J(t+0.01,t)$.

A.10 Short form of creep and shrinkage prediction model B3 for structures of medium sensitivity (1996)

As the title of this model [12] indicates, this model should be used for structures, which are less sensitive to creep and shrinkage. The main structure of the model is kept the same as in the more general model, see equation A.38.

Specific basic creep is based on the log double-power law [17] and has only one free parameter q_0.

$$C_0(t,t') = q_0 \ln\left[1 + \psi\left(t'^{-m} + \alpha\right)(t-t')^n\right] \tag{A.45}$$

with $m = 0.5$, $n = 0.1$, $\alpha = 0.001$ and $\psi = 0.3$.

Specific drying creep is described by

$$C_d(t,t',t_0) = q_5\sqrt{\exp\left(-3H(t)\right) - \exp\left(-3H(t')\right)} \tag{A.46}$$

where the meaning of function $H(t)$ is the same as in the full-form of model B3.

Comparing to the full version of model B3, here the prediction formulae for q_0, q_1 and q_5 use only the mean compressive strength f_{cm} and the elastic modulus E_{28}.

The simplicity of this model is outweighed by increase in COV (31% for creep and 41% for shrinkage) as well as by poor properties such as divergence of the compliance function or change of sign of the relaxation function.

A.10.1 Shrinkage

The same formula as in [10] is used for description of shrinkage. The first difference is simplifying formula for the shrinkage halftime

$$\tau_{sh} = 4.9D^2 \tag{A.47}$$

with D being the effective cross-section thickness [cm] ($D = 2v/s$, v = volume, s = drying surface). The second difference is based on the assumption, that in most cases the sum of shrinkage half-time and curing time is 607 days, and hence $\varepsilon_{sh,\infty} = \varepsilon_{s,\infty}$.

A.11 GZ model (1993)

Prediction model [55] proposed by Gardner and Zhao gives formulae for estimation of elastic modulus, shrinkage, and both basic and drying creep of concrete. This purely phenomenological material model is somewhat different from all other, because it is based on idea, that not only concrete creep is unbounded (similarly to e.g. Bažant's models), but the same holds also for shrinkage. Prediction is based on input parameters which are in common practice available already during the general design phase: (average) concrete strength, cement type, volume-to-surface ratio, curing period and the environmental humidity. The elastic modulus at time t is defined by

$$E_c(t) = 3500 + 4300\sqrt{f_{cm}(t)} \tag{A.48}$$

which is quite similar to the ACI recommendation. The evolution of the average compressive strength in time is given by

$$f_{cm}(t) = f_{cm,28}\frac{t^{3/4}}{a + bt^{3/4}} \tag{A.49}$$

where values of a and b depend on cement type.

Creep coefficient is defined by quite complex formula

$$\varphi(t,t') = \frac{7.27 + \ln(t-t')}{17.18}\left(1.57 + 2.98\frac{f_{cm,28}}{f_{cm}(t')}\sqrt{\frac{25}{f_{cm,28}}}\left(1-h_{\text{env}}^2\right)\frac{t-t'}{t-t'+0.1\,(V/S)^2}\right) \tag{A.50}$$

where V/S is the volume-to-surface ratio [mm].

Shrinkage is defined by

$$\varepsilon_{sh}(t) = \varepsilon_{sh,u}\beta(h_{\text{env}})\beta(t) \tag{A.51}$$

where

$$\varepsilon_{sh,u} = 900K\sqrt{\frac{f_{cm,28}}{f_{cm}(t_0)}}\sqrt{\frac{25}{f_{cm,28}}} \times 10^{-6} \tag{A.52}$$

is the ultimate shrinkage influenced by cement type (parameter K), average compressive strength at the age of 28 days and at the onset of drying; $\beta(h_{\text{env}}) = (1-h_{\text{env}}^4)$ if $h_{\text{env}} < 0.99$ or $\beta(h_{\text{env}}) = -0.2$ for $h_{\text{env}} = 1.0$. The time-evolution function combining Ross-type relationship for size effects with a logarithmic time reads

$$\beta(t) = \frac{7.27 + \ln(t-t_0)}{17.18}\frac{t-t_0}{t-t_0+0.0125(V/S)^2} \tag{A.53}$$

A.12 GL2000 model (2001, 2004)

Material model named GL2000 [54] [53] for prediction of concrete creep further improves the previously proposed model [55]. Formulae for the elastic modulus (A.48) (in both references) and the time development of concrete strength (A.49) remain unchanged, but the model uses different formula relating mean and characteristic compressive strength

$$f_{cm,28} = 1.1f_{ck,28} + 5 \tag{A.54}$$

Reference [53] uses modified CEB formula for the development of compressive strength,

$$f_{cm}(t) = f_{cm,28}\left[\exp\left(\frac{s}{2}\left(1-\sqrt{28/t}\right)\right)\right]^2 \tag{A.55}$$

where s is a constant depending on the cement type.

Compliance function is defined as a sum of initial compliance and delayed deformation expressed by terms of creep coefficient

$$J(t,t') = \frac{1}{E_{cm}(t')} + \frac{\varphi(t,t',t_0)}{E_{cm,28}} \tag{A.56}$$

The formula for the creep coefficient reads

$$\begin{aligned}\varphi(t,t',t_0) = \Phi(t',t_0)\Bigg(&2\frac{(t-t')^{0.3}}{(t-t')^{0.3}+14} + \sqrt{\frac{7}{t'}}\sqrt{\frac{t-t'}{t-t'+7}} + \\ &+ 2.5(1-1.086h^2)\sqrt{\frac{t-t'}{t-t'+0.15(V/S)^2}}\Bigg)\end{aligned} \tag{A.57}$$

Coefficient $\Phi(t', t_0)$ takes into account effect of drying before loading, which reduces both basic and drying creep; if $t' = t_0$, $\Phi = 0$, when $t' > t_0$

$$\Phi(t', t_0) = \sqrt{1 - \sqrt{\frac{t' - t_0}{t' - t_0 + 0.15\,(V/S)^2}}} \tag{A.58}$$

Comparing to the previous model [55], this model uses additive split of total creep into basic creep and drying creep. Other remarkable difference is that this model is equilibrated around relative humidity of the environment $h_{\text{env}} = 0.96$ (both for drying creep and shrinkage), while the former had zero contribution to the drying creep for $h_{\text{env}} = 1.0$ and zero contribution to shrinkage was not possible (because for $h_{\text{env}} = 1.0$ the coefficient $\beta(h_{\text{env}}) = -0.2$).

The basic equation for shrinkage is the same as in the previous model GZ, but its components differ

$$\varepsilon_{sh}(t) = \varepsilon_{sh,u}\beta(h)\beta(t) \tag{A.59}$$

$$\varepsilon_{sh,u} = 1000K\sqrt{\frac{30}{f_{cm,28}}} \times 10^{-6} \tag{A.60}$$

$$\beta(h_{\text{env}}) = \left(1 - 1.18h_{\text{env}}^4\right) \tag{A.61}$$

$$\beta(t) = \sqrt{\frac{t - t_0}{t - t_0 + 0.15(V/S)^2}} \tag{A.62}$$

The GL models presented in [54] and later in [53] differ only slightly. The updated model uses constant 900. instead of 1000. in (A.60), and the coefficient 0.15 in (A.57), (A.58), (A.62) is replaced by 0.12.

A.13 SAK model (1993)

The SAK model, presented in [89], [88], provides prediction formulae for concrete creep and shrinkage. The input parameters are cement and water content, relative humidity of the environment, the onset of drying and the age of loading.

The compliance function is split into three parts, the instantaneous deformation (according to [50]), and the delayed deformation composed of specific basic creep and specific drying creep. Time evolution of basic creep and drying creep is described by the same function, with a limit value 1.0 (bounded creep).

$$J(t, t', t_0) = \frac{1}{E_{cm}(t')} + \left(C_B(t') + C_D(t_0)\right)\left(1 - \exp\left(-0.09\,(t - t')^{0.6}\right)\right) \tag{A.63}$$

$$C_B(t') = 1.5(c + w)^2(100w/c)^{2.4}(\ln t')^{-0.67} \times 10^{-5}\ [10^{-10}/\text{MPa}] \tag{A.64}$$

$$C_D(t_0) = 0.0045(100w/c)^{4.2}(c + w)^{1.4}(\ln(V/S))^{-2.2}(1 - h_{\text{env}})^{0.36}t_0^{-0.3}\ [10^{-10}/\text{MPa}] \tag{A.65}$$

In these equation V/S [cm] is the volume-to-surface ratio, and c [kg/m^3], w [kg/m^3] represent the cement and water content, respectively.

Time development of shrinkage is defined as

$$\varepsilon_{sh}(t, t_0) = \varepsilon_{sh,\infty}\left[1 - \exp\left(0.108\,(t - t_0)^{0.56}\right)\right] \tag{A.66}$$

with its ultimate value

$$\varepsilon_{sh,\infty} = -60 + 78\,(1 - \exp(h_{\text{env}})) + 38\ln(w) - 5\,(\ln(V/S))^2 + 4\ln(t_0)\ \ [10^{-5}] \tag{A.67}$$

A.14 fib Model Code 2010 - first draft (2010)

The Model Code 2010 [48] continues from the former CEB-FIP documents, the Model Code 1990 [50] (1993) and from its updated version (1999) [47]. The structure of the equations is almost the same, only several correction factors have been corrected, and the range of the present Model Code has been widened to cover also special concretes. Comparing to the other design codes and material models for concrete creep and shrinkage, the present model covers not only the drying shrinkage, but takes into account also the autogenous shrinkage, which in modern can represent significant part of deformation. The model also covers temperature effects on maturity of concrete, creep and shrinkage.

A.14.1 Instantaneous deformation

The modulus of elasticity is related closely to the mean value of the compressive strength and to the type of aggregates which is used in the concrete mixture. Its value at the age of 28 days is given by

$$E_{c,28} = 21.5\,\alpha_E\,(f_{cm}/10)^{1/3} \tag{A.68}$$

where α_E is a coefficient depending on used aggregates

Development of the modulus of elasticity with time may be estimated from the following expression

$$E_c(t) = E_{c,28}\sqrt{\beta_{cc}(t)} \tag{A.69}$$

where $\beta_{cc}(t)$ is the function expressing the evolution of concrete strength in time.

$$\beta_{cc}(t) = \exp\left[s\left(1 - \sqrt{28/t}\right)\right] \tag{A.70}$$

with t in days and coefficient s depending on the strength class of cement, see Table A.2

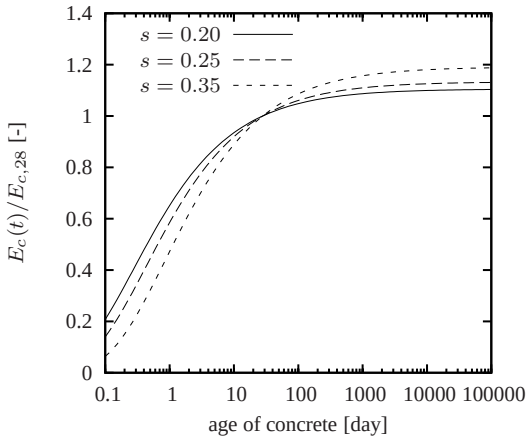

Figure A.1: Development of the elastic modulus in time for different grades of cement.

Time evolution of the elastic modulus is different for different temperatures; it depends on the maturity of concrete, which is closely related to the degree of hydration of cement paste. Higher temperature leads to faster hydration and thus to higher growth of elastic modulus, on the other hand at lower temperature the growth of elastic modulus in time is slower. For this

purpose Model Code introduces temperature adjusted age of concrete, t_T, which replaces the actual age t in (A.70). The temperature adjusted age of concrete is given by

$$t_T = \sum_{i=1}^{n} \Delta t_i \exp\left[13.65 - \frac{4000}{273 + T\,(\Delta t_i)}\right] \tag{A.71}$$

where Δt_i is the number of days where temperature T (in $^\circ$C) prevails.

Effect of the elevated or reduced temperature on the value of elastic modulus in the time of testing (concrete of the age 28 days is assumed) should be also reflected by modifying $E_{c,28}$.

$$E_{c,28,T} = E_{c,28}(1.06 - 0.003\,T) \tag{A.72}$$

where T is temperature in centigrades.

Figure A.2 shows the time evolution of the elastic modulus for five different temperature levels and for $s = 0.25$. The left figure uses only the modified age of concrete according to (A.69) with (A.71); at early ages this results in accelerated development of the elastic modulus for higher temperatures, however, later the same value is approached for all temperatures. This seems to be reasonable, because the elevated or reduced temperature only accelerates of slows down the kinetics of the cement hydration reaction, but the final degree of hydration is independent of the temperature. The right figure combines the temperature adjusted age at loading (A.71) with (A.72); for higher values of temperature the elastic modulus grows faster, but its final value is lower.

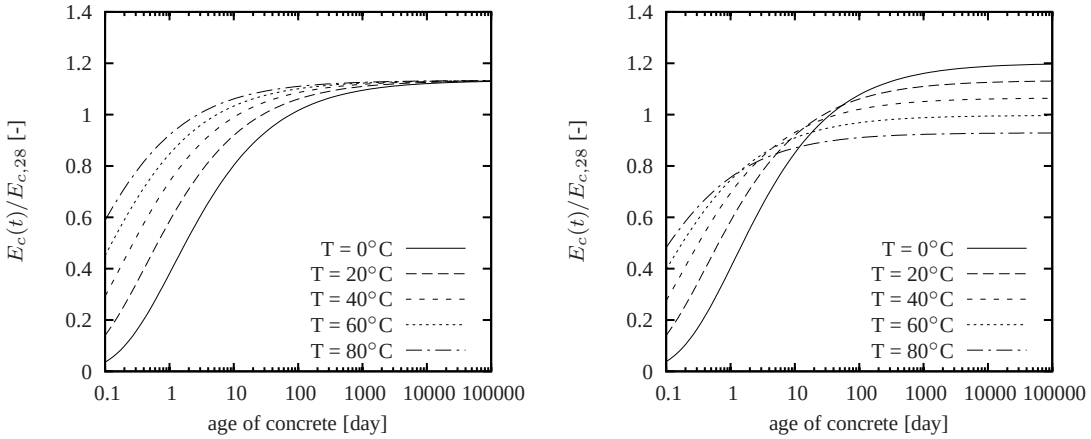

Figure A.2: Development of modulus of elasticity in time according to (a) equation (A.69) with modified age of concrete according to (A.71) (b) equations (A.69), (A.71) and (A.72).

A.14.2 Creep

In the Model Code 2010 [48] concrete is considered to behave as an aging linear visco-elastic material. Range of applicability is restricted to (compressive) stresses lower than 40 % of the mean compressive strength at the age of loading. Temperature should be in interval $0\,^\circ C < T < 80\,^\circ$C (mean $5\,^\circ C < T < 30\,^\circ$C) and relative humidity $h_{\rm env} > 0.4$, which is usually sufficient. The curing time should not exceed 14 days and the age of loading should be at least one day.

The relations used in this model are empirical and were calibrated on the basis of experimental data (creep in compression). Since this prediction model is intended to be used by structural designers, only few parameters are taken into account: characteristic strength of concrete f_{ck}, type of cement, age at loading, duration of loading, cross-sectional properties of the member and the mean relative humidity of the environment.

The present model does not separate the basic creep and drying creep and introduces this compliance function:

$$J(t,t') = \frac{1}{E_c(t')} + \frac{\varphi(t,t')}{E_{c,28}} \tag{A.73}$$

The first fraction in this term corresponds to the instantaneous compliance at the age of loading and the other to creep compliance. The aging creep coefficient is defined as a product of the notional creep coefficient which depends on the age of concrete at loading and the time function expressing the time development of creep after loading.

$$\varphi(t,t') = \varphi_0(t')\beta_c(t,t') \tag{A.74}$$

The notional creep coefficient is given by

$$\varphi_0 = \varphi_{RH}\frac{16.8}{\sqrt{f_{cm}}}\frac{1}{0.1+(t')^{0.2}} \tag{A.75}$$

where

$$\varphi_{RH} = \left[1 + \frac{1-h_{\text{env}}}{0.1\sqrt[3]{h}}\left(\frac{35}{f_{cm}}\right)^{0.7}\right]\left(\frac{35}{f_{cm}}\right)^{0.2} \tag{A.76}$$

and the notional size of member is $h = 2A_c/u$ in [mm]. A_c stands for the cross-sectional area and u is the perimeter in contact with the atmosphere.

Time development of creep after loading is given by

$$\beta_c(t,t') = \left[\frac{t-t'}{\beta_h + t - t'}\right]^{0.3} \tag{A.77}$$

where

$$\beta_h = 1.5h\left[1 + (1.2h_{\text{env}})^{18}\right] + 250\sqrt{35/f_{cm}} \leq 1500\sqrt{35/f_{cm}} \tag{A.78}$$

If provided, the type of cement can be also taken into account by adjusting the age at loading

$$t' = t'_T\left[\frac{9}{2+(t')_T^{1.2}}\right]^{\alpha_c} \tag{A.79}$$

where t'_T is the temperature adjusted age of concrete at loading expressed by (A.71) and α_c is a coefficient depending on the type of cement, see Table A.2.

The effect of temperature should be reflected not only by employing the temperature-adjusted time at loading t'_T, but also by modifying the creep and some other coefficients. The value of β_h in (A.78) is multiplied with β_T

$$\beta_T = \exp\left(\frac{1500}{273+T} - 5.15\right) \tag{A.80}$$

The creep coefficient φ_{RH} in (A.76) is replaced with

$$\varphi_{RH,T} = \varphi_T + (\varphi_{RH} - 1)\,\varphi_T^{1.2} \tag{A.81}$$

with

$$\varphi_T = \exp\left[0.015\,(T-20)\right] \tag{A.82}$$

The transient thermal creep is reflected by adding $\Delta\varphi_{T,trans}$ into (A.74)

$$\varphi(t,t',T) = \varphi_0(t')\beta_c(t,t') + \Delta\varphi_{T,trans} \tag{A.83}$$

where

$$\Delta\varphi_{T,trans} = 0.0004(T-20)^2 \tag{A.84}$$

The Model Code 2010 provides also corrections applicable for the stress range from 0.4 to $0.6f_{cm}$. To reflect this nonlinearity in this interval, the notional creep coefficient φ_0 should be multiplied by $\exp\left[1.5\,(\sigma/f_{cm}(t') - 0.4)\right]$.

A.14.3 Shrinkage

The Model code introduces subdivision of the total shrinkage strain $\varepsilon_{cs}(t,t_0)$ into two components, autogenous shrinkage $\varepsilon_{cas}(t)$ and drying shrinkage or swelling $\varepsilon_{cds}(t,t_0)$.

$$\varepsilon_{cs}(t,t_0) = \varepsilon_{cas}(t) + \varepsilon_{cds}(t,t_0) \tag{A.85}$$

Evolution of the autogenous shrinkage is defined as

$$\varepsilon_{cas}(t) = -\alpha_{as}\left(\frac{f_{cm}/10}{6+f_{cm}/10}\right)^{2.5}\left(1-\exp(-0.2\sqrt{t})\right)\times 10^{-6} \tag{A.86}$$

where α_{as} is a constant depending on the cement class.

The formula for drying shrinkage (or swelling) reads

$$\varepsilon_{cds}(t,t_0) = \varepsilon_{cds0}(f_{cm})\beta_{RH}(h_{\text{env}})\beta_{ds}(t-t_0) \tag{A.87}$$

where

$$\varepsilon_{cds0}(f_{cm}) = (220+110\alpha_{ds1})\exp\left(-\alpha_{ds2}f_{cm}\right)\times 10^{-6} \tag{A.88}$$

$$\beta_{RH}(h_{\text{env}}) = -1.55\left[1-(h_{\text{env}})^3\right] \text{ if } 0.4 < h_{\text{env}} < 0.99\;\beta_{s1} \tag{A.89}$$

$$\beta_{RH}(h_{\text{env}}) = 0.25 \text{ otherwise} \tag{A.90}$$

$$\beta_{s1} = (35/f_{cm})^{0.1} \leq 1.0 \tag{A.91}$$

$$\beta_{ds}(t-t_0) = \sqrt{\frac{t-t_0}{0.035h^2+t-t_0}} \tag{A.92}$$

At high temperatures, the hydration reaction is accelerated and therefore the formula describing the autogenous shrinkage (A.86) must be modified. However, it is sufficient to replace the actual age of concrete t by the temperature-adjusted equivalent age t_T (A.71).

The drying shrinkage (or swelling) formulae change as follows:

$$\varepsilon_{cds}(t,t_0) = \varepsilon_{cds0}(f_{cm})\beta_{RH,T}(h_{\text{env}},T)\beta_{ds,T}(t-t_0,T) \tag{A.93}$$

where

$$\varepsilon_{cds0}(f_{cm}) = (220 + 110\alpha_{ds1}) \exp\left(-\alpha_{ds2} f_{cm}\right) 10^{-6} \tag{A.94}$$

$$\begin{aligned} \beta_{RH,T}(h_{\text{env}}, T) &= -1.55\left(1 - (h_{\text{env}})^3\right)\beta_{s,T} \text{ if } 0.4 < h_{\text{env}} < RH_T/100 && \text{(A.95)} \\ \beta_{RH,T}(h_{\text{env}}) &= 0.25\beta_{s,T} \text{ otherwise} && \text{(A.96)} \end{aligned}$$

$$RH_T = 99\beta_{s1} + \beta_{s1,T} \leq 100 \tag{A.97}$$

$$\beta_{s1} = (35/f_{cm})^{0.1} \leq 1.0 \tag{A.98}$$

$$\beta_{sT} = 1 + \left(\frac{4}{103 - 100h_{\text{env}}}\right)\left(\frac{T-20}{40}\right) \tag{A.99}$$

$$\beta_{s1,T} = \left(\frac{T-20}{25}\right)^3 \tag{A.100}$$

$$\beta_{ds,T}(t - t_0) = \sqrt{\frac{t - t_0}{0.035h^2 \exp(-0.06(T-20)) + t - t_0}} \tag{A.101}$$

Table A.2: Model Code 2010: cement-type dependent constants.

strength class of cement	s	α_{as}	α_{ds1}	α_{ds2}	α_c
32.5 N	0.38	800	3	0.013	-1
32.5 R and 42.5 N	0.25	700	4	0.012	0
42.5 R, 52.5 N, 52.5 R	0.2	600	6	0.012	1

A.15 fib Model Code 2010 - final draft (2012)

In the final draft of the fib Model Code 2010 [49] the expressions for the elastic deformation as well as for shrinkage were adapted from the first draft [48] but the concept of the creep deformation was completely changed – comparing to the first draft, the basic creep is now considered as unbounded. What persists is that the creep deformation is expressed with respect to the modulus at the age of 28 days using the creep coefficient.

Now, similarly to the B3 model, the creep coefficient is decomposed into two parts, the basic creep and drying creep coefficient

$$\varphi(t, t') = \varphi_b(t, t') + \varphi_d(t, t') \tag{A.102}$$

The basic creep coefficient is computed from

$$\varphi_b(t, t') = \frac{1.8}{(f_{cm,28})^{0.7}} \ln\left[\left(\frac{30}{t'_c} + 0.035\right)^2 (t - t') + 1\right] \tag{A.103}$$

where t'_c is the modified age at loading according to (A.79)

The drying creep coefficient is expressed as

$$\varphi_d(t,t') = \beta_{dc,fcm}\,\beta_{dc,RH}\,\beta_{dc,t'}\,\beta_{dc} \tag{A.104}$$

with

$$\beta_{dc,fcm} = \frac{412}{(f_{cm,28})^{1.4}} \tag{A.105}$$

$$\beta_{dc,RH} = \frac{1-h_{\text{env}}}{(h/1000)^{1/3}} \tag{A.106}$$

$$\beta_{dc,t'} = \frac{1}{0.1+(t'_{mod})^{0.2}} \tag{A.107}$$

$$\beta_{dc} = \left[\frac{t-t'}{\beta_h + t - t'}\right]^{\gamma_{dc}} \tag{A.108}$$

where

$$\gamma_{dc} = \frac{1}{2.3 + 3.5\,(t'_{mod})^{-0.5}} \tag{A.109}$$

$$\beta_h = 1.5h + 250\sqrt{35/f_{cm}} \le 1500\sqrt{35/f_{cm}} \tag{A.110}$$

The meaning of the symbols is the same as in the Section A.14.

The effect of temperature should be reflected not only by employing the temperature-adjusted time at loading t'_T, but also by modifying the basic and drying creep coefficients and other constants. The value of β_h in (A.110) is multiplied with β_T

$$\beta_T = \exp\left(\frac{1500}{273+T} - 5.12\right) \tag{A.111}$$

The basic creep coefficient φ_b in (A.103) is multiplied by φ_T from equation (A.82) and the drying creep coefficient by $(\varphi_T)^{1.2}$. The transient thermal creep is reflected by adding $\Delta\varphi_{T,trans}$ to (A.102) with $\Delta\varphi_{T,trans}$ defined in (A.84)

A.16 ACI 209R-92 (1992, reapproved 1997), ACI 209.2R-08 (2008)

In the American design codes ACI 209R-92 [2] and ACI 209.2R-08 [3], the evolution of creep and shrinkage is described by the same type of hyperbolic function based on the Ross formula. The total stress-induced strain can be expressed by means of the compliance function

$$J(t,t') = \frac{1+\varphi(t,t')}{E(t')} \tag{A.112}$$

which, comparing e.g. to Model Codes [48] does not relate the creep coefficient to the 28-days elastic modulus, but to the instantaneous.

A.16.1 Instantaneous deformation

The elastic modulus (modulus of elasticity, which corresponds to the deformation caused by load from 1 to 5 minutes) can be estimated from the mean compressive strength.

$$E(t) = 0.043\gamma_c^{1.5}\sqrt{\frac{t}{a+bt}f_{cm,28}}\ [\mathrm{MPa}] \tag{A.113}$$

where γ_c [kg/m^3] is concrete density and a and b are constants depending on the cement and curing type.

A.16.2 Creep

The creep is deemed to be bounded; the time development of creep coefficient is described by

$$\varphi(t,t') = \frac{(t-t')^{\psi}}{d+(t-t')^{\psi}}\varphi_u \tag{A.114}$$

where φ_u is the ultimate creep coefficient and d and ψ are constants depending on the specimen shape and size. The ultimate creep coefficient can be taken as 2.35 and if more complex analysis is required, it can be multiplied by six correction factors (type of curing, ambient relative humidity, volume-to-surface ratio, slump, aggregate grades, and air content). Parameters d and ψ can be taken as 10. and 0.6, respectively, or in case when more accurate prediction is necessary, $\psi = 1.0$ and $d = f$ from (A.116)

A.16.3 Shrinkage

The formula proposed by ACI committee 209, which lumps together drying shrinkage, autogenous shrinkage, and carbonation shrinkage has the following form

$$\varepsilon(t,t_0) = \frac{(t-t_0)^{\alpha}}{f+(t-t_0)^{\alpha}}\varepsilon_{shu} \tag{A.115}$$

where f reflects the notional size of the drying member, ε_{shu} is the ultimate shrinkage and $\alpha = 1.0$.

$$f = 26\exp\left(1.42V/S\times 10^{-2}\right) \tag{A.116}$$

with V being the volume (in mm^3) and S the area of the drying surface (in mm^2).

If the particular information about the composition and curing conditions are missing (or are similar to the "standard conditions"), the ultimate shrinkage can be taken as

$$\varepsilon_{shu} = 780\times 10^{-6} \tag{A.117}$$

which is the average value of the ultimate shrinkage based on 356 shrinkage data points and according to [2] also $f = 35$.

According to [2] the size and shape of the drying and shrinking specimen can be treated using two different approaches. The first one consists in replacing the actual drying time $t - t_0$ in A.115 by $(t - t_0)/\tau_{sh}$ where τ_{sh} is the shrinkage half-time [40]. The other approach uses correction factor $\gamma_{sh,vs}$ multiplying the value of the ultimate shrinkage.

The shrinkage half-time is defined as

$$\tau_{sh} = 600 \left(\frac{\lambda_s d_c}{150} \right)^2 \frac{C_1}{(C_1)_a} \tag{A.118}$$

where λ_S is coefficient depending on the shape of cross section (1.00 for an infinite long slab, 1.15 for an infinite long cylinder, 1.25 for an infinite long square prism, 1.30 for sphere and 1.55 for a cube), d_c is twice the volume to surface ratio in mm, C_1 is the drying diffusivity of concrete (approx. 10 mm^2/day), and $(C_1)_a$ is the age dependence coefficient in the form

$$(C_1)_a = C_7 \lambda_T \left(0.05 + \sqrt{6.3/t_0} \right) \tag{A.119}$$

with $C_7 = w/8 - 12$ but not more than 21 or less than 7, and

$$\lambda_T = \frac{T}{t_0} \exp\left(\frac{5000}{T_0} - \frac{5000}{T} \right) \tag{A.120}$$

where T is the concrete temperature and T_0 is the reference temperature (both in Kelvin).

Using the second approach, the value of the ultimate shrinkage can be corrected by factors γ depending on particular conditions (similar to creep).

The specimen shape and thickness can be captured either by $\gamma_{sh,vs}$ (volume-to-surface ratio method) or by $\gamma_{sh,d}$ (average thickness method).

$$\varepsilon_{shu} = 780 \gamma_{sh,tc} \gamma_{sh,RH} \gamma_{sh,vs} \gamma_{sh,s} \gamma_{sh,\psi} \gamma_{sh,c} \gamma_{sh,\alpha} \times 10^{-6} \tag{A.121}$$

$$\varepsilon_{shu} = 780 \gamma_{sh,tc} \gamma_{sh,RH} \gamma_{sh,d} \gamma_{sh,s} \gamma_{sh,\psi} \gamma_{sh,c} \gamma_{sh,\alpha} \times 10^{-6} \tag{A.122}$$

All shrinkage correction factors are summarized in the table A.2. The product of correction factors should not be less than 0.2; for seasonal drying and wetting conditions, $\varepsilon_{shu} \geq 100 \times 10^{-6}$ and $\varepsilon_{shu} \geq 150 \times 10^{-6}$ if concrete is under sustained drying.

A.17 JSCE (2007)

The formulae in the Japanese standard [74] for ordinary (compressive strength up to 55 MPa or 70 MPa if water-to-cement ratio was decreased in order to increase strength) and high-strength concrete are different. Comparing to other standards, the difference consists not only in few constants, but in the whole structure.

A.17.1 Shrinkage

The Japanese standard highly recommends experimental verification of the predicted results. Otherwise all ultimate shrinkage strains should be multiplied by factor 1.5. In the linear analysis of statically indeterminate structures the shrinkage strain can be taken as 150×10^{-6}. This value already covers shrinkage reduction due to creep of concrete.

Temperature-adjusted age of concrete (for temperature different from the room temperature) is captured by the fib formula (A.71).

Shrinkage of an ordinary concrete is defined by

$$\varepsilon_{sh}(t, t_0) = \left(1 - \exp\left(-0.108 \left(t - t_0 \right)^{0.56} \right) \right) \varepsilon_{sh,u} \tag{A.123}$$

Table A.3: ACI 209R-92: shrinkage correction factors

factor	influence	formula	remark
$\gamma_{sh,tc}$	curing time	$1.202 - 0.2337 \log(t_0)$	for moist curing
		1.0	for steam curing 1 - 3 days curing
$\gamma_{sh,RH}$	ambient humidity	$1.4 - 1.02 h_{\text{env}}$	$0.4 \leq h_{\text{env}} \leq 0.8$
		$3.0 - 3.0 h_{\text{env}}$	$0.8 \leq h_{\text{env}} \leq 1.0$
		≥ 1.0	$h_{\text{env}} \leq 0.4$
$\gamma_{sh,vs}$	notional size	$1.2 \exp(-0.00472 V/S)$	
$\gamma_{sh,d}$	average thickness	$1.23 - 0.006 V/S$	$37.5 \leq V/S \leq 95.$, $t - t_0 \leq 1$ year
		$1.17 - 0.00456 V/S$	$37.5 \leq V/S \leq 95.$, $t - t_0 \geq 1$ year
$\gamma_{sh,s}$	slump	$0.89 + 0.00161 s$	s = slump [mm]
$\gamma_{sh,\psi}$	aggregates	$0.3 + 0.014\psi$	$\psi \leq 50\%$
		$0.9 + 0.002\psi$	$\psi > 50\%$
	ψ = fine / total agg.	by weight	
$\gamma_{sh,c}$	cement content	$0.75 + 0.00061 c$	c = cement content [kg/m^3]
$\gamma_{sh,\alpha}$	air content	$0.95 + 0.008\alpha \geq 1$	α = air content [%]

where

$$\varepsilon_{sh,u} = \left[-50 + 78\left(1 - \exp\left(h_{\text{env}}\right)\right) + 38 \ln(w) - 5\left(\ln\left(0.1 V/S\right)\right)^2\right] \times 10^{-6} \tag{A.124}$$

is the ultimate value of shrinkage with the volume-to-surface V/S ratio in mm. The formulae (A.123) and (A.123) are restricted to h_{env} in the interval from 0.45 to 80, water content w from 130 to 230 kg/m^3, the volume-to-surface ratio from 100 to 300 mm, and the water-to-cement ratio from 0.4 to 0.65. The formula (A.124) was derived for Portland cement.

Total shrinkage of concrete with the mean compressive strength exceeding 55 MPa is composed of two parts - drying shrinkage and autogenous shrinkage.

$$\varepsilon_{sh}(t, t_0) = \varepsilon_{sh,d}(t, t_0) + \varepsilon_{sh,a}(t, t_0) \tag{A.125}$$

The formula for the drying shrinkage then reads

$$\varepsilon_{sh,d}(t, t_0) = \frac{t - t_0}{\beta + t - t_0} \varepsilon_{sh,d\infty} \tag{A.126}$$

where

$$\beta = \frac{4w\sqrt{V/S}}{100 + 0.7 t_0} \tag{A.127}$$

and

$$\varepsilon_{sh,d\infty} = \frac{\alpha\ w\ (1 - h_{\text{env}})}{1 + 150 \exp(-500/f_{cm,28})} \cdot \frac{10^{-6}}{1 + \left(15 \exp\left(0.007 f_{cm,28}\right) + 0.25 w\right) t_0 10^{-4}} \tag{A.128}$$

In the last equation (A.128) α represents the influence of cement type (11 for ordinary or low-heat cement and 15 for high early-strength cement). Formulae (A.125) – (A.128) are

applicable for water content w from 130 to 230 kg/m^3, the volume-to-surface ratio from 100 to 300 mm, h_{env} from 0.4 to 0.9, and t_0 from 1 to 98 days (if $t_0 > 98$ days then $t_0 = 98$).

The autogenous shrinkage in (A.125) is described by

$$\varepsilon_{sh,a}(t,t_0) = 3070\,\gamma\exp(-7.2w/c)\left[1-\exp\left(-a(t-t_s)^b\right)\right]\times 10^{-6} \tag{A.129}$$

where t_s is the start of setting in days and a and b are composition-dependent constants given in the stadard (e.g. for $w/c = 0.4$ $a = 0.1$ and $b = 0.7$).

A.17.2 Creep

Similarly to shrinkage, the standard [74] provides different formulae for creep of normal and high-strength concrete.

The following relation describes the specific creep of an ordinary concrete

$$C(t,t') = \left[1-\exp\left(-0.09(t-t')^{0.6}\right)\right]\cdot(C_{b,\infty}+C_{d,\infty}) \tag{A.130}$$

The ultimate values of the basic and drying specific creep are defined by

$$C_{b,\infty} = 15(c+w)^2(w/c)^{2.4}\left(\ln t'\right)^{-0.67}\times 10^{-10}/\mathrm{MPa} \tag{A.131}$$

$$C_{d,\infty} = 4500(c+w)^{1.4}(w/c)^{4.2}\left(\ln\left(0.1V/S\right)\right)^{-2.2}\left(1-h_{\mathrm{env}}\right)^{0.36}t_0^{-0.3}\times 10^{-10}/\mathrm{MPa} \tag{A.132}$$

Specific creep of concrete with compressive strength in interval from 55 MPa (or 70 MPa if the strength was reached by decrease in water-to-cement ratio) to 80 MPa is described by

$$C(t,t') = \frac{4w(1-h_{\mathrm{env}})+350}{12+f_{cm}(t')}\ln(t-t'+1) \tag{A.133}$$

B Implementation in the Finite Element Package OOFEM

B.1 Concept of the staggered approach

All the simulations of creep and shrinkage (except for the basic creep) used a numerical scheme referred to as the "staggered approach"; this scheme is outlined in Fig. B.1. The analysis is run in consecutive time steps. The length of the time steps is usually nonuniform, the steps are shorter during and soon after loading and/or temperature changes. The maximum step length depends on the stability and the demanded accuracy of the sub-problems.

In every time step, the transport problem is solved first and the field variables (relative humidity and/or temperature) are exported and read by the material for the structural analysis. The problem is not fully coupled, i.e. the results of the structural analysis do not influence the transport properties.

The FE meshes of the two problems do not have to coincide; this brings about nonnegligible advantages regarding the computational and memory requirements. The size of the elements in the FE mesh for the transport problem is usually more graded than for the structural analysis where the mesh is more uniform.

In the current implementation, the time steps are either a priori defined in one of the sub-problems or they are defined in the control file of the staggered analysis. However, in some cases it would be advantageous to adjust the step length according to the convergence rate – both the structural and transport problems can have convergence issues. The other improvement could be not to solve both sub-problems in every time step, but instead, to skip few time steps in one of the sub-problems. This procedure could be applied when the time step length becomes unnecessarily fine in one sub-problem but appropriate for the other.

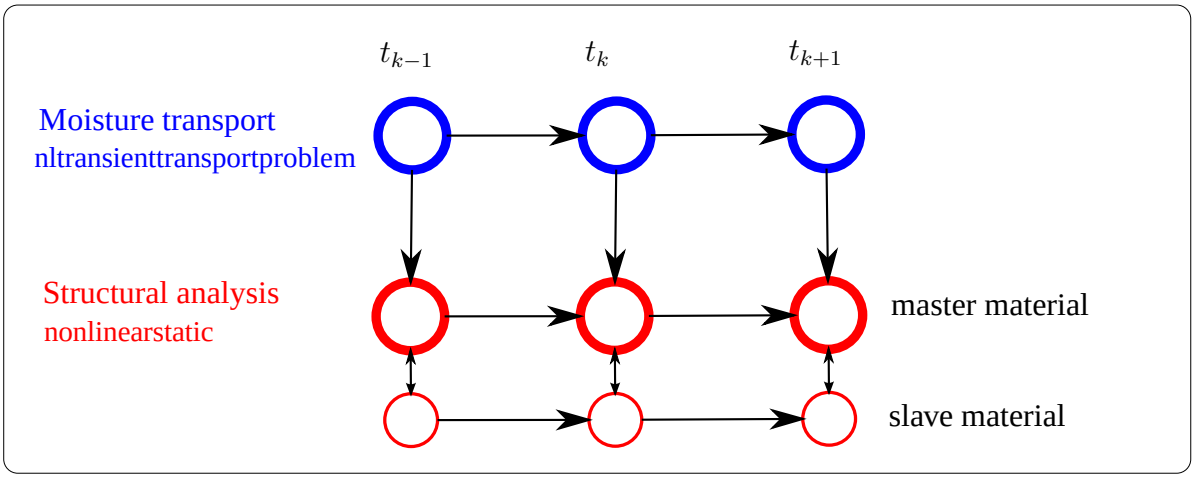

Figure B.1: Schematic algorithm of the staggered approach.

B.2 Models for (heat and) moisture transport

In program OOFEM, all the material models for the heat and/or moisture transport are derived from the generic abstract class `TransportMaterial` providing methods that are common for such problems: mainly the methods for computing the capacity and conductivity matrices.

The state and the internal variables characteristic of the solved problem are managed by a complementary class to the given material model. This class has the same name as the material extended with "Status".

In each Gauss point, there are two sets of state variables. The first one is the value from the end of the previous step and the second one, usually of the same name extended by "Temp", is the temporary unequilibrated value. When the iteration/convergence criteria are met, the "Temp" value replaces the value from the previous step and the analysis advances to the next time step.

The scheme of the classes for moisture and coupled heat and moisture transport is outlined in Fig. B.2.

Another purely abstract class which is derived directly from the `TransportMaterial` class represents a parent class for all materials for moisture transport, it is labeled `IsotropicMoistureTransferMaterial`. It defines methods for computing moisture permeability and moisture capacity and a method for assembling the conductivity matrix of an isotropic transport material in 1D/2D/3D.

The first and simplest material class inherited from `IsotropicMoistureTransferMaterial` is the isotropic linear material for moisture transfer, `IsoLinMoistureMaterial`, this class returns only two constants: moisture capacity and permeability.

The second derived class `BazNajMoistureTransferMaterial` implements the model based on Bažant and Najjar [39], in this model the desorption isotherm is assumed to be a straight line which means that the moisture capacity is constant. However, the moisture permeability (in this case equal to diffusivity) is highly nonlinear, see equation (5.14).

The third inherited class is a general nonlinear isotropic model `NlIsoMoistureMaterial` providing 7 options for an isotherm (linear, bilinear, piece-wise linear, according to Ricken [67], Künzel [67], Hansen [52] and BSB [44]) and 4 options for permeability (piece-wise linear, Bažant and Najjar expression for diffusivity [39], permeability according to Xi [92], and according to Kunzel [67]). The implementation of Künzel's material is simplified in this class, only the moisture distribution is solved, the temperature field is prescribed. However, this implementation becomes very handy when the temperature is normal and almost constant. The analysis allows for longer time steps without losing numerical stability and also the memory requirements are lower.

The last two models derived directly from the `TransportMaterial` class serve for the simultaneous heat and moisture transport. In case of `HeMoBazNajMaterial` the processes are uncoupled (=zero off-diagonal terms), the Bažant and Najjar [39] model is used for moisture diffusion and the isotropic linear model for heat conduction. This model was used primarily for calibration of the MPS model. The last mentioned class `HeMoKunzelMaterial` implements Künzel's [67] model with several extensions.

B.3 Models for the analysis of creep and shrinkage

All material models for concrete creep and shrinkage (see Fig. B.3) are derived from the abstract class `RheoChainMaterial` which is inherited from the generic class `StructuralMaterial`. In the class `RheoChainMaterial`, the compliance function of the material is always approximated using the Dirichlet series. For this reason this class defines methods for evaluating the compliance function, determining stiffnesses and characteristic times (retardation or relaxation) of the rheological chain, and computing the incremental modulus and shrinkage

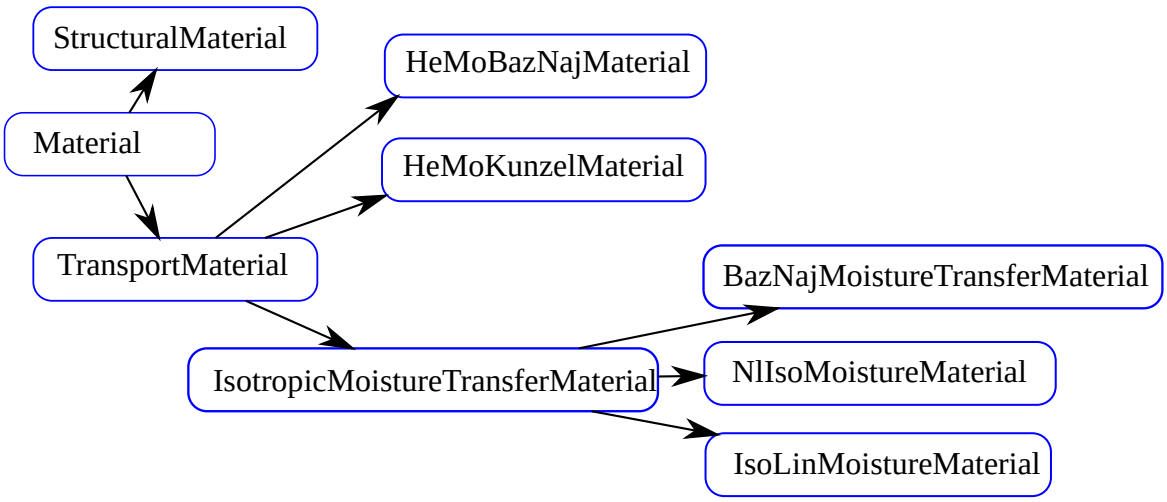

Figure B.2: Class hierarchy - models for (heat and) moisture transfer.

strain. Three classes are derived from this class.

The oldest one, `MaxwellChainMaterial` approximates the compliance function by the Maxwell chain whose parameters are determined in each time step using the least-squares method. Since the Kelvin chain is more natural for the description of the compliance function, the first class is kept only for compatibility of the derived classes `B3Material`, `CebFip78Material` and `DoublePowerLawMaterial`.

The newer implementation of the B3 model – `B3SolidMaterial` – is inherited from the `KelvinChainMaterial` class. This version is based on the concept of solidification, a special type of aging, which enables to determine the properties of the Kelvin chain only once on the beginning of the simulation and to store them. The material model implemented in this class can simulate the drying creep and creep at elevated/variable temperatures using the microprestress theory. This class also allows for implementation of different and more general types of aging.

The newest version of the B3/MPS model is derived from the class `KelvinChainSolidMaterial` which exploits the algorithm presented in Appendix C. The class covers only the part of the compliance function which is specific for the solidifying Kelvin chain. Except for the Kelvin chain it contains also one elastic spring but it has a different meaning than the instantaneous modulus E_0 in the B3 model. It covers the compliance which occurs before the fastest unit of the Kelvin chain starts deforming; the compliance function was introduced in (4.1). The properties of the components in the solidifying Kelvin chain are computed from the retardation spectrum of the compliance function [62]. The rest of the compliance function is added to the compliance of the Kelvin chain in the class `MPSMaterial`. The algorithm uses the numerically more efficient and straightforward approach based on viscosity instead of microprestress. The material behavior remains fully equivalent to the original formulation. The new implementation also allows for unconventional values of exponent p (or $\tilde{p}$).

The true benefit of the object-oriented design in the program OOFEM is represented by the extension of the MPS model for tensile cracking. Instead of extending the `MPSMaterial` class, the new implementation makes use of the already existing isotropic damage model for tensile failure. The new viscoelastic model with cracking called `MPSDamMaterial` is derived from `IsotropicDamageMaterial1` class. The main difference is that the model

replaces the conventional elastic modulus with the incremental modulus computed by the so-called slave material; the other function of the "slave" material is to return the eigenstrains due to shrinkage and creep. On one hand this approach made the code is more transparent and saved non-negligible time of programming, on the other hand the demands on computer memory have increased. In every Gauss-point it is now necessary to store two material statuses instead of one.

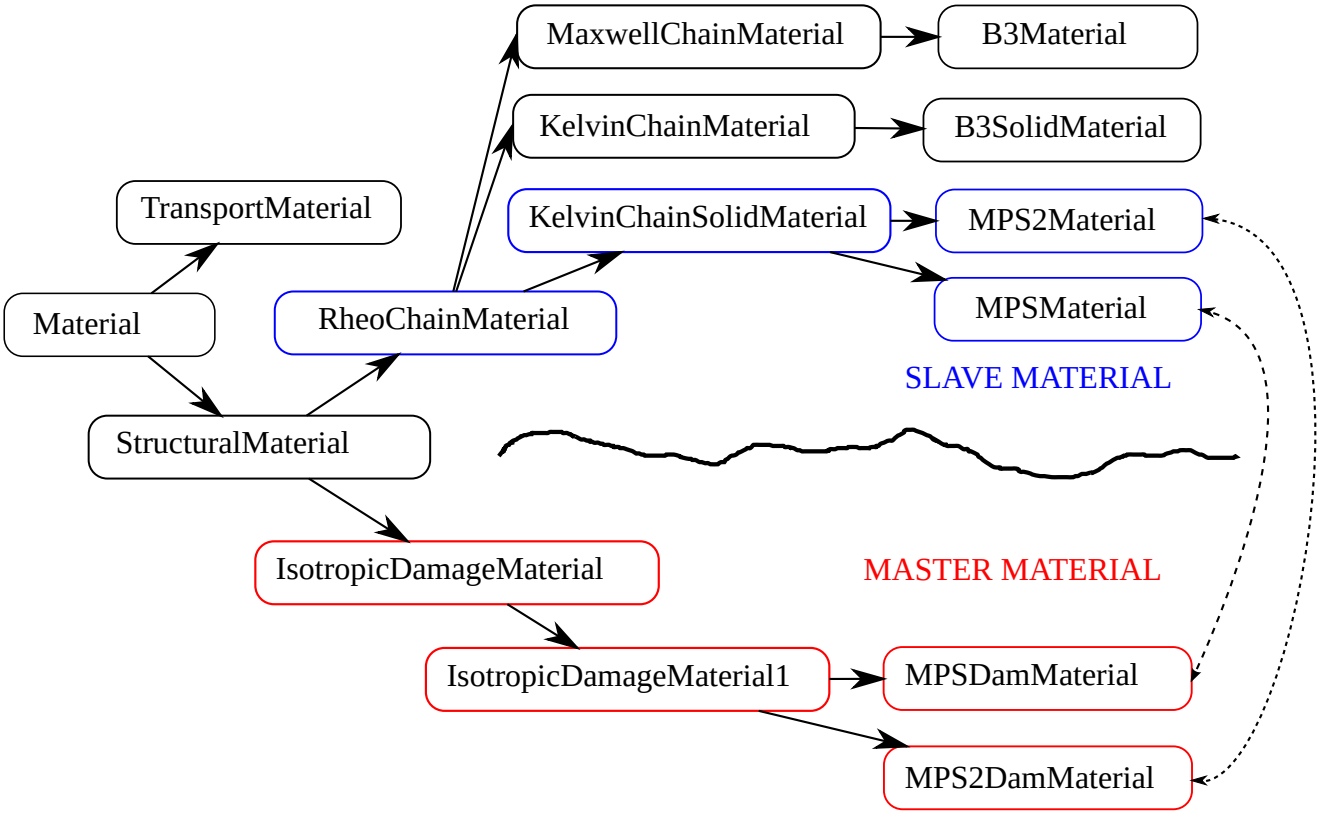

Figure B.3: Hierarchy of the B3/MPS and damage material classes.

C Numerical algorithm for the MPS theory

This section presents the step-by-step algorithm [22] for the material model based on the Microprestress-solidification theory which has been implemented into the finite element package OOFEM and was used in all numerical simulations of creep and shrinkage.

C.1 Incremental stress-strain relation for creep and shrinkage

The analysis starts at time t_0 which is the time when the temperature or humidity starts changing or the specimen is loaded. At this time the values of the internal variables are set to their initial value.

$$\eta_{f0} \equiv \eta_f(t_0) = t_0/q_4 \tag{C.1}$$

$$\sigma_{v\mu,0} = 0, \quad \mu = 1, 2 \dots M \tag{C.2}$$

$$t_{e,0} = t_0 \tag{C.3}$$

$$\psi_{r,0} = \beta_{rh}(h(t_0))\beta_{rT}(T(t_0)) \tag{C.4}$$

$$\tilde{\eta}_0 = \frac{\eta_1}{\psi_{r,0}} \tag{C.5}$$

$$k = 0 \tag{C.6}$$

where $\sigma_{v\mu,0}$ is the stress in the dashpot of the μ-th unit of the solidifying Kelvin chain.

Then for every time-step from t_k to $t_{k+1} = t_k + \Delta t_k$, $k = 1, 2, \dots N$, where N is the number of time steps, and for given history of temperature and pore relative humidity repeat the following steps.

1. Evaluate factors

$$\psi_{e,k+1/2} = \beta_{eh}(h_{k+1/2})\beta_{eT}(T_{k+1/2}) \tag{C.7}$$

$$\psi_{r,k+1} = \beta_{rh}(h_{k+1})\beta_{rT}(T_{k+1}) \tag{C.8}$$

$$\psi_{s,k+1/2} = \beta_{sh}(h_{k+1/2})\beta_{sT}(T_{k+1/2}) \tag{C.9}$$

2. Compute the equivalent age and the volume growth function v

$$\Delta t_{e,k} = \psi_{e,k+1/2}\Delta t_k, \qquad t_{e,k+1} = t_e + \Delta t_{e,k} \tag{C.10}$$

$$v_{k+1/2} = v(t_{e,k} + 0.5\Delta t_{e,k}) \tag{C.11}$$

3. Calculate the increment of reduced time and auxiliary factors

$$\Delta t_{r,k} = \frac{1}{2}(\psi_{r,k} + \psi_{r,k+1})\Delta t_k \tag{C.12}$$

$$\beta_{\mu,k} = \mathrm{e}^{-\Delta t_{r,k}/\tau_\mu}, \qquad \mu = 1, 2, \dots M \tag{C.13}$$

$$\lambda_{\mu,k} = (1 - \beta_{\mu,k})\frac{\tau_\mu}{\Delta t_{r,k}}, \qquad \mu = 1, 2, \dots M \tag{C.14}$$

4. Prepare factors for viscosity evaluation and compute viscosity η_f at the end of the step

- $p = 2$ (or equivalently $\tilde{p} = 2$)

$$A = \sqrt{\frac{\mu_S \left| T_{k+1} \ln h_{k+1} - T_k \ln h_k \right|}{\Delta t_k T_0}} \tag{C.15}$$

$$B = \sqrt{\frac{\psi_{s,k+1/2}}{q_4}} \tag{C.16}$$

if $AB\Delta t_k > 10^{-6}$

$$\tilde{e} = \mathrm{e}^{-2AB\Delta t_k} \tag{C.17}$$

$$\eta_{k+1} = \frac{B}{A} \frac{B(1-\tilde{e}) + A\eta_k(1+\tilde{e})}{B(1+\tilde{e}) + A\eta_k(1-\tilde{e})} \tag{C.18}$$

else

$$\eta_{k+1} = \frac{\eta_k + B^2 \Delta t_k}{1 + A^2 \eta_k \Delta t_k} \tag{C.19}$$

- $p = \infty$ (or equivalently $\tilde{p} = 1$)

$$A = k_3 \frac{\left| T_{k+1} \ln h_{k+1} - T_k \ln h_k \right|}{\Delta t_k T_0} \tag{C.20}$$

where k_3 introduced in (7.5) is in this case a dimensionless constant

$$B = \frac{\psi_{s,k+1/2}}{q_4} \tag{C.21}$$

if $A\Delta t_k < 10^{-14}$

$$\eta_{k+1} = \eta_k + B\Delta t_k \tag{C.22}$$

if $A\Delta t_k > 30$

$$\eta_{k+1} = \eta_k \tag{C.23}$$

else

$$\eta_{k+1} = \left(\eta_k - \frac{B}{A} \right) \exp(-A\Delta t_k) + \frac{B}{A} \tag{C.24}$$

- $p < 0$ (or equivalently $\tilde{p} \in (0, 1)$)

$$A = \mu_S^{\frac{1}{p-1}} \cdot \frac{\left| T_{k+1} \ln h_{k+1} - T_k \ln h_k \right|}{\Delta t_k T_0} \tag{C.25}$$

$$B = \frac{\psi_{s,k+1/2}}{q_4} \tag{C.26}$$

The value of viscosity at the end of the time step, η_{k+1}, is computed using the Newton's method.

(a) set $\Delta\eta_k = 0$, $\delta\eta_k = 0$, $\eta_{min} = 10^{-6}$

(b) repeat until error $<$ tolerance

$$f = \frac{\Delta\eta_k}{\Delta t_k} + A(\eta_k + \Delta\eta_k)^{p/(p-1)} - B \tag{C.27}$$

$$\delta f = \frac{1}{\Delta t_k} + A\frac{p}{p-1}(\eta_k + \Delta\eta_k)^{1/(p-1)} \tag{C.28}$$

$$\delta\eta_k = -\frac{f}{\delta f} \tag{C.29}$$

$$\Delta\eta_k = \Delta\eta_k + \delta\eta_k \tag{C.30}$$

if $\eta_k + \Delta\eta_k < 0$ set $\Delta\eta_k = \eta_{min} - \eta_k$

$$\text{error} = \left|\frac{\delta\eta_k}{\Delta\eta_k}\right| \tag{C.31}$$

(c) evaluate viscosity at the end of the time step

$$\eta_{k+1} = \eta_k + \Delta\eta_k \tag{C.32}$$

5. Evaluate the modified viscosity and its increment

$$\tilde{\eta}_{k+1} = \frac{\eta_{k+1}}{\psi_{r,k+1}} \tag{C.33}$$

$$\Delta\tilde{\eta}_k = \tilde{\eta}_{k+1} - \tilde{\eta}_k \tag{C.34}$$

6. Compute the viscous flow strain increment at constant stress and the incremental viscous flow compliance

if $|\Delta\tilde{\eta}_k| > 10^{-4}\,\tilde{\eta}_k$

$$L_k = \ln\left(1 + \frac{\Delta\tilde{\eta}_k}{\tilde{\eta}_k}\right) \tag{C.35}$$

$$\Delta\varepsilon''_{f,k} = \frac{\Delta t_k}{\Delta\tilde{\eta}_k} L_k \boldsymbol{C}_v \sigma_k \tag{C.36}$$

$$\bar{C}_{f,k} = \frac{\Delta t_k}{\Delta\tilde{\eta}_k}\left(1 - \frac{\tilde{\eta}_k}{\Delta\tilde{\eta}_k} L_k\right) \tag{C.37}$$

else

$$\Delta\varepsilon''_{f,k} = \frac{\Delta t_k}{\tilde{\eta}_k}\left[1 - \frac{\Delta\tilde{\eta}_k}{2\tilde{\eta}_k} + \frac{1}{3}\left(\frac{\Delta\tilde{\eta}_k}{\tilde{\eta}_k}\right)^2\right]\boldsymbol{C}_v \sigma_k \tag{C.38}$$

$$\bar{C}_{f,k} = \frac{\Delta t_k}{\tilde{\eta}_k}\left(\frac{1}{2} - \frac{\Delta\tilde{\eta}_k}{3\tilde{\eta}_k}\right) \tag{C.39}$$

7. Compute the incremental modulus

$$\bar{E}_k = \left(\frac{1}{E_0} + \frac{1}{v_{k+1/2}} \sum_{\mu=1}^{M} \frac{1-\lambda_{\mu,k}}{E_\mu^\infty} \bar{C}_{f,k} \right)^{-1} \tag{C.40}$$

8. Evaluate the strain increment due to creep (at constant stress), and the increments of shrinkage and thermal strain

$$\Delta\varepsilon''_k = \frac{\boldsymbol{C}_v}{v_{k+1/2}} \sum_{\mu=1}^{M} \frac{1-\beta_{\mu,k}}{E_\mu^\infty} \sigma_{v\mu,k} + \Delta\varepsilon''_{f,k} \tag{C.41}$$

$$\Delta\varepsilon_{sh,k} = k_{sh}(h_{k+1} - h_k) \tag{C.42}$$

$$\Delta\varepsilon_{T,k} = \alpha_T(T_{k+1} - T_k) \tag{C.43}$$

9. For given strain increment compute the stress increment

$$\Delta\sigma_k = \bar{E}_k \boldsymbol{D}_\nu (\Delta\varepsilon_k - \Delta\varepsilon''_k - \Delta\varepsilon_{sh,k} - \Delta\varepsilon_{T,k}) \tag{C.44}$$

10. Update internal variables and increment the step counter

$$\sigma_{v\mu,k+1} = \lambda\mu, k\Delta\sigma_k + \beta_{\mu,k}\sigma_{v\mu,k} \tag{C.45}$$

$$k = k + 1 \tag{C.46}$$

NOTES:

- To diminish the sensitivity to the choice of pore relative humidity of sealed specimens and to reduce the effect of temperature cycles on concrete creep (see Section 7.1), replace $|T_{k+1} \ln h_{k+1} - T_k \ln h_k|$ in (C.15), (C.20), (C.25) with $\left| \frac{(T_{k+1}+T_k)(h_{k+1}-h_k)}{h_{k+1}+h_k} - \kappa_T(T_{k+1} - T_k) \right|$, where κ_T is defined in (7.2).

C.2 Algorithm for creep and shrinkage with cracking

The extension of the MPS model for tensile cracking is in the current implementation based on the isotropic damage model which is simple but fully sufficient for the present purposes. Two different approaches are implemented. The first one (#1) reduces the stiffness only in the directions of tension (in case the tensile strength is exceeded). A full stiffness is restored in compression and after unloading from tension. This is useful mainly for realistic simulation of shrinkage experiments; during the first part of drying the surface layer of the specimens is in tension and cracking occurs, however, in the later stage of drying the stresses redistribute and the outer part becomes compressed. If the original stiffness was not restored, the final shrinkage deformation would have been smaller.

The other approach (#2) is the standard isotropic damage model which reduces the stiffness equally in all directions independently of loading. This approach leads to faster convergence because the secant stiffness can be used instead of the incremental viscoelastic stiffness which must be used in the first approach. The second approach becomes useful when the loading is

monotonic or when the benefit of the accelerated computation prevails over the consequences of the reduced/underestimated stiffness in compression.

Both concepts use the Rankine definition of the equivalent deformation defined as the biggest principal effective stress divided by the elastic modulus. The increment of the effective stress in the time step k is approximated as

$$\Delta\sigma_{\mathrm{eff},k} = \bar{E}_k \boldsymbol{D}_\nu (\Delta\varepsilon_k - \Delta\varepsilon''_k - \Delta\varepsilon_{sh,k} - \Delta\varepsilon_{T,k}) \tag{C.47}$$

which has the same form as (C.44). Only now the stress is interpreted as effective.

The following algorithm is used to compute the stress vector (in each time step and until the iteration criteria are met):

1. Compute effective stress

$$\sigma_{\mathrm{eff},k+1} = \sigma_{\mathrm{eff},k} + \bar{E}_k \boldsymbol{D}_\nu (\Delta\varepsilon_k - \Delta\varepsilon''_k - \Delta\varepsilon_{sh,k} - \Delta\varepsilon_{T,k}) \tag{C.48}$$

2. Compute principal effective stresses $\sigma_{\mathrm{eff},1}$, $\sigma_{\mathrm{eff},2}$, $\sigma_{\mathrm{eff},3}$

3. Evaluate equivalent deformation

$$\tilde{\varepsilon} = \max(\sigma_{\mathrm{eff},1}, \sigma_{\mathrm{eff},2}, \sigma_{\mathrm{eff},3})/E \tag{C.49}$$

4. If the stress exceeds the material strength, initialize the fracture parameters.

   The tensile strength f_t and the fracture energy G_f can be either explicitly specified or evaluated according to the *fib* recommendations [49] based on the compressive strength and age (equivalent time t_e of the MPS theory in this case) as

$$f_{cm} = \exp\left[s\left(1 - \sqrt{28/t_e}\right)\right] f_{cm,28} \tag{C.50}$$

$$f_{tm} = 0.3(f_{cm} - 8\ \mathrm{MPa})^{2/3} \tag{C.51}$$

$$G_f = 73(f_{cm})^{0.18} \tag{C.52}$$

   where s is the cement-type-dependent parameter specified in Table A.2. The resulting tensile strength is in MPa and the fracture energy in N/m.

   The strain at peak stress ε_0 and the fracturing strain ε_f are given by

$$\varepsilon_0 = f_t/E \tag{C.53}$$

   - linear softening:

$$\varepsilon_f = \frac{2G_f}{f_t\, h} \tag{C.54}$$

   - exponential softening:

$$\varepsilon_f = \frac{G_f}{f_t\, h} \tag{C.55}$$

   where h is the characteristic length of the finite element in the direction of the biggest principal stress. The length h is introduced in order to guarantee that a proper amount of energy is dissipated independently of the element size.

5. Evaluate corresponding damage

   - linear softening: if $\varepsilon_0 < \tilde{\varepsilon} < \varepsilon_f$

   $$\omega = \frac{\varepsilon_f}{\tilde{\varepsilon}} \cdot \frac{\tilde{\varepsilon} - \varepsilon_0}{\varepsilon_f - \varepsilon_0} \tag{C.56}$$

   - exponential softening if $\tilde{\varepsilon} > \varepsilon_0$

   $$\omega = 1 - \frac{\varepsilon_0}{\tilde{\varepsilon}} \exp\left(-\frac{\tilde{\varepsilon} - \varepsilon_0}{\varepsilon_f - \varepsilon_0}\right) \tag{C.57}$$

6. Compute principal nominal stresses

   - approach #1:
     for $i = 1, 2, 3$
     if $\sigma_{\text{eff},i} > 0$, $\sigma_i = (1 - \omega)\sigma_{\text{eff},i}$
     else $\sigma_i = \sigma_{\text{eff},i}$
   - approach #2:
     for $i = 1, 2, 3$
     $\sigma_i = (1 - \omega)\sigma_{\text{eff},i}$

7. Construct the stress vector in the original configuration

   $$\boldsymbol{\sigma} = \boldsymbol{T}\boldsymbol{\sigma}_{princ} \tag{C.58}$$

   where $\boldsymbol{T}$ is the stress transformation matrix.

D Case study

D.1 Photographs

Figure D.1: Prepared mold for the four sets of prismatic specimens (different thicknesses) and three sets of cylinders (different heights).

Figure D.2: Specimens at the age of three days, the prisms are just before demolding. Before this picture was taken, all specimens were covered with plastic foil to reduce evaporation.

Figure D.3: Prismatic specimens just after demolding. The circular steel bars attached to the gages pass through the holes in the U-profile which in this picture holds the specimens together.

Figure D.4: The medium sized prismatic specimens coated with epoxy resin and one layer of glass fabric.

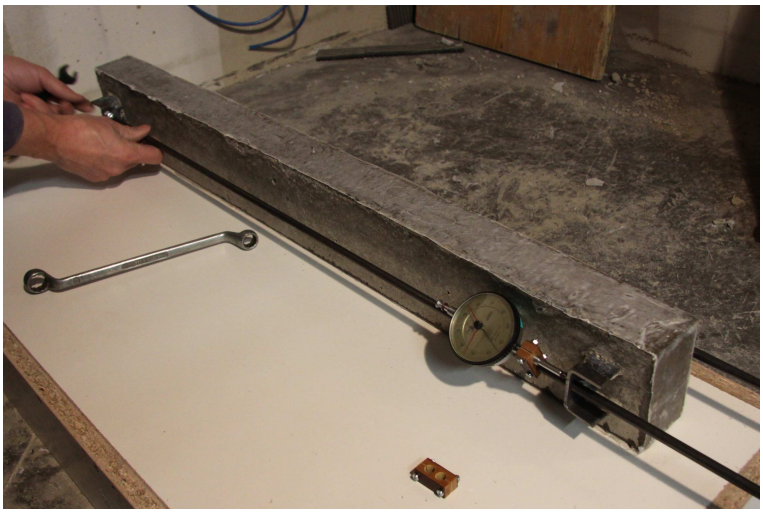

Figure D.5: The measuring equipment is being attached to one of the thinnest prismatic specimens.

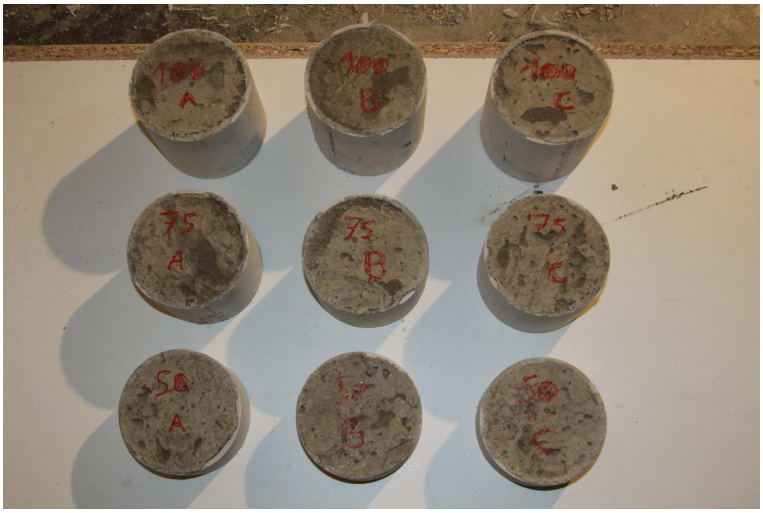

Figure D.6: Nine cylindrical specimens for measurements of weight/moisture loss. Concrete is cast inside a polythene pipes of different heights.

Figure D.7: Instrumented prismatic specimens, zero readings are taken (December 5^{th}).

Figure D.8: Garbage placed on the top of the specimens, some of the gages shifted or destroyed. A yellow truck is parked just few centimeters next to the marks for the precise surveying (February 2014).

D.2 Results of numerical simulations

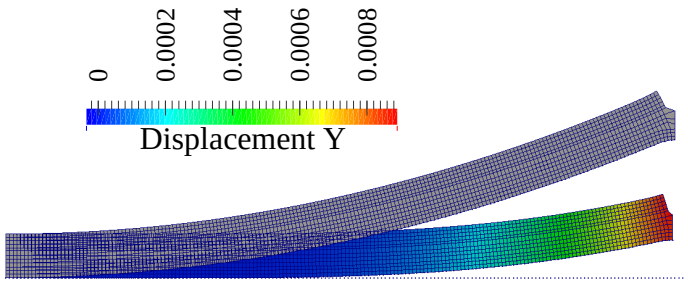

Figure D.9: Comparison of the deformed shape with and without self-weight, $t - t_0 = 90$ days.

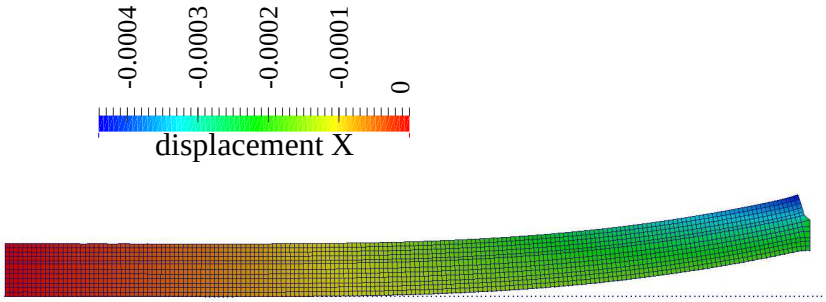

Figure D.10: Displacements in horizontal direction [m], $t - t_0 = 90$ days.

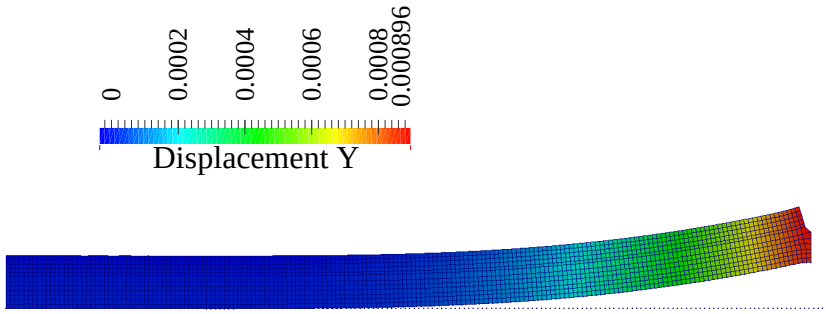

Figure D.11: Displacements in vertical direction [m], $t - t_0 = 90$ days.

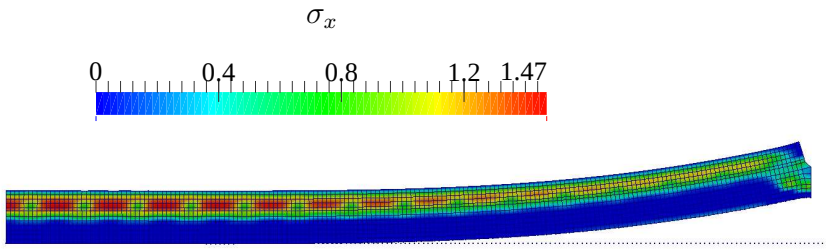

Figure D.12: Normal stress σ_x [MPa], $t - t_0 = 90$ days.

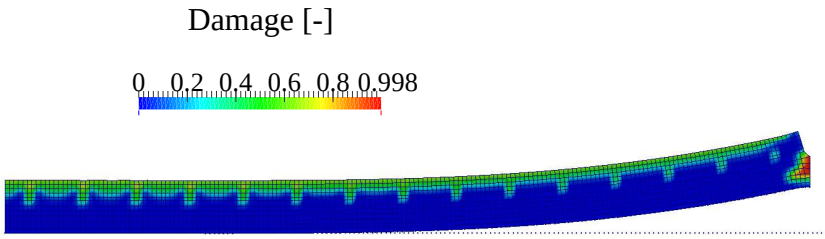

Figure D.13: Scalar damage ω [-], $t - t_0 = 90$ days.

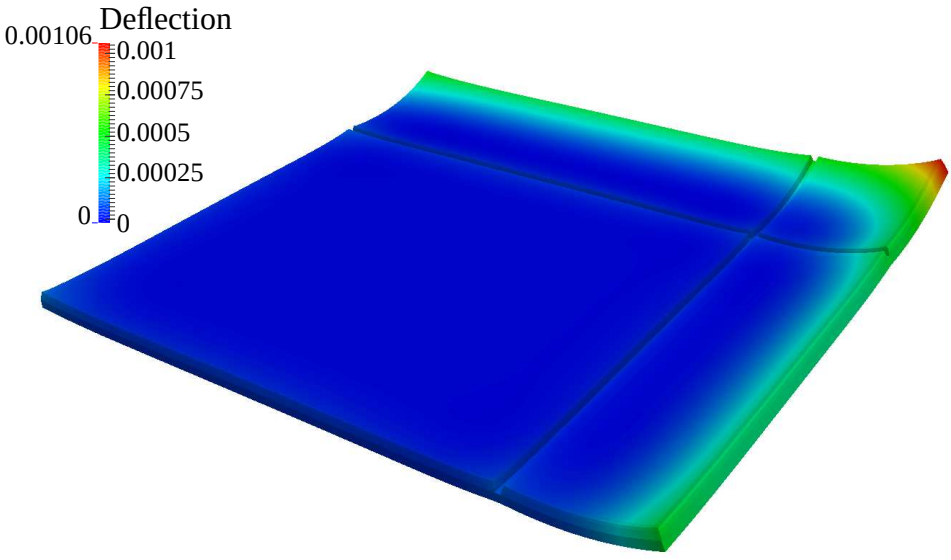

Figure D.14: Results of the FE simulation: vertical deflections [m] for $t - t_0 = 31$ days.

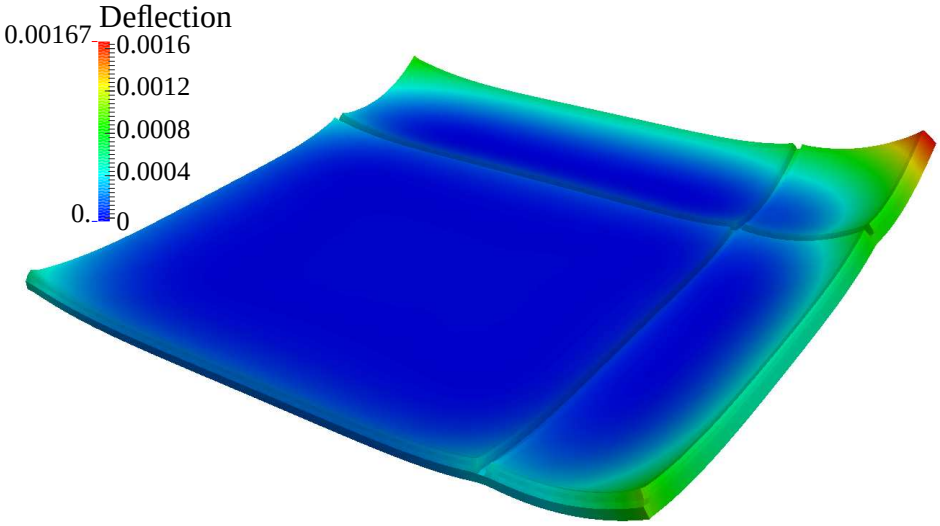

Figure D.15: Results of the FE simulation: vertical deflections [m] for $t - t_0 = 55$ days.

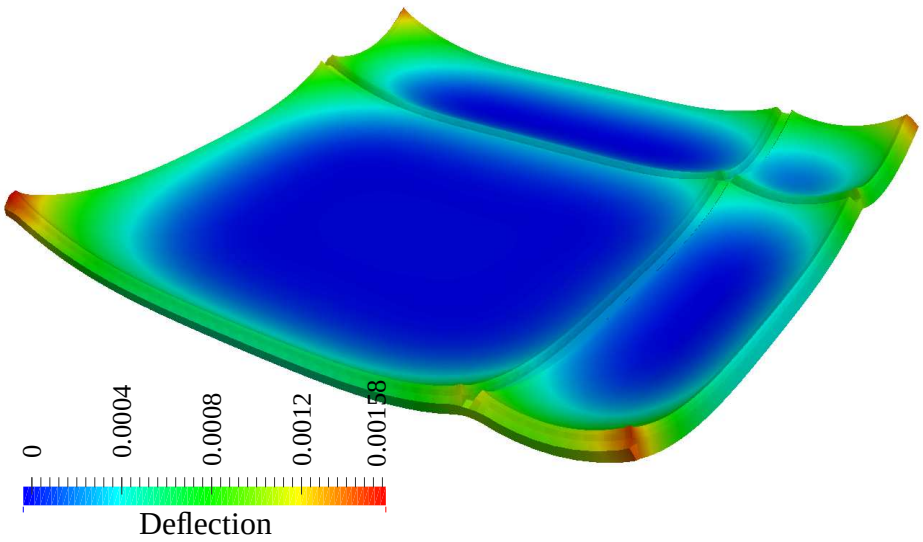

Figure D.16: Results of the FE simulation: vertical deflections [m] for $t - t_0 = 72$ days.

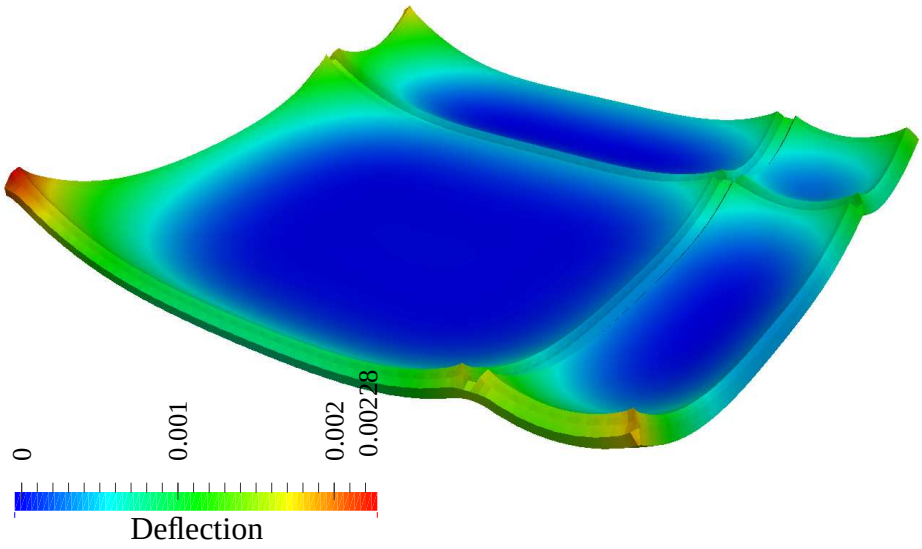

Figure D.17: Results of the FE simulation: vertical deflections [m] for $t - t_0 = 92$ days.

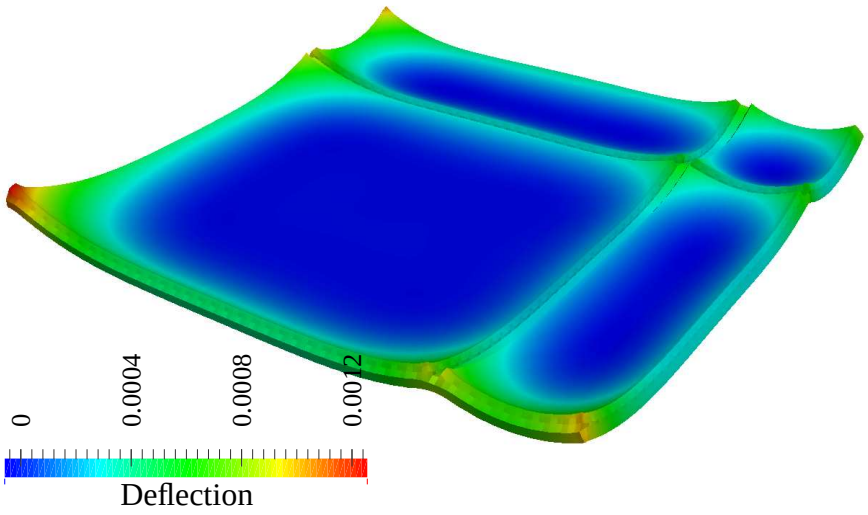

Figure D.18: Results of the FE simulation: vertical deflections [m] for $t - t_0 = 161$ days.

E Publications

E.1 Refereed publications

P. Havlásek and M. Jirásek. Modeling of Concrete Creep Based on Microprestress-Solidification Theory. *Acta Polytechnica*, 52(2):34–42, 2012.

M. Jirásek and P. Havlásek. Accurate Approximations of Concrete Creep Compliance Functions Based on Continuous Retardation Spectra. *Computers and Structures*, 132:155–168, 2014.

M. Jirásek and P. Havlásek. Microprestress-Solidification Theory of Concrete Creep: Reformulation and Improvement. *Cement and Concrete Research*, 60:51–62, 2014.

E.2 Conference papers

P. Havlásek and M. Jirásek. Aproximace funkce poddajnosti založená na spojitém retardačním spektru. In *Engineering Mechanics 2010*, pages 34–40, Prague, Czech Republic, 2010. Ústav termomechaniky AV ČR.

P. Havlásek and M. Jirásek. Modeling of Concrete Creep Based on Microprestress-solidification Theory. In *Proceedings of International Conference on Modelling and Simulation 2010 in Prague*, pages 1–6, Prague, Czech Republic, 2010. České vysoké učení technické v Praze.

P. Havlásek and M. Jirásek. Stanovení hodnot parametrů v teorii solidifikace a mikropředpětí. In *Nano a Makro Mechanika 2010*, pages 37–44, Prague, Czech Republic, 2010. ČVUT, Fakulta stavební.

P. Havlásek and M. Jirásek. Description of Concrete Creep Based on Microprestress-solidification Theory. In *Applied Mechanics 2011*, pages 67–70, Brno, Czech Republic, 2011. Ústav fyziky materiálů AV ČR.

P. Havlásek and M. Jirásek. Modeling of Concrete Creep Based on Microprestress-Solidification Theory. In *NMM 2011 Nano & Macr Mechanics*, pages 35–44, Praha, Czech Republic, 2011. České vysoké učení technické v Praze, Fakulta stavební.

P. Havlásek and M. Jirásek. Určení hodnot parametrů v modelu B3 a v teorii solidifikace a mikropředpětí In *Juniorstav 2011 - Sborník anotací*, pages 216, Brno, Czech Republic, 2011. Vysoké učení technické v Brně, Fakulta stavební.

R. Pukl, P. Havlásek, T. Sajdlová and V. Červenka. Advanced Modelling of Fibre Reinforced Concrete Structures. In *The 7th Central European Congress on Concrete Engineering 2011*, pages 381–384, Lausanne, Switzerland, 2011. fib - fédération internationale du béton.

R. Pukl, T. Sajdlová and P. Havlásek. Identification of material parameters for nonlinear modeling of fibre reinforced concrete structures. In *Fibre Concrete 2011 - Technology, Design, Application (Collection of Abstracts)*, pages 45–46, Praha, Czech Republic, 2011. České vysoké učení technické v Praze, Fakulta stavební.

P. Havlásek and M. Jirásek. Modeling of Concrete Creep Based on Microprestress-Solidification Theory. In *Proceedings of The 9th fib International PhD Symposium in Civil Engineering*, pages 453–458, Karlsruhe, Germany, 2011. Karlsruher Institut für Technologie.

P. Havlásek and M. Jirásek. Modeling of Concrete Creep Based on Microprestress-Solidification Theory. In *14th International Conference Applied Mechanics 2012 - Conference Proceedings*, pages 69–72, Plzeň, Czech Republic, 2011. Západočeská Universita.

P. Havlásek and M. Jirásek. Modeling of Concrete Creep Based on Microprestress-Solidification Theory. In *Life-Cycle and Sustainability of Civil Infrastructure Systems*, pages 1390–1394, Leiden, The Netherlands, 2012. CRC Press/Balkema.

P. Havlásek and M. Jirásek. Modeling of Nonlinear Moisture Transport in Concrete. In *Proceedings of the 3rd Conference Nano and Macro Mechanics NMM 2012*, pages 53–62, Praha, Czech Republic, 2012. České vysoké učení technické v Praze, Fakulta stavební.

P. Havlásek and M. Jirásek. Deficiencies of the Microprestress-Solidification Theory. In *Proceedings of the 4th Conference Nano & Macro Mechanics*, pages 51–60, Prague, Czech Republic, 2013. Czech Technical University in Prague.

Z.P Bažant, P. Havlásek and M. Jirásek. Microprestress-Solidification Theory: Modeling of Size Effect on Drying Creep. In N. Bicanic, H. Mang, G. Meschke, and R. de Borst, editors, *Computational Modelling of Concrete Structures - Proceedings of EURO-C 2014*, pages 749–758, EH Leiden, The Netherlands, 2014. CRC Press/Balkema.

P. Havlásek and M. Jirásek. Deficiencies of the Microprestress-Solidification Theory for Concrete Creep and Shrinkage. In *Juniorstav 2014 - Sborník anotací*, pages 228, Brno, Czech Republic, 2014. Vysoké učení technické v Brně, Fakulta stavební.

E.3 Other publications

P. Havlásek and M. Jirásek. Modeling of concrete creep based on Microprestress-solidification theory. In J. Kruis, editor, *Computer and Experimental Analysis of Civil Engineering Materials and their Multilayered Systems II*, pages 147–161, Prague, Czech Republic, 2010. CTU, Faculty of Civil Engineering.

P. Havlásek and M. Jirásek. Modeling of concrete creep based on Microprestress-solidification theory. In J. Kruis, editor, *Computer and Experimental Analysis of Civil Engineering Materials and their Multilayered Systems III*, pages 194–206, Prague, Czech Republic, 2011. CTU, Faculty of Civil Engineering.

P. Havlásek and M. Jirásek. Modeling of Nonlinear Moisture Transport in Concrete. In J. Kruis, editor, *Computer and Experimental Analysis of Civil Engineering Materials and their Multilayered Systems IV*, pages 134–143, Prague, Czech Republic, 2012. CTU, Faculty of Civil Engineering.